THE UNIVERSITY *of* EDINBURGH

The University of Edinburgh

A cell-wide web of cytoplasmic nanocourses coordinates calcium signalling

By

Jingxian Duan

Thesis submitted for the degree of doctor of philosophy at the University of Edinburgh

2018

Disclaimer

I, Jingxian Duan, composed the thesis and performed all the experiments presented in this thesis unless stated otherwise in the text. No part of my work has been or is being submitted for any other degree or qualification. Any included published data are my own work, except where indicated throughout the thesis and cited appropriately, and no full publication has been included.

Signature:

Date:

Acknowledgements

First of all, I would like to thank my supervisor, Prof. A Mark Evans, for his continuous guidance, advise, patience and supports throughout the years. I have learnt so much from him, without him I would never become who I am.

I would also like to thank all the current and former members of the Evans' lab, Sandy, Javi, Jorge, Olu and Sophie. Thank you all for taking me in, being my friends when I needed it the most. Living alone in a foreign country for the first time is not an easy task, but you guys make it a lot more enjoyable.

I must say "thank you" to my parents, although they cannot understand English. I started the degree self-funded, it was them who supported me with their savings and gave me the encourage to move forward. Speaking of money, I must also thank the China Scholarship Council, who funded me since the second year of my PhD. Money cannot buy happiness, but there was no happiness at all when I was under the pressure of self-funding. I was truly lucky, that was the best thing that happened to me during this PhD.

There were countless nights when I had to work very late and went home with an empty stomach. I would like to thank Tesco and Sainsbury, for providing food, light and warmth, which comforted me at least a little bit in those cold nights.

Finally, I would like to thank Xu, my boyfriend, who came over for a year when I needed company; listened to my complaints when I lost my mind; comforted me when I burst into tears; encouraged me when I hit the bottom; and transferred me money when I want to buy things that I could not afford. I would never make this far without him.

This PhD is a great adventure, and now I'm ready to come home.

Table of Contents

Abstract

Ca^{2+} signals determine smooth muscle contraction and the switch from a contractile to a migratory-proliferative phenotype(s), which requires changes in gene expression. However, the mechanism by which different Ca^{2+} signals are selective for these processes is enigmatic. In the thesis, I built on the “panjunctional sarcoplasmic reticulum” hypothesis, and described the evidence in support of the view that a variety of Ca^{2+} pumps and release channels, with different kinetics and affinities for Ca^{2+}, are strategically positioned within the cytoplasmic nanocourses of pulmonary arterial smooth muscle cells (PASMCs), and they serve to demarcate different Ca^{2+} signalling. Nanocourses of the SR are formed in the perinuclear, extraperinuclear, subplasmalemmal regions and the nucleus. Different subtypes of ryanodine receptors (RyRs) are targeted to those nanocourses. Immunocytochemistry results suggest that RyR1s was preferentially targeted to the subplasmalemmal and nuclear nanocourses of PASMCs, they gave rise to a spatially restricted Ca^{2+} signal within the nanocourses upon stimulation, without affecting global Ca^{2+} concentration. The Ca^{2+} signals in the subplasmalemmal nanocourses were shown to induce arterial smooth muscle cell relaxation. On the other hand, the RyR2 and 3 were shown to target to the perinuclear and extraperinuclear nanocourses. Upon stimulation, they generate propagating Ca^{2+} waves in the cytoplasmic nanocourses, which trigger arterial smooth muscle cell contraction. However, during this process, no Ca^{2+} transient was observed within the subplasmalemmal nanocourses, suggesting that the regulation of both contraction and relaxation of smooth muscle cells are achieved by spatially restricted Ca^{2+} signals within different nanocourses.

Invaginations of the nucleoplasmic reticulum in arterial myocytes form trans-nuclear networks of cytoplasmic nanospaces, generate Ca^{2+} signals by strategically positioned Ca^{2+} pumps (SERCA1) and release channels (RyR1). Within a subpopulation of nuclear invaginations, evoked Ca^{2+} signals via ryanodine receptors exhibited spatial and temporal separation from adjacent Ca^{2+} signals within a single “activated” nuclear invagination, and also from those Ca^{2+} signals arising within different nuclear invaginations. Moreover, nuclear invaginations provide sites for transcriptional suppression, because lamin A and/or emerin line the entire surface of their inner nuclear membranes and co-localise with nesprin-1 positive puncta. More intriguing still, a subpopulation of these nuclear invaginations harboured punctate regions of colocalisation between lamin A and the suppressive heterochromatin mark

H3K9me2, while emerin-positive invaginations harboured puncta of BAF (Barrior to autointegration factor) co-localisation and thus an alternative pathway to the regulation of gene expression. I propose that nuclear invaginations form cytoplasmic nanotubes within which nano-patterning of Ca^{2+} signals may support stochastic modulation of transcriptional suppressors.

Together, the cytoplasmic nanocourses form a cell-wide web for Ca^{2+} signalling and the regulation of various arterial smooth muscle functions, ranging from the regulation of blood pressure by vasodilation and vasoconstriction to gene expression.

Lay Summary

Ca^{2+} signals determine smooth muscle functions. However, the mechanism by which different Ca^{2+} signals select for various processes is enigmatic. It was generally accepted that the bulk cytoplasm serves as a container of diverse ions that can diffuse freely across the entire cytoplasm. In this thesis, this understanding is challenged. The Ca^{2+} releasing channels are targeted to the membrane of the intracellular Ca^{2+} storage organelles where they serve to transport the Ca^{2+} from the Ca^{2+} store to the cytoplasm. My data suggest that instead of diffusing across the cytoplasm, the released Ca^{2+} is restricted within nanospaces defined by the membrane of Ca^{2+} stores. These nanospaces were named as cytoplasmic nanocourses, and these cytoplasmic nanocourses extend from the cell periphery to the nucleus, forming a cell-wide web. Within the nanocourses, unique Ca^{2+} signals are generated for the regulation of smooth muscle functions. Due to the fact that the Ca^{2+} signals are retained within the nanocourses, global Ca^{2+} concentration remains unaffected. Moreover, Ca^{2+} receptors that target to different nanocourses seem to show distinct properties, this determined that the Ca^{2+} signals generated within different nanocourses exhibit distinct characteristics. As the result, varied Ca^{2+} signals are formed, and they are proposed to modulate different smooth muscle functions. To summarize, the formation of the cell-wide web of cytoplasmic nanocourses allowed precise and elaborated regulation of diverse smooth muscle functions by a single signalling ion.

List of Abbreviations

BAF---Barrier to Autointegration Factor

BKca---Big Potassium (large-conductance) Calcium-activated Channel

cADPR--- cyclic Adenosine Diphosphate-Ribose

CICR---Calcium induced Calcium Release

CSQ--- Calsequestrin

ER---Endoplasmic Reticulum

H3k9me2---Histone 3 lysine-9 dimethylation

INM---Inner Nuclear Membrane

IP3R---Inositol 1,4,5-trisphosphate receptor

LAD---Lamin Associated Domain

LINC---Linker of Nucleoskeleton and Cytoskeleton

MHC---Myosin Heavy Chain

mTOR--- mechanistic Target of Rapamycin

NAADP---Nicotinic Acid Adenine Dinucleotide Phosphate

NCX---Na^{+}/ Ca^{2+} exchanger

NE---Nuclear Envelope

NET---Nuclear Envelope Transmembrane

NMJ--- Neuromuscular Junction

NR---Nucleoplasmic Reticulum

ONM---Outer Nuclear Membrane

PASMC---Pulmonary Arterial Smooth Muscle Cell

PM---Plasma Membrane

ROC--- Receptor-Operated Ca^{2+} Channel

RYR---Ryanodine Receptor

SERCA--- Sarco/Endoplasmic Reticulum Ca^{2+}-ATPase

SOC---Store-Operated Ca^{2+} Channel

SR---Sarcoplasmic Reticulum

TG---Thapsigargin

TPC---Two Pore Channel

TTC---Tetracaine

2APB---2-Aminoethoxydiphenyl borate

Chapter 1: General Introduction

1.1 Smooth muscle physiology

The blood pressure is regulated by the constriction and dilation of blood vessels, because the blood vessels are built with smooth muscle cells that can contract or relax in response to biological cues. The walls of blood vessels are composed of, from outside to inside, loose connective tissues, layers of smooth muscle cells with elastic lamina, basal lamina and a thin sheet of endothelial cells (Alberts, 2002). Among these, smooth muscle cells count for the vast majority. Moreover, it has been reported that vascular smooth musle cell contraction can produce a change in blood pressure (Crowley et al., 2005, Brozovich et al., 2016), which puts smooth muscle cells in an important position when discussing hypentension and health.

Vascular smooth muscle contraction is regulated by intracellular Ca^{2+} signalling. Local increase in Ca^{2+} concentration would saturate the four Ca^{2+} binding sites on camodulin, which activates myosin light chain kinase. The kinase would phosphorylate the light chains of myosin which generate the force that drives smooth mucle contraction (Wilson et al., 2002). On the other hand, smooth muscle relaxation is driven by the net loss of intracellular Ca^{2+} level which opposes contraction. The increase of Ca^{2+} concentration near the plasma membrane could activate the BKca channels (Ca^{2+} activated big potassium channels), causing memebrane hyperpolarization and consequencial closing of voltage gated Ca^{2+} channels at the plasma membrane, while favouring Ca^{2+} extrution via the Na^{+}/Ca^{2+} exchangers (Boittin et al., 2003, Nelson et al., 1995, Khalil et al., 2017). To understand smooth muscle physiology, one must start with intracellular Ca^{2+} signalling.

1.2 Intracellular Ca^{2+} signalling

Ca^{2+} is a chemical messenger that serves to convey information for the regulation of a variety of cellular processes including gene expression, muscle contraction and relaxation, neurosecretion and programmed cell death. To understand the concept of Ca^{2+} signalling, one must bear in mind that Ca^{2+} causes protein and nucleic acid aggregation, which breaks lipid membranes and leads to the precipitation of phosphates (Case et al., 2007, Tsien and Barrett, 2005). Consequently, high intracellular Ca^{2+} concentration hampers the cells. Therefore, Ca^{2+} must be stowed

away, and a Ca^{2+} homeostatic system must be developed to maintain the intracellular Ca^{2+} concentration at a low level. This in turn makes Ca^{2+} a favourable signalling molecule, because the intracellular Ca^{2+} concentration is maintained at around 100 nM whereas the extracellular Ca^{2+} concentration is significantly higher (Case et al., 2007). As the result, it was postulated that a small influx of Ca^{2+} from the extracellular space could effectively raise the intracellular Ca^{2+} concentration to a level that induces significant changes (Tsien and Barrett, 2005).

Due to the cytotoxicity of high intracellular Ca^{2+} concentration, it now becomes clear that the intracellular Ca^{2+} handling is not a simple case of modulating the Ca^{2+} concentration within the "bulk" cytoplasm, the intracellular Ca^{2+} signals must be spatially restricted (Case et al., 2007). However, to reach the cell interior, the Ca^{2+} flux originating from the extracellular space must travel a long distance. To overcome the problem and to maintain intracellular Ca^{2+} homeostasis, intracellular Ca^{2+} stores were developed. For example, the endoplasmic reticulum (ER) is an intracellular Ca^{2+} store which exhibits high luminal free Ca^{2+} concentration. The total ER Ca^{2+} concentration within its lumen is around 200 µM or more (Mogami et al., 1998), which is 2000 times greater than the intracellular free Ca^{2+} concentration. The ER forms a wide-spread network within the cell, with Ca^{2+} releasing channels and Ca^{2+} transporters targeted to the ER membranes (Mekahli et al., 2011). This allows for the control of the site of action by dictating local Ca^{2+} release from the intracellular Ca^{2+} stores. On the other hand, rapid closing of the Ca^{2+} releasing channels leads to the dissipation of the signals by diffusion and local buffering (i.e. moving the Ca^{2+} back to the ER by the Ca^{2+} transporters)(Cardenas et al., 2010, Case et al., 2007, Mekahli et al., 2011). Therefore, intracellular Ca^{2+} stores facilitate the generation of spatially and temporally restricted Ca^{2+} signals whilst avoiding the detrimental effect of universal and prolonged rises in Ca^{2+}. Furthermore, it is the spatial and temporal characteristics of the Ca^{2+} signals that encode the messages, allowing a single ion to regulate a wide variety of physiological processes (i.e. from muscle contraction to gene expression)(Evans et al., 2016).

The means by which Ca^{2+} coordinates various physiological processes are far more complicated than the simple sketch depicted above, and the investigation of this must build on top of the understanding of how Ca^{2+} is sequestered and released from the

intracellular Ca^{2+} stores, and how the Ca^{2+}signals are restricted once they are released from the Ca^{2+} stores.

1.3 The endoplasmic/sarcoplasmic reticulum serves as the largest mobilisable intracellular Ca^{2+} store

The endoplasmic reticulum (ER) is the largest organelle in most of the mammalian cells (Tagaya and Simmen), this dynamic structure is essentially an interconnected network formed by tubules and rough sheets. The sizes of the ER sheets varies, but the luminal spaces of the sheets are generally around 50 nm (Bernales et al., 2006). The sheets appear in a stacked conformation and are connected through regions of twisted membranes with helical edges (Terasaki et al., 2013). A large number of ribosomes can be identified on the cytoplasmic surface of the ER sheets, and these represent the main sites of protein synthesis, folding and post-translational modifications. In contrast, fewer ribosomes can be identified on the cytosolic surface of ER tubules. The ER tubules are smooth and curvy, forming a dynamic network that is constantly reconfigured. The primary function of the ER includes protein synthesis, folding and modification, lipid biogenesis and translocation (Schwarz and Blower, 2016). More importantly, the ER serves as the major intracellular Ca^{2+} store, and this is the aspect that my thesis focuses on.

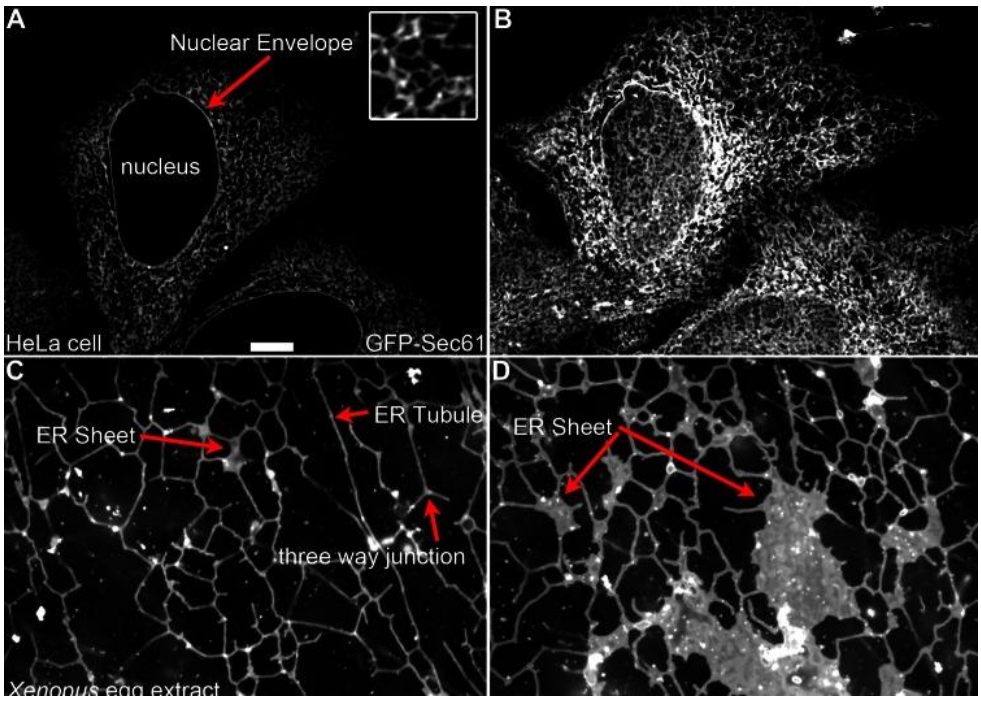

Figure 1.1 Structure of the endoplastic reticulum.

(A) Location of the ER in relation to the nuclear envelope (red arrow).

(B) ER morphology.

(C) Morphology of ER sheets and tubules,

(D) ER sheets containing ribosomes (red arrow). Scale bar is 10 mM. Figure adapted from "The endoplasmic reticulum: structure, function and response to cellular signalling", by Schwarz and Blower (Schwarz and Blower, 2016).

The function of the ER is tightly related to its structure (Schwarz and Blower, 2016). The ER can be sub-divided into the rough ER and the smooth ER. The rough ER is characterized by the large number of membrane bound ribosomes found on the ER surface, and is majorly involved in protein synthesis and secretion. The smooth ER, on the other hand, lacks the membrane bound ribosomes, provides the primary releasable Ca^{2+} store and also supports the synthesis of lipids and steroids. In muscle cells, a form of specialized smooth ER is present, and it is referred to as the sarcoplasmic reticulum (SR). Electron microscopy of smooth muscle showed that the SR forms a network of membranes (Figure 1.1) composed of tubules and sacs. The SR network is wide-spread across the cell, the peripheral SR is close to the plasma membrane and caveolae, whereas the central SR projects deeper into the cell, forms

close associations with the mitochondria and is continuous with the outer nuclear membrane (ONM; see review (Pozzan et al., 1994)).

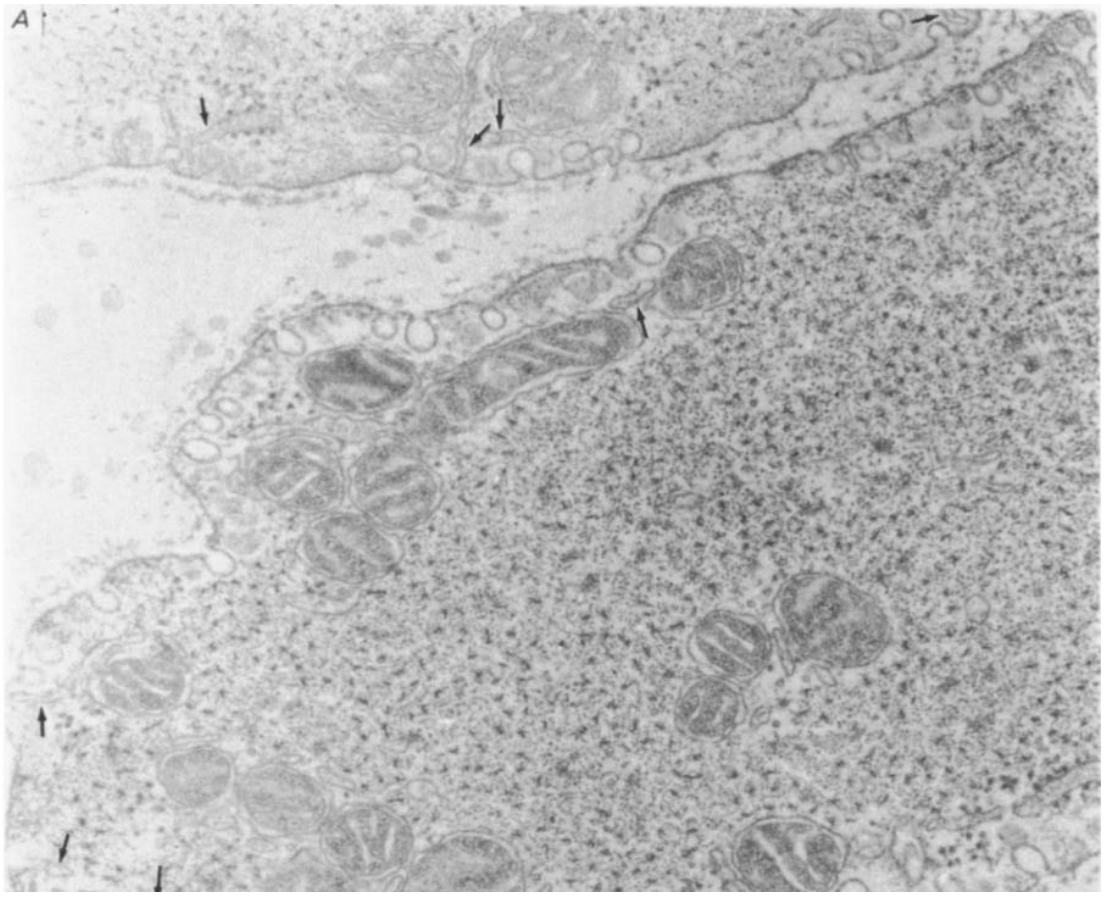

Figure 1.2 Ultrastructure of the sarcoplasmic reticulum under electron microscopy.

The sarcoplasmic reticulum in a smooth muscle cell from guinea pig portal vein. Peripheral sarcoplasmic reticulum is indicated by arrows. Figure adapted from "Release and recycling of Ca^{2+} by the sarcoplasmic reticulum in guinea-pig portal vein smooth muscle", by Bond et al (Bond et al., 1984).

The function of the SR in smooth muscle cells has been extensively studied. One early investigation used strontium as the surrogate for Ca^{2+}, and showed that the strontium was accumulated in the SR of aorta and pulmonary arterial smooth muscle cells. It was postulated that Ca^{2+} is stored in the SR and it may serve as the activator for contraction (Somlyo and Somlyo, 1971). More direct evidence came from the

electron-probe X-ray microanalysis which showed that the Ca^{2+} concentration within the SR decreased upon agonist stimulation, and that Ca^{2+} is released from and recycled back to the SR during muscle contraction and relaxation (Kowarski et al., 1985, Bond et al., 1984). This release and recycling of Ca^{2+} to and from the SR proved that the SR is a mobilisable intracellular Ca^{2+} store which harbours Ca^{2+} transporters, Ca^{2+} storage proteins and Ca^{2+} releasing channels.

1.3.1 Sequestration of Ca^{2+} by the sarcoplasmic/endoplasmic reticulum Ca^{2+}ATPase

Intracellular Ca^{2+} can be sequestrated into the sarcoplasmic /endoplasmic reticulum (S/ER) by the sarcoplasmic/endoplasmic reticulum Ca^{2+} ATPases (SERCAs). SERCA proteins are encoded by ATP2A1, 2 and 3 genes located on 3 chromosomes, and by alternative splicing they transcribe into more than 14 SERCA mRNAs that can be further translated to species and tissue specific SERCA isoforms (Lipskaia et al., 2014, Chemaly et al., 2017). For example, the APT2A1 gene encodes for adult SERCA1a and neonatal SERCA1b, both of them were identified in skeletal muscle. APT2A 2 gene encodes for SERCA2a and SERCA2b, SERCA2a is the dominant isoform found in cardiac muscle whereas both of them were identified in smooth muscles. APT2A encodes for SERCA3a-f, that have been found co-expressed with SERCA2b in many cell types including endothelial cells of the intestine, salivary glands and cerebellar purkinje neurons (see review (Chemaly et al., 2017)).

The SERCAs are referred to as Ca^{2+} pumps due to the fact that they bring the cytosolic free Ca^{2+} into the lumen of S/ER and other Ca^{2+} stores, maintaining Ca^{2+} homeostasis in the cytoplasm. To “pump” the Ca^{2+} to the S/ER store, the SERCAs undergo a catalytic cycle as Figure 1.2 demonstrates. The cycle is the transformation between two conformational states, namely the E1 and E2. The major difference between the E1 and E2 conformation is that E1 shows two Ca^{2+} binding sites with high affinity for Ca^{2+}, when they are facing the cytoplasm; whereas in E2 the Ca^{2+} binding sites exhibit a low affinity for Ca^{2+} when they are facing the lumen of the S/ER. Upon binding to Ca^{2+}, the SERCA is in the $2Ca^{2+}$-E1-ATP form, which is then phosphorylated to yield $2Ca^{2+}$-E1-P. In this high-energy phospho-intermediate, the two bound Ca^{2+} ions are occluded. Next, it is converted to the low-energy form $2Ca^{2+}$-E2-P, during which the

Ca^{2+} binding sites are oriented towards the S/ER lumen and the affinity for Ca^{2+} is decreased. Finally, the Ca^{2+} is released to the S/ER lumen, and the SERCA in E2 state is transformed back to the E1 state (Wuytack et al., 2002). The sequestration of Ca^{2+} is achieved by SERCAs, but the refilling of the SR is a far more complicated process that involves multiple proteins and intracellular structures, and the subject will be discussed in detail in relation to the PM-SR nanojunction in section 1.6.3.1.

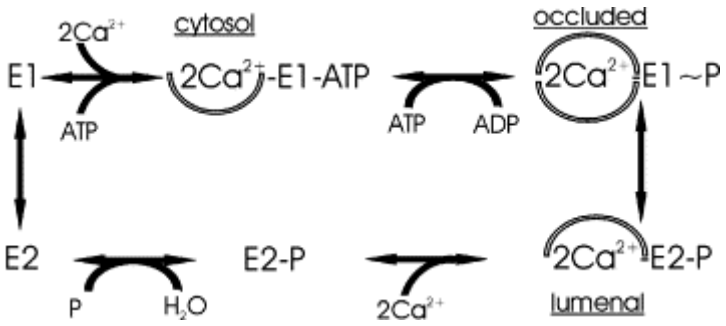

Figure 1.3 Scheme of the E1/E2 model of the SERCA catalytic cycle.

Basic steps of the SERCA catalysis cycle is shown, with E1 and E2 representing the 2 conformational states of SERCAs. Figure adapted from “Molecular physiology of the SERCA and SPCA pumps”, by Wuytack et al (Wuytack et al., 2002).

The SERCA isoforms share structural similarities. However, they display functional variations by exhibiting diverse affinities for Ca^{2+} and speeds of action. One early experiment reported that SERCA2b has a higher affinity for Ca^{2+} ($K_{0.5}$ 0.17±0.01μM) compared to SERCA2a ($K_{0.5}$ 0.31±0.02μM) (Verboomen et al., 1992). SERCA1 exhibits a similar affinity for Ca^{2+} to SERCA2a, whereas SERCA3 displays 3 to 4-fold lower affinity for Ca^{2+}. Moreover, SERCA2b and SERCA3 display lower turnover rates and lower Vmax compared to SERCA2a and SERCA1 (Verboomen et al., 1994, Lytton et al., 1992).

The inhibition of SERCA can be achieved by endogenous proteins or small molecules. For example, phospholamban (PLN) and sarcolipin (SLN) are two SR membrane proteins that could effectively inhibit SERCA activity. PLN is a 6080 Da

transmembrane protein that is found in the S/ER of muscle cells, it serves as a reversible inhibitor of SERCA by decreasing SERCA's affinity for Ca^{2+} while having no effect on its Vmax (Simmerman and Jones, 1998). The inhibition can be reversed by phosphorylating the PLN at Ser16 by PKA and/or Thr17 by CaMKll (Wuytack et al., 2002, Sharma et al., 2001). Similarly, SLN is a 3733 Da transmembrane protein that can be found in the S/ER. It was reported to increase the K_m for Ca^{2+} thus to decrease the affinity of SERCAs (Odermatt et al., 1998). Similar to PLN, the inhibitory effect of SLN on SERCAs can be reversed by phosphorylation at Ser4 and Thr5 by serine threonine kinase (Gramolini et al., 2004). Moreover, SERCAs can be inhibited by either thapsigargin or cyclopiazonic acid (Lytton et al., 1991, Martinez-Azorin, 2004), blocking SERCAs with thapsigargin was shown to deplete the S/ER Ca^{2+} store (Du et al., 1994).

In terms of post-translational modifications, the activity of SERCA2a can be modulated by sumoylation. In the cardiomyocytes of heart failure patients, restoring sumoylation increased SERCA2a activity and prolonged the lifetime of the cell (Kho et al., 2011). Moreover, glutathionylation of SERCA at cysteine 674 residue activates SERCA and was shown to increase Ca^{2+} uptake (Adachi et al., 2004).

The activation of SERCAs can be achieved by the interaction with small molecules or transmembrane micropeptides. For example, CDN1163 was shown to be an allosteric activator of SERCA2, increasing SERCA2b activity in liver cells (Kang et al., 2016). 6-gingerol was also shown to be a novel cardiotonic agent that activates SERCAs in skeletal and cardiac SR (Kobayashi et al., 1987). On the other hand, DWORF, a transmembrane micropeptide, was shown to increase SR Ca^{2+} load by enhancing the activity of SERCA2a. It effectively competes with SERCA inhibitors (i.e. phospholamban) for binding to SERCA2a (Nelson et al., 2016).

1.3.2 Ca^{2+} release by the sarcoplasmic / endoplasmic reticulum

Two families of Ca^{2+} releasing channels are targeted to the S/ER, they are the ryanodine receptors (RyRs) and Inositol 1,4,5-trisphosphate receptors (IP_3Rs) (Curtis et al., 2004, Jaggar et al., 1998, Smith and Parker, 2009, Dickinson et al., 2012, Mekahli et al., 2011).

1.3.2.1 Ca^{2+} release from the RyRs

In mammalian cells, 3 isoforms of RyRs have been identified. RyR1 was first isolated from skeletal muscles (Takeshima et al., 1989) whereas RyR2 was widely expressed in cardiac muscles (Otsu et al., 1990), RyR3 was found originally in the brain (Hakamata et al., 1992). Each of the three isoforms of RyRs can be selectively expressed in certain cell types, as described above. However, they can also co-exist in a single cell type. For example, RyR1, RyR2 and RyR3 were found in the SR of pulmonary arterial smooth muscle cells (Clark et al., 2010a, Yang et al., 2005).

The RyRs are the largest ion channels discovered to date (Lanner et al., 2010). The structure of the receptor has been extensively studied. All three subtypes are similar, sharing ~65% sequence homology. RyRs form homotetramers in the shape of a square prism. They are composed of cytoplasmic domains and transmembrane domains. The carboxy terminus of the protein forms the transmembrane domain, where the ion-conducting pore is formed. The cytoplasmic domains are also referred to as the “foot”, which is an area full of cavities and microstructures that constitutes the binding sites for small molecules and modulator proteins. The cytoplasmic domains are subdivided into 15 subdomains including the clamps, handle, central rim and column. Notably, the clamps undergo major conformational changes during the opening and closing of the channel, and they are possibly the sites for modulation by regulatory molecules (Lanner et al., 2010).

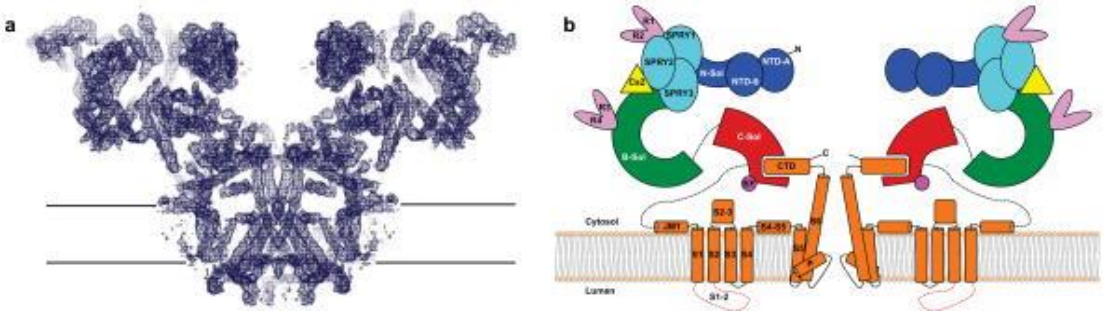

Figure 1.4 Structure of RyR1

(A) Structure of RyR1 in relation to the SR membrane indicated by black lines.

(B) As for **(A),** but showing the schematic model. Figure adapted from “Structure of a mammalian ryanodine receptor”, by Zalk et al (Zalk et al., 2015).

As the name indicates RyRs can be activated by ryanodine, but only at the nanomolar range. When exposing to ryanodine at 10-100 micromolar or more, RyRs are inhibited (Meissner, 1986). Ca^{2+} opens RyRs, which allows further Ca^{2+} release from the SR. This signal amplification process is called Ca^{2+} induced Ca^{2+} release (CICR). However, Ca^{2+} can also trigger the closing of RyRs. This dual-role of Ca^{2+} is supported by different binding sites on RyRs, each exhibiting different affinities for Ca^{2+}. The resultant relationship between RyR open probability (P_0) and Ca^{2+} concentration is bell-shaped (Meissner et al., 1986). Moreover, it should be noted that although all the RyR subtypes have similar thresholds for activation by Ca^{2+} when cytoplasmic Ca^{2+} concentration is higher than 100 nM, each RyR subtypes display different half maximal activation by Ca^{2+} (EC_{50}) and threshold for inactivation by Ca^{2+} (Chen et al., 1997, Li and Chen, 2001).

RyRs can also be modulated by multiple intracellular proteins. Calmodulin is a protein containing 4 EF-hand Ca^{2+} motifs, it was reported that a single calmodulin bind to a single RyR monomer in a Ca^{2+} independent manner (Balshaw et al., 2001). However, other studies showed that it binds to RyRs in the absence or presence of Ca^{2+} for the regulation of Ca^{2+} release from the SR (Song et al., 2011). Calmodulin decreases the open probability of RyR2 in the presence of Ca^{2+} in the micromolar range (Balshaw et al., 2001). Moreover, calmodulin was reported to increase the duration of closing time and decrease the frequency of opening of RyRs, leading to the cessation of Ca^{2+} release (Xu and Meissner, 2004). Intriguingly, when calmodulin binds to RyR1, it appears to inhibit RyR1 activity in the presence of micromolar Ca^{2+} concentrations, while activating RyR1 at nanomolar Ca^{2+} concentrations (Balshaw et al., 2001, Buratti et al., 1995). This biphasic regulation of RyR activity by calmodulin suggests that the paradox might be more complicated than people manage to understand.

RyRs are also subject to phosphorylation and dephosphorylation by kinases and phosphatases. It was reported that the PPA, PP2A and PKA bind to RyR2 through their adaptor proteins spinophilin, PR130 and Makap. The PKA/Makap, PPA/spinophilin and PP2A/PR130 complexes target the RyRs via the LZ motifs between the adaptor proteins and the RyRs (Marx et al., 2001). Moreover, 3 phosphorylation sites on the RyRs have been identified. Ser2080 in RyR2 and Ser2843 in RyR1 can be phosphorylated by PKA and CaMKII; Ser2814 in RyR2 can

be phosphorylated by CaMKII; and Ser2030 of RyR2 can be phosphorylated by PKA as reviewed by Song et al (Song et al., 2011). The phosphorylation state of RyRs is determined by the interplay between the phosphatases and the kinases, the impact of the phosphorylation is controversial and thus will require further investigation before any conclusion can be made.

In relation to my thesis, it is important to note that the activity of RyRs can also be regulated by exogenous application of calcins (Xiao et al., 2016), the membrane traversing proteins derived from scorpion venom, and can be blocked by tetracaine (Laver and van Helden, 2011, Xu et al., 1993). Maurocalcine is a RyR1 agonist, it selectively activates RyR1, locking it in a long-lasting subconductance which results in sustained Ca^{2+} release from the S/ER (Chen et al., 2003). The selectivity of maurocalcine is supported by the fact that while it is able to bind to RyR2 but the binding fails to open the channel (Altafaj et al., 2007). In contrast, tetracaine is a non-selective antagonist of RyRs, it was shown to block all three types of RyRs (Laver and van Helden, 2011).

1.3.2.2 Ca^{2+}release from the IP_3Rs

IP_3Rs also mediate Ca^{2+} release from the S/ER. In the case of IP_3Rs, the most common understanding is that the IP_3 binds to and gates IP_3Rs on the S/ER, resulting in Ca^{2+} release from the S/ER into the cytoplasm (Berridge et al., 2000). Three IP_3R subtypes have been identified in mammalian cells (Blondel et al., 1993), namely IP_3R1, 2 and 3. The expression of IP_3Rs subtypes exhibits tissue specificity. IP_3R1 is the predominantly expressed subtype in arterial smooth muscle, with little co-expression of IP_3R2 and IP_3R3 (Grayson et al., 2004). By contrast, rat portal vein myocytes mainly express IP_3R1 and IP_3R2, while urethral myocytes express IP_3R1 and IP_3R3 (Wojcikiewicz, 1995, Morel et al., 2003, Wray and Burdyga, 2010).

Similar to the RyR subtypes, the 3 IP_3R subtypes also display different characteristics in relation to their function. It was reported that each subtype exhibits different sensitivities to IP_3: IP_3R1 has an EC_{50} of 4.7μM; IP_3R2 has an EC_{50} of 0.35 μM whereas IP_3R3 has an EC_{50} of 18.6 μM (Miyakawa et al., 1999). However, the activity

of the receptor is modulated not only by IP_3 but also by the cytoplasmic concentration of Ca^{2+}. Ca^{2+} concentrations below 300 nM activates IP_3R1 whereas increases on Ca^{2+} concentration above 300 nM inhibit this receptor. However, similar concentration-dependent regulation is not reported with the other two subtypes (Patel et al., 1999). The direct binding of Ca^{2+} to the receptors may trigger CICR from the S/ER. The diverse affinities and sensitivities for ligands displayed by the different subtypes of IP_3Rs and RyRs suggest that those S/ER membrane bound Ca^{2+} receptors may target to distinct subcellular compartments that give rise to different Ca^{2+} signals within the local microenvironments, and the features of the subtypes are optimal for regulating the Ca^{2+} homeostasis within those microenvironments.

1.3.3 Ca^{2+} buffering proteins of the sarcoplasmic / endoplasmic reticulum

The S/ER contains Ca^{2+} buffering proteins that ensure the free Ca^{2+} concentration within the lumen is maintained near or below 1 mM (MacLennan et al., 2002). The Ca^{2+} buffering proteins exhibit high capacity and low affinity for Ca^{2+}, allowing the S/ER to effectively store Ca^{2+} (Volpe et al., 1994). Calsequestrin (CSQ) and calreticulin are the two extensively studied Ca^{2+} buffering proteins found in the S/ER.

CSQ has been shown to present in multiple cell types, and two isoforms of the protein have been identified, namely the fast-twitch skeletal form and the cardiac form (Volpe et al., 1994, Beard et al., 2004). The skeletal muscle form of CSQ has a low affinity for Ca^{2+} (K_d 0.8 mM) and binds 40-50 Ca^{2+} ions per CSQ molecule. The cardiac form of CSQ binds around 20 Ca^{2+} ions with a binding constant of 0.5 mM (Volpe et al., 1994, MacLennan et al., 2002). It was reported that both forms of CSQ are present in the smooth muscle cells (Volpe et al., 1994). In terms of the mode of action, CSQs display a high negative charge and are thought to bind Ca^{2+} via pairs of acidic residues (Wang et al., 1998). Moreover, CSQ was reported to associate with other S/ER proteins including triadin and junction, which results in a physical association with RyRs; (Guo and Campbell, 1995). CSQ is also found in the vicinity of IP_3Rs. Together these proteins form S/ER complexes that facilitate the Ca^{2+} handling within the S/ER and effective Ca^{2+} release via the RyRs and IP_3Rs.

Calreticulin is another Ca^{2+} buffering protein that is identified in the ER/SR of many

cell types (Michalak et al., 1992). It is also expressed in other organelles and may thus affect cell adhesion, antithrombotic activity, long-term memory and development as reviewed (Johnson et al., 2001). However, here I only focus on its function of buffering Ca^{2+} in the S/ER lumen. Calreticulin has a low affinity (K_d 2 mM) Ca^{2+} binding domain with high capacity for Ca^{2+} binding (18 mol of Ca^{2+}/mol of protein) in the C-terminal domain, where the high Ca^{2+} binding capacity is determined by a region rich in acidic amino acid residues (Michalak et al., 1999, Baksh and Michalak, 1991). Moreover, calreticulin may bind to the luminal tail of SERCAb and decrease its activity when the SR Ca^{2+} concentration is high (Michalak et al., 1999). Like CSQ, calreticulin buffers Ca^{2+} in the S/ER lumen, allowing the rapid release of Ca^{2+} upon activation of Ca^{2+} release channels within the ER/SR, via, for example, IP_3Rs and RyRs.

1.4 Acidic lysosomal Ca^{2+} stores

Considering that Ca^{2+} is such a versatile signalling ion, it is not surprising that more than one organelle serves as the intracellular Ca^{2+} store. Among these, the endosomes and lysosomes represent a releasable acidic Ca^{2+} store, identifiable by their high luminal H^+ concentration.

Studies on the role of lysosomes as an intracellular Ca^{2+} store were inspired by the finding that nicotinic acid adenine dinucleotide phosphate (NAADP) evoked Ca^{2+} release from acidic organelles that are called reserve granules in sea urchin eggs (Churchill et al., 2002). Boittin et al demonstrated in mammalian cells that NAADP mobilised Ca^{2+} from an intracellular Ca^{2+} store other than the SR (Boittin et al., 2002), which has been shown to be an acidic, lysosome-related store (Kinnear et al., 2004).

Subsequently, NAADP-sensitive channels were identified on liver lysosomes (Zhang and Li, 2007), cementing the view that lysosomes may serve as the Ca^{2+} store that supports NAADP-induced Ca^{2+} release. Indeed, it was observed that lysosomes contain a high luminal Ca^{2+} concentration, which is around 0.4 to 0.6 mM (Christensen et al., 2002, Yagodin et al., 1999, Lloyd-Evans et al., 2008). More direct evidence came from studies that utilised glycyl-phenylamine 2-naphthylamide (GPN). GPN is membrane permable, therefore it can diffuse into the lysosomes, where it is cleaved by cathepsin C, an exopeptidase found exclusively within lysosomes, into its

constituent amino acids upon entering the lysosomes. The resulting amino acids are unable to pass through the lysosomal membrane and therefore they are accumulated within the lysosomal lumen, causing high osmotic pressure and eventually lyse the lysosomes. (Berg et al., 1994, Jadot et al., 1984). Addition of GPN, which causes the rupture of lysosomes and the release of the lysosomal content, resulted in an increase in the intracellular Ca^{2+} concentration in both mammalian and non-mammalian cells (Yagodin et al., 1999, Churchill et al., 2002, Haller et al., 1996, Srinivas et al., 2002). Moreover, NAADP induced Ca^{2+} release was inhibited by the addition of GPN in myometrial cells (Soares et al., 2007). Given the above, it was concluded that the lysosomes can serve as a releasable Ca^{2+} store.

1.4.1 Sequestration of Ca^{2+} by lysosomes

The process by which lysosomes sequester Ca^{2+} remains unclear. However, it is generally accepted that lysosomes take up Ca^{2+} from the cytosol in a pH dependent manner, given that the intracellular Ca^{2+} concentration of the lysosome decreased upon the increase of luminal pH (Christensen et al., 2002). Experiment in mouse macrophages showed that 3 compounds (FCCP, nigecerin and NH_3) that can disrupt the lysosomal proton gradient inhibited Ca^{2+} uptake into lysosome-related organelles (Churchill et al., 2002). Moreover, the vacuolar proton pump (V-H^+-ATPase) inhibitor bafilomycin A1 inhibited Ca^{2+} uptake into lysosomes (Christensen et al., 2002). This led to the proposal that lysosomal Ca^{2+} stores contain a V-H^+-ATPase that can generate a proton gradient, which perhaps favours the H^+/Ca^{2+} exchanger in the mode that accumulates Ca^{2+} (Churchill et al., 2002, Christensen et al., 2002). Two Ca^{2+} transporters that pump Ca^{2+} into the vacuole (lysosome equivalent in plants) have been identified in plants, one is a homolog of the mammalian plasma membrane Ca^{2+}-ATPases that consumes ATP, the other is a Ca^{2+}/H^+ exchanger that removes H^+ in exchange of Ca^{2+} (Hirschi et al., 1996, Geisler et al., 2000). However, no such homologs have been found in mammalian cells.

1.4.2 Ca^{2+} release channels in lysosomes

1.4.2.1 TRPMLs

TRPML1 (Transient Receptor Potencial Mucolipin channel 1) belongs to the mucolipin family of proteins which consists of the cation channels TRPML1,2 and 3. TRPML1 is

majorly targeted to the lysosomes whereas TRPML2 is mostly found in the endosomes. TRPML3 can be found both in lysosomes and on the plasma membrane (see review (Xiong and Zhu, 2016)). The lysosome dominant subtype is TRPML1, which can be activated by $PI(3,5)P_2$ and mediates Ca^{2+}release from the lysosomes. TRPML1 is proven to play a part in endocytic vesicle trafficking, lysosome exocytosis and vesicle fusion.

1.4.2.2 Two pore channels

In 2009, it was shown that NAADP evoked Ca^{2+} release form endo/lysosomes, which was supported by two pore channels (TPCs)(Calcraft et al., 2009). TPCs are voltage-gated ion channels that are localised to acidic organelles including vacuoles in plants and endolysosomes in mammals. In mammalian cells, 3 subtypes of TPCs have been identified. TPC1 and TPC2 are expressed in all animals whereas TPC3 is expressed in vertebrates apart from human and rodents (see review (Xiong and Zhu, 2016). In terms of subcellular localisation, TPC2 is targeted to lysosomes whereas TPC1 is found within the endolysosomal system, ER and plasma membrane.

1.5 Ca^{2+} handling by mitochondria

Mitochondria are not generally considered as a releasable Ca^{2+} store, but they have been proposed to act as spatial Ca^{2+} buffer that sequesters Ca^{2+} (Duchen, 2000). The mitochondrial Ca^{2+} uptake is essential to the mitochondrial functions, including mitochondrial metabolism, coopering oxidative stress and regulation of cell death. The mitochondria have been shown to accumulate Ca^{2+} via uniporters or the Na^{+}-Ca^{2+} exchanger as reviewed (Duchen, 2000). The Ca^{2+} uniporters facilitate mitochondrial Ca^{2+} uptake from the cytoplasm. Upon mitochondrial respiration, large potential gradients are established across the mitochondrial outer membrane which results in a mitochondrial membrane potential of 150-200 mV (negative to the cytosol). Together with the low mitochondrial Ca^{2+} concentration, this promotes mitochondrial Ca^{2+} uptake. The voltage-dependent anion channels (VDACs) on the outer mitochondrial membrane allow Ca^{2+} diffusion across the outer membrane (Rapizzi et al., 2002, Rizzuto et al., 1993), following which Ca^{2+} is transported into the mitochondrial matrix by Ca^{2+} uniporters (Michels et al., 2009). Once the mitochondria are loaded with Ca^{2+}, the unloading process would be activated by

favouring Ca^{2+} extrusion via $3Na^{+}/Ca^{2+}$-exchanger, which may in part facilitate SR re-loading (Malli et al., 2003). It was also proposed that mitochondrial Ca^{2+} uptake can be achieved by the mitochondrial Na^{+}-Ca^{2+} exchanger in the mode that favours Ca^{2+} entry. It was reported that mitochondria in rat cardiomyocytes may become Ca^{2+} loaded by the reversal of the Na^{+}-Ca^{2+} exchanger during hypoxia (Griffiths et al., 1998).

1.6 Nucleoplasmic reticulum can serve as a Ca^{2+} store

The primary role of the nuclear envelope (NE) is to isolate the nucleoplasm from the cytoplasm. However, the nucleoplasmic reticulum (NR) is continuous with the S/ER, and estimation of the Ca^{2+} concentration within its lumen using a low affinity fluorescent probe indicated that the NE holds Ca^{2+} at 250-350 μM (Petersen et al., 1998). Therefore, it is now generally accepted that the NR can serve as a releasable Ca^{2+} pool (Papp et al., 2003). Several studies have confirmed that the NR can serve as a perinuclear Ca^{2+} store that supports the generation of highly localised Ca^{2+} signals in order to modulate gene expression (see review (Bootman et al., 2009)).

On the membrane of NE, Ca^{2+} releasing channels including IP_3Rs and RyRs have been identified, which may direct Ca^{2+} release from NR into the nucleoplasm. For example, IP_3 has been shown to induce intranuclear Ca^{2+} elevations in isolated acinar pancreatic nuclei (Gerasimenko et al., 2003). Moreover, RyRs have been visualized on the NE of pancreatic cells with BODIPY-Ry (Gerasimenko et al., 2003), and on the NE and NR of myoblastic cells by immunolabelling (Marius et al., 2006). Both RyRs and IP_3Rs have the capacity to generate nuclear Ca^{2+} signals, and they were proposed to cooperate for the maintenance of nuclear Ca^{2+} homeostasis.

To summarize, multiple intracellular Ca^{2+} stores are identified including the S/ER, endo-lysosomes, mitochondria and nucleus. They harbour Ca^{2+} releasing channels and transporters for intracellular Ca^{2+} handling. Most importantly, as Figure 1.3 shows, these Ca^{2+}stores are actively interacting, with evidence from a variety of studies showing that Ca^{2+} can be transferred between the SR and all the other Ca^{2+} handling organelles (Rizzuto et al., 1998, Kinnear et al., 2008, van Breemen et al., 2013).

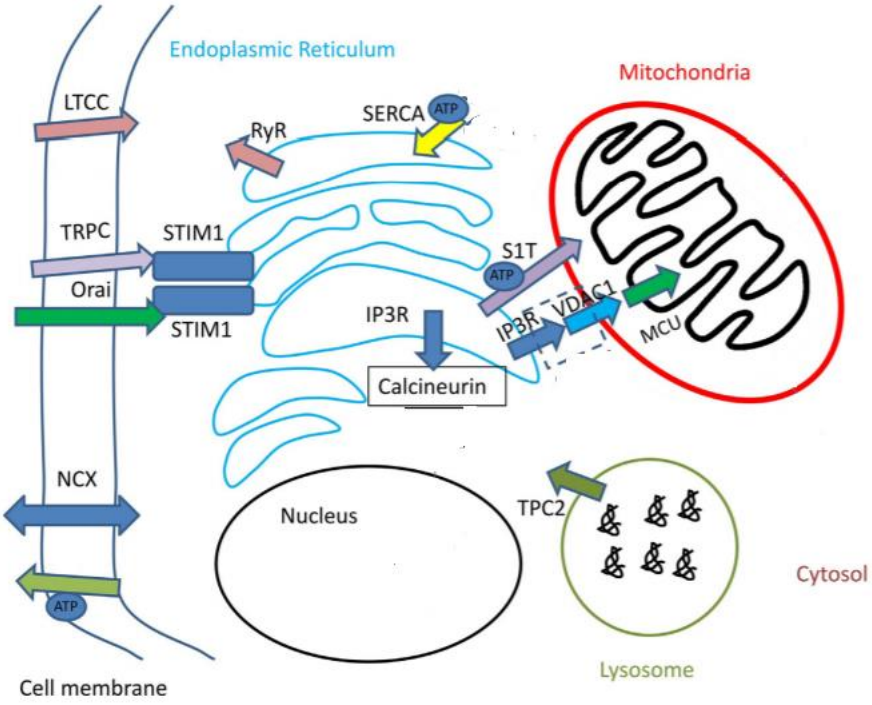

Figure 1.5 Schematic image shows the overview of intracellular Ca^{2+} handling.

Intracellular Ca^{2+} influx and efflux between organelles, and Ca^{2+} channels and transpoters involved in the processes . Abbreviation used are as follow: IP3R, inositol1,4,5-trisphosphate (IP3) receptor; NCX, Na^{+}/Ca^{2+} exchanger; RyR, Ryanodine Receptor; MCU, mitochondrial Ca^{2+} uniporter; LTCC, L-type Ca^{2+} channel; SERCA, Sarco/Endoplasmic Reticulum Ca2+ ATPase; TPC2, two-pore channel 2; TRPC, transient receptor potential canonical; STIM1, Stromal interaction molecule 1; VDAC, voltage-dependent anion channel. Figure adapted from “SERCA control of cell death and survival”, by Chemaly et al (Chemaly et al., 2017).

1.7 From contraction and dilation to gene expression: Do nanojunctions of the sarcoplasmic reticulum support site- and function-specific Ca^{2+} signals necessary for the coordination of cell function?

As stated at the beginning of this chapter, sustained increases in cytoplasmic Ca^{2+} concentration are cytotoxic to cells. Therefore, Ca^{2+} must be stored in the intracellular organelles and released in the form of transient Ca^{2+} signals, causing the increase in local Ca^{2+} concentration. For example, for the induction of CICR via RyRs, the cytoplasmic Ca^{2+} concentration must rise to the micromolar range (Kim et al., 1983), which is evidently higher than the cytoplasmic Ca^{2+} concentration at rest (~100 nM). However, cell-wide increases in Ca^{2+} concentration within the micromolar range would require a very large influx of Ca^{2+} that might be expected to compromise the cell. The

optimal solution to this is to build a narrow cytoplasmic space between the target membrane and releasable Ca^{2+} stores such as the SR. Within these cytoplasmic spaces, increases in Ca^{2+} concentration can be readily achieved by a relatively small Ca^{2+} flux, with released Ca^{2+} quickly recycled back into cellular Ca^{2+} stores or extruded from the cell. In this instance, Ca^{2+} signals would be restricted within the narrow space therefore the global Ca^{2+} concentration remains unaffected. In fact, such delicately designed structures have already been discovered within cells, and the dimensions of these functionally segregated compartments appear to be on the nanoscale. For example, the regulation of excitation-contraction coupling observed in all types of muscles is accomplished by the interactions between Ca^{2+} release channels in the sarcoplasmic reticulum (SR) and voltage-gated Ca^{2+} channels (VGCCs) on the plasma membrane or membrane invaginations including T-tubules and caveolae. The underpinning mechanisms require strategic positioning of cellular Ca^{2+} release channels and Ca^{2+} transporters to the membrane-membrane junctions that are separated by less than 50 nm across (van Breemen et al., 2013). These narrow junctional spaces are widely distributed across cells, and they have been referred to as nanojunctions.

1.7.1 Intercellular nanojunctions: the neuromuscular junction

The first membrane-membrane junction that was identified with a clear functional significance in terms of signalling was the neuromuscular junction, which is the synapse located between motor neurons and skeletal muscle fibers (Del Castillo and Katz, 1956). This intercellular junction is formed between the presynaptic motor axon and the plasma membrane of post-synaptic skeletal muscle fibers. It coordinates the control of skeletal muscle contraction by the central nervous system. The motor nerve terminal harbours synaptic vesicles that contain a neurotransmitter, acetylcholine, whereas the post synaptic membrane of skeletal muscle fibers displays deep folds with the crests of folds carrying acetylcholine receptors. Upon the transmission of impulses, nerve action potentials trigger Ca^{2+} influx within the motor nerve terminal, which leads to the fusion of synaptic vesicles with the terminal membrane at the active zones. As a result, acetylcholine is released into the synaptic clefts, which typically have junctional widths ~20 nm (Siksou et al., 2007). This is narrow enough to ensure rapid (within 1ms) neurotransmitter diffusion and binding to acetylcholine receptors on the plasma membrane of muscle fiber. Acetylcholine receptor activation elicits

inward currents into the muscle fiber, which results in depolarization of the endplate potential that is more than sufficient to breach the threshold for the generation of an action potential in the muscle fiber.

In this event, three morphological and physiological properties of the neuromuscular junction contribute to its proper function. First, the width of the synaptic cleft is around 20 nm, the narrow separation is required for fast diffusion of the neurotransmitter, which facilitates rapid post-junctional actions; the importance of such junctional complexes is relevant not only here at the NMJ but also at synapses across the peripheral and central nervous system. Second, the length of a neuromuscular junction ranges from 200 to 500 nm (Siksou et al., 2007, Schikorski and Stevens, 1997). Considering the average diameter of a synaptic vesicle (35-50 nm), this length ensures efficient acetylcholine can be released into the junctional space per unit time. Third, acetylcholine receptors are targeted to the membrane that defines the neuromuscular junction, which is crucial for signal transmission (Siksou et al., 2007).

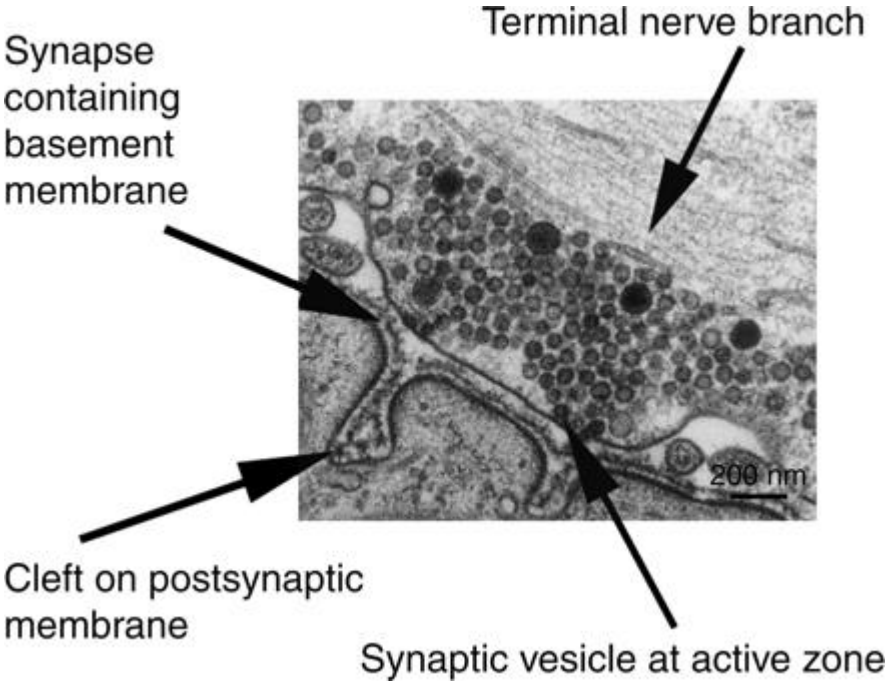

Figure 1.6 Structure of the neuromuscular junction.

The structure of the neuromuscular junction is revealed under electron microscope. The key components are indicated by black arrows. Figure adapted from “Neuromuscular junction in health and disease”, by Hirsch. N. P (Hirsch, 2007).

1.7.2 Intracellular nanojunctions

Although little attention has thus far been paid to intracellular nanojunctions, it is evident that such structures exist and share similar morphological and physiological properties with the neuromuscular junction. Among these, one intracellular nanojunction has received significant attention, which is the junction formed between the terminal cisternae of the sarcoplasmic reticulum (SR) and T-tubes of the sarcolemma in skeletal and cardiac muscle cells (Figure 1.4). This junctional complex exhibits clear similarities when compared to the NMJ, which is perhaps not surprising given that both structures play key roles in the process of excitation-contraction coupling by directing transmitter/ion flux across the junctional space. In both cases the junctional membrane pairs are separated by less than 20 nm (Franziniarmstrong, 1964, Franzini-Armstrong, 1970, Langer and Peskoff, 1996, Franzini-Armstrong et al., 1999). However, the mechanisms through which excitation-contraction coupling is elaborated within triads and diads of skeletal and cardiac muscle is slightly different, and tailored to the requirements of each cell.

The triads in skeletal muscles are formed by positioning a T-tubule between two terminal cisternae of the SR, the membranes of terminal cisternae and the membranes of the opposing T-tubules are so closely aligned that they enclose junctional gaps that are separated by 9-20 nm (Franziniarmstrong, 1964, Franzini-Armstrong, 1970). Ryanodine receptor type 1 (RyR1) is targeted to the membrane of the SR, and the cytoplasmic domain of the RyRs are referred as the junctional feet that span the junctional space. On the membrane of the T-tubules, clusters of dihydropyridine receptors (DHPRs), namely the tetrads, were observed, and the position of tetrads mirrors that of the junctional feet. Upon excitation-contraction coupling, an action potential passes along the surface of T-tubules that form an extensive network, and the resulting depolarization is detected by the DHPRs. The DHPRs serve as voltage sensors. The voltage-dependent movements of electrical charge in the skeletal DHPRs are coupled to the opening of RyR1 on the opposing membrane of SR. The DHPRs directly interact with RyR1 to achieve an efficient fast control over Ca^{2+} release which subsequently causes vigorous muscle contraction, and is ceased when the Ca^{2+} release is stopped. This termination of signal occurs immediately once the voltage sensors are inactivated.

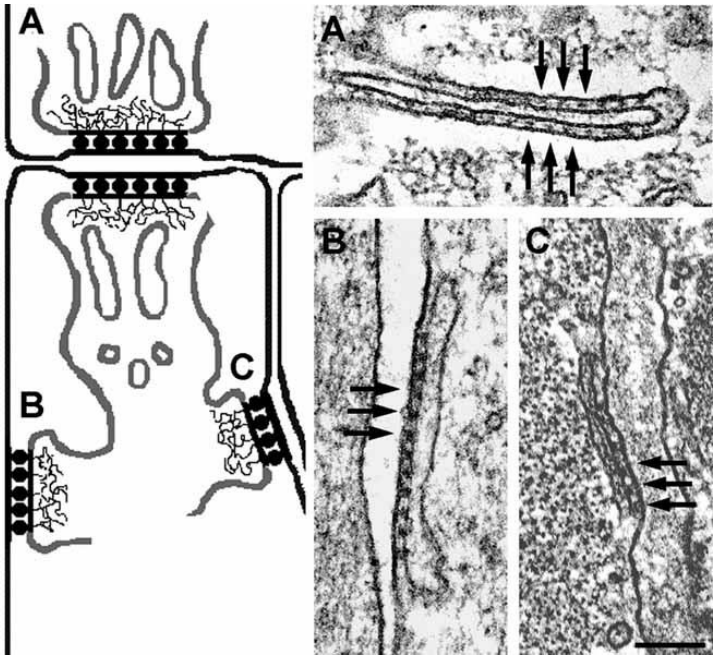

Figure 1.7 Electron micrographs and schematic model showing triads and diads.

(A) Triads formed betweenone T-tubule and two SR cisternae in adult toadfish swimbladder muscle.
(B) Dyadse formed between one SR vesicle and the surface membrane or a T-tubule in a BC3H1 cell.
(C) As for B, but showing dyad in canine heart
Figure adapted from“Structural interaction between RYRs and DHPRs in Ca2+ release units of cardiac and skeletal muscle cells”, by F. Protasi (Protasi, 2002).

Diads are junctions defined by the membrane of terminal cisternae of the sarcoplasmic reticulum (SR) and the membrane T-tubules of the sarcolemma in cardiac muscles (Langer and Peskoff, 1996). Again, these junctions are separated by around 5-15 nm with clusters of RyR2 targeted to the SR membrane juxtaposed to the T-tubule membrane that is lined by DHPRs (Langer and Peskoff, 1996, Franzini-Armstrong et al., 1999). However, in cardiac muscle cells, both the dominant subtype of RyRs and DHPRs are different from the subtypes found in skeletal muscle cells.

Notably, the distribution of DHPR clusters is irregular and it does not match the disposition of the junctional feet. When action potentials pass through the surface membrane of cardiac T-tubules, it activates the DHPRs that allow influx of extracellular Ca^{2+} into the cytoplasm. The Ca^{2+} binds and opens RyR2 on the SR membrane, resulting in further Ca^{2+} release from the SR by CICR via RyR2. Importantly, this Ca^{2+} efflux then triggers Ca^{2+} release from other adjacent clusters of RyR2. Rapid and accurate control of contraction in cardiac muscle is possible because fast control of RyRs on the adjacent SR can be achieved due to the short distances of communication conferred by the nanojunctions.

At this stage it is important to highlight that in each case the nanojunction between the sarcolemma and the T-tubule is less than 20 nm across, with receptors and Ca^{2+} release channels targeted to the junctional membranes in order to coordinate signalling across each junctional space. Furthermore, it is evident that in triads and diads similar physiological outcomes are achieved by different subtypes of a given protein, through their very distinct coupling mechanisms that were underpinned by the differential positioning of the receptors and channels.

1.7.3 The PM-SR nanojunction of smooth muscles

The PM-SR junction of smooth muscle was first identified in the early 1970s and was described as a narrow cytoplasmic space located between the PM and superficial SR (Gabella, 1971, Devine et al., 1972). It was found majorly in the vicinity of caveolae, from which it was inferred that the PM-SR junction might be associated with smooth muscle activation. A few years later it was proposed that the PM-SR junction could restrict ion diffusion, and thus allow the superficial SR to modulate Ca^{2+} flux from the plasma membrane to the myofilaments, hence regulating smooth muscle contractility (Van Breemen, 1977). Interestingly, further studies revealed a more complicated model through which smooth muscle contraction was manipulated. It was shown that a depolarization-activated net Ca^{2+} uptake would trigger fast large force development when the Ca^{2+} entered rapidly. In contrast, if the same Ca^{2+} uptake entered slowly but with longer durations of flux, a small and slow contraction would be stimulated instead (van Breemen and Saida, 1989). From these facts, the authors postulated that a Ca^{2+} pump of the SR (SERCAs) must determine outcomes. Importantly, the SERCA pump

near the plasma membrane was found to have a limited V_{max}, and it was saturated when fast Ca^{2+} flux was delivered through the voltage-gated Ca^{2+} channels (VGCC) to the cytoplasm. However, when encountering a slow and sustained Ca^{2+} flux, the SERCA of the superficial SR could remove the cytoplasmic Ca^{2+} efficiently and pump it into the SR. These studies led to the “superficial buffer barrier” hypothesis, which states that the narrow cytoplasmic spaces formed between the PM and SR could effectively restrict Ca^{2+} diffusion, which facilitates SR Ca^{2+} intake from the junctional space, and this would serve as the buffer barrier to attenuate Ca^{2+} flux from the PM to the deep myoplasm (van Breemen et al., 1995, Van Breemen, 1977). The theory has since been confirmed by several research groups (Rembold and Chen, 1998, Shmigol et al., 1999, Yoshikawa et al., 1996).

When considered alongside the NMJ, triads and diads, the PM-SR junctions highlight one question that has yet to be answered. Why is the junctional gap always maintained at 20 nm or less？ To answer this question, computational models have been developed to simulate Ca^{2+} flux across the PM-SR junction in smooth muscle cells. The results suggest that the junctional membrane pairs cannot be separated by more than 50 nm without compromising the integrity of the junction. Junctional integrity is therefore required for the compartmentalized Ca^{2+} signalling within the junctional space, and these signals will be progressively lost to random diffusion once the opposing membrane pairs are separated more than 50 nm (Fameli et al., 2007).

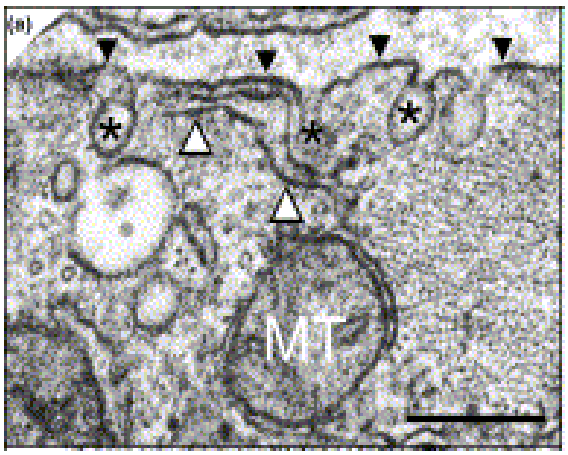

Figure 1.8. PM-SR junction formed between the superficial SR and plasma membrane.

The PM-SR junction formed between the superficial SR (white arrowheads) and the PM (black arrowheadsin smooth muscle cells. Scale bar=400 nm. Figure adapted from “Organellar junctions promote targeted Ca^{2+} signalling in smooth muscle: why two membranes are better than one”, by D. Poburko et al (Poburko et al., 2004).

Apart from muscle contraction, it was also proposed that the superficial SR was involved in a variety of physiological processes, for example, vasodilation triggered by vasodilators. In arterial smooth muscles, cADPR activates RyRs located on the superficial SR that are in close contact with the plasma membrane. Here evoked Ca^{2+} release causes membrane hyperpolarization which eventually leads to vasodilation (Boittin et al., 2003). Moreover, it is evident that the superficial SR may be able to behave bidirectionally: when extracellular Ca^{2+} is removed, Ca^{2+} release from the superficial SR to the cytoplasm is triggered (Nazer and van Breemen, 1998); when the store is depleted, Ca^{2+} influx across the PM-SR junction may be triggered in order to refill the SR (Spinelli and Trebak, 2016).

1.7.3.1 Refilling of the SR

The SR store in smooth muscles is replenished through receptor-operated channels acting in association with the Na^{+}/Ca^{2+} exchanger in its reverse mode (Lemos et al.,

2007, Poburko et al., 2007), or store depletion activated Ca^{2+} entry via the stromal interaction molecule (STIM)/Orai system (Soboloff et al., 2012). Moreover, Ca^{2+} influx via L-type voltage dependent channels in part fills the store (Flores-Soto, Reyes-Garcia, Sommer, & Montano, 2013). Interestingly, PM-SR nanojunctions are involved in all the pathways above and may be either formed or enhanced at the PM-SR interface, thus restricting the distances of Ca^{2+} diffusion for SERCA Ca^{2+} intake and store refilling.

SR store refilling by Ca^{2+} influx via L-type voltage dependent channels requires Ca^{2+} influx into PM-SR junctions, which is pumped into the superficial SR by SERCAs. It was proposed that the Ca^{2+} near sarcolemma acts as a messenger to convey information on functional SR content by regulating Ca^{2+} –activated potassium channels (BK_{Ca} channels). Depletion of SR store results in reduced activity of BK_{Ca} channels, which causes membrane deperpolarization and thus Ca^{2+} entry via L-type Ca^{2+} channels from the extracellular space (Flores-Soto et al., 2013, Wu et al., 2002). Consistent with the “superficial buffer barrier” theory, it was proposed that the Ca^{2+} flux from the L-type Ca^{2+} channel was restricted in the PM-SR junction, which was pumped into the superficial SR by SERCAs for store refilling. In this way, the store refilling is independent of changes in bulk sarcoplasmic Ca^{2+} level.

The initiation of SR loading via receptor-operated Ca^{2+} entry pathways requires the activation of those non-selective cation-permeable receptor-operated receptors on the cell membrane. For example, the transient receptor potential canonical channel 6 (TRPC6). It has been shown that localised, transient elevations in sodium concentration were dependent on TRPC6 (Poburko et al., 2007). The elevated local sodium concentration and the resulting membrane depolarization favour the reversal mode of Na^+/ Ca^{2+} exchanger that facilitates Ca^{2+} entry into the “local cytoplasm”, or to be specific, the cytoplasmic nanodomain demarcated by PM-SR junctions. Early studies stated that elevation of the sodium concentration within the junctional space was sufficient to generate sodium concentrations required to mediate reversal of NCX and thus NCX-mediated Ca^{2+} entry (Dai et al., 2005). Moreover, it is evident that the junctional clustering of Ca^{2+} and Na^+ transporters would support the NCX-mediated Ca^{2+} entry (Poburko et al., 2007). On the basis of these facts it was proposed that the geometry of PM-SR junctions facilitates the elevation of local Na^+ concentration via

TRPC6, which then enhances Ca^{2+} entry through the NCX in its reverse mode (Lemos et al., 2007). Again, as the superficial buffer barrier theory stated, the junctional Ca^{2+} would be pumped into the superficial SR by SERCAs, hence the SR store is replenished (Poburko et al., 2008).

PM-SR nanojunctions can also be formed upon STIM/Orai complex formation, which ensures that the extracellular Ca^{2+} can be fed directly into the SR through the trams-membrane complex (Soboloff et al., 2012, Trebak, 2012). The depletion of the stores is able to activate dimerization of stromal interaction molecules (STIMs), which act as SR Ca^{2+} sensors (Liou et al., 2005). STIM1, for example, is a transmembrane protein that contains an N-terminal EF-hand motif with low Ca^{2+} affinity, and it serves to sense luminal Ca^{2+} changes within the SR/ER. STIM1 loses associated Ca^{2+} upon the depletion of the Ca^{2+} store, which leads to the interactions between the EF-hand-SAM domains within STIM1, and this causes the formation of an extended configuration that exposes the STIM-Orai activating region (SOAR). The STIM dimmers further oligomerize and migrate to the PM-SR/ER junctions, where STIMs were anchored to the plasma membrane to fully expose the SOAR. It was observed that the SOAR interacts with the C- and N- termini of Orai, which is a store-operated Ca^{2+} channel (SOC) (Park et al., 2009). Orais are tethered together by STIMs to form tetramers that mediate Ca^{2+} release-activated Ca^{2+} current (CRAC), which allows Ca^{2+} entry to the SR store. Furthermore, STIM1 might recruit POST (partner of STIM1), an adaptor protein that could further recruit SERCAs to the junctional space to assist ER/SR Ca^{2+} loading (Krapivinsky et al., 2011). Following SR store depletion, POST binds and moves STIM1 to shorten PM-SR/ER junctional distances. Moreover, the POST mediated organization of SERCA pumps within the STIM/Orai junction, effectively controls and directs the entering Ca^{2+} into the SR.

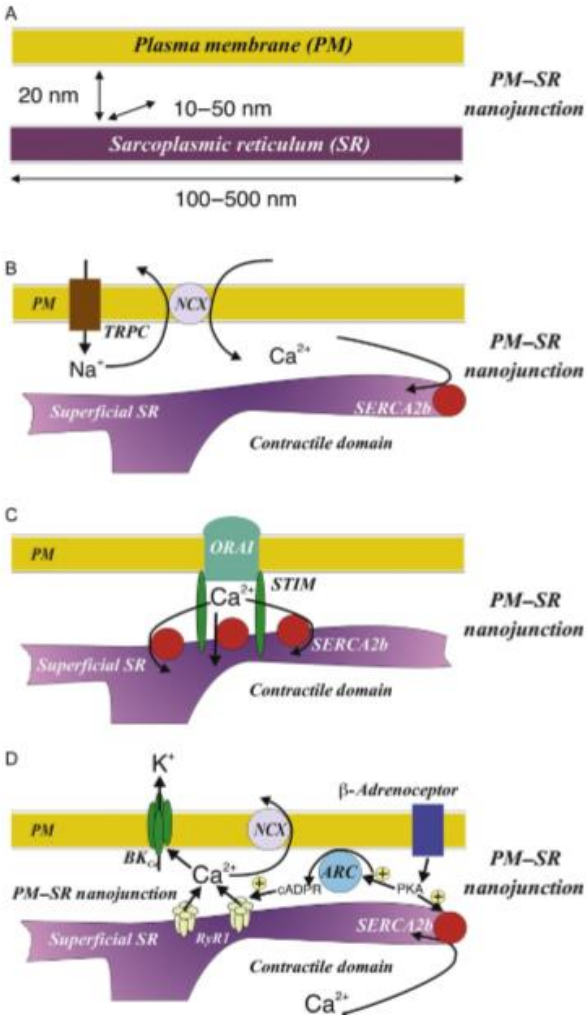

Figure 1.9 PM-SR junction in SR refill.

The SR can be refilled by different mechanisms facilated by the PM-SR junction, for example, the receptor-operated refill (B), the store-operated refill (C) and through the Na^+/Ca^{2+} exchanger in the reverse mode. Figure adapted from “Vascular pharmacology: smooth muscle, Chapter one”, by Khalil et al and A. M. Evans (Khalil et al., 2017).

It is important to note that all three mechanisms for SR refilling can be observed in a single type of smooth muscle cell (Tang et al., 2010, Ogawa et al., 2012, Kato et al., 2013). It still remains unclear how these different SR refilling mechanisms contribute to the coordination of store refilling within smooth muscle cells, but there is no doubt that the PM-SR junctions play a crucial role in this process.

1.7.3.2 Emptying of the SR and vasodilation

When the smooth muscle cells are at rest, the NCX in the PM function in the forward mode which allows SR unloading via the PM-SR junctions, and this contributes partially to the maintenance of cellular Ca^{2+} homeostasis (Lee et al., 2002). Moreover, muscle relaxation may also be promoted by vasodilator-induced unloading of SR Ca^{2+} into PM-SR junctions (Boittin et al., 2003). The intracellular Ca^{2+}- and voltage-activated K channels, BK_{Ca}, located on the plasma membrane, drive membrane hyperpolarization that underpins vasodilation (Brayden, 1990). Hyperpolarization of plasma membrane closes voltage-dependent Ca^{2+} channels, which serves as a feedback mechanism to decrease global Ca^{2+}. In 1995, it was shown that activation of BK_{Ca} channels is coordinated by the release of highly localised Ca^{2+} sparks delivered by RyR clusters positioned on the superficial SR adjacent to BK_{Ca} channels in the PM (Nelson et al., 1995), confirming the original proposal of Benham and Bolton (Benham and Bolton, 1986). As described above, this ultimately leads to vasodilation and extrusion of Ca^{2+} released by the SR via NCX (Brayden and Nelson, 1992, Knot et al., 1998).

Later studies indicated that in pulmonary arterial myocytes, Ca^{2+} sparks were possibly released through RyR1 by showing that only RyR1 was preferentially targeted to the subplasmalemmal region, which is adjacent to the plasma membrane (Clark et al., 2010a); although in cerebral arterial myocytes it has been suggested that RyR2 might support this process (Nelson et al., 1995). The study by Clark et al (Clark et al., 2010a) also pointed out that SERCA2b was strategically targeted to the subplasmalemmal region of pulmonary arterial myocytes, i.e. to the superficial SR. Together, SERCA2b and RyR1 appear to line PM-SR junctions and may serve to coordinate superficial SR unloading and refilling. Accordingly, blocking peripheral SERCA with cyclopiazonic acid or blocking RyRs with the high concentrations of ryanodine markedly inhibited vasodilation in response to beta-adrenoceptor activation (Boittin et al., 2003).

1.7.4 Lysosome-SR nanojunction

Lysosome-SR (L-SR) nanojunctions, as the name indicates, are the narrow junctional spaces demarcated by juxtaposed membranes of lysosomes and perinuclear SR. Little attention had been paid to the L-SR junctions until 2004, when

one study proposed that the L-SR junctions form a trigger zone for Ca^{2+} signalling by NAADP (Kinnear et al., 2004). The study suggested that lysosome clusters and a subpopulation of RyRs, which was later confirmed to be RyR3(Kinnear et al., 2008), colocalised within L-SR junctional complexes. Within this trigger zone, it was proposed that NAADP induced Ca^{2+} release from acidic, lysosomal Ca^{2+} stores may trigger Ca^{2+}-induced Ca^{2+} release (CICR) from the RyR3s and give rise to a global Ca^{2+} wave. In 2014, standard 2D transmission electron microscopy and tomography revealed for the first time the ultrastructure of the L-SR junctions (Fameli et al., 2014). The membrane pairs that define L-SR junctions were separated by 30 nm or less, and were around 300 nm in extension. The existence of L-SR junctions was also confirmed in cardiac ventricular myocytes (Aston et al., 2017), where the junctional width was also less than 30 nm, and they were 200-400 in extension.

Notably, the formation of Ca^{2+} trigger zone by the L-SR junction heavily relies on the close opposition of the junctional membrane pairs. To illustrate this, a 3D stochastic Monte Carlo model of Ca^{2+} transport in L-SR junction was built based on its characteristics. Both Ca^{2+} releasing channels (TPC2, RyR2) and Ca^{2+} transporters (SERCA2a) as well as their features (thresholds, kinetics) were included (Fameli et al., 2014). Computational simulations with the model suggested that the narrow junctional space restricted free Ca^{2+} diffusion, which guaranteed that the junctional Ca^{2+} transient from TPC2 could easily breach the threshold for CICR via RyR3. If the junctional space was separated by 50 nm or more, junctional integrity was disrupted and the NAAPD induced Ca^{2+} burst from TPC2 failed to trigger CICR from RyR3. This explains why the global Ca^{2+} waves were observed in an all-or-none manner. This example emphasized again that the nanoscale-geometry is required for tight regulation of ion transport and signal transduction, and perhaps diverse physiological processes.

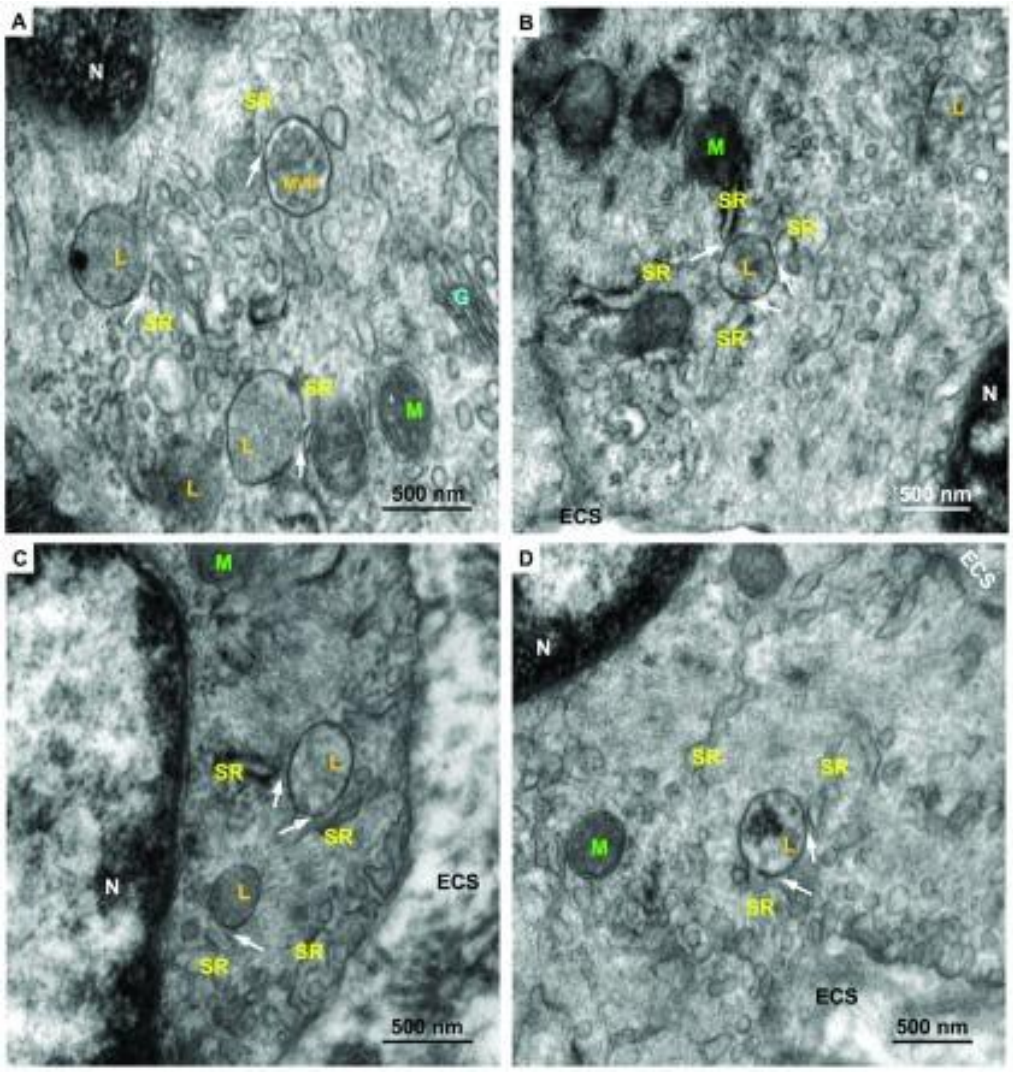

Figure 1.10 Lysosome-SR junction in smooth muscle cells

Lysosomes (L), SR cisterns and examples of L-SR junctions in pulmonary arterial smooth muscle cells are indicated by arrows. Scale bars: 500 nm. Adapted from "Cytoplasmic nanojunctions between lysosomes and sarcoplasmic reticulum are required for specific Ca2+ signalling", by N. Fameli et al (Fameli et al., 2014).

1.7.4.1 Ca^{2+} release channels in L-SR junction

Based on the proposal that L-SR junction forms a trigger zone for Ca^{2+} signalling, immunocytochemistry was conducted to identify the RyR subtype that was responsible for the observed CICR (Kinnear et al., 2008). A lysosome specific protein alphalgP120 was used to identify lysosome clusters, and it was reported that the lysosomes were clustered majorly within the perinuclear region, where RyR3 was

also primarily localised. Furthermore, colocalisation between alphalgP120 and RyRs significantly declined outside the perinuclear region. Taking into account that NAADP induced Ca^{2+} bursts failed to induce global Ca^{2+} waves when RyR3 and RyR1 were selectively blocked, it was concluded that L-SR junction was formed primarily in the perinuclear region, and it forms a trigger zone that gives rise to global Ca^{2+} waves by CICR via RyR3.

Early studies conducted on pulmonary arterial smooth muscle showed that IP_3 induced Ca^{2+} waves were unaffected when the acidic Ca^{2+} stores were depleted with bafilomycin, or the RyRs were inhibited with ryanodine in a high concentration (Boittin et al., 2002, Kinnear et al., 2004). Additionally, NAADP induced global Ca^{2+} waves were not blocked by the IP_3R blocker Xestospongin C. Together these facts indicated that IP_3 induces Ca^{2+} waves through a pathway that is independent of NAADP and RyRs, and that NAADP-evoked Ca^{2+} waves are mediated via RyRs but not IP_3Rs. Conversely, in other cell types, for example oligodendrocyte progenitor cells (Haak et al., 2001) or smooth muscle cells isolated from portal vein (Gordienko and Bolton, 2002), crosstalk between RyRs and IP_3Rs were observed, which suggest that the lysosome-SR coupling might involve IP_3R in these cell types.

It was proposed that NAADP-evoked Ca^{2+} bursts from lysosomes are likely supported by two-pore segmented channels (TPCs) targeted to the endolysosomes (Calcraft et al., 2009). This study suggested that TPCs represent a family of NAADP receptors. In recombinant HEK293 where human TPC2 was restricted to the lysosome membrane, NAADP triggered Ca^{2+} release from lysosome-related Ca^{2+} stores via TPC2, which is amplified by CICR via IP_3Rs in this cell type. Consistent with this view, it was reported that although NAADP could induce Ca^{2+} release from TPC1, 2 and 3 in recombinant HEK293, only the Ca^{2+} bursts through lysosome targeted TPC2 and endosome targeted TPC3 displayed the magnitude that was required to couple with the ER for CICR (Ogunbayo et al., 2015). Here it can be concluded that within the L-SR junction, NAADP would induce Ca^{2+} release from the lysosome via membrane targeted TPC2s, which will be amplified by CICR from the SR and give rise to a global Ca^{2+} wave.

1.7.4.2 Ca^{2+} transporters in L-SR junction

When discussing Ca^{2+} handling, the Ca^{2+} transporters cannot be neglected. Considering the L-SR junction was localised to the perinuclear region, it can be inferred that SERCA2a would serve as the Ca^{2+} transporter to supply the perinuclear SR for the CICR (Clark et al., 2010a). On the lysosomal membrane, Ca^{+}-Mg^{2+} ATPase was discovered in rat liver cells, which may supply Ca^{2+} to the lysosome (Ezaki et al., 1992). In plant vacuoles, the Ca^{2+}/H^{+} exchanger was considered as the key to Ca^{2+} supplement in conjugated with the vATPase that dominate H^{+} influx (Hirschi et al., 1996).

1.8 Aims and hypotheses

The aim of the study is to investigate the intracellular Ca^{2+} signalling supported by the nanospaces in pulmonary arterial smooth muscle cells. By exploring how the cytoplasmic nanospaces demarcate site- and function- specific Ca^{2+} signalling, I wish to learn how they modulate multiple smooth muscle functions as an integrity. In particular, the function of one type of intracellular nanotube, the nuclear invaginations, remains controversial over decades. Hence, I envisage to study the function of nuclear invaginations. By investigating how Ca^{2+} signals were modulated within nuclear invaginations, I wish to investigate whether this local Ca^{2+} signal may direct gene expression.

I hypothesize that the intracellular nanospaces in pulmonary arterial smooth muscle cells demarcate Ca^{2+} signalling (Figure 1.11), their capacity for Ca^{2+} handling is conferred by Ca^{2+} releasing channels and transporters targeted to the membranes. Nuclear invaginations, as an intracellular nanospace, give rise to independent local Ca^{2+} signals that may modulate gene expression.

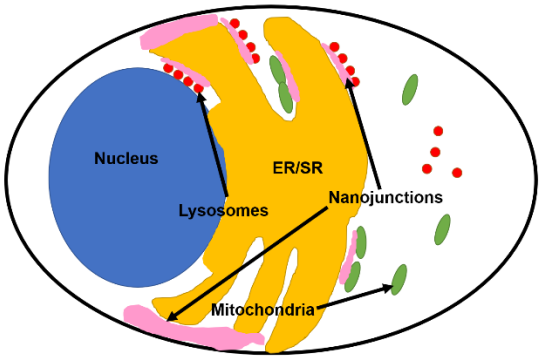

Figure 1.11 Skematic figure showing nanospaces in smooth muscle cells

Nanospaces for restricted Ca^{2+} signalling are predicted to form between the ER/SR and the plasma membrane, lysosomes and mitochondria as the pink regions indicated.

Chapter 2: Materials and methods

2.1 Dissection and identification of intrapulmonary arteries

All experiments were performed under the United Kingdom Animals (Scientific Procedures) Act 1986. Adult male Sprague Dawley rats (≈300 g) were sacrificed by cervical dislocation. Heart and lungs were removed and placed on ice in physiological salt solution (PSS) of the following composition (mmol/L): 130 NaCl, 5.2 KCl, 1 $MgCl_2$, 1.7 $CaCl_2$, 10 glucose, and 10 HEPES, pH 7.4.

The dissection of intrapulmonary arteries was conducted under a dissection microscope (model PZM, World Precision Instruments, Sarasota FL, USA) with dissection forceps and spring bow scissors (Duckworth & Kent, England, UK). During the process, lung lobes were bathed in ice cold PPS, one individual lobe was pinned onto a Sylgard coated dissection dish with the cut of the trachea facing up. The airway was cut open along the length of it from where the trachea entered the lobe, and the artery was identified as the parallel semi-translucent tube that was running below the trachea. To expose the artery, the parenchyma and the connective tissues on both sides of the artery and the trachea need to be fully removed. The artery was extracted with care to guarantee minimal damage, and the connective tissues attached to the artery was carefully cleaned before the artery was cut open and immersed in ice cold PPS for further experimental procedures.

2.2 Dissociation of pulmonary arterial smooth muscle cells

Primary, secondary and tertiary order branches of the pulmonary arteries were dissected out using the method described in section 2.1, and single pulmonary arterial smooth muscle cells were dissociated by either of the two protocols described below.

2.2.1 Acute isolation of pulmonary arterial smooth muscle cells

Overnight digestion protocol for pulmonary arterial smooth muscle cell dissociation

As described in Clark et al (Clark et al., 2010a), arteries were placed in low Ca^{2+} solution of the following composition (mM): 110 NaCl, 5 KCl, 2 $MgCl_2$, 0.5 NaH_2PO_4, 5 KH_2PO, 15 $NaHCO_3$, 0.16 $CaCl_2$, 0.5 EDTA, 10 glucose, 10 taurine and 10 HEPES,

pH 7.4. After 10 minutes the arteries were placed in the same solution containing 0.5 mg/ml papain and 1 mg/ml bovine serum albumin and kept at 4 ^{o}C overnight. Papain is a cysteine protease that cleaves peptide bonds of basic amino acids, leucine or glycin. It exhibits broad specificity and will digest most protein substrates, and it also hydrolyses esters and amides. Papain was widely used in cell isolation, notably, it was able to isolate rat vascular smooth muscle cells with good viability without compromising the sensitivity of the cells to stimuli (Bolzon and Cheung, 1989). The overnight treatment allowed papain to penetrate the tissue. The following day 0.2 mmol/L 1,4-dithio-DL-threitol (DTT) was added to the solution, and the preparation was incubated for 1 hour at room temperature (22 ^{o}C). The proteolytic activity of papain requires a free sulfhydryl group, and DTT is able to maintain the sulfhydryl group in a reduced state, as the result papain would be activated. The tissue was then washed 3 times in fresh low Ca^{2+} solution without enzymes, and single smooth muscle cells were isolated by gentle trituration with a fire-polished Pasteur pipette. Cells were stored in suspension at 4 ^{o}C until required.

Fast digestion protocol for pulmonary arterial smooth muscle cells dissociation

Arteries were immersed in Ca^{2+} free solution of following composition (mM): 130 NaCl, 5.2 KCl, 2.5 $MgCl_2$, 10 glucose, 10 Hepes, pH 7.4. The dissociation solution was prepared by adding 1mg/ml papain, 0.8 mg/ml DTT and 0.7mg/ml bovine serum albumin into the Ca^{2+} free solution. Arteries were placed in the dissociation solution for 15 minutes at 37 ^{o}C, which was followed by 3 times of wash in fresh Ca^{2+} free solution. Single smooth muscle cells were isolated by gentle trituration with a fire-polished Pasteur pipette, and cells were stored in suspension at 4 ^{o}C until required. Compared to the overnight digestion protocol, the fast digestion protocol allows the isolation to be done within an hour and the cells can be used for experiments on the day of artery dissection, which improved cell viability. However, the protocol does not provide a very long time for papain to penetrate the tissue, which compromises the efficiency of isolation.

The choice of protocol was determined by the requirements of the experiment.

2.3 Cell culture and sample fixation

2.3.1 Culture of pulmonary arterial smooth muscle cells.

Freshly isolated pulmonary arterial smooth muscle cells were suspended in low Ca^{2+} solution or Ca^{2+} free solution depending on the isolation method used, with the density of 10^5 -2x10^5 cells per ml. 100 µl, 90 µl, 50 µl or 25 µl of cell suspension was added to each Fluorodish (WPI, USA) and cultured for 1, 2, 4 or 7 days. If culture for immunocytochemistry, the same amount of cell suspension was added to a 13 mm circular coverslip sat in a 12-well plate. The cells were allowed to attach for 45 min at room temperature in a cell culture hood, 2 ml of culture medium of following composition (44.5% Waymouth's Medium, 44.5% Ham's F12 Nutrient Mixture, 10% foetal bovine serum, 1% Penicillin-Streptomycin) was added to each Fluorodish or each well of the 12-well plate, and the cells were incubated at 37 ^{o}C with 5% CO_2. Foetal bovine serum contains multiple growth factors that enhance cell growth as well as cell proliferation (Franke et al., 2014), whereas antibiotics were added to reduce the chance of infection. The culture medium was replaced every 3 days for the best outcomes.

2.3.2 Acutely isolated cell fixation with methanol

Freshly isolated pulmonary arterial smooth muscle cells were suspended in low Ca^{2+} solution or Ca^{2+} free solution depending on the isolation method with the cell density of 10^5 -2x10^5 cells per ml. 100 µl cell suspension was added to a 13 mm circular cover glass that sat in a 12-well plate, and the cells were allowed to attach for 45 minutes at room temperature. 2 ml of ice-cold methanol was added into each well, and the 12-well plate was sealed with parafilm and stored at -20 ^{o}C for 10 minutes or longer. Alcohol fixatives act by denaturing proteins through the removal of water, it is a very fast fixation process, but it will result in tissue shrinkage because of dehydration (Howat and Wilson, 2014). Generally, it was considered as a less toxic alternative to formaldehyde for studies of membrane bound proteins.

2.3.3 Cultured cell fixation with methanol

Cultured pulmonary arterial smooth muscle cells were taken out of the incubator and were washed 3 times with PPS that was pre-warmed to 37 ^{o}C. 2 ml of ice-cold

methanol was added into each well, and the 12-well plate sealed with parafilm and stored at -20 °C for at least 10 minutes.

2.3.4 Sample fixation with paraformaldehyde

Acutely isolated or cultured pulmonary arterial smooth muscle cells were prepared as described in section 2.2 or 2.3.1. Instead of adding methanol, 1ml of 4% paraformaldehyde was added to each well of the 12-well plate and the cells were incubated at 37 °C for 20 minutes. 4% paraformaldehyde was prepared by dissolving paraformaldehyde in phosphate buffer which contains 650 mM $Na_2HPO_4 \cdot 2H_2O$ and 174 mM $NaH_2PO_4 \cdot 2H_2O$ with pH adjusted to 7.4. Following the fixation, cells were permeabilized by incubating with 0.2% Triton X-100 (prepared with PPS) for 10 minutes at room temperature. Paraformaldehyde is polymerized formaldehyde, and formaldehyde fixatives act by cross-linking side chain amino groups of lysine without affecting the secondary and tertiary structures of proteins (Howat and Wilson, 2014), it was used instead of methanol when the secondary and tertiary structures of proteins need to be retained.

2.4 Immunocytochemistry

2.4.1 Primary and secondary antibodies for immunocytochemistry

Sequence-specific primary antibodies that were used in my studies are listed in table 2.1.

Table 2.1 Primary antibodies used in immunocytochemistry and information on dilution factor, immunogen, animal origin, supplier and commercial catalogue number.

Antibody name	Description	Dilution	Immunogen	Supplier	Catalogue number
Anti-Lamin A antibody	Rabbit polyclonal	1:200	Residues 550 to the C-terminus of Human Lamin A	Abcam	ab26300
Anti-Lamin A antibody	Mouse monoclonal	1:100	Amino acid 598-611 of human Lamin A	Abcam	ab8980
Anti-SUN2 antibody	Rabbit monoclonal	1:200	C-terminal residues of Human SUN2	Abcam	EPR6557
Anti-emerin antibody	Rabbit polyclonal	1:200	Amino acid 3-254 of full-length Human emerin	Santa Cruz	sc-15378
Anti-dimethyl Histone H3 (Lys9)	Mouse monoclonal	1:200	Amino acid1-19 of human Histone H3, dimethylated on Lys9	Millipore	05-1249
Anti-BAF antibody	Goat polyclonal	1:50	C terminal residues of Human BAF	Santa Cruz	sc-9744
Anti-Nesprin-1 antibody	Mouse monoclonal	1:50	Recombinant full-length nesprin-1- α proteins	Gift from Dr. Eric Schirmer (Reference: NT Duong et al, 2014)	MANNES1E (8C3)

Samples fixed by either method described in section 2.3 were washed three times with Tris-buffered saline containing 140 mM NaCl, 25 mM Tris-base, 1.3 mM KCl (PH 7.4), followed by a 30 minutes incubation with blocking buffer of the following composition: 1% bovine serum albumin, 1% goat serum, 10% donkey serum, 10% foetal bovine serum and 0.1% Tween-20 in phosphate-buffered saline, pH 7.4. The blocking buffer contains serum and bovine serum albumin to prevent any unspecific labelling of the primary antibodies, and this improves the signal to noise ratio of the imaging taken from the labelled sample. After blocking, primary antibodies that were diluted in blocking buffer based on the dilution factors described in Table 2.1 were applied to the samples and the samples were incubated overnight at 4 ^{o}C in dark. The following day, samples were washed 3 x 10 minutes with Tris-buffered saline containing 0.1% Tween-20 to remove the residual primary antibody. To visualize the distribution of the target proteins that were labelled by primary antibodies, secondary antibodies that were conjugated to fluorescent molecules were applied to the samples. Each secondary antibody was raised against immunoglobulin of the species that one primary antibody was raised in, which allows specific targeting. The secondary antibodies used in the experiments are displayed in the table below.

Table 2.2 Secondary antibodies used in immunocytochemistry and information on dilution factor, excitation and emission wavelengths, animal origin, supplier and commercial catalogue number.

Antibody name	Description	Dilution	Excitation wavelength	Emission wavelength	Supplier	Catalogue number
Donkey anti-Mouse IgG (H+L) Secondary Antibody	Alexa Fluor 488	1:200	495	519	Thermo Fisher Scientific	A21202
Donkey anti-Rabbit IgG (H+L) Secondary Antibody	Alexa Fluor 568	1:200	578	603	Thermo Fisher Scientific	A10042
Donkey anti-Goat IgG (H+L) Secondary Antibody	Alexa Fluor 647	1:100	650	668	Thermo Fisher Scientific	A21447

Samples were incubated with secondary antibodies diluted in blocking buffer (as suggested in Table 2.2) for 2 hours at room temperature in dark. To visualize nuclei, the samples were incubated with 4-,6-diamidino-2-phenylindole (Dapi, 1µg/ml; excitation 358nm, emission 461nm) for 15 minutes at room temperature. Then, the samples were washed 3 times with phosphate-buffered saline containing 0.1% Tween-20 and 2 times with phosphate-buffered saline. After 5 minutes of air dry the coverslips were attached to slides by anti-fading mountant (2.4 g Mowiol 4–88, 6 g of glycerol, 2 ml of 0.2 M Tris-HCl, pH 8.5, 2.5% 1,4 diazabicyclo (2.2.2.) octane). To

preserve the samples for longer, the coverslips were sealed with transparent nail polisher and stored at 4 ^{o}C. Notably, samples that were incubated with primary antibodies or secondary antibodies only, as well as samples that were not labelled were mounted as controls, which provided information on whether the primary or secondary antibody caused any non-specific labelling, and the level of cell autofluorescence when excited by laser scans. The fluorescence spectra for the excitation and emission wavelengths of the secondary antibodies are displayed in Figure 2.1.

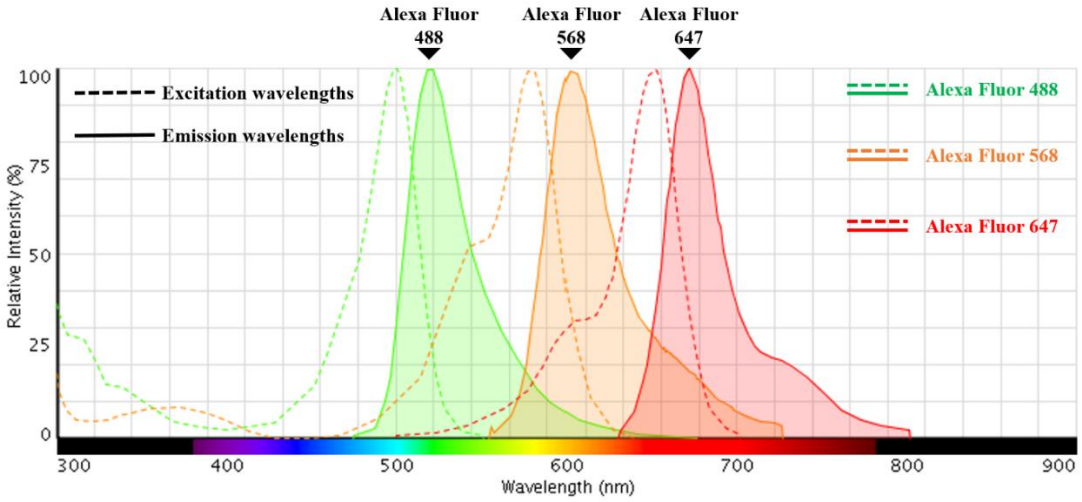

Figure 2.1 Fluorescent spectral profiles. The fluorescent spectral profiles of the excitation (dashed lines) and emission wavelengths of Alexa Fluor 488 (green), Alexa Fluor 568 (orange) and Alexa Fluor 647 (red) are shown.

2.5 Fluorescence labelling of live pulmonary arterial smooth muscle cells

2.5.1 Identification of endoplasmic reticulum, sarcoplasmic reticulum and outer nuclear membrane with ER-tracker

ER-Tracker blue-white DPX (Thermo Fisher Scientific, catalogue number E12353) is a type of dapoxl dye that displays high extinction coefficients, high quantum yields and lower cell toxicity compared to the conventional ER stain $DiOC_6$. The product has high selectivity for the endoplasmic reticulum, and can also be used to identify the sarcoplasmic reticulum and nucleoplasmic reticulum (Marius et al., 2006). Pulmonary

arterial smooth muscle cells were freshly isolated as described in section 2.2, or cultured as described in section 2.3 and washed 3 times with PSS. 1μM ER-tracker dissolved in PSS was then applied to the cells and incubated for 30 minutes at 37 ºC. The cells were washed 5 times with dye-free PSS prior to imaging. The excitation and emission wavelengths for ER-Tracker white-blue are 375 nm and 550 nm, respectively (Figure 2.2).

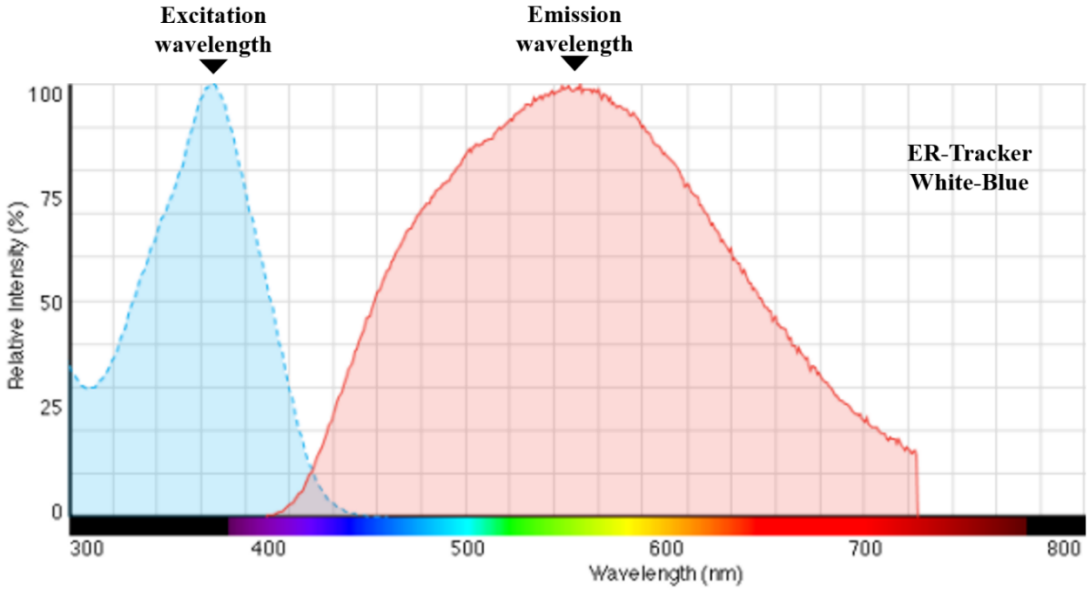

Figure 2.2 Fluorescent spectral profiles. The fluorescent spectral profiles of the excitation (blue) and emission (red) wavelengths of ER-Tracker white-blue are shown.

2.5.2 Identification of the intracellular Ca^{2+} stores

Calcium Orange (Thermo Fisher Scientific) is a Ca^{2+} indicator that was used for visualizing intracellular Ca^{2+}, and it was essentially an acetoxymethyl (AM) ester. AM esters are carboxylic acid derivatives that are able to penetrate plasma membranes. Once inside the cells, AM esters are cleaved by intracellular esterase, and the resulting products could chelate cytosolic Ca^{2+} to generate fluorescence (Hamad et al., 2015). Upon binding Ca^{2+}, the fluorescence intensity of Calcium Orange increases by 3 folds, which makes it less than ideal for assessing Ca^{2+} flux in the cytoplasm.

However, it is good for identifying intracellular Ca^{2+} stores considering that compartmentalization of the dye is facilitated at 37 ºC (see product instruction sheet). Calcium Orange was dissolved in DMSO that contains 1% pluronic F127 which serves as a surfactant to facilitate the loading of the dye, the concentration of Calcium Orange in DMSO was 10 mM. The solution was then applied to acutely isolated or cultured pulmonary arterial smooth muscle cells with a final concentration of 5µM. The cells were incubated at 37º C for 30 minutes, which was followed by 5 x washes with fresh PSS. If the cells were to be colabelled with ER-tracker, Calcium Orange and ER-tracker were added at the same time and incubated at 37º C for 30 minutes prior to imaging. The excitation and emission wavelengths of Calcium Orange are 549 nm and 576 nm, respectively (Figure 2.3).

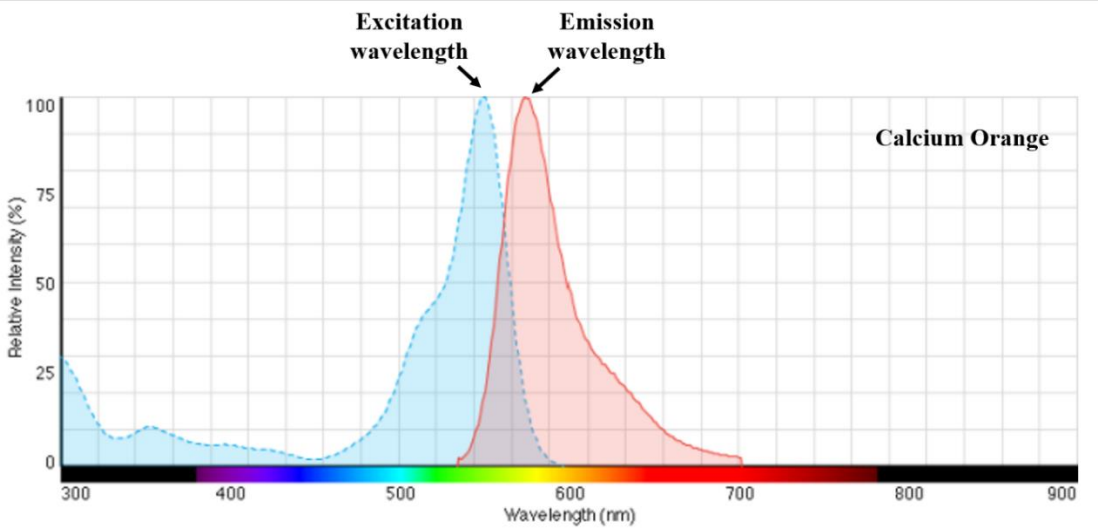

Figure 2.3 Fluorescent spectral profiles. The fluorescent spectral profiles of the excitation (blue) and emission (red) wavelengths of Calcium Orange are shown.

2.5.3 Fluo-4 loading for Ca^{2+} imaging

Fluo-4 is available as an AM ester, and is a Ca^{2+} indicator that exhibits a dramatic increase in fluorescence when Ca^{2+} is bound. Unlike Calcium Orange, the fluorescence intensity of Fluo-4 increases at least 100-fold upon binding Ca^{2+}, which

makes it the ideal Ca^{2+} indicator for studying Ca^{2+} signalling by confocal microscopy.

10 mM Fluo-4 was first dissolved in DMSO that contained 1% pluronic F127, sonicated for 10 minutes, and then loaded into acutely isolated or cultured smooth muscle cells that were bathed in PPS at a final concentration of 5µM. Following 30 minutes of loading at room temperature, the cells were washed with 5 times in fresh PPS, and the cells were allowed to equilibrate for at least 30 minutes before imaging. The excitation and emission wavelengths of Fluo-4 are 494 nm and 506 nm, respectively (Figure 2.4). When Fluo-4, ER-Tracker and/or Calcium Orange were used in the same experiment, Fluo-4 was loaded at 25 ºC and the cells washed before the cells were incubated with the other dyes.

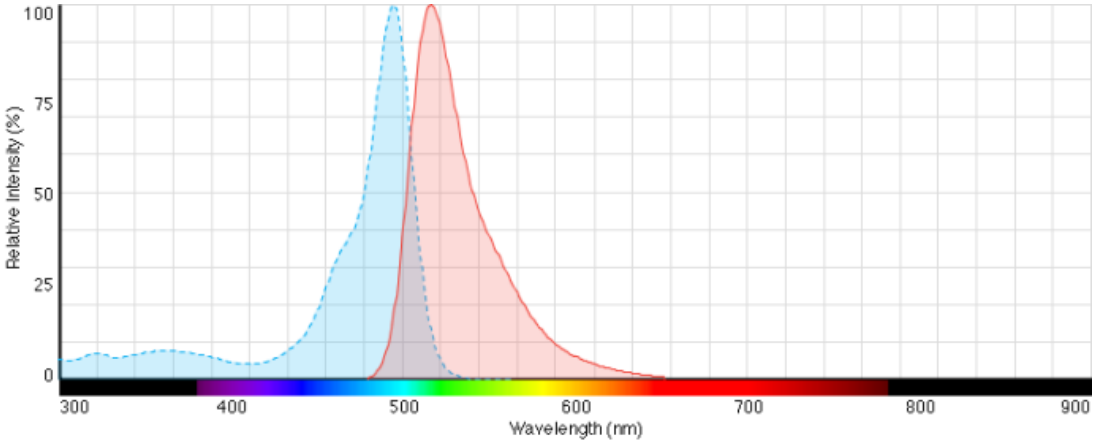

Figure 2.4 Fluorescent spectral profiles. The fluorescent spectral profiles of the excitation (blue) and emission (red) wavelengths of Fluo-4 are shown.

2.5.4 Identification of the nuclei with Draq 5

Draq 5 is a fluorescent probe that labels double stranded DNA in live cells, the excitation and emission wavelengths of the dye are 647 nm and 681 nm respectively. Prior to imaging, 1 µM Draq 5 (dissolved and diluted in PSS) was applied to acutely isolated or cultured pulmonary arterial smooth muscle cells and incubated for at least 1 minute at room temperature. The cells can be imaged immediately without washing off the dye, and cells were always imaged immediately after addition of Draq5 to avoid

cellular toxicity.

2.6 Confocal imaging

Confocal microscopes are widely used in optical imaging for higher resolution and contrast, achieved by the application of pinhole apertures. As shown in Figure 2.5, two pinhole apertures are positioned in the confocal system; one sits between the light source and the dichroic mirror and the other one lies between the dichroic mirror and the detector. The light source, which is a light beam with a selected wavelength, is focused by the first pinhole aperture, and is reflected by the dichroic mirror and illuminates the sample. The fluorophores within the sample are excited, and therefore they emit fluorescent light of another wavelength which will pass through the dichroic mirror and reach the second pinhole aperture. Only the light emitted by the object in the focal plane can pass through the pinhole (indicated by solid red lines) and reach the detector, the light emitted by the object that is out of focus will be blocked by the pinhole aperture (dashed red lines), as the result the background noise would be largely reduced.

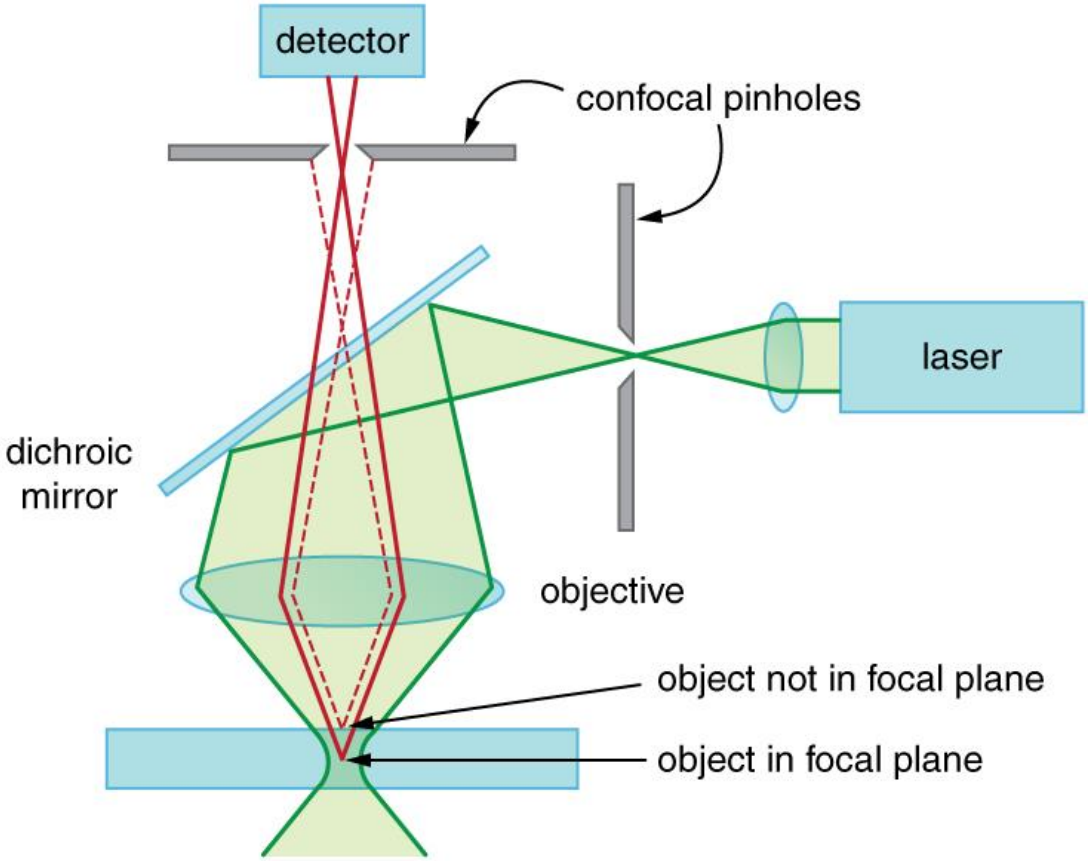

Figure 2.5 Schematic diagram showing the principle of confocal microscopy. Adapted from Nikon Instrument instruction, access online from https://www.nikoninstruments.com/en_GB/Products/Confocal-Microscopes/A1R

Both the live cell Ca^{2+} imaging and the visualization of immunocytochemistry labelling were conducted with a Nikon A1Rplus confocal system. Live cell experiments were recorded at 22 °C with a sampling frequency of 0.5 Hz, via a Nikon Eclipse Ti inverted microscope with a Nikon Apo 40x λS DIC N2, 1.25 n.a. water immersion objective (Nikon Instruments Europe BV, Netherlands). Immunocytochemistry samples were visualized with the same system and same settings, but a Nikon CFI Plan Apo VC 60X oil immersion objective (Nikon Instruments Europe BV, Netherlands).

Two types of experiments were conducted with the confocal system: Z stacks through the cell and single Z section versus time. Unhealthy cells were excluded, only elongated (typical shape of the differentiated pulmonary arterial smooth muscle cell) acutely isolated cells were selected. Rhomboid shaped cells are typical of proliferating pulmonary arterial smooth muscle cells, and they were selected when studying cultured cells. Fixed cells were labelled by fluorescent secondary antibodies for the investigation of nuclear membrane structure. Only cells with good labelling were picked and viewed under the 60X oil immersion objective. The nuclei were selected as the region of interest at the highest magnification possible, and Z stacks of the entire nuclei were taken with a step interval of 100-200 nm. Similarly, live cells labelled by ER-tracker, Calcium Orange or Fluo-4 were viewed under a 40X water immersion objective, and only cells with good loading were selected. Z stacks that covered the entire cells were defined and scanned with the step interval of 150-200 nm. Live cells loaded with Fluo-4 with or without Draq 5 were viewed with 40X water immersion objective. Cells with good loading and visible nuclear invaginations, that did not photo-bleach or respond to the laser heat were selected for time-course experiments. During the experiments, stimuli were added to the cells and the changes of Ca^{2+} concentration reflected by changes in the fluorescent intensity of Fluo-4 within the

regions of interests were recorded over time, and saved as time course videos. The images and time course videos generated with the confocal system have the resolution of 150 nm to 200 nm.

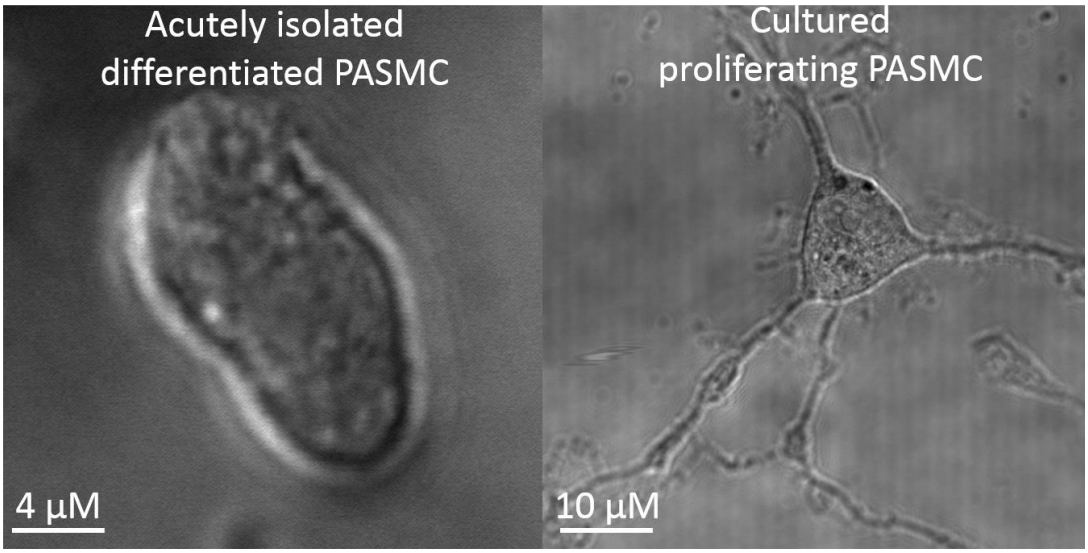

Figure 2.6 Shape of differentiated or cultured PASMCs.

Bright field image of a typical morphology of a healthy acutely isolated, differentiated pulmonary arterial smooth muscle cell (left), and a cultured, proliferating pulmonary arterials smooth muscle cell (right) are shown.

2.7 Deconvolution and image processing

2.7.1 Improving the resolution of the images and time course videos by deconvolution

The Point Spread Function (PSF) defines the basic building block of acquired images. The PSF is the spread of fluorescence from a single point recorded by an optical device. It is described by the Linear System theory of an incoherent imaging system (i.e. fluorescence microscopes), the imaging of one independent objects does not affect the imaging of the other at the same time. This means that any image can be computed as a sum of PSFs at a different position, which is the idea of convolution. As the figure below shows, the images recorded by fluorescence microscopy are the

reconstruction of 3D PSFs, which are replacements of the original sub-resolution light source.

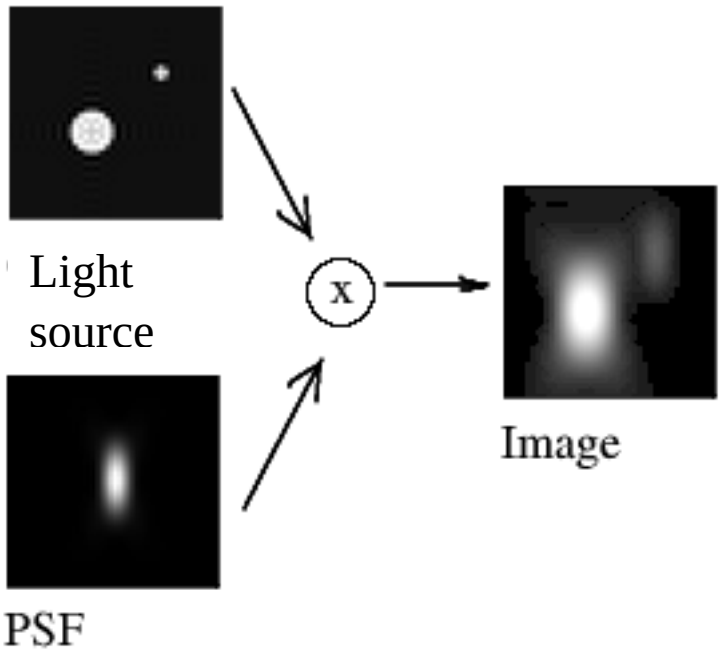

Figure 2.7 Schematic figure explaining blurring caused by PSF. Adapted from Huygens Essential instruction, accessed online from https://svi.nl/HuygensEssential.

Image blurring is caused by the PSF, the whole acquired image was degraded by convolution, and the process can be mathematically described by the convolution equation:

$$g = h * f$$

Where *g* stands for the image acquired, which arises from both the original light source *f* and the PSF which is *h* in the equation. The wider the PSF is, the more degraded the image will become.

The PSF can be measured by recording beads, but here we used the Huygens Essential software (Scientific Volume Imaging B.V., Netherlands) to compute a theoretical PSF based on the model of our confocal microscope and microscopic parameters (i.e. excitation and emission wavelengths).

To obtain images with higher resolution, deconvolution can be conducted, which is the reverse of convolution. Based on the convolution equation, as the convolved image *g* is known and the PSF *h* is calculated, the distribution of the original light source f can be inferred. After deconvolution, the dynamic range of the images is increased and the signal to background noise ratio is significantly improved, which will bring the resolution up to 100 nm-150 nm. In our experiments, all the images and time course videos recorded by confocal microscopy were deconvolved with Huygens Essential software (Scientific Volume Imaging B.V., Netherlands), which allowed us to visualize nanotubes in the cells. The images before and after deconvolution can be seen in the figure below.

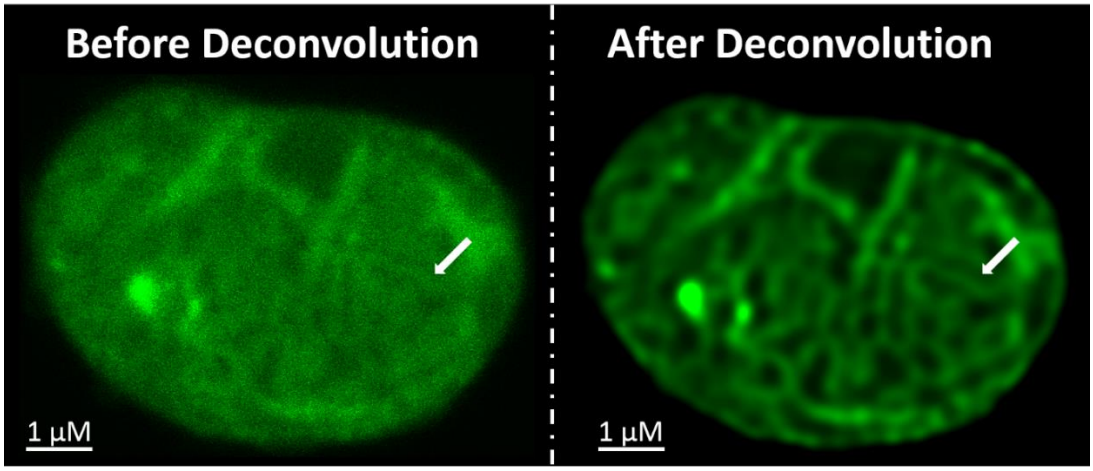

Figure 2.8 Deconvolution improves resolution. Confocal images of an acutely isolated pulmonary arterial smooth muscle cell loaded with Fluo-4 (green), before (left) and after (right) deconvolution. One example nanotube was indicated by an arrow to show the improvement in resolution.

2.7.2 3D reconstruction of confocal Z-stack and the application of digital skin

Z stacks of acutely isolated or cultured pulmonary arterial smooth muscle cells with fluorescent labelling were taken by confocal microscopy as described in section 2.6. The Z stacks were deconvolved as described in section 2.7.1, and imported to Imaris (Bitplane, Oxford Instruments, UK) for 3D reconstruction and analysis. For the ease of illustrating intracellular structures, a digital skin was applied to the 3D reconstruction, which gives better definition.

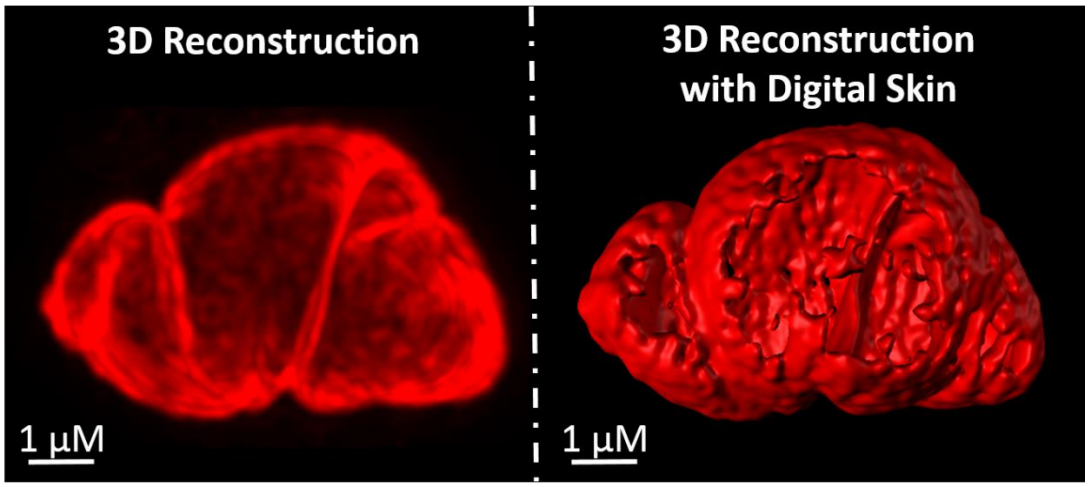

Figure 2.9 3D reconstruction and digital skin. 3D reconstruction of a series of confocal Z-stacks showing lamin A (red) labelled nucleus of an acutely isolated pulmonary arterial smooth muscle cell with (right) and without digital skin.

If the sample was labelled by two or more dyes or antibodies, the colocalization between different staining can be calculated with Imaris as illustrated in Figure 2.10, which will generate a measurement of the volume of colocalization and Pearson's correlation coefficient. The volume of colocalization of one staining is compared to the total volume of the staining, which gives the percentage of volume of this staining colocalised with the other. The Pearson's correlation ecoefficiency (sometimes referred as Pearson's correlation coefficient) measures the linear correlation between two staining. It has a value between +1 and −1, where 1 is total positive linear correlation, 0 is no linear correlation, and −1 is total negative linear correlation.

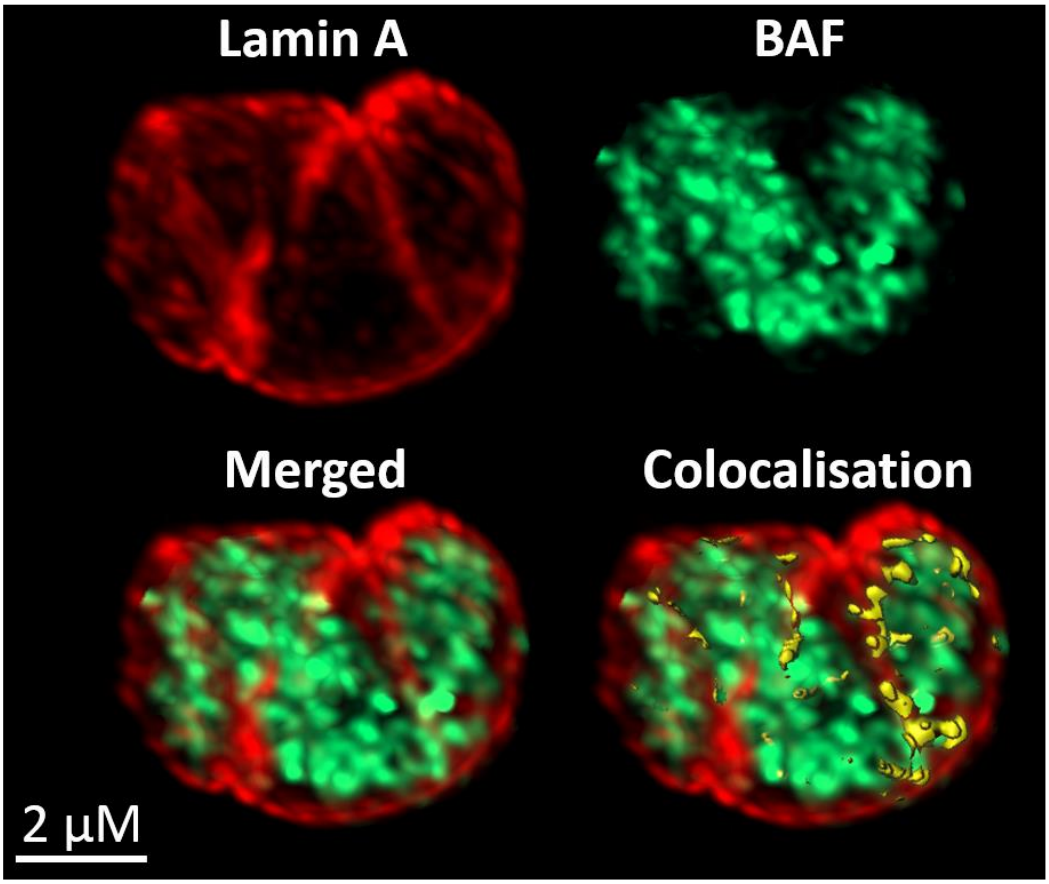

Figure 2.10 Colocalisation between two staining generated by Imaris. An acutely isolated pulmonary arterial smooth muscle cell was labelled by lamin A (red, upper panel at left) and BAF (green, upper panel at right). The red and green staining were merged as showed in the left lower panel, the colocalization between the two channels was calculated and displayed in the yellow coated with digital skin (lower panel at right).

2.8 Ca^{2+} imaging analysis

2.8.1 Generating Ca^{2+} intensity plots

Confocal time course videos were deconvolved as described in section 2.7, and were imported into Image J. Video records of the response of cells loaded with Ca^{2+} indicators were compiled, with the changes in Ca^{2+} concentration reflected by the fluorescent intensity of the Ca^{2+} indicator. To semi-quantify the Ca^{2+} concentration

within different regions of interest, a line was drawn across all the regions of interest and fluorescent intensity was measured along the line (as showed in Figure 2.11) with the plot profile tool.

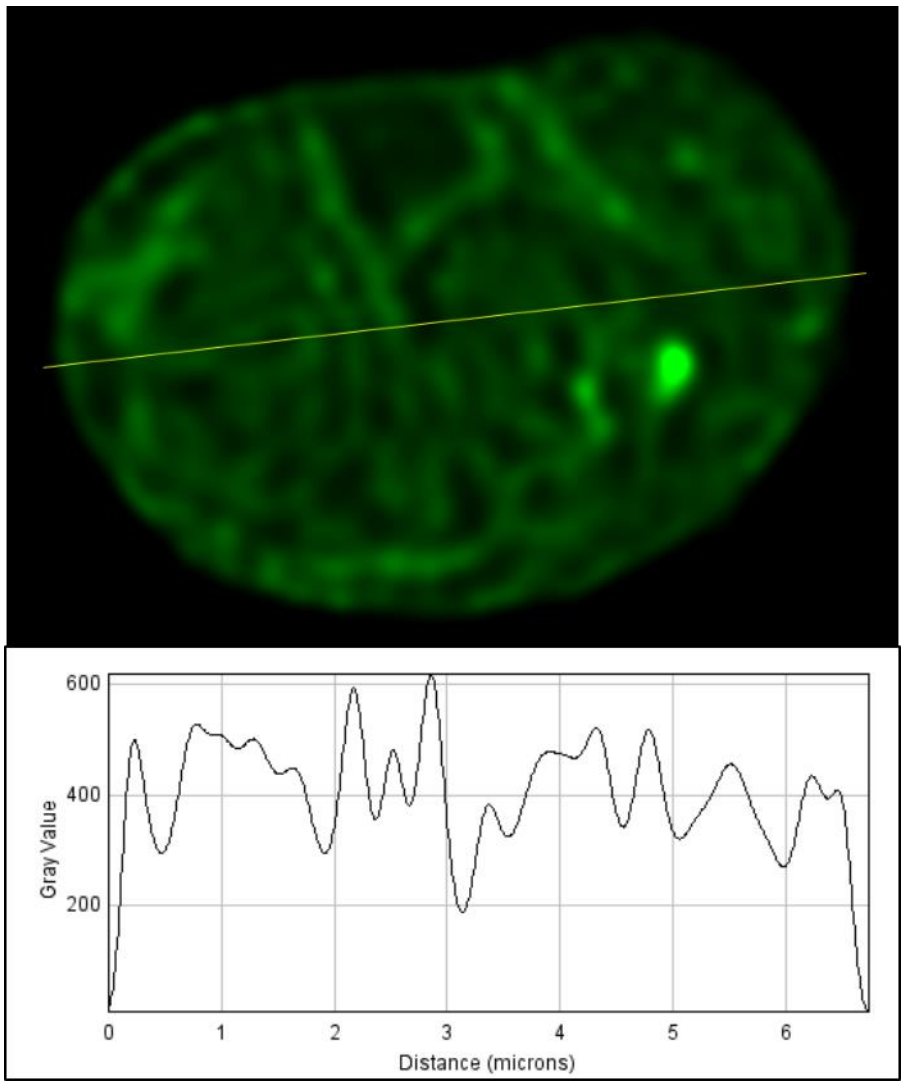

Figure 2.11 Intensity plot of a pulmonary arterial smooth muscle cell loaded with Fluo-4.

A confocal scan through the middle of a pulmonary arterial smooth muscle cell loaded with Fluo-4 was deconvolved, and a line was drawn across the cell (upper panel), the Fluo-4 fluorescent intensity of the regions of interest along the line was measured and showed in gray value as the lower panel displayed.

2.8.2 Analysis of the live cell response to stimuli

As described in section 2.6, time course videos that reflect the response of live cells to stimuli were recorded, and they were deconvolved as described in section 2.7 and opened with Image J. Three regions of interest were selected as shown in the figure

2.12, with the ROI manager tool. Draq 5 labelling defined where the nucleus was, based on which the regions of nucleus, cytoplasm and nuclear invaginations were selected.

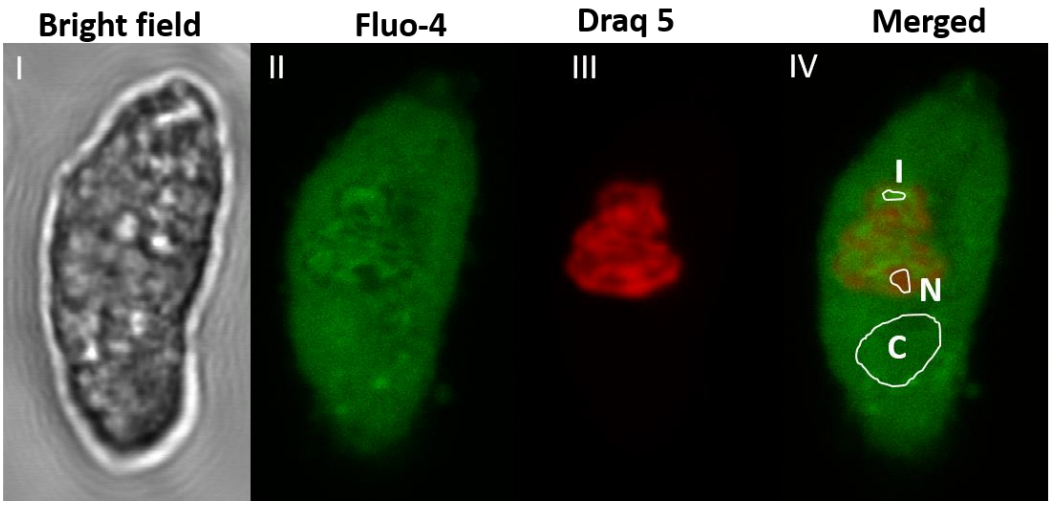

Figure 2.12 Selecting ROIs for measurement.

An acutely isolated pulmonary arterial smooth muscle cell was loaded with Fluo-4 and Draq 5 to reveal Ca^{2+}distribution and the position of the nucleus. (I) Bright filed image of the cell. (II) Fluo-4 loading. (III) Drag 5 loading indicating where the nucleus was. (IV) Merged image of the Fluo-4 loading and Draq 5 labelling. Three ROIs were selected, drawn and labelled with letters. I indicates nuclear invagination, N indicates nucleus and C indicates cytoplasm.

Once ROIs were selected, mean fluorescence intensity over time within the ROIs was measured using ROI manager. Upon the addition of stimuli, cell contraction might be observed, which would lead to the displacement of the ROIs from the desired region of interest. Therefore, the position of ROIs was adjusted for each frame acquired, to ensure that the desired regions of interest were always positioned within the ROIs as originally drawn. For example, the cell in Figure 2.13A contracted slightly and the invagination analysed moved downwards in Aii compared to Ai. To minimize the bias caused by cell contraction, ROI 1 was moved downward to trace the invagination as

the figure showed. Each image file was assessed manually to ensure accuracy and consistency of measurement within the regions of interest specified. We excluded from analysis any cell that exhibited contraction sufficient to alter the focal plane or other movement artefacts that might compromise our ability to take reliable measurements within desired regions of interest.

The measured Fluo-4 fluorescent intensity was converted to a fluorescence ratio (F_X/F_{C0}) that normalize records and allow for cross-comparison between different cells. Here F_x is the mean fluorescence intensity of the selected ROI and F_{C0} represents the fluorescence intensity of the selected perinuclear cytoplasmic region at time point 0, which is prior to drug addition.

As shown in Figure 2.13, the converting of arbitrary units into a fluorescence ratio does not modify the shape of the response curve. However, it provided a measurement that can be compared to other cells while ignoring the differences in basal fluorescent intensity. The fluorescence ratio at the timepoint of drug addition was considered as the baseline, and the delta peak change was calculated by comparing the baseline and the fluorescence ratio of the peak of the response.

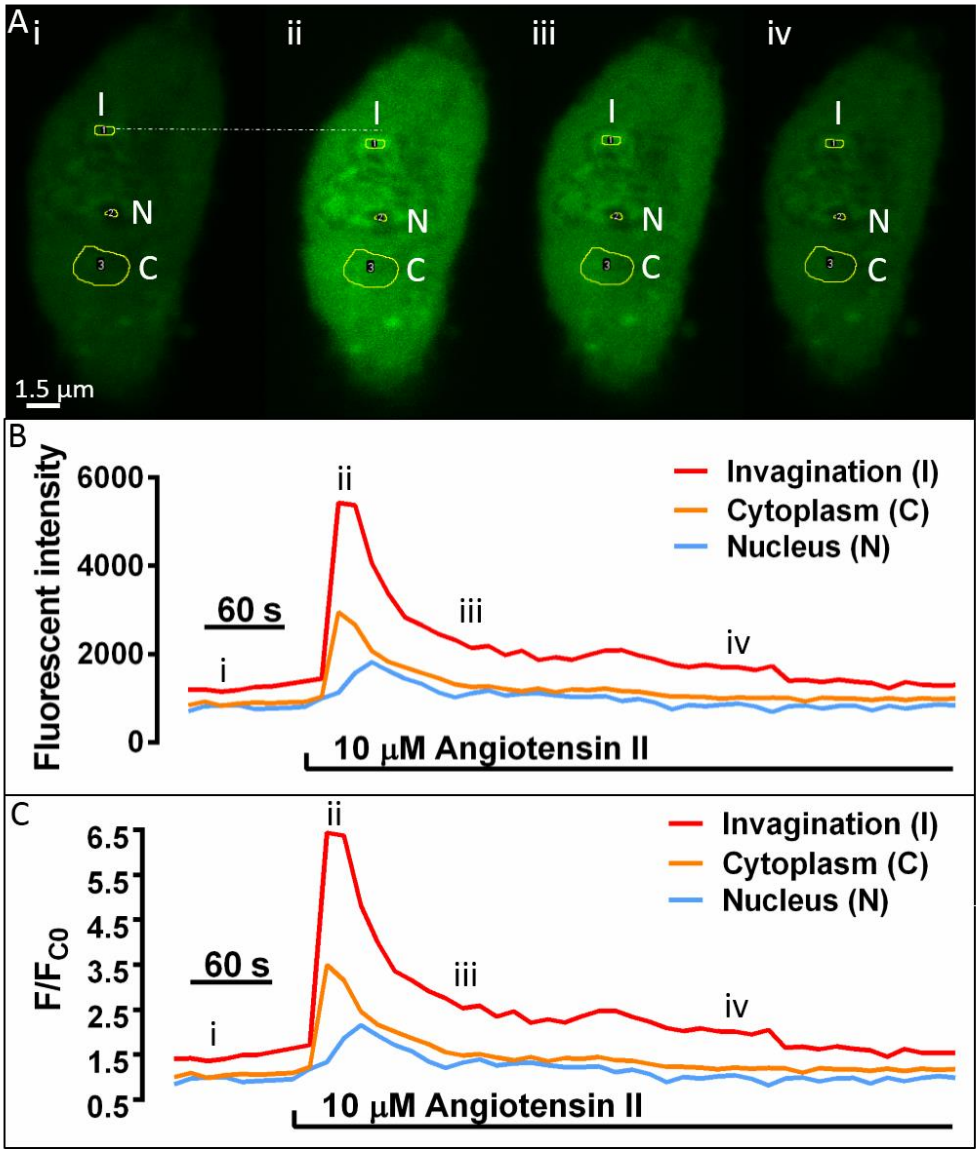

Figure 2.13 Quantification of confocal Ca^{2+} imaging.

(A) An acutely isolated pulmonary arterial was loaded with Fluo-4, 10 µM Angiotensin II was added to the cell and the response over time was recorded. 4 representative frames at 4 distinct time points of the record were showed in Ai, Aii, Aiii, Aiv. ROIs were circled and labelled, I for Invagination, N for Nucleus and C for cytoplasm. The white dashed line between Ai and Aii shows how the ROI was moved.

(B) The fluorescent intensity within the selected region of invagination (red), nucleus (blue) and cytoplasm (orange) was plotted against time. The four time points selected in A was indicated on the plot.

(C) The fluorescent ratio within the selected region of invagination (red), nucleus (blue) and cytoplasm (orange) was plotted against time. The four time points selected in A was indicated on the plot.

2.8.3 3D surface plot

To demonstrate that the fluorescence intensity in different ROIs were distinct and the responses to stimuli were asynchronized, the 3D surface plot was produced. Pseudocolor (Fire LUT) was applied to the files using ImageJ. By choosing surface plot under the catalogue of analysis, the 3D surface plot was produced. It can be saved as a video, and each frame can be saved independently as an image.

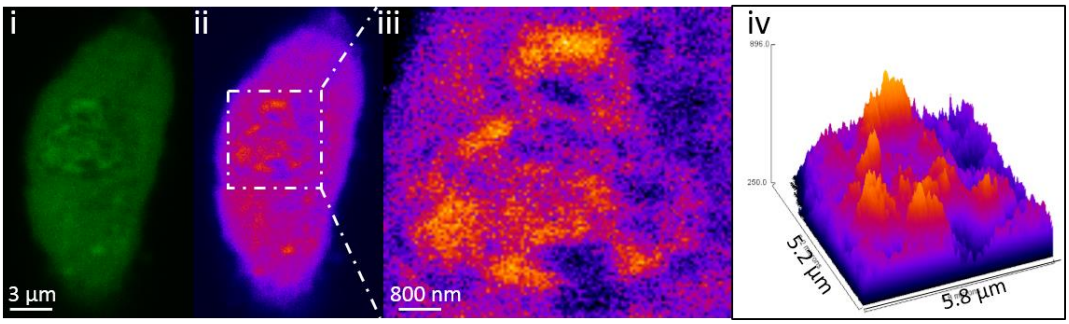

Figure 2.14 Process of making a 3D surface plot.

An acutely isolated pulmonary arterial was loaded with Fluo-4, an image was recorded with confocal and viewed with Image J. (i)The original file. (ii) Pseudocolor was applied, in the fire LUT fluorescent intensity lies on the spectrum, yellow indicates high fluorescent intensity whereas purple is for low fluorescent intensity. (iii)The nucleus was cropped out and enlarged. (iv) 3D surface plot of the nucleus was generated.

2.9 RNA extraction, cDNA generation and qPCR

2.9.1 RNA extraction

Total RNA was extracted from first, second and third order branches of the pulmonary arterial tree, acutely isolated pulmonary arterial smooth muscle cells and cultured pulmonary arterial smooth muscle cells using Trizol reagent according to the manufacturer's instructions (Invitrogen, UK).

All extraction steps were performed at room temperature unless stated otherwise. Pulmonary artery trees were dissected out as section 2.2 showed, endothelial cells

on the surface of the arteries were removed by gentle rubbing with a cotton bud. The tissue was homogenized with a homogenizer, 1ml of the Trizol reagent was added to 80 mg of the homogenized tissue to lyse the cells.

Acutely isolated cells in suspension were centrifuged at 1800 rpm at 4°C for 10 minutes to collect the cell pellet without disrupting the cell membrane. The supernatant was discarded and 1ml of Trizol reagent was added to roughly 2 million cells to lyse the membrane and release DNA, RNA and protein. To assist the lysing process, the cell lysate was passed through a blunt 20-gauge needle for at least 5 times.

Proliferating pulmonary arterial smooth muscle cells cultured on poly-D-lysine coated 6-well plates for 7 days, were first washed three times with 37°C PPS to remove the culture medium, and 1 ml Trizol reagent was added to approximately 2 million cells. The cells were then gently scraped down with a 22 mm sterile plastic scrapper (VWR, US), and the cell lysate passed through a blunt 20-gauge needle for at least 5 times to breakdown the membrane.

The cell lysate was left at room temperature for 5 minutes, and 200 µl of chloroform added to 1ml of cell lysate, which was followed by vigorous shaking. After shaking the lysate was centrifuged at 4°C for 15 minutes with the speed of 12000g. The spinning is supposed to separate the lysate into three layers based on the size, weight and affinity of the components; the top clear layer is the RNA layer, the middle layer that is cloudy and dense is composed of the genomic DNA, and the bottom pink layer is full of proteins and cell debris. The top RNA layer was carefully removed into a new 1ml Eppendorf, the typical yield of RNA suspension from 1ml of cell lysate is around 200 µl. To extract RNA from the suspension, 500 µl 2-propanol, 70 µl 3M sodium acetate (PH 5.2) and 20 µg were added to 200 µl RNA suspension and incubated at -20°C overnight. The following day, the suspension was centrifuged at 15000g for 20 minutes at 4°C for the collection of RNA pellet. To eliminate chemical contamination, the pellet was washed with 70% ethanol (in DEPC water) for 3 times by centrifuging at 7500g for 5 minutes. The pellet was air dried for 15-30 minutes until the ethanol was evaporated without drying out the pellet completely, and the RNA was

resuspended in 20-40 µl of TE buffer and for long term storage at -20°C or -80°C.

2.9.2 Checking the quality, quantity and integrity of the extracted RNA.

The quantity and quality of extracted RNA were checked by Nanodrop spectrophotometer (Therofisher scientific, US), RNA concentration was provided as ng/µl; the A260/280 and A260/230 reading were measured and calculated to show the quality of RNA. The ratio of the absorbance at 260 and 280 nm (A260/280) is calculated to assess the quality (purity) of nucleic acids based on the fact that proteins absorb light at a wavelength of 280 nm. The A260/280 of pure DNA is around 1.8 while that of pure RNA is approximately 2.0. If the A260/280 is lower than 1.8 the sample was generally considered as contaminated with protein or other chemicals that absorb light at 280 nm (e.g. phenol). In our case, samples with the A260/280 above 1.96 were considered as pure RNA without DNA contamination.

The ratio of the absorbance at 260 and 230 nm (A260/230) is used to assess whether the sample was contaminated with chemicals, especially chemicals that absorb light at 230 nm including EDTA, guanidine HCL, carbohydrates and phenolic solutions like Trizol reagent. Samples with good purity should display an A260/230 between 2.0-2.2, samples with higher or lower A260/230 were excluded.

RNA electrophoresis was conducted to check the integrity of RNA samples. 1% agarose gel was prepared with Tris-base, acetic acid and EDTA (TAE) buffer. 1 µl RNA loading buffer containing 50% glycerol, 1mM EDTA, 0.4% Orange G and DEPC water was added to 0.5 µg RNA sample and was topped up to 10 µl with DEPC water. The mixture was heated at 65 °C for 45 minutes to denature the RNA, which could unwind the secondary and tertiary RNA structure. 10 µl of the denatured mixture was added to each well of the agarose gel, and the gel was run at 6v/cm for 45 minutes. In the gel that has RNA samples with good integrity, clear ribosomal RNA bands should be seen, while the degraded RNA sample would generate a smear with a band at a very small molecular weight.

2.9.3 cDNA generation

Reverse transcription was carried out using the Transcriptor First Strand cDNA Synthesis Kit from Roche Science (UK). The cDNA generation was conducted in two steps. First, 0.5 µl anchored-oligo(dT)18 primer and 1ul random hexamer primers were added to 1ng-4µg RNA with DEPC water, and the mixture was denatured by heating the mixture at 65 °C for 10 minutes. Then I added Transcriptor Reverse Transcriptase with buffer, RNase inhibitor, deoxynucleotide mix, Dithiothreitol and reverse transcriptase to the mixture, which was then incubated at 50 °C for 30 mins to allow cDNA generation. Transcriptor Reverse Transcriptase was inactivated by heating to 85°C for 5 minutes. The derived cDNA was stored at -20 °C. The amount of each reagent required for this process is summarized in the tables below.

Table 2.3 Reagents required in the first step of reverse transcription

First Step		
Components	Volume	Final Concentration
Total RNA	Variable	1ng-4µg
Anchored oligo	0.5 µl	2.5 µM
Random hexamer	1 µl	60 µM
DEPC water	Depending on RNA	Top up to 11.4µl

Table 2.4 Reagents required in the second step of reverse transcription

Second Step		
Components	Volume	Final Concentration
Transcriptase buffer 5x	4 µl	1x
RNase inhibitor 40V	0.5 µl	20V
Deoxynucleotide mix, 10mM	2 µl	1mM
Dithiothreitol	1 µl	5mM
Reverse transcriptase	1.1 µl	10V
Final Volume	20 µl	N/A

2.9.4 Real-time qPCR

Real-time quantitative polymerase chain reaction (qPCR) is a technology that was used to monitor the amplification of targeted cDNAs. It was able to detect the production of the targeted cDNAs quantitatively because a non-specific fluorescent dye, SYBR Green, was used during PCR and it intercalates with double-stranded DNA. By monitoring the changes in the fluorescence intensity of SYBR Green, the relative production rate of the targeted cDNAs can be inferred.

Master mixes were prepared prior to qPCR. 2 µl of cDNA template, 10 µl of SYBR Green mix (Roche, UK) and 1.6 µl of primer mix, were added to 6.4 µl of DEPC water, and the total volume of the master mix for 1 PCR run was 20 µl. Sequence specific primers that can selectively amplify rat nesprin-1, SUN 2, and lamin A cDNA were purchased from Qiagen (Germany), sequence specific primers that can selectively amplify rat emerin gene was purchased from Bio-rad (US). The master mixes were added to heat proof 96-well plates (20 µl) per well. Apart from mixes containing cDNA sample, positive control that was generated using cDNA without RNA sample, and negative control that did not contain cDNA template were also included. The real-time

qPCR was run by StepOnePlus™ Real-Time PCR System (Thermo Fisher Scientific, US), using the quantitative comparative delta CT SYBR Green mode for 2 hours. The results were exported and analysed in Microsoft Excel 2016 (Microsoft, US).

2.10 Data presentation and statistical analysis

Data are presented as the mean ± SEM for 'n' experiments. The analysis, comparison and figure production were carried out using GraphPad Prism (US). If comparing two datasets, t-test was conducted. If comparing between three or more groups of data, the variances of datasets were checked by either the one-way variance test (in Graphpad) or a mixed factor model (in Minitab). If the data sets have similar variances and fall into the normal distribution, the number of independent variables must be considered. For the comparison of data set that has one independent variable, the analysis was carried out with one-way ANOVA followed by a Tukey or holm-sidak multiple comparisons test. In terms of the data set that has two independent variables, the comparisons between the groups were carried out using two-way ANOVA followed by a Tukey's multiple comparisons test. On the other hand, if the data sets have significantly different variances, the unpaired data sets were compared by the Kruskal-Wallis test whereas the paired data sets were compared by the Friedman test followed by Dunn's multiple comparison. Probability values less than 0.05 were considered to be statistically significant. *= $P \leq 0.05$, **= $P \leq 0.01$, ***= $P \leq 0.001$ and ****= $P \leq 0.0001$.

2.11 Drugs and chemicals

All compounds were from Sigma Aldrich unless stated otherwise, detailed information regarding the chemicals used in this study were shown in the table below.

Table 2.5 Description, supplier, catalogue number and concentration of the chemicals used in the study

Name	Supplier	Catalogue Number	Concentration used	Drug vehicle
Angiotensin II	Abcam	ab120183	10 µm, 30 µm	Distilled water
Maurocalcine	Alomone Labs	RTM-100	100 nM, 200 nM, 300 nM	Distilled water
Thapsigargin	Abcam	ab120286	1 µm	DMSO
Ionomycin	Sigma-Aldrich	P6188-1MG	1 µm	DMSO
Ryanodine	Enzo life sciences	ALX-630-062-M001	100 µm	DMSO
Fluo-4, AM, cell permeant (Molecular Probes®)	Life Technologies	F-14201	5 µm	DMSO
DRAQ5™ Fluorescent Probe Solution (5 mM)	Thermo scientific	D62251	5 µm	PSS
Calcium Orange™, AM, cell permeant	Thermo scientific	C3015	5 µm	DMSO
ER-Tracker™ Blue-White DPX	Thermo scientific	E12353	1 µm	DMSO
DAPI (4\',6-Diamidino -2-Phenylindole, Dihydrochloride	Life Technologies	D1306	1 µm	DMSO

Chapter 3: Cytoplasmic nanocourses form a cell-wide web for Ca^{2+} signalling

3.1 Introduction

3.1.1 Multiple releasable pools of SR Ca^{2+}

The PM-SR junction, as introduced in Chapter 1, is the junctional space formed between the plasmamembrane and superficial SR. It was proposed that the narrow cytoplasmic spaces formed between the PM and SR could effectively restrict Ca^{2+} diffusion, which facilitates SR Ca^{2+} intake from the junctional space, and this would serve as a buffer barrier to attenuate Ca^{2+} flux from the PM to the deep myoplasm (van Breemen et al., 1995). This superficial buffer barrier hypothesis indicates that centrally located SR compartments must serve to support other smooth muscle functions, for example, muscle contraction. Indeed, early studies had considered the possibility that the central and peripheral SR are separate compartments within the smooth muscle cells (Nixon et al., 1994). By staining the tissues with osmium ferricyanide they studied the ultrastructure of smooth muscle SR, and the results showed that the central and peripheral SR were parts of one continuous organelle, that appeared to somehow form separate compartments. The direct evidence of functionally segregated SR compartments was revealed later on, which showed two separate releasable pools of SR Ca^{2+} in response to different pharmacological stimuli (Golovina and Blaustein, 1997).

3.1.2 Functionally segregated SR Ca^{2+} stores in pulmonary arterial smooth muscle cells

Functionally segregated SR compartments have been reported in pulmonary arterial smooth muscle cells (PASMCs) (Yang et al., 2005, Clark et al., 2010a). It was first observed that the sarco/endoplasmic reticulum Ca2+-ATPase (SERCA) pump inhibitor cyclopiazonic acid seemed to deplete one releasable pool of SR Ca^{2+} while having little effects on another SR Ca^{2+} pool which supported Ca^{2+} release by cADPR (Dipp et al., 2001, Dipp and Evans, 2001). This suggests that segregated SR Ca^{2+} pools exist in PASMCs. In support of this view, it was shown that nicotinic acid adenine dinucleotide phosphate (NAADP) induced spatially restricted Ca^{2+} transients that initiated a global Ca^{2+} wave and contraction in PASMCs by subsequently triggering Ca^{2+} induced Ca^{2+} release (CICR) from the SR via ryanodine receptors

(RyRs); by contrast, blocking Inositol trisphosphate receptors (IP_3R) had no effect on the NAADP induced Ca^{2+} signal (Boittin et al., 2002). Therefore, it was proposed that NAADP mobilises Ca^{2+} via a 2-pool mechanism, and that initial Ca^{2+} bursts are amplified by subsequent SR Ca^{2+} release via RyRs but not IP_3Rs. This study suggests that RyRs and IP_3Rs may target segregated SR Ca^{2+} pools. This view gained further support from the fact that cyclic ADP ribose-dependent SR Ca^{2+} release via RyRs also supported smooth muscle relaxation in the same cell type, by releasing Ca^{2+} proximal to the plasma membrane BKCa channels in response to activation of adenylyl cyclase-coupled receptors (Boittin et al., 2003). Combined with early research, this seems to show that Ca^{2+} release via RyRs from the SR underpins both vasodilation and vasoconstriction, and the signalling segregation is possibly conferred by segregated SR Ca^{2+} stores located either in the vicinity of BKca channels (near the plasma membrane) or near the contractile apparatus (central).

The presence of multiple SR Ca^{2+} stores is supported by differential targeting of RyR subtypes. It was shown that the density of RyR3 labelling is highest within the perinuclear region. Lysosomes colocalised with RyR3 to form a trigger zone for NAADP-dependent Ca^{2+} signalling by the vasoconstrictor endothelin-1 in rat PASMCs (Kinnear et al., 2004, Kinnear et al., 2008). The density of labelling for RyR2 in the extraperinuclear region was not only significantly higher than the other regions, but also greater than the density of labelling for RyR1 or RyR3 within the extraperinuclear region. Comparatively, the density of RyR1 labelling was markedly higher in the subplasmalemmal region compared to the perinuclear or extraperinuclear region (Kinnear et al., 2008).

A later study showed that SERCA2a and SERCA2b were also differencially targeted to functionally segregated SR compartments. In PASMCs, immunolabelling of SERCA2a and SERCA2b suggested that around 70% of the SERCA2b labelling fell into the subplasmalemmal region, 20% of its labelling was found in the perinuclear region and the rest was in the extraperinuclear region. This finding supported the argument that SERCA2b was primarily targeted to superficial SR which underpins the function of PM-SR junction (Evans et al., 2016). In contrast, SERCA2a labelling majorly localised to the central cytoplasm with 90% of the labelling fell into the perinuclear region. Moreover, it was proposed that SERCA2a supplies the central SR

and supports Ca^{2+} fluxes which underpin vasoconstriction (Clark et al., 2010a).

To summarise, RyR1 is localised in the subplasmalemmal region where SERCA2b serves as the dominant Ca^{2+} pump, it is presumed that they are targeted to the superficial SR and possibly mediate Ca^{2+} signalling within PM-SR junctions for vasodilation. By contrast RyR3 is primarily targeted to the perinuclear region where SERCA2a is the predominant SERCA, they serve the central SR which, in part, forms lysosome-SR junction, and gives rise to global Ca^{2+} signals amplified by RyR2s distributed in the extraperinuclear region (Gilbert et al., 2014, Clark et al., 2010a) that support vasoconstriction (Kinnear et al., 2008, Evans et al., 2016). That there may be different subcompartments of the SR was further highlighted by the findings of Boittin et al (Boittin et al., 2002) which suggested that IP_3Rs and RyRs may also be found in segregated SR compartments. However, the nature of such signal segregation remains unclear.

3.1.3 Aim

Segregated SR Ca^{2+} pools are observed in PASMCs, which is supported by the strategic targeting of different subtypes of RyRs and SERCAs. In some cases, it was proposed that the segregated SR compartments give rise to Ca^{2+} signals that are spatially restricted within nanospaces (i.e. PM-SR junction, lysosome-SR junction), and mediate distinct smooth muscle functions. Therefore, the aim of this Chapter is to investigate the possibility that Ca^{2+} signalling is segregated by cytoplasmic nanospaces, which are conferred by nanojunctions of the SR in a manner that supports the generation of spatially and functionally segregated Ca^{2+} signals, and differentially regulate discrete functions in PASMCs.

3.2 Results

3.2.1 Cytoplasmic nanocourses of the sarcoplasmic reticulum form a cell-wide web in PASMCs

Cytoplastic nanojunctions have been identified in multiple types of muscle cells. For example, the T-tube-SR junction in skeletal and cardiac muscle cells (Franzini-Armstrong, 1970, Langer and Peskoff, 1996), the PM-SR nanojunction and lysosome-SR junction in pulmonary arterial smooth muscle cells (van Breemen et al., 2013, Fameli et al., 2014), and the mitochondria-SR junction in resistant arterial smooth muscle cells (Tong et al., 2009). These structures were visualized by electron microscopy, and they were proposed, on the basis of indirect functional evidence, to restrict free Ca^{2+} diffusion and demarcate local Ca^{2+} release (van Breemen et al., 2013, Fameli et al., 2014). The fact that more than one type of cytoplasmic nanojunctions co-exist in PASMCs led to the consideration that these cytoplasmic nanojunctions may demarcate functionally segregated cytoplasmic nanodomains. To investigate this possibility, I decided to explore the cytoplasmic nanodomains further by applying deconvolution to Z scans of PASMCs loaded with a Ca^{2+} indicator.

Considering the proposal that nanojunctions are defined, at least in part, by membrane-membrane junctions of the SR/ER that restrict Ca^{2+} diffusion (Fameli et al., 2014, van Breemen et al., 2013), I first labelled acutely isolated PASMCs with ER-tracker and loaded the cells with the Ca^{2+} indicator Fluo-4. Figure 3.1 shows an exemplary cell labelled with ER-tracker (orange). A scan through the middle of the cell was deconvolved (Figure 3.1B), revealing a network of ER-tracker labelling spanning the entire cell. Fluo-4 fluorescence (green) of the same deconvolved Z section (Figure 3.1C) illustrated that the intracellular free Ca^{2+} was not uniformly distributed as one may expect. Instead, the free Ca^{2+} appears to outline a network of “cytoplasmic nanocourses”. To specify where the structures are formed, Draq 5 (blue, Figure 3.1 D) was applied to identify the nucleoplasm. By merging the Fluo-4 loading with Draq 5 labelling (Figure 3.1G) it was clear that those linear structures highlighted by Fluo-4 fluorescence were observed proximal to the plasma membrane (PM), or within the extraperinuclear and perinuclear region of the cell, in a manner consistent with but more extensive than previously proposed (Clark et al., 2010a, Evans et al., 2016, van Breemen et al., 2013). To my surprise, however, these cytoplasmic nanocourses extended beyond the perinuclear region of the cell, penetrating into the

nucleus (Figure 3.1 H). By conducting confocal microscopy followed by deconvolution, the resolution was improved to 100-150 nm. This allowed for reliable estimation of the sizes of these linear structures, which were generally less than 300 nm wide. Therefore, I conclude that cellular nanocourses are defined by the SR of acutely isolated PASMCs, forming a cell-wide web that extends from the cell periphery to the nucleus. Moreover, I propose that these nanocourses might be capable of restricting and/or directing Ca^{2+} flux.

The nanocourses that project into the nucleus seem to be defined by the extension of the nuclear membrane as Figure 3.1 F shows, consistent with previous proposals that ER/SR is continuous with the outer nuclear membrane (OMN), which has been shown to extend into the nucleus to form nuclear invaginations in various cell types (Fricker et al., 1997b). Interestingly, as shown in Figure 3.1 E&G, the nuclear invaginations observed in acutely isolated PASMCs are continuous with perinuclear cytoplasmic nanocourses, suggesting that the lumen of nuclear invaginations are essentially cytoplasmic domains that hold free Ca^{2+}.

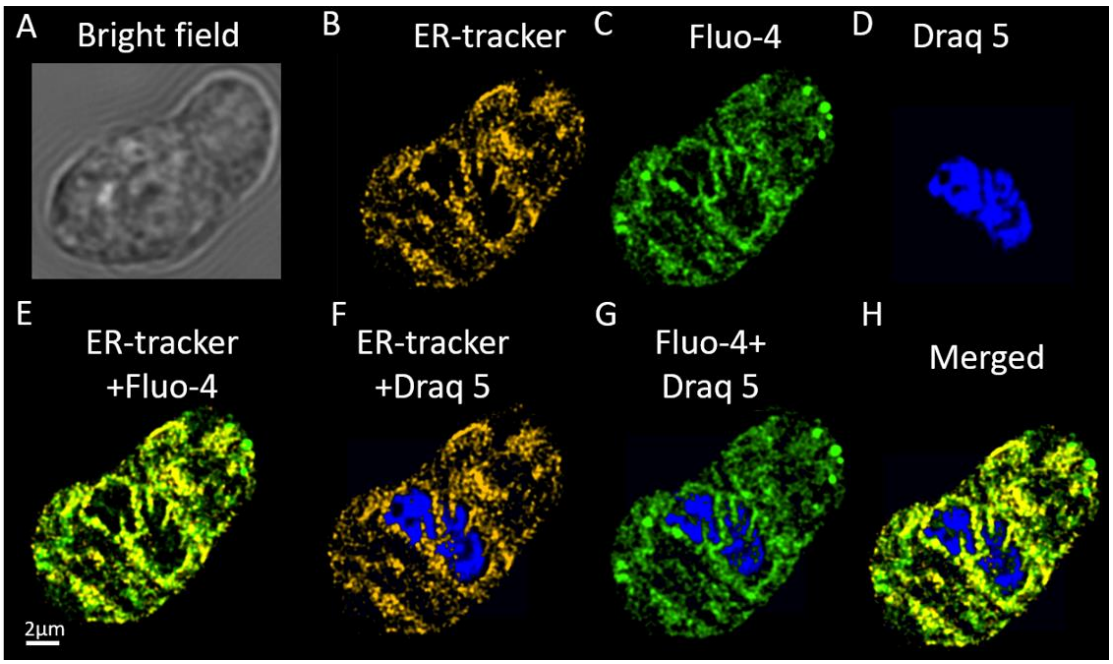

Figure 3.1 Cytoplasmic nanocourses observed in acutely isolated PASMCs form a cell-wide web

(A) Bright filed image of a pulmonary arterial smooth muscle cell

(B) Deconvolved confocal Z section through the middle of a pulmonary arterial myocyte showing ER-tracker identified ER, SR and outer nuclear membrane (orange). **(C)** As for (A) but showing the distribution of cytoplasmic Ca^{2+} (green) by the Ca^{2+} indicator Fluo-4 loaded at 25 ^{o}C.

(D) As for (A) but showing the nucleoplasm identified by Draq5 (blue).

(E) Merged ER-tracker labelling with Fluo-4 fluorescence.

(F) Merged ER-tracker labelling with Draq5 staining.

(G) Merged Fluo-4 fluorescence with Draq5 staining.

(H) Merged image of all three types of labelling.

3.2.2 Cytoplasmic nanocourses harbour clusters of RyRs, which give rise to spontaneous Ca^{2+} fluxes at rest.

To further characterize the nanocourses, time course videos of the Fluo-4 loaded acutely isolated PASMCs at rest were recorded and analyzed. Due to the fact that

ER-tracker is cytotoxic, and heavy photobleaching of the ER-tracker signal is always observed within 3 minutes, it was not possible to incorporate ER-tracker labelling in confocal time course experiments. However, my data described above clearly show that the cytoplasmic nanocourses can be identified by Fluo-4 fluorescence alone (Figure 3.1). Given the above, I further studied time series of raw and deconvolved confocal Z sections of acutely isolated PASMCs loaded with Fluo-4 alone. Figure 3.2 Ai shows a confocal scan through the middle of an acutely isolated PASMC loaded with Fluo-4 (green), with Draq 5 (blue) applied to indicate the nucleoplasm. Under confocal microscopy where the resolution was around 200 nm, cytoplasmic nanocourses could not be distinguished. By contrast, deconvolved images of the same confocal Z section revealed the cell-wide web of cytoplasmic nanocourses (Figure 3.2 Aii). They are very dynamic, some of the nanocourses constantly rearrange over time. Pseudocolour was applied to the images to indicate relative Ca^{2+} concentrations within the nanocourse, low Ca^{2+} concentration was indicated by black and high concentration by white (Figure 3.2 Aiii). In order to further characterize basal activities within cytoplasmic nanocourses, they were divided into 4 groups based on the functional segregation of SR proposed previously (Clark et al., 2010a), where the cytoplasmic volume within 1.5 μm of the nucleus but excluding the nucleus was defined as the perinuclear region, the cytoplasmic volume within 1.5 μm of the plasma membrane was defined as the subplasmalemmal region, and the rest of the cytoplasm in between the two regions was defined as the extraperinuclear region. I defined cytoplasmic nanocourses that fall into each region accordingly, and they refer to four loosely defined subgroups, namely subplasmalemmal nanocourses, extraperinuclear nanocourses, perinuclear nanocourses and nuclear invaginations.

One example of a subplasmalemmal (white), extraperinuclear (blue) and perinuclear (green) nanocourse and one nuclear invagination (yellow) were selected for detailed characterization in each cell studied (Figure 3.2 Aiii). Magnified images of each nanocourse are shown in Figure 3.2 Bi-Ei. The upper, middle and lower panels show images of these cytoplasmic nanocourses at 3 time points. Interestingly, the Fluo-4 distribution seems to suggest that the Ca^{2+} concentration was not uniform distributed along the lengths of any of these nanocourses. The images clearly show that there were hotspots (circled in the lower panels of Figure 3.2 B, C, D and E) of Ca^{2+} flux within the cytoplasmic nanocourses. The Fluo-4 intensity of the hotspots varied with

time. For example, in Figure 3.2Bi, two hotspots H1 and H2 indicated by regions of interest (ROIs, grey) exhibited different Fluo-4 fluorescence intensities at t = 4s (upper panel). By contrast, both H1 and H2 exhibited relatively low Fluo-4 fluorescence intensity at time 12s (middle panel), with subsequent increases in fluorescence intensity evident for both hotspots at 14s (lower panel). Moreover, the hotspots of Ca^{2+} activity and asynchronous Ca^{2+} fluxes derived from adjacent hotspots were observed in all the cytoplasmic nanocourses, as the examples of subplasmalemmal (Figure 3.2B), extraperinuclear (Figure 3.2C), perinuclear (Figure 3.2D) nanocourses and nuclear invaginations (Figure 3.2 E) show. Two exemplar hotspots H1(black) and H2 (orange) were selected from each cytoplasmic nanocourse for semi-quantitative analysis.

The activity of the hotspots was further investigated by plotting the Fluo-4 F_X/F_0 against time (F_X=mean Fluo-4 intensity within the region of interest at time point x; F_0 = mean Fluo-4 intensity within the region of interest at time point 0 (Figure 3.2 Bii-Eii). Across all four nanocourses, the activity of the two chosen hotspots (black for H1, orange for H2) revealed consistently high levels of spontaneous changes in Ca^{2+} flux. That said, the activities of two adjacent hotspots were sometimes synchronized, although the majority of hotspots within a single nanocourse act asynchronously with respect to Ca^{2+} flux (Figure 3.2 Bii-Eii). Plots of the average Fluo-4 F_X/F_0 of entire nanocourses (red, Figure 3.2 Biii-Eiii, regions of interests indicated in the upper panels of Figure 3.2 B-E) emphasizes that the Ca^{2+} activities arise at defined hotspots because the amplitude of fluctuations in Ca^{2+} flux was markedly reduced compared to that of corresponding hotspots. This observation shows that the nanocourses, as narrow as they are, are not the basic Ca^{2+} releasing unit. Instead, the hotspots within the nanocourses are the basic releasing unit that supports resting Ca^{2+} fluxes.

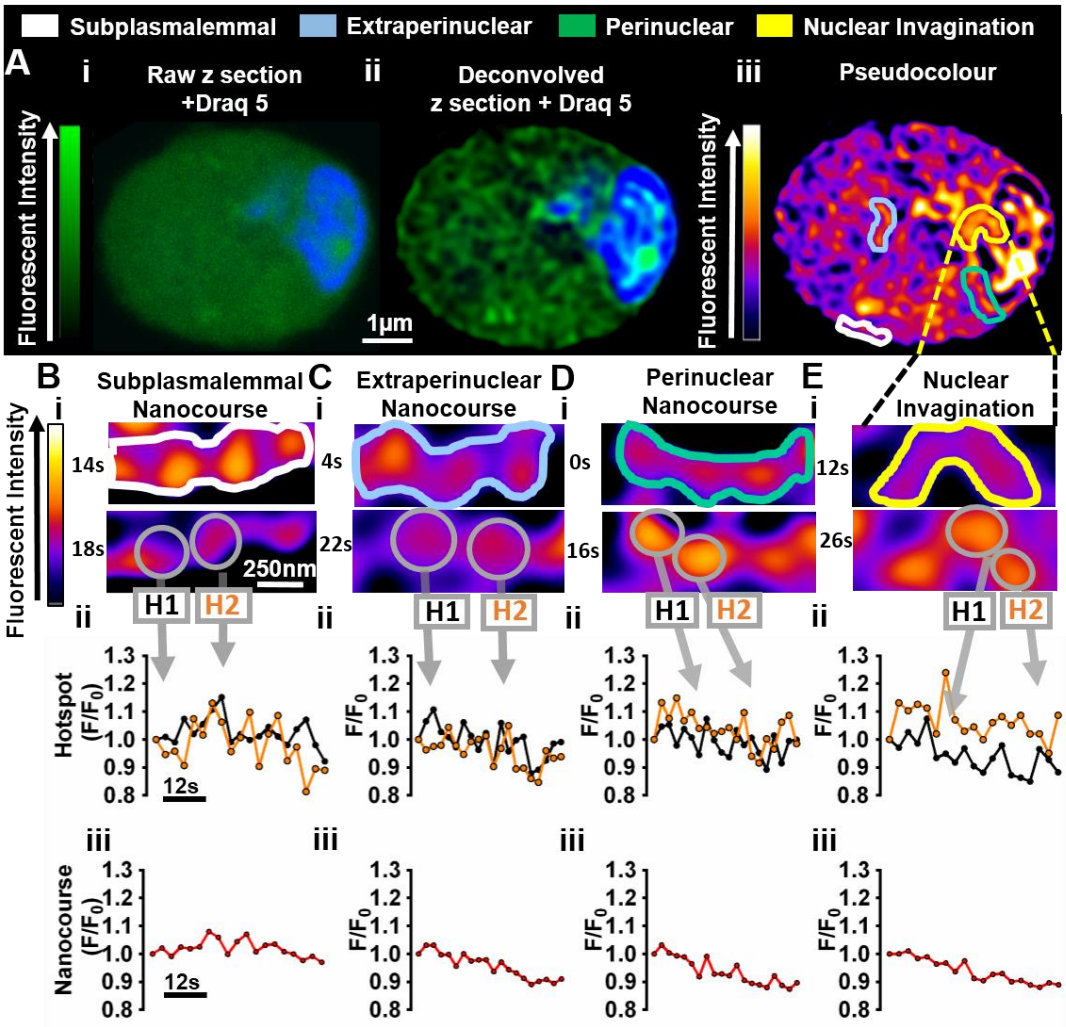

Figure 3.2 Hotspots of Ca^{2+} fluxes are observed within the cytoplasmic nanocourses of acutely isolated arterial myocytes.

(Ai) A confocal scan through the middle of a pulmonary arterial smooth muscle cell loaded with Fluo-4 (green) at 25 ^{o}C. The nucleus was indicated by Draq 5 (blue). (ii)As for (i) but showing the deconvolved image. (iii) Pseudocolour was applied to the confocal scan showed in (ii), black-purple indicates low Fluo-4 fluorescence intensity and white-yellow shows high Fluo-4 fluorescence intensity. One subplasmalemmal nanocourse is pointed out with white outline, one extraperinuclear nanocourse is indicated with blue outline, one perinuclear nanocourse is drawn out by green outline, and one nuclear invagination is circled by yellow. N=5 cells from 3 rats.

(Bi) One subplasmalemmal nanocourse is shown at higher magnification. The upper, middle and lower panels show the same subplasmalemmal nanocourse at three time points. Hotspot 1 (H1, black) and hotspot 2 (H2, orange) were pointed out by grey circles. (ii) Fluo-4 fluorescence ratio (F_x/F_{C0}) versus time for hotspot 1(H1, black) and hotspot 2 (H2, orange) were plotted. F_0 = Fluo-4 fluorescence intensity for the chosen hotspot at time 0; Fx = fluorescence intensity for the chosen hotspot at time point x. (iii) Fluo-4 fluorescence ratio (F_x/F_{C0}) versus time for the nanocourse was plotted. F_0 = Fluo-4 fluorescence intensity for the nanocourse at time 0; F_x = fluorescence intensity for the nanocourse at time point x

(C) As for (B), but showing an extraperinuclear nanocourse.

(D) As for (B), but showing a perinuclear nanocourse.

(E) As for (B), but showing a nuclear invagination.

Spontaneous Ca^{2+} sparks within smooth muscle cells at rest were observed and characterized in the 1990s using waterfall plots derived from time series acquired in line-scan mode (Nelson et al., 1995). However, until now no one has attempted to study "Ca^{2+} sparks" by cell wide Z scan versus time. Analysis of my data indicates that the amplitude ($\Delta F_X/F_0$) of Ca^{2+} fluxes at the hotspots within different cytoplasmic nanocourses were slightly different. The average amplitudes of Ca^{2+} fluxes of the subplasmalemmal hotspots, extraperinuclear hotspots, perinuclear hotspots and nuclear hotspots were 0.18±0.02, 0.15±0.01, 0.16±0.01 and 0.15±0.02 (black, Figure 3.6B; n=5, Appendix 1, Table 3.2) respectively. The amplitudes of the Ca^{2+} fluxes are on a similar scale to the amplitudes of the spontaneous Ca^{2+} sparks reported in early studies (Curtis et al., 2004, Jaggar et al., 1998), which suggests that the observed Ca^{2+} fluxes might be the Ca^{2+} sparks arose from RyRs.

Indeed, this fluctuation of Ca^{2+} concentration at the hotspots is likely caused by the spontaneous release of Ca^{2+} from SR resident Ca^{2+} channels, i.e. IP_3Rs or RyRs (Curtis et al., 2004, Jaggar et al., 1998, Smith and Parker, 2009, Dickinson et al., 2012). Based on my observations, I decided to investigate the impact of depleting SR Ca^{2+} stores and blocking RyRs on the activity of hotspots within defined cytoplasmic nanocourses.

To study whether depletion of SR Ca^{2+} stores has any effect on spontaneous Ca^{2+} flux at identified hotspots, PASMCs were preincubated with the SERCA inhibitor thapsigargin for 1 hour (Du et al., 1994). Time series of confocal Z sections (deconvolved) confirmed that the network of cytoplasmic nanocourses was still identifiable under the condition (Figure3.3 Aii&iii). Significantly, while spontaneous

transient Ca^{2+} flux was still observed at defined hotspots, the amplitudes of these Ca^{2+} transients were markedly reduced compared to control cells. Following SR Ca^{2+} store depletion, the amplitudes of Ca^{2+} flux at hotspots within the subplasmalemmal nanocourses, extraperinuclear nanocourses, perinuclear nanocourses and nuclear invaginations were significantly reduced to 0.07±0.008, 0.08±0.007, 0.07±0.007, 0.07±0.008 (blue, Figure 3.6B; n=3, Appendix 1, Table 3.3) respectively compared to the control cells (0.18±0.02, 0.15±0.01, 0.16±0.01 and 0.15±0.02 respectively, $p<0.001$ for all 4 comparisons,). Moreover, the frequency of transient Ca^{2+} flux at identified hotspots within different cytoplasmic nanocourses was similar (Figure 3.4). Measurements at the subplasmalemmal, extraperinuclear, perinuclear and nuclear hotspots respectively were 0.15±0.006 s^{-1}, 0.15±0.006 s^{-1}, 0.15±0.007 s^{-1} and 0.14±0.006 s^{-1} under control conditions (Blue bars, Figure 3.4; n=3, Appendix 1, Table 3.4) and 0.16±0.010 s^{-1}, 0.16±0.012 s^{-1}, 0.16±0.006 s^{-1}, 0.16±0.006 s^{-1} after pre-incubation with 1 μM thapsigargin (n=3; $p>0.05$ in each case compared to the control cells; Appendix 1, Table 3.5). This shows that the available luminal Ca^{2+} load / concentration within the SR determines the capacity for Ca^{2+} flux to the cytoplasm at identified hotspots within cytoplasmic nanocourses, but not the frequency at which Ca^{2+} flux is gated.

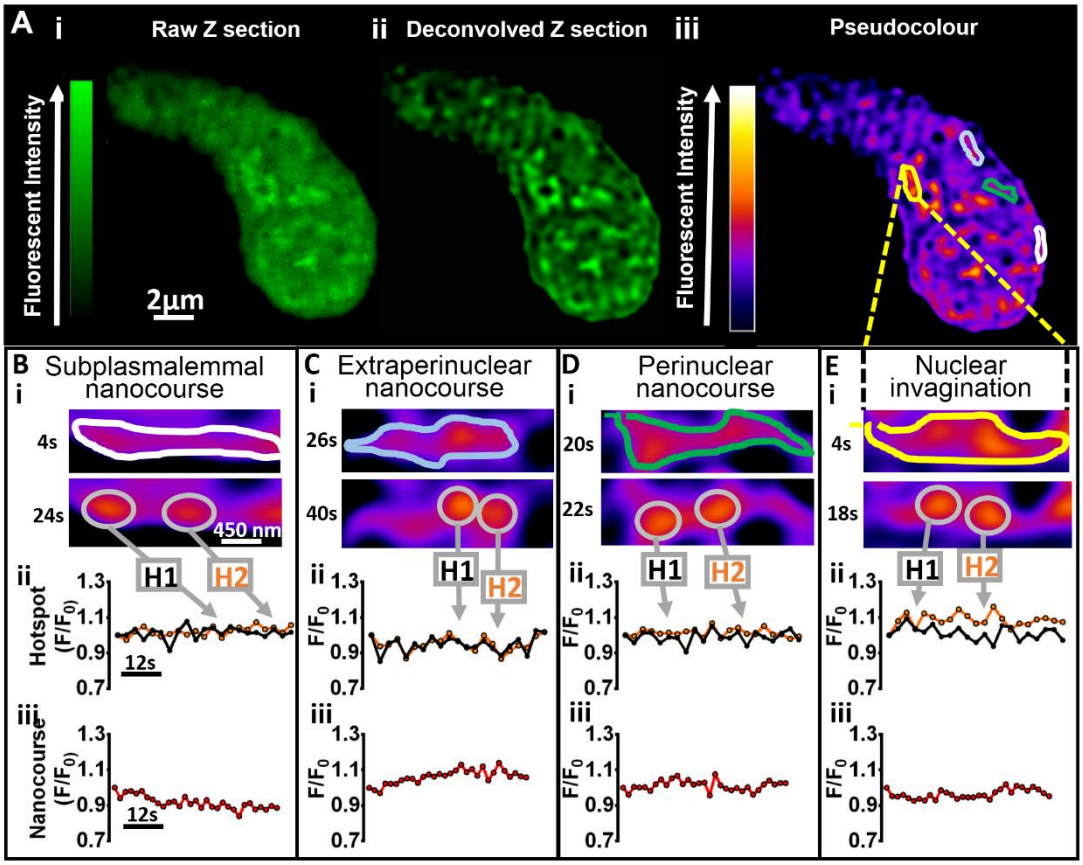

Figure 3.3. Activity of Ca^{2+} flux observed in the cytoplasmic nanocourses was suppressed following SR Ca^{2+} store depletion by thapsigargin.

(Ai) A confocal scan through the middle of a pulmonary arterial smooth muscle cell loaded with Fluo-4 at 25 ^{o}C, preincubated with 1µM of thapsigargin for 1 hour. (ii)As for (i) but showing the deconvolved image. (iii) Pseudocolour was applied to the confocal scan showed in (ii), black-purple indicates low Fluo-4 fluorescence intensity and white-yellow shows high Fluo-4 fluorescence intensity. One subplasmalemmal nanocourse is pointed out with white outline, one extraperinuclear nanocourse is indicated with blue outline, one perinuclear nanocourse is drawn out by green outline, and one nuclear invagination is circled by yellow. N=3 cells.

(Bi) One subplasmalemmal nanocourse is shown at higher magnification. The upper, middle and lower panels show the same subplasmalemmal nanocourse at three time points. Hotspot 1 (H1, black) and hotspot 2 (H2, orange) were pointed out by grey circles. (ii) Fluo-4 fluorescence ratio (F_x/F_{C0}) versus time for hotspot 1(H1, black) and hotspot 2 (H2, orange) were plotted. F_0 = Fluo-4 fluorescence intensity for the chosen hotspot at time 0; Fx = fluorescence intensity for the chosen hotspot at time point x. (iii) Fluo-4 fluorescence ratio (F_x/F_{C0}) versus time for the nanocourse was plotted. F_0 = Fluo-4 fluorescence intensity for the nanocourse at time 0; F_x = fluorescence intensity for the nanocourse at time point x

(C) As for (B), but showing an extraperinuclear nanocourse.

(D) As for (B), but showing a perinuclear nanocourse.

(E) As for (B), but showing a nuclear invagination.

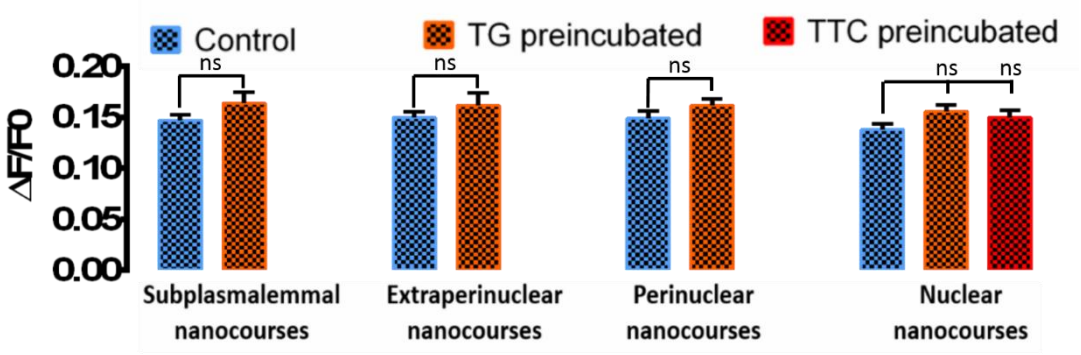

Figure 3.4 Frequencies of Ca^{2+} fluxes within the sub subplasmalemmal, extraperinuclear and perinuclear nanocourses and nuclear invaginations were similar.

Frequency of the Ca^{2+} fluxes at the hotspots within the subplasmalemmal, extraperinuclear, perinuclear nanocourses and nuclear invaginations are shown in the bar chart. Blue bars are for control cells, orange bars represent cells preincubated with 1μM of thapsigargin for 1 hour, and red bar shows cells preincubated with 1mM of tetracaine for 4 hours. Data are shown as mean±SEM, ns=not significant. n=5 for control, n=3 for thapsigargin preincubated, n=4 for tetracaine preincubated.

Next, I decided to investigate the nature of the SR Ca^{2+} release channels that support observed spontaneous Ca^{2+} flux within the cytoplasmic nanocourses. PASMCs were preincubated with the non-selective RyR inhibitor tetracaine for 4 hours, which has been shown to block all three subtypes of RyRs (Laver and van Helden, 2011). Following the block of RyRs with tetracaine, the cytoplasmic nanocourses were no longer well defined in either raw or deconvolved Z sections, although some evidence of such networks was seen on occasion but not in every Z section captured. Figure 3.5 shows 2 consecutive frames from one deconvolved time course video, which shows one tetracaine treated PASMC that exhibited, albeit poorly defined, evidence of cytoplasmic nanocourses. As the result, I cannot confidently trace and reliably analyze most of the cytoplasmic nanocourses after tetracaine preincubation.

As Figure 3.5 shows, I was still able to identify nuclear invaginations by Fluo-4

intensity in all tetracaine preincubated cells, as indicated by the white star, and these were maintained throughout the entire time series. This suggests three possibilities (1) the unique geometry of nuclear invaginations and / or their demarcation by SERCA allows them to retain Ca^{2+} when other regions of the cell cannot, (2) only partial block by tetracaine of RyRs within nuclear invaginations was achieved after 4 hour pre-incubation, or (3) other Ca^{2+} channels, i.e. IP_3Rs, are targeted to the nuclear invaginations. My further analysis showed that while the frequency of spontaneous Ca^{2+} flux at hotspots within nuclear invaginations of tetracaine preincubated PASMCs (0.15±0.007 s^{-1}, red, Figure 3.4; n=3, Appendix 1, Table 3.6) was similar to control (0.14±0.006 s^{-1}), the amplitude of these spontaneous events (0.1±0.01, Figure 3.6C; n=4, Appendix 1, Table 3.6) was significantly reduced compared to the control cells (0.15±0.01). Therefore, spontaneous Ca^{2+} flux at hotspots within nuclear invaginations is very likely supported by RyRs, and the majority of the Ca^{2+} fluxes observed within other cytoplasmic nanocourses are very likely Ca^{2+} sparks derived from clusters of RyRs.

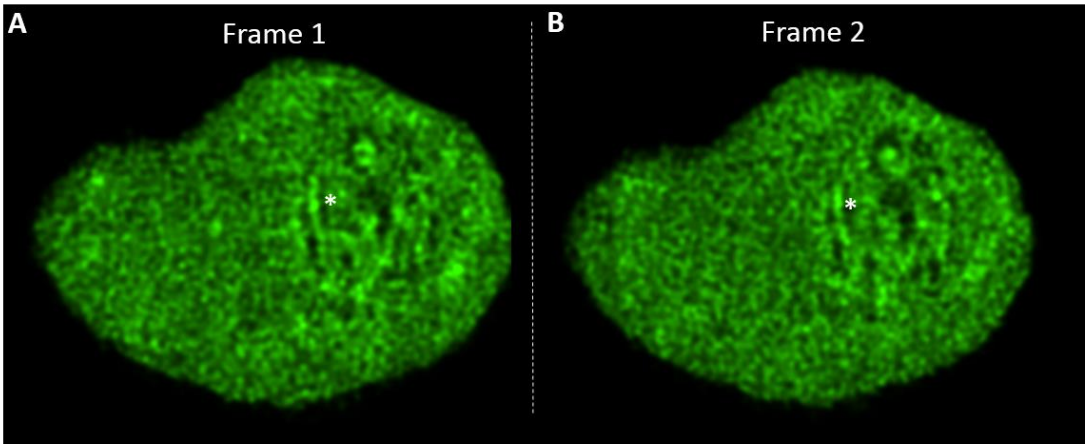

Figure 3.5 The cytoplasmic nanocourses were not well maintained when RyRs were blocked.

(A) A confocal scan through the middle of a pulmonary arterial smooth muscle cell showing the cell loaded with Fluo-4 (green) at 25 ^{o}C, preincubated with 1mM of tetracaine for 4 hours. Anuclear invagination is indicated with *.

(B) As for (A), but showing a consecutive frame.

In support of this view, I show that the separation between the hotspots of Ca^{2+} flux fall in to the range of 200-700 nm, similar to the distances of separation (around 300-800 nm) reported for the RyR clusters in atrial myocytes and cardiac myocytes (Soeller et al., 2007, Macquaide et al., 2015). However, my analysis suggests that the distances of separation of hotspots were different for the subplasmalemmal (white), extraperinuclear (blue) and perinuclear (green) nanocourses and nuclear invaginations (yellow) (Figure 3.6 A). On average, the hotspots in the nuclear invaginations were separated by 350±13 nm (yellow, Figure 3.6 A; n=3, Appendix 1, Table 3.1), which is similar to 359±15 nm for the distance of separation between hotspots of subplasmalemmal nanocourses (white, Figure 3.6 A; n=3, Appendix 1, Table 3.1).

However, the distance of separation between hotspots within extraperinuclear nanocourses exhibited larger degrees of variability and was significantly greater on average at 414±22 nm ($p<0.05$ compared to the subplasmalemmal hotspots and nuclear hotspots, Figure 3.6 A; n=3, Appendix 1, Table 3.1). The distances of separation between hotspots of perinuclear nanocourses is 452±32 nm (green, Figure 3.6 A; n=3, Appendix 1, Table 3.1), which is slightly larger than that for hotspots within extraperinuclear nanocourses and greater than that observed for either subplasmalemmal nanocourses or nuclear invaginations. This observation suggests that different RyR subtypes might target to the SR that demarcates nanocourses in different regions of the cell, because the separation between different subtypes of RyR clusters appear to be different (details discussed in section 3.3.3).

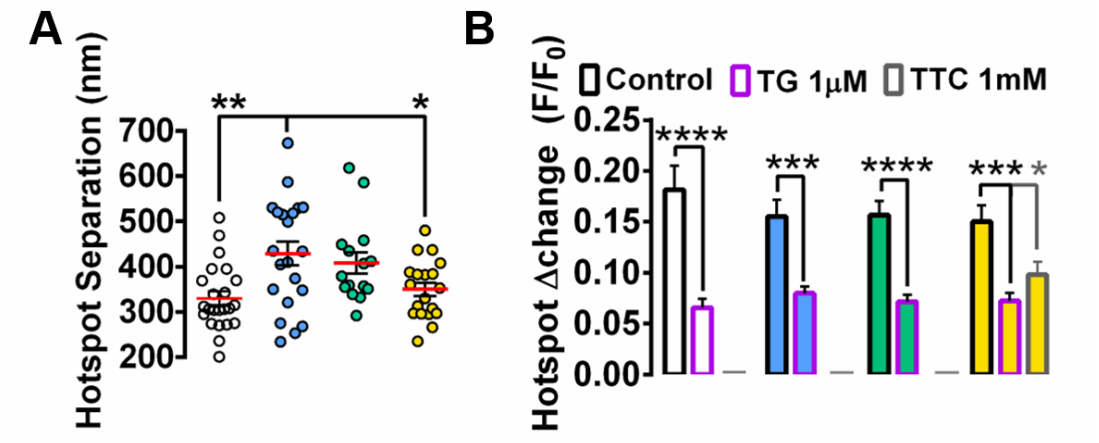

Figure 3.6 Distance of separation between hotspots and amplitudes of Ca^{2+} fluxes within the subplasmalemmal, extraperinuclear and perinuclear nanocourses and nuclear invaginations were different.

(A) Distance of separation between hotspots within the subplasmalemmal (white), extraperinuclear (blue) and perinuclear (green) nanocourses and nuclear invaginations (yellow) were measured and shown (nm), data are presented as mean±SEM, n =3 cells from 3 rats.

(B) Amplitudes of the Ca^{2+} fluxes at the hotspots within the subplasmalemmal (white), extraperinuclear (blue), perinuclear nanocourses (green) or nuclear invaginations (yellow) are shown in the bar chart. Bars with black outline are for control cells, bars with purple outline represent the measurements of cells preincubated with 1μM of thapsigargin for 1 hour, and the bar with grey outline shows cells preincubated with 1mM of tetracaine. Data are shown as mean±SEM, *=p<0.05, **=p<0.01, *** =P<0.001, ****=p< 0.0001, n=3 cells from 3 rats.

3.2.3 Different types of RyRs and SERCA pumps are strategically targeted to different regions of the cell including nuclear invaginations.

I have shown that the nuclear invaginations support Ca^{2+} fluxes at rest in a manner retained by local cytoplasmic nanospaces. Both RyR inhibition by tetracaine and SERCA pump inhibition by thapsigargin attenuated the Ca^{2+} flux, which indicates that RyRs and SERCA pumps may target to nuclear invaginations. This possibility gained unexpected support from previous studies using sequence-specific antibodies against each of the multiple types of SERCAs (Clark et al., 2010b, Eggermont et al., 1990) and RyRs (Herrmann-Frank et al., 1991, Neylon et al., 1995, Kinnear et al., 2008)

expressed in arterial smooth muscles.

3.2.3.1 SERCA1 is strategically targeted to nuclear invaginations while SERCA2a/b are targeted to cytoplasmic nanocourses

Previous work of Dr. Jill Clark in the Evans laboratory showed not only that SERCA 2a and 2b were expressed in PASCMs, but that the former is restricted to the perinuclear region and the latter to the subplasmalemmal region of PASMCs (Clark et al., 2010a). Moreover, as yet her unpublished data show that SERCA1 is selectively targeted to the nucleus. This is evident from 3D reconstruction of deconvolved Z sections of SERCA1 labelling of PASMCS (Figure 3.7 A; n = 12), which shows that SERCA1 labelling (green) was found only within the boundary of the Dapi labelled nucleus (blue). Furthermore, SERCA1 labelling defined tubular, intranuclear networks consistent with nuclear invaginations (Figure 3.1). This unique, isoform-specific distribution was confirmed by semi-quantitative analysis of the density of labelling for each SERCA type within the nucleus, perinuclear region, extraperinuclear region and the subplasmalemmal region of the cell (Figure 3.7B; n = 10). SERCA1 may therefore function to supply Ca^{2+} to the NR and its invaginations, and thus provide for a Ca^{2+} store that is spatially and functionally segregated from the perinuclear SR, fed by SERCA2a, and the superficial SR, fed by SERCA2b (Clark et al., 2010b).

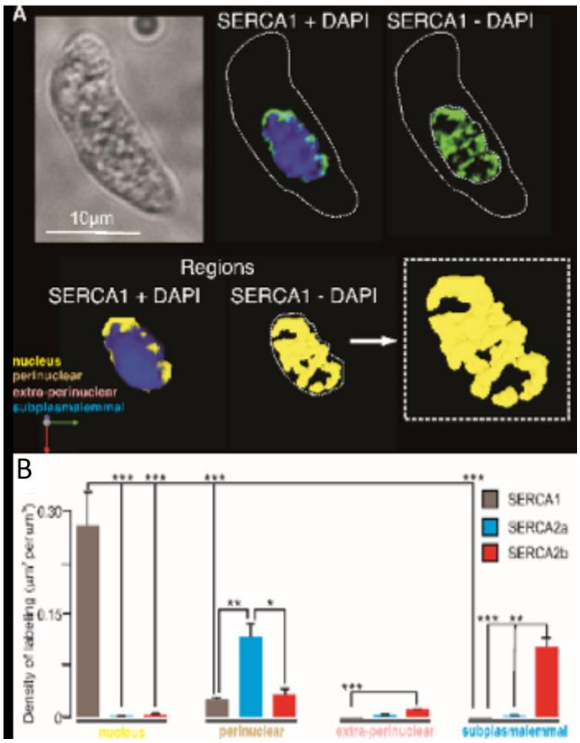

Figure 3.7 SERCA1 is targeted to nuclear invaginations.

(A) Upper panels show, from left to right, a bright field image of a pulmonary arterial smooth muscle cell and 3D rendered, deconvolved fluorescence images of SERCA1 labelling (green) with and without DAPI labelling of the nucleus (blue). Lower panels show, from left to right, a digital surface blending encapsulating SERCA1 labelling (rotated relative to upper panels) with and without DAPI labelling and then magnified.

(B) Bar chart shows the density of labelling (mean±SEM) for SERCA1, SERCA2a and SERCA2b (μm^3 perμm^3), labelling within the 4 designated regions of the cell. Colours indicate labelling within the nucleus (yellow), surrounding perinuclear region (gold; within 1.5 µm of the nucleus) extraperinuclear region (pink) and subplasmalemmal regions (blue; within 1.5 µm of the plasma membrane).

*=p<0.05, **=p<0.01, *** =P<0.001, ****=p< 0.0001.

3.2.3.2 RyR1 is strategically targeted to invaginations of the nucleoplasmic reticulum

Dr. Jill Clark's unpublished work also showed that allied with the targeting of SERCA1 to nuclear invaginations, RyR1 was found to target to defined tubular, intranuclear networks (red, Figure 3.8A, n = 10) within the boundary of the Dapi labelled nucleus (blue). Moreover, of the three RyR subtypes expressed in PASMCs (Yang et al., 2005), only RyR1 was identified within the boundary of the Dapi labelled nucleus (blue, Figure 3.8B). Importantly, RyR1 labelling, like SERCA1, depicted tubular structures within the nucleus, suggesting that it is targeted to the nuclear invaginations. Therefore, NR resident SERCA1 and RyR1 are strategically positioned within nuclear

invaginations and likely support the local release of Ca^{2+} to the cytoplasmic lumen demarcated by each nuclear invagination. Of further note is the fact that RyR1 was also identified as the predominant RyR subtype targeted to the subplasmalemmal region of the cell, where the distances of separation for the hotspots of Ca^{2+} flux is similar to that for hotspots within nuclear invaginations. By contrast, Clark and co-workers showed that RyR3 was restricted to the perinuclear region of the cell and RyR2 to the extraperinuclear region, where significantly greater distances of separation were observed for hotspots within these cytoplasmic nanocourses.

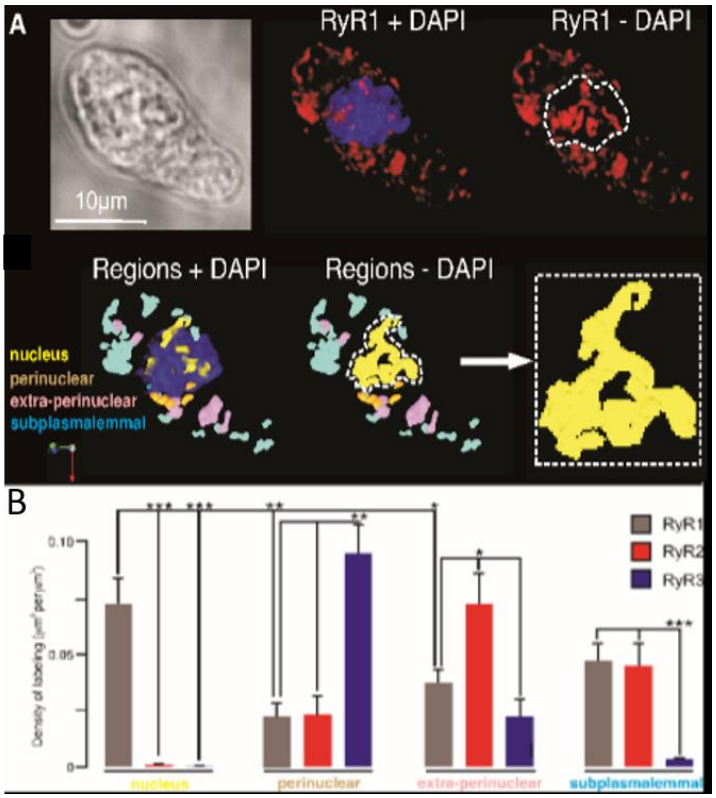

Figure 3.8 RyR 1 is targeted to nuclear invaginations.

(A) Upper panels show, from left to right, a bright field image of a pulmonary arterial smooth muscle cell and 3D rendered, deconvolved fluorescence images of RyR1 labelling (red) with and without Dapi labelling of the nucleus (blue). Lower panels show, from left to right, a digital surface blending encapsulating RyR1 labelling (rotated relative to upper panels) with and without Dapi labelling and then magnified. Colours indicate labelling within the nucleus (yellow), surrounding perinuclear region (gold; within 1.5 μm of the nucleus) extraperinuclear region (pink) and subplasmalemmal regions (blue; within 1.5 μm of the plasma membrane).

(B) Bar chart shows the density of labelling (mean±SEM) for RyR1, RyR2 and RyR3

labelling (μm^3 perμm^3) within the 4 designated regions of the cell. *=p<0.05, **=p<0.01, *** =P<0.001, ****=p< 0.0001.

3.2.4 RyR1 supports selective Ca^{2+} release into nuclear invaginations and cytoplasmic nanocourses of the subplasmalemmal region in pulmonary arterial myocytes

Given above, I hypothesized that different subtypes of RyRs are preferentially targeted to the subplasmalemmal, extraperinuclear, perinuclear nanocourses and nuclear invaginations. To test this hypothesis, I investigated the effects of the extracellular application of a RyR1 agonist on Ca^{2+} flux within PASCMs. The RyR1 agonist maurocalcine is a membrane traversing peptide from scorpion venom that can selectively activate RyR1 and lock it in a long-opening subconductance (Altafaj et al., 2007).

Figure 3.9 Ai-iii show the effect of extracellular addition of the RyR1 agonist maurocalcine on an acutely isolated PASMC loaded with Fluo-4. Consistent with the preferential targeting of RyR1 to subplasmalemmal region and nuclear invaginations of PASMCs, maurocalcine preferentially induced an increase in Fluo-4 fluorescence within subplasmalemmal nanocourses and nuclear invaginations. To illustrate this, examples of a subplasmalemmal nanocourse (white), an extraperinuclear nanocourse (blue), a perinuclear nanocourse (green) and a nuclear invagination (yellow), are indicated in Figure 3.9 Ai and shown on an enlarged scale in Figure 3.9 Bi-Ei. The 4 panels from top to bottom show the response of each nanocourse at 4 time points (from baseline to peak). Panel ii and iii show the Fluo-4 fluorescence intensity against time (F_X/F_0) for each hotspot identified by ROI (Figure 3.9 Bii-Eii) and for each nanocourse as a whole (Figure 3.9 Biii-Eiii). It is evident that maurocalcine-induced increases in Ca^{2+} flux (indicated by the increase of Fluo-4 intensity) did not propagate away from the nanocourses, i.e. these Ca^{2+} signals were confined within the nanocourses within which they arise. Figure 3.9 B-E clearly show that maurocalcine induced drastic Ca^{2+} release at defined hotspots within the subplasmalemmal nanocourses and nuclear invaginations. Moreover, an increase in

mean Ca^{2+} concentration within these cytoplasmic nanocourses was observed after maurocalcine application, which was restricted within the nanospace. This is evident from the marked increase in mean Fluo-4 fluorescence against time for the entire area of the selected subplasmalemmal nanocourse (Figure 3.11B). That maurocalcine preferentially increases Ca^{2+} flux within subplasmalemmal nanocourses is emphasized by the response of a second example cell (Figure 3.10) within which concomitant activation of an entire series of subplasmalemmal nanocourses is evident within one confocal plane, with the increase in Fluo-4 fluorescence appearing as a bright ring spanning the entire perimeter of the cell (Figure 3.10 Aiii). Figure 3.9 Bii shows that in response to maurocalcine, Ca^{2+} flux is triggered at all hotspots (H1 in black and H2 in orange) within the subplasmalemmal nanocourse, and adjacent hotspots are activated in an asynchronous manner. This observation shows that the observed subplasmalemmal hotspots appear to be clusters of RyR1s. In contrast to outcomes for subplasmalemmal nanocourses, there was significantly smaller Ca^{2+} flux in the extraperinuclear (Figure 3.9 C) nanocourses and perinuclear nanocourses in response to maurocalcine (Figure 3.9 D). However, within the nuclear invaginations, a pronounced increase in Ca^{2+} flux was evoked by maurocalcine (Figure 3.9 E). These data provide strong corroboration of my hypothesis that RyR1 preferentially supports SR Ca^{2+} release into subplasmalemmal nanocourses and nuclear invaginations.

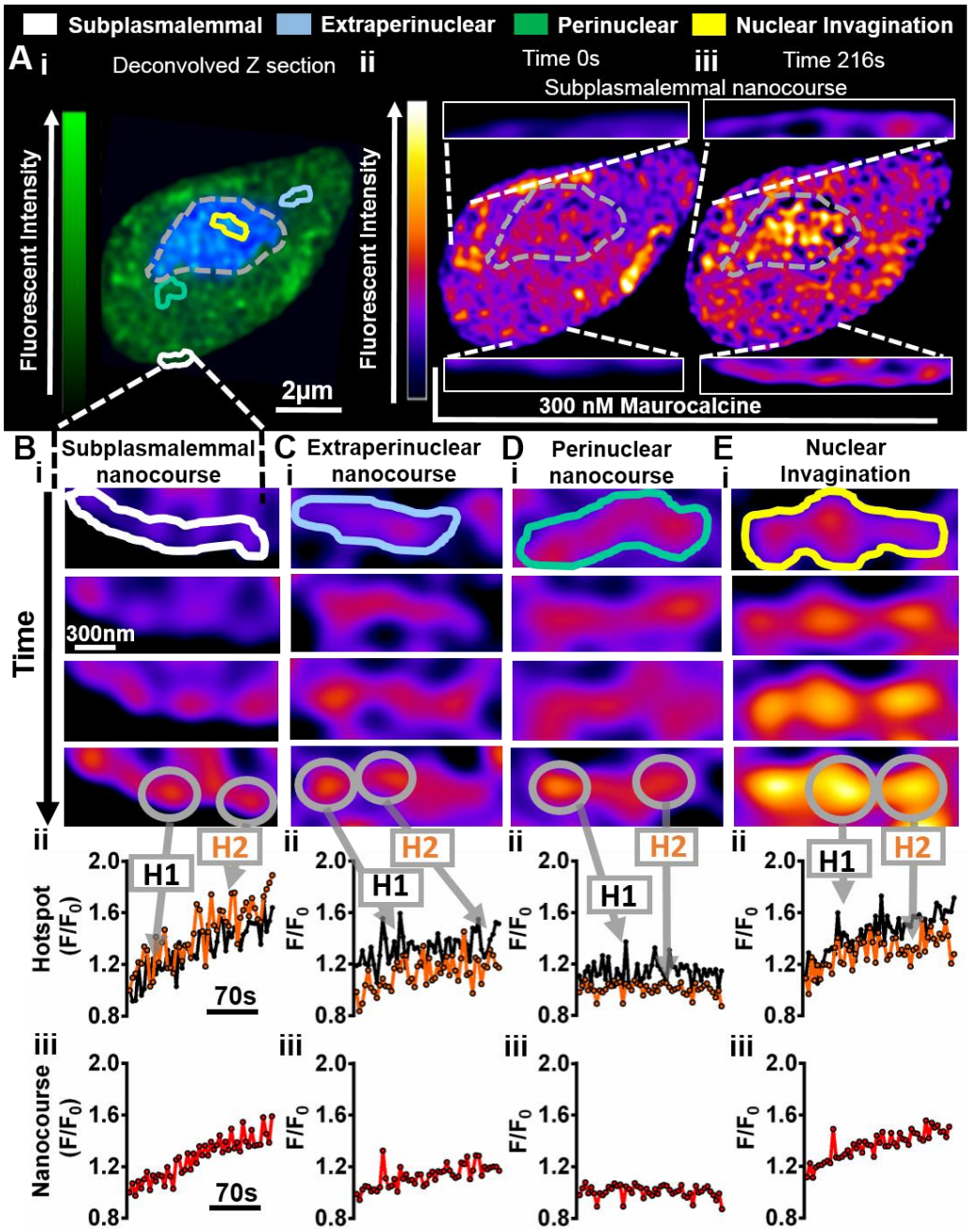

Figure 3.9 Maurocalcine triggers Ca^{2+} release majorly in the subplasmalemmal nanocourses and nuclear invaginations.

(Ai) Confocal scan through the middle of a pulmonary arterial smooth muscle cell loaded (25° C) with Fluo-4 (green) is shown. Draq 5 was applied to indicate the nucleus (blue). (ii) Pseudocolour was applied to indicate high Fluo-4 intensity in white-yellow and low Fluo-4 intensity in black-purple. The nucleus was drawn out by grey dotted line. Subplasmalemmal nanocourses were magnified in the white boxes. (iii) As in (ii), but showing the response of the cell following the extracellular addition of 300 nM maurocalcine. n=3 cells from 3 rats.

(Bi) Higher magnification images of one example subplasmalemmal nanocourse are shown. 300nM maurocalcine was added to the cell and the response was recorded,

images of the cell at 4 time points (from top to bottom) are displayed to illustrate the response. (ii) Fluo-4 fluorescence ratio (Fx/FC0) versus time for hotspot 1(H1, black) and hotspot 2 (H2, orange) were plotted. F_0 = Fluo-4 fluorescence intensity for the chosen hotspot at time 0; Fx = fluorescence intensity for the chosen hotspot at time point x. (iii) Fluo-4 fluorescence ratio (F_x/F_{C0}) versus time for the nanocourse was plotted. F_0 = Fluo-4 fluorescence intensity for the nanocourse at time 0; F_x = fluorescence intensity for the nanocourse at time point x

(C) As for (B), but showing an extraperinuclear nanocourse.

(D) As for (B), but showing a perinuclear nanocourse.

(E) As for (B), but showing a nuclear invagination.

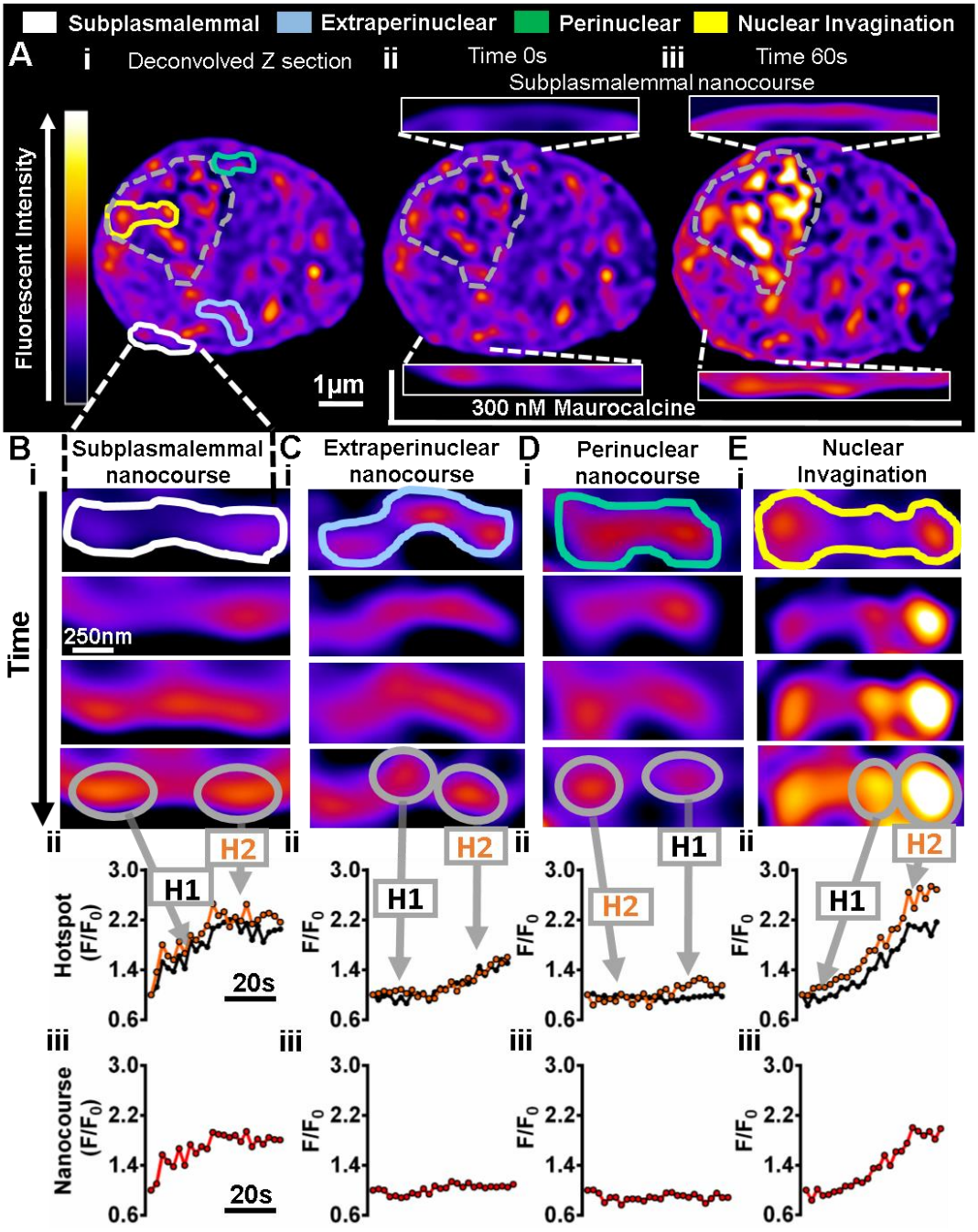

Figure 3.10 Maurocalcine triggers Ca^{2+} release majorly in the subplasmalemmal nanocourses and nuclear invaginations.

(Ai) Confocal scan through the middle of a pulmonary arterial smooth muscle cell loaded (25° C) with Fluo-4 (green) is shown. Draq 5 was applied to indicate the nucleus (blue). (ii) Pseudocolour was applied to indicate high Fluo-4 intensity in white-yellow and low Fluo-4 intensity in black-purple. The nucleus was drawn out by grey dotted line. Subplasmalemmal nanocourses are magnified in the white boxes. (iii) As in (ii), but showing the response of the cell following the extracellular addition of 300 nM maurocalcine.

(Bi) Higher magnification images of one example subplasmalemmal nanocourse are

shown. 300nM maurocalcine was added to the cell and the response was recorded, images of the cell at 4 time points (from top to bottom) are displayed to illustrate the response. (ii) Fluo-4 fluorescence ratio (Fx/FC0) versus time for hotspot 1(H1, black) and hotspot 2 (H2, orange) were plotted. F_0 = Fluo-4 fluorescence intensity for the chosen hotspot at time 0; Fx = fluorescence intensity for the chosen hotspot at time point x. (iii) Fluo-4 fluorescence ratio (F_x/F_{C0}) versus time for the nanocourse was plotted. F_0 = Fluo-4 fluorescence intensity for the nanocourse at time 0; F_x = fluorescence intensity for the nanocourse at time point x

(C) As for (B), but showing an extraperinuclear nanocourse.

(D) As for (B), but showing a perinuclear nanocourse.

(E) As for (B), but showing a nuclear invagination.

These observations received support from the quantitative analysis of the peak change in Fluo-4 fluorescence within identified hotspots and corresponding cytoplasmic nanocourses as a whole. The peak change for maurocalcine-induced increases in Fluo-4 fluorescence of hotspots within nuclear invaginations was the greatest, measuring 1.5±0.3 (Figure 3.11 B, yellow bar; n=3, Appendix 1, Table 3.7). The peak change for hotspots within subplasmalemmal nanocourses was as large as 1.1±0.1(Figure 3.11 B, white bar; n=3, Appendix 1, Table 3.7). Both of them exhibited greater increases in Fluo-4 fluorescence than either extraperinuclear hotspots (0.5±0.02; Figure 3.11 B, blue bar; n=3, Appendix 1, Table 3.7), or perinuclear hotspots (0.4±0.04; Figure 3.11 B, green bar; n=3, Appendix 1, Table 3.7). Analysis of nanocourse wide Fluo-4 fluorescence gave similar outcomes, the peak change of the Ca^{2+} signals within nuclear invaginations was 1.2±0.3 (Figure 3.11 B, yellow bar; n=3, Appendix 1, Table 3.8), the peak change of Ca^{2+} flux generated in subplasmalemmal nanocourses was 1.0±0.03 (Figure 3.11 B, white bar; n=3, Appendix 1, Table 3.8), and both were greater compare to that of either extraperinuclear nanocourses (0.4±0.03, Figure 3.11 B, blue bar,; n=3, Appendix 1, Table 3.8) or perinuclear nanocourses (0.2±0.03, Figure 3.11 B, green bar; n=3, Appendix 1, Table 3.8). Moreover, the activities of subplasmalemmal and nuclear hotspots were enhanced following addition of maurocalcine, which gains some

support from the comparison of the standard deviation of the Fx/F0 under control and test conditions (Figure 3.11 C). Although not statistically significant, values measured from the subplasmalemmal hotspots and nuclear hotspots were both higher after drug application.

In contrast to outcomes for measures of basal activity, it is notable that in response to maurocalcine the peak change in Fluo-4 fluorescence for hotspots was slightly higher than but not significantly different from that measured for the corresponding nanocourses, suggesting the induced Ca^{2+} fluxes were restricted within the nanocourses.

The differential activation of these nanocourses by maurocalcine supports the view that RyR1 is preferentially targeted to the subplasmalemmal nanocourses and the nuclear invaginations. Moreover, outcomes are consistent with the proposal that vasodilators such as β-adrenoceptor agonists trigger Ca^{2+} flux into the PM-SR junction of pulmonary arterial smooth muscle cells in order to promote cell relaxation through, in part, consequent activation of BK_{ca} channels and plasma membrane hyperpolarization (Boittin et al., 2003). I observed not only preferential increases in Ca^{2+} flux within subplasmalemmal nanocourse (Figure 3.9&3.10 Aiii), but also concomitant cell relaxation upon application of maurocalcine. The cell area significantly increased from 27±3 μm^2 to 30±3 μm^2 (Figure 3.11 A, Appendix 1, Table 3.9, $p<0.05$) following the addition of maurocalcine.

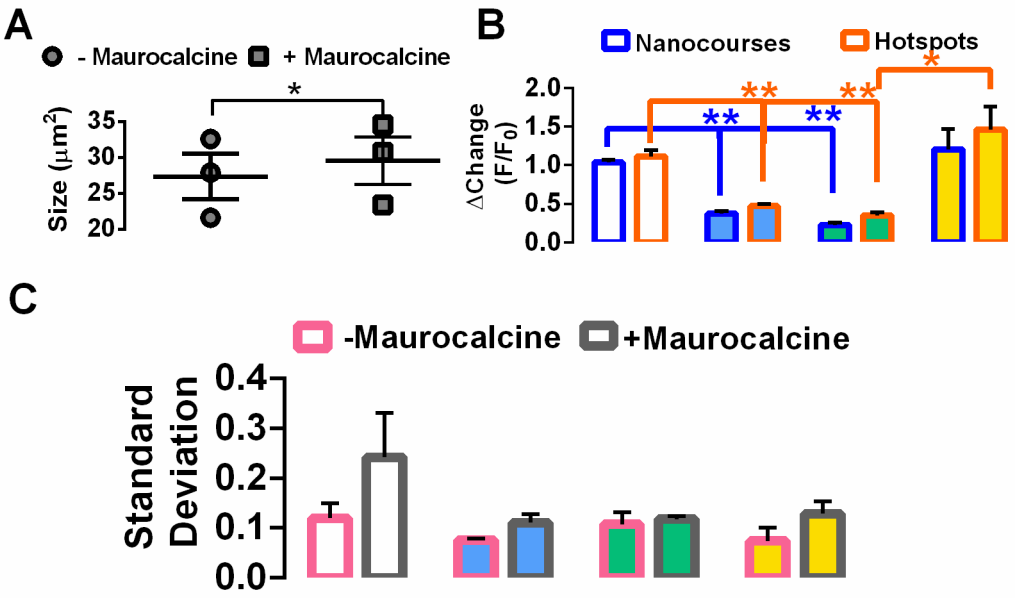

Figure 3.11 Maurocalcine triggers Ca^{2+} release into the subplasmalemmal nanocourses and nuclear invaginations, and leads to arterial myocytes relaxation.

(A) Cell area (μM^2) before and after extracellular application of 300 nM maurocalcine was calculated and plotted, data presented as mean±SEM, n=3 cells from 3 rats.

(B) Peak changes of the Ca^{2+} fluxes after extracellular application of 300 nM maurocalcine was calculated (Fx/F0), the peak changes of the subplasmalemmal, extraperinuclear, perinuclear and nuclear nanocourses (blue) or hotspots (red) were shown in the bar chart. Data are shown as mean±SEM, *=p<0.05, **=p<0.01, *** =P<0.001, ****=p< 0.0001, n=3 cells from 3 rats.

(C) Standard deviation of the Fx/F0 values for the subplasmalemmal, extraperinuclear, perinuclear and nuclear hotspots were calculated, the standard deviation before maurocalcine addition (green) or after maurocalcine addition was compared. Data are shown as mean±SEM, n=3 cells from 3 rats.

3.2.5 Angiotensin II induces myocytes contraction by selective activation of Ca^{2+} flux into perinuclear and extraperinuclear nanocourses

The fact that Ca^{2+} release into subplasmalemmal nanocourses triggers PASMC relaxation led to another consideration, which is whether vasoconstrictors can also selectively induce Ca^{2+} release into nanocourses that specify cell contraction. To test this, 30 µM angiotensin II was applied to acutely isolated PASMCs and the responses were recorded by confocal microscopy as above. Figure 3.12 A shows an acutely isolated PASMC before and during extracellular application of the vasoconstrictor angiotensin II. The responses observed were yet more complex than I expected. Figure 3.12 Ai-iv shows 6 frames from the time series of deconvolved confocal images that were selected to illustrate the response at key time points. The cell is first shown at rest (Figure 3.12 Ai; see also Figure 8.1 in appendix 1). Following addition of angiotensin II, it was striking that the Fluo-4 fluorescence within all cytoplasmic nanocourses fell (Figure3.12 Aii) immediately before the leading edge of a subsequent Ca^{2+} wave was initiated within one well defined, extraperinuclear nanocourse at one pole of the cell (A iii), the Ca^{2+} wave propagated across to the opposite pole of the cell (Figure 3.12 Aiv) as Fluo-4 fluorescence declined in its wake (Figure 3.12 Av). In marked contrast, there was a relatively small change in Fluo-4 fluorescence within subplasmalemmal nanocourses (Figure 3.12 Ai-v, insets), which is more evident in Figure 8.1 (appendix 1).

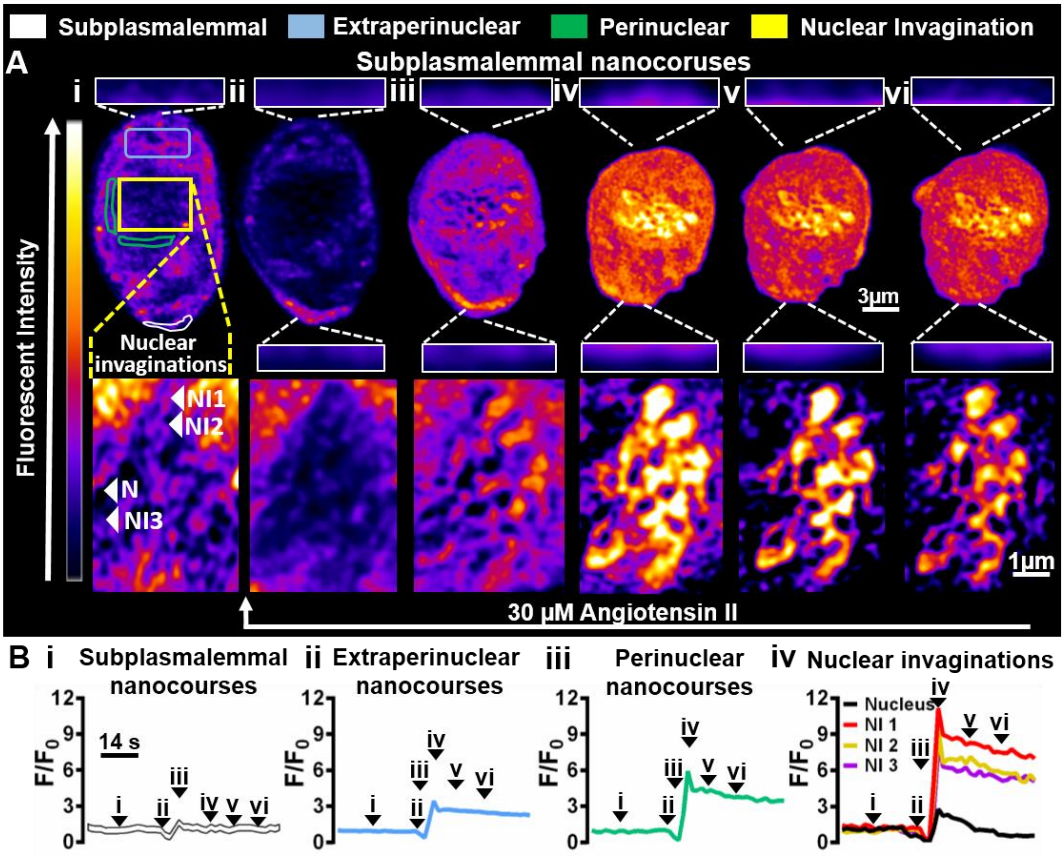

Figure 3.12 Vasoconstrictor triggers Ca^{2+} release in the extraperinuclear, perinuclear nanocourses and nuclear invaginations.

(A) A series of confocal scans through the middle of a pulmonary arterial smooth muscle cell loaded (25° C) with Fluo-4 is shown in the upper panels. Pseudocolour was applied to indicate high Fluo-4 intensity in white-yellow and low Fluo-4 intensity in black-purple. The nucleus was drawn out by a yellow box. Subplasmalemmal nanocourses were magnified in the white boxes aligned at top and bottom. The response of the cell following the extracellular addition of 30 µM angiotensin II is shown by displaying the images of the cell at 6 time points (i-vi). The lower panels show the higher magnification images of the nucleus at the 6 time points (i-vi). Detection threshold was modified to show clearly the nuclear invaginations without signal saturation. The nucleus (N) and three sites of the nuclear invaginations (NI1, NI2 and NI3) are indicated by white arrow heads.

(B) Fluo-4 fluorescence ratio (Fx/FC0) versus time for the regions of interests (subplasmalemmal region in white, extraperinuclear region in blue, perinuclear region in green, nucleus in black, nuclear invaginations in yellow, NI1 in red, NI2 in yellow, and NI3 in purple) were plotted. F_0 = Fluo-4 fluorescence intensity for the region of interest at time 0; Fx = fluorescence intensity for the chosen region of interest at time point x.

Unfortunately, the propagating Ca^{2+} wave triggered by angiotensin II was accompanied by such marked cell contraction that it was impossible to track most of cytoplasmic nanocourses, although I was able to track individual nuclear invaginations in most cells studied. Therefore, instead of quantifying the Ca^{2+} increase in the nanocourses, I plotted the Ca^{2+} increase in the subplasmalemmal, extraperinuclear and perinuclear regions as well as in the nuclear invaginations. The peak change in Fluo-4 fluorescence ratio measured 1.0± 0.2 in the extraperinuclear region (Figure 3.13B; n=8, Appendix 1, Table 3.10), 1.3±0.3 in the perinuclear nanocourses (Figure 3.13B; n=8, Appendix 1, Table 3.10). By contrast, only small increase in Fluo-4 fluorescence was observed within the subplasmalemmal region (0.4±0.2; Figure 3.13B; n=8, Appendix 1, Table 3.10). As one might expect, the Ca^{2+} wave induced by angiotensin II was accompanied by contraction of all PASMCs, the area of cells reduced from 101±11 μm^2 to 89±10 μm^2 (Figure 3.13B, $p<0.05$; n=8, Appendix 1, Table 3.11). Publication showed that RyR3 is primarily targeted to the perinuclear region while the RyR2 is preferentially targeted to the extraperinuclear region of PASMCs (Clark et al., 2010a). It was therefore proposed that the Ca^{2+} transients released from RyR3 would be amplified by RyR2 as propagating Ca^{2+} waves, and the global Ca^{2+} waves may trigger vasoconstriction. Not entirely consistent with this view, I show that the vasoconstrictor angiotensin II induced Ca^{2+} release in both the extraperinuclear nanocourses and perinuclear nanocourses (which was initiated from extraperinuclear nanocourses), causing contraction of the pulmonary arterial myocytes.

Surprisingly, the biggest response to angiotensin II appeared within the nuclear invaginations, with the peak change reaching 1.7±0.4 (Figure 3.13B; n=8, Appendix 1, Table 3.10), yet no increase in Fluo-4 fluorescence was evident within the nucleoplasm. The angiotensin II induced increase in Fluo-4 fluorescence within nuclear invaginations was larger than that measured in response to maurocalcine but not significantly, which may be relevant to the differential action of vasoconstrictors versus vasodilators at the level of the nucleus.

To conclude, the cytoplasmic nanocourses form a cell-wide web for the coordination

of Ca^{2+} signalling and the regulation of smooth muscle function. Ca^{2+} signals in the subplasmalemmal nanocourses trigger smooth muscle relaxation while Ca^{2+} release into the perinuclear and extraperinuclear nanocourses induce smooth muscle contraction. This coordination of Ca^{2+} signalling is underpinned by strategic positioning of different subtypes of RyRs in the cytoplasmic nanocourses. To be specific, RyR1 is preferentially targeted to the subplasmalemmal nanocourses whereas RyR3 is majorly targeted to the perinuclear nanocourses, RyR2 is perhaps mostly found in the extraperinuclear nanocourses.

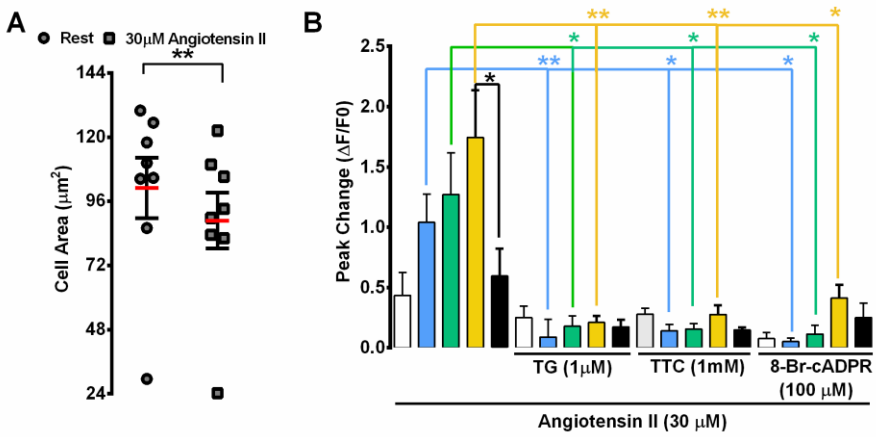

Figure 3.13 Angiotensin II triggers Ca^{2+} release into the perinuclear and extraperinuclear nanocourses, and leads to arterial myocytes contraction.

(A) Cell area (μM^2) before and after extracellular application of 30 μM angiotensin II was calculated and plotted, data presented as mean±SEM, n=8.

(B) Peak changes of the Ca^{2+} transients after extracellular application of 30 μM angiotensin II was calculated (Fx/F0), the peak changes within the subplasmalemmal, extraperinuclear, perinuclear and nuclear nanocourses (blue) or hotspots (red) were shown in the bar chart, in the absence or presence of 1μM thapsigargin, or 1mM tetracaine, or 100μM 8-bromo-cADPR Data are shown as mean±SEM, *=p<0.05, **=p<0.01, *** =P<0.001, ****=p< 0.0001, n=7 for control cells, n=5 for thapsigargin preincubated cells, n=4 for tetracaine preincubated cells and n=3 for 8-bromo-cADPR preincubated cells.

3.2.6 Nuclear invaginations demarcate Ca^{2+} signalling.

My aforementioned data suggest that nuclear invaginations might represent a discrete signalling domain. To explore this further, I first assessed whether the NR holds a releasable Ca^{2+} store.

3.2.6.1 Nuclear invaginations define cytoplasmic nanodomains that can shape Ca^{2+} signals arisen from the adjacent NR Ca^{2+} store

Nuclear invaginations are able to generate independent Ca^{2+} signals in response to the RyR1 agonist, which arise from a thapsigargin-sensitive SR store. Consistent with this view, previous studies have shown that the NR is continuous with ER (Echevarria et al., 2003), suggesting that the NR has the capacity to function as a Ca^{2+} store. In order to determine whether or not this was the case in PASMCs, I co-labelled acutely isolated cells with ER-tracker and a Ca^{2+} indicator, Calcium Orange (Figure 3.14, n=7), with the nucleoplasm identified by Draq 5 (blue). A series of confocal Z sections through a PASMC (step interval of 200 nm) revealed the SR and the NR by way of ONM labelling by ER-tracker (yellow; Figure 3.14B upper panel). Loading of the SR and NR lumen with the Ca^{2+} indicator Calcium Orange (red) in the absence (Figure 3.14B middle panel) and presence of ER-tracker (Figure 3.14B lower panel) revealed that the NR held a Ca^{2+} store that appeared to be continuous with the perinuclear SR. Figure 3.14 Aii&iii Show the nucleus at higher magnification, and illustrate the fact that the NR is essentially a Ca^{2+} store, that might support the local generation of Ca^{2+} signals within the nuclear invaginations.

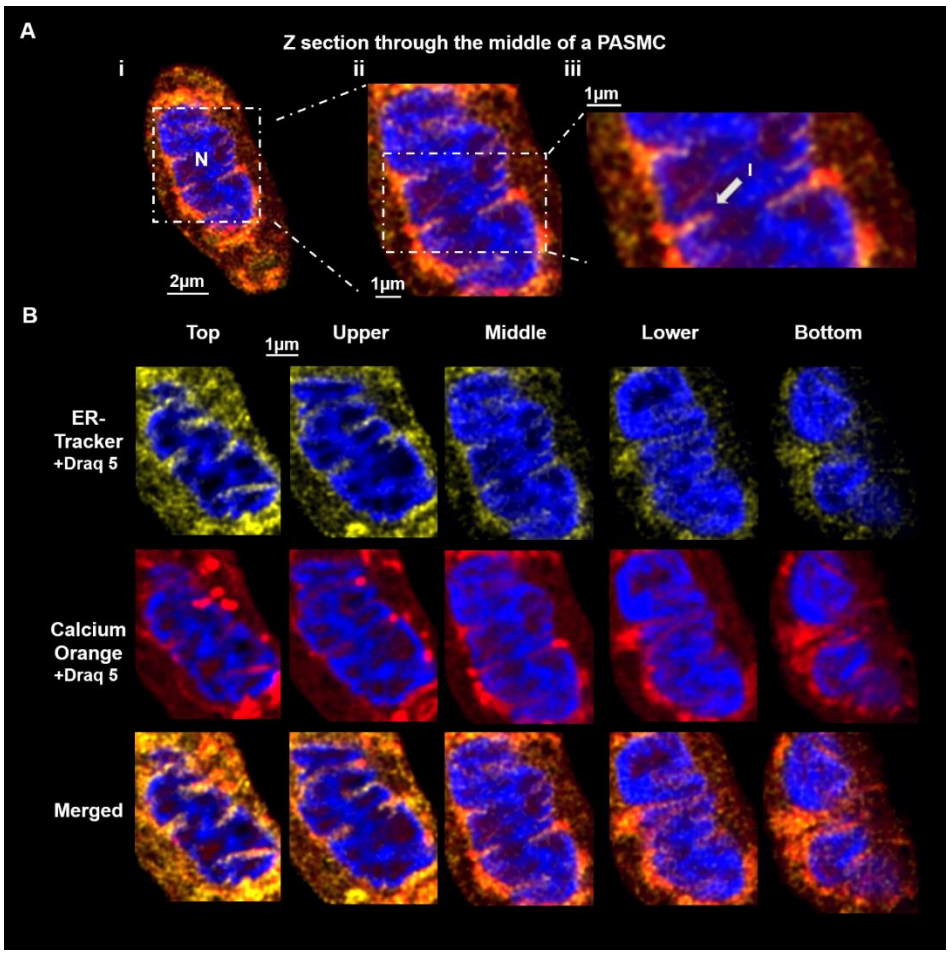

Figure 3.14 The nucleoplasmic reticulum holds a Ca^{2+} store.

(A) confocal Z sections through the middle of a PASMC labelled with ER-tracker (yellow), Calcium Orange at 37 ^{o}C (red) and Draq 5 (blue) shows that the nucleoplasmic reticulum (NR) serves as a Ca^{2+} store that is continuous with the perinuclear ER/SR. The nucleoplasm is labelled by Draq5 (N, blue), and one example of nuclear invagination is indicated with I. n=7.

(B) The upper panel shows a series of confocal Z sections through a PASMC with the SR and nuclear membrane identified by ER-tracker (yellow) and the nucleoplasm by Draq5 (blue). The middle panel shows the same focal planes but for Calcium Orange (red) and Draq 5 (blue) labelling. The lower panel shows the same focal planes but with all three types of staining merged.

3.2.6.2 Nuclear invaginations give rise to temporally and spatially restricted Ca^{2+} signals

The nuclear invaginations are perhaps the most intriguing cytoplasmic nanocourses of all kinds, considering that they display the highest increase in Fluo-4 fluorescence intensity upon stimulation compared to other cytoplasmic nanocourses. My findings in this respect are surprising, when one considers this and the fact that the role of nuclear invaginations in coordinating Ca^{2+} signalling received little attention before. Until now nuclear invaginations have been considered to be little more than an extension of the nuclear envelope, which has been proposed to either serve as a " buffer barrier" to buffer the cytoplasmic Ca^{2+} from entering the nucleoplasm (al-Mohanna et al., 1994), or provide the surface area necessary to maximize direct Ca^{2+} entry from the cytoplasm or Ca^{2+} release from the nucleoplasmic reticulum (see review (Bootman et al., 2009). My data suggest a model that does not entirely agree with either of these proposals, in that activation of RyR1 clusters within nuclear invaginations triggers an increase in Ca^{2+} (indicated by Fluo-4 fluorescence) within the cytoplasmic nanospaces demarcated by each activated invagination, that neither propagate to the nucleoplasm nor the proximal cytoplasm (Figure 3.9, 3.10 &3.12).

More detailed statistical analysis supports this proposal. The mean Fluo-4 fluorescence intensity within the nucleus was significantly lower than that within the nuclear invaginations at rest ($p<0.0001$, Figure 3.15 A, Appendix 1, Table 3.12). In response to maurocalcine, the amplitude of Ca^{2+} transients in the nuclear invaginations reached 1.2±0.3 (yellow, Figure 3.15 C, Appendix 1, Table 3.13), which is significantly higher than the peak change in the nucleus (0.4±0.2, black bar, $p<0.01$, Figure 3.15 C, Appendix 1, Table 3.13). Notably, the nuclear increase of Fluo-4 fluorescence is most likely an overestimate of the true values due to out of focus fluorescence from the adjacent nuclear invaginations. Following depletion of thapsigargin-sensitive Ca^{2+} stores, maurocalcine-induced Ca^{2+} release within nuclear invaginations was abolished (Figure 3.15 C). Moreover, inhibiting RyRs with tetracaine also abolished the maurocalcine induced Ca^{2+} signals in the nuclear invaginations (Figure 3.15 C). Taking these facts together, it can be concluded that RyR1s are targeted to the ONM of nuclear invaginations, maurocalcine evokes RyR1-dependent Ca^{2+} release into the cytoplasmic nanodomain of nuclear invaginations, from a thapsigargin-sensitive NR Ca^{2+} store. Consistent with this, angiotensin II also

induced marked Ca^{2+} release into the nuclear invaginations but not the nucleoplasm as Figure 3.15 B shows. The peak change in Fluo-4 fluorescence within nuclear invaginations reached 1.7±0.4 (Figure 3.15 B, Appendix 1, Table 3.14), which is significantly higher than the peak change in Fluo-4 fluorescence within the nucleoplasm (0.6±0.2, black bar, $p<0.01$, Figure 3.15 B, Appendix 1, Table 3.14). Angiotensin II induced Ca^{2+} signals were abolished by the depletion of the thapsigargin-sensitive Ca^{2+} store, by the inhibition of RyRs with tetracaine. Although angiotensin II may induce Ca^{2+} release from both the RyRs and IP_3Rs by inducing cADPR and IP_3 production (Dolgacheva et al., 2016), my data seem to suggest that RyRs are the main Ca^{2+} releasing channels responsible for the induced Ca^{2+} release within nuclear invaginations. Moreover, the Angiotensin II induced Ca^{2+} release was suppressed by the preincubation of 8-bromo cyclic ADP-ribose, a cyclic ADP-ribose (cADPR) antagonist. This is consistent with published data that angiotensin II may trigger Ca^{2+} release from RyRs in a cADPR-dependent manner (Fellner and Arendshorst, 2005).

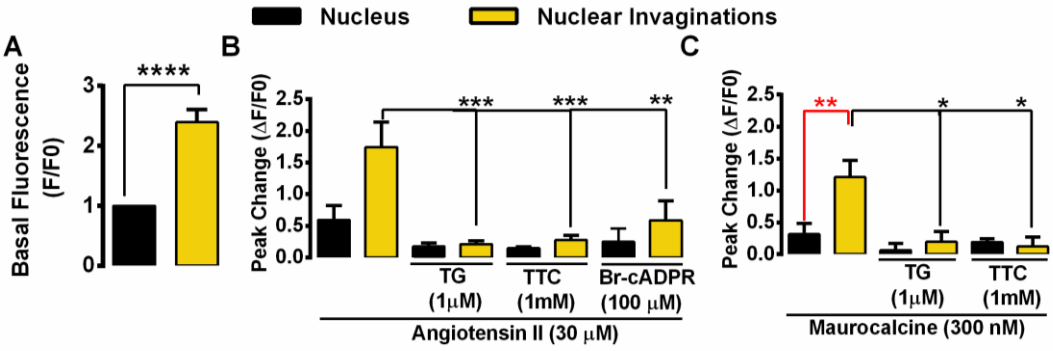

Figure 3.15 Induced Ca^{2+}signals were generated within the nuclear invaginations but not the nucleoplasm.

(A) Basal Ca^{2+} concentration (F/F0) within the nucleus or the nuclear invaginations was calculated. Data are shown as mean±SEM, *=p<0.05, **=p<0.01, *** =P<0.001, ****=p< 0.0001, n=7

(B) Peak changes of the Ca^{2+} transients after extracellular application of 30 µM angiotensin II was calculated (Fx/F0), the peak changes in the nucleus (black) or the nuclear invaginations (yellow) are shown in the bar chart. The cells were untreated (n=7), or preincubated with 1 µM thapsigargin (n=5), or preincubated with 1 mM tetracaine (n=4), or preincubated with 100 µM 8-bromo cyclic ADP ribose (n=3). Data are shown as mean±SEM, *=p<0.05, **=p<0.01, *** =P<0.001, ****=p< 0.0001.

(C) Peak changes of the Ca^{2+} transients after extracellular application of 300 nM maurocalcine was calculated (Fx/F0), the peak changes in the nucleus (black) or the

nuclear invaginations (yellow) are shown in the bar chart. The cells were untreated (n=3), or preincubated with 1 µM thapsigargin (n=4), or preincubated with 1 mM tetracaine (n=4). Data are shown as mean±SEM, *=p<0.05, **=p<0.01, *** =P<0.001, ****=p< 0.0001.

However, it is evident that Ca^{2+} signalling within nuclear invaginations is more complicated than one might expect, even when considering my findings thus far. As Figure 3.12 A lower panels show, the degrees of Angiotensin II-dependent "activation" varied between different invaginations within a single cell, and between different sites along the length of the same nuclear invaginations. To investigate whether the nuclear invaginations within the same cell would exhibit differential capacity to generate Ca^{2+} signals, I analyzed further the response of nuclear invaginations to maurocalcine. Acutely isolated PASMCS were loaded with Fluo-4, confocal Z sections were taken through the middle of one exemplar cell, and deconvolved. A 3D surface plot of the cell was built with pseudocolour representation of variations in Fluo-4 fluorescence intensity (Figure 3.16Aii-B). Following extracellular addition of maurocalcine, Ca^{2+} transients were induced in the nuclear invaginations. Figure 3.16 Bi-iv shows 4 selected frames from the time series, with 3D surface plots of the nucleus illustrating the response at each time points. Figure 3.16 Bi shows the nucleus at rest, and nuclear invaginations can be clearly seen. Two nuclear invaginations were selected as examples, I1 indicates one nuclear invagination that is above I2, while I2a and I2b refer to two sites along the length of the same nuclear invagination, all of which were further magnified as shown in Figure 3.16 C. Interestingly, little Ca^{2+} increase was observed in I1, although a small transient was observed within I1 at time point 4 (Figure 3.16 C, upper panels). By contrast, marked increases in Fluo-4 fluorescence was observed in I2b via two hotspots; the increase was initiated at time point 2 and was evident at time point 3. Interestingly, I2a represents a site that is adjacent to I2b on the same nuclear invagination. Increases in Fluo-4 fluorescence within I2a were limited in terms of propagation, and it was clear that induced changes were asynchronous to I2b (see time point 3). Given the above, it can be concluded that the

magnitude and kinetics of Ca^{2+} signals evoked within adjacent invaginations or adjacent sites along the same invagination vary markedly.

Some of the confocal imaging mentioned in this Chapter (i.e. the angiotensin II experiments with thapsigargin preincubated cells) were done in collaboration with Dr. Jorge Navarro-Dorado, who also kindly provided technical supports and did some of the confocal imaging.

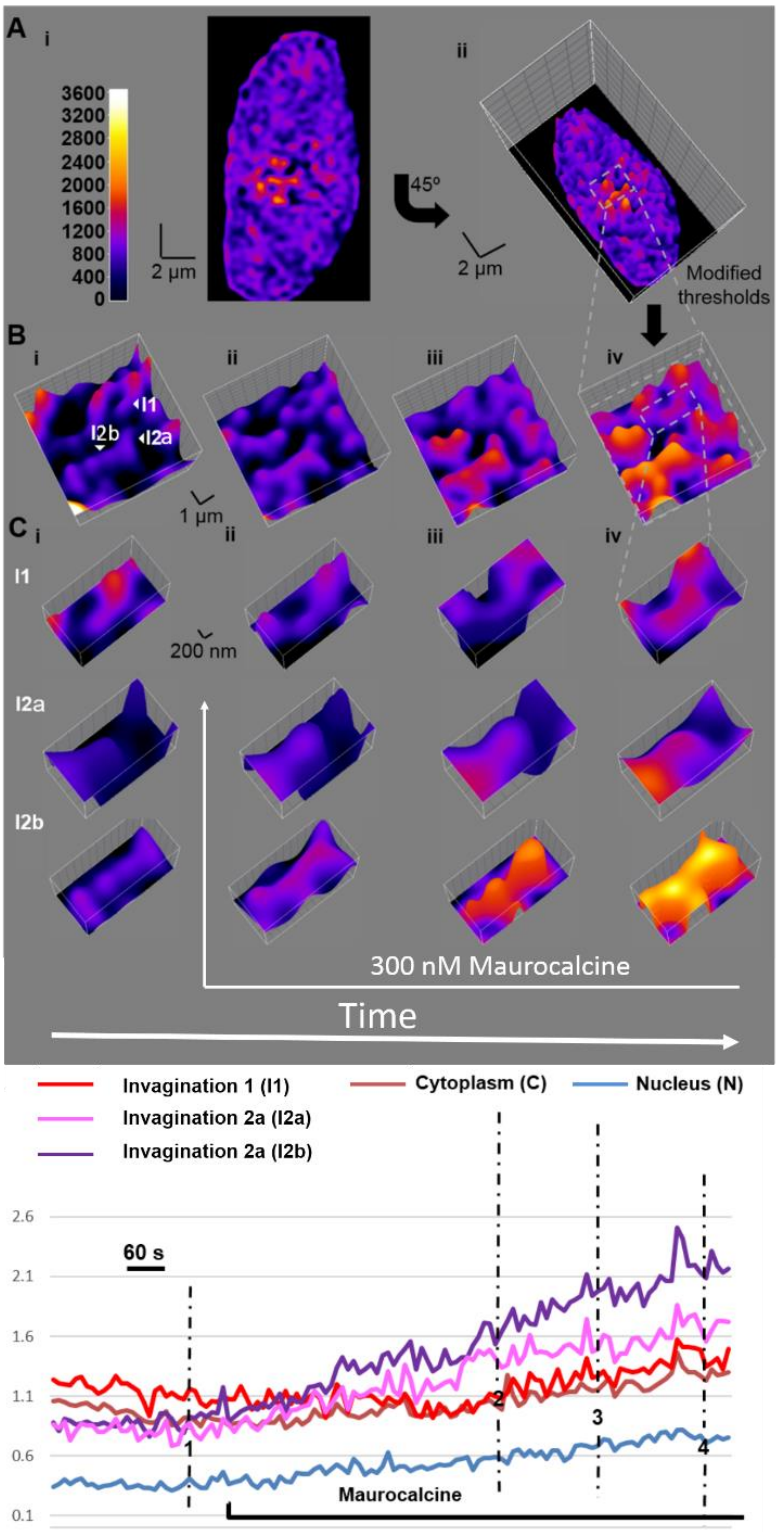

Figure 3.16 Nuclear invaginations give rise to temporally and spatially restricted Ca^{2+} signalling in arterial smooth muscle cells.

(Ai) Confocal Z section of a pulmonary arterial smooth muscle cell loaded (25° C) with Fluo-4 is shown, the fluorescence intensity indicated by pseudocolour representation on the vertical axis as per the scale shown in the look up table. (ii) 45° rotation of the

3D surface plot built from the image shown in (i).

(B) Higher magnification confocal Z sections of nuclear region selected within (A) are shown at (from left to right) different time points (i, ii, iii and iv) following extracellular application of maurocalcine (200 nM).

(C) As for (B) but showing higher magnification confocal Z sections of each of the 2 nuclear invaginations (I1, I2a and I2b) indicated.

(D) F/FC0 record ploted against time in selected region of interest.

3.3 Discussion

3.3.1 Summary of findings

Chapter 3 shows that cytoplasmic nanocourses are defined by the SR in PASMCs, and they form a cell-wide web for the segregation of Ca^{2+} signaling that is underpinned by strategic positioning of RyRs. RyR1 is preferentially targeted to the subplasmalemmal nanocourses and nuclear invaginations whereas RyR2 and RyR3 may target to the extraperinuclear and perinuclear regions respectively, as reported before (Clark et al., 2010a). It seems likely, therefore, that Ca^{2+} signals arising from different cytoplasmic nanocourses may support different smooth muscle functions. Consistent with this view I showed that the Ca^{2+} signals in the subplasmalemmal nanocourses trigger PASMC relaxation, whereas Ca^{2+} signals arising in the perinuclear and extraperinuclear nanocourses lead to PASMC contraction. Spatially restricted Ca^{2+} signals were also generated within the nuclear invaginations. Ca^{2+} pumps (SERCA1) and release channels (RyR1) are strategically positioned in the nuclear invaginations for the generation of Ca^{2+} signals arising from the NR, in a manner that may regulate gene expression (see Chapter 4).

Therefore, the cytoplasmic nanocourses of the PASMCs form a cell-wide web extending from the cell periphery to the nucleus, where they provide a mechanism for the spatial and functional segregation of intracellular Ca^{2+} signals, that may coordinate different smooth muscle functions.

3.3.2 Cytoplasmic nanocourses form a cell-wide web in PASMCs, within which hotspots of spontaneous Ca^{2+} flux was observed.

By conducting high resolution live cell confocal followed by deconvolution, the network of cell-wide nanocourses that exhibit high Ca^{2+} concentrations at rest were successfully revealed for the first time. These nanocourses are far more extensive and complicated than one might expect from previous proposals regarding the extent and function of nanojunctions of the sarcoplasmic reticulum (Evans et al., 2016, van Breemen et al., 2013). Based on early studies, cytoplasmic nanocourses were divided into 3 groups, namely the subplasmalemmal nanocourse, extraperinuclear nanocourse and perinuclear nanocourses (Gilbert et al., 2014, Clark et al., 2010a).

Interestingly, I observed hotspots of Ca^{2+} activities within all cytoplasmic nanocourses identified, the Ca^{2+} fluxes within which were suppressed by SR depletion, and following RyR inhibition. This suggests that at least a major part of the Ca^{2+} fluxes within cytoplasmic nanocourses of differentiated PASMCs are Ca^{2+} sparks generated by spontaneous SR Ca^{2+} release via RyRs. I do not exclude the possibility that some of the spontaneous Ca^{2+} flux observed are Ca^{2+} puffs from IP_3Rs (Shuai et al., 2006) as I have not tested the effect of IP_3R inhibition on the Ca^{2+} activities, but if this is the case the contribution made at rest would appear to be small.

People started to pay attention to spontaneous Ca^{2+} sparks in the 1990s (Gordienko et al., 1998, Nelson et al., 1995), and these studies characterize Ca^{2+} sparks arising in the subplasmalemmal region of muscle cells. Here, I have completed the first cell-wide characterization of spontaneous Ca^{2+} fluxes that has revealed a cell-wide web of cytoplasmic nanocourses within acutely isolated PASMCs, consistent with but more extensive than original predications (Evans et al., 2016). These hotspots in the nanocourses actively generate oscillating Ca^{2+} fluxes of a similar frequency within the cytoplasmic nanocourses, and with similar amplitudes for hotspots of Ca^{2+} flux within each region of approximately 0.16 ($\Delta F_X/F_0$). These measures are not inconsistent with those for spontaneous Ca^{2+} sparks observed in the smooth muscle cells in several previous studies. In retinal arteriolar smooth muscle cells, Ca^{2+}sparks with half maximum full width of 1.25±0.05 μm were recorded by line scan, the amplitude of the sparks was 0.81±0.04 ($\Delta F_X/F_0$), and the frequency was 0.56±0.06 per second (Curtis et al., 2004). In cerebral arterial smooth muscle cells, spontaneous Ca^{2+} sparks appeared at the frequency of 0.24±0.15 per second, the amplitude of the sparks was around 0.79 ($\Delta F_X/F_0$), which was calibrated as being equivalent to a local Ca^{2+} concentration of ~229 nM (Jaggar et al., 1998). In airway smooth muscle cells 3-35 Ca^{2+} sparks were observed per minute (Sieck et al., 1997), and in ileum smooth muscle cells the Ca^{2+} spark amplitude was 1.75±0.23 ($\Delta F_X/F_0$). Before comparing these results with my data it must be noted that these experiments were mostly conducted with confocal line scan at lower resolution, the spread of the Ca^{2+} spark ranges from 1-3μm. Considering the size of the nanocourses, it is likely that these "Ca^{2+} sparks" observed in the early studies are the combined effects of the Ca^{2+} sparks generated within multiple nanocourses by a number of hotspots, which are

perhaps behaving asynchronously according to my observation. This perhaps explains why the frequency of Ca^{2+} sparks I measured (which is from a single hotspot) is smaller than the published data on other smooth muscle cells (which is the combined outcome of a number of asynchronous hotspots). Moreover, due to the fact that different Ca^{2+} indicators were applied across these different studies, and the Ca^{2+} indicators display diverse gain of fluorescence upon binding to Ca^{2+} (Russell, 2011), the amplitude of Ca^{2+} sparks calculated based on (F_X/F_0) likely varies across studies, but they are on a similar scale to my measurement. Notably, the early studies mainly documented the Ca^{2+} sparks in the subplasmalemmal region. In addition to this, I have characterized and compared the Ca^{2+} fluxes in different intracellular nanocourses across the cells. My results also suggested that different subtype of RyR might target to different nanocourses.

3.3.3 RyR1, 2 and 3 are selectively targeted to different cytoplasmic nanocourses.

As discussed above, the hotspots are likely clusters of RyRs. These hotspots are generally separated by 300-500 nm in PASMCs. This observation is consistent with the published data which reported that the RyR clusters are separated by 376 ± 17 nm in sheep atrial myocytes (Macquaide et al., 2015). Intriguingly, my data showed that the distances of separation of nuclear hotspots and subplasmalemmal hotspots are more closely aligned when compared to the same measures for perinuclear and extraperinuclear hotspots. It has been reported that the separation between RyR2 clusters is around 0.97-1.87 μm in ventricular myocytes and 0.92-1.69 μm in atrial myocytes (Chen-Izu et al., 2006), 660 ± 60 nm in rat ventricular myocytes and 780 ± 70 nm in human ventricular myocytes (Soeller et al., 2007). This is larger than the average separation of RyR clusters in PASMCs, suggesting that the separation between RyR2 clusters might be larger than the separation of RyR1 or RyR3 clusters. Inferring from this, the nuclear, perinuclear, extraperinuclear and subplasmalemmal hotspots might be clusters of RyRs of different subtypes. For example, the extraperinuclear hotspots exhibit greater separation of distance, suggesting that the extraperinuclear nanocourses may harbour more RyR2 clusters than other cytoplasmic nanocourses.

Consistent with the above, I showed that the RyR1 agonist maurocalcine (Chen et al., 2003) triggers marked increases in Ca^{2+} flux from the nuclear and subplasmalemmal hotspots, but there was limited increase in Ca^{2+} release from the extraperinuclear and perinuclear hotspots within the same cell. This shows that the subplasmalemmal and nuclear hotspots are very likely supported by clusters of RyR1s. Moreover, my findings suggest that although some RyR1 clusters may be present in the extraperinuclear region, they are not the dominant subtype. Consistent with previous proposals, there is less RyR1 cluster targeted to the perinuclear region and thus the perinuclear nanocourses (Clark et al., 2010a, Kinnear et al., 2008).

The perinuclear hotspots are likely dominated by clusters of RyR3 because it was reported that the RyR3 preferentially target to the perinuclear region (Kinnear et al., 2008, Clark et al., 2010a). The extraperinuclear nanocourses may harbour a mixed population of RyR1, 2, and 3 clusters because the distance of extraperinuclear hotspots separation falls into a broader range, but the RyR2 clusters might be more commonly seen because 1) it was reported that RyR2s are dominant in the extraperinuclear region (Clark et al., 2010a); 2) the extraperinuclear hotspots exhibit greater distance of separation as discussed above.

It has been noted previously that each RyR subtype displays differential thresholds for activation and inactivation by Ca^{2+} (Chen et al., 1997, Li and Chen, 2001). It is therefore plausible that RyRs subtypes of different properties are strategically targeted different cytoplasmic nanocourses, resulting in segregated signalling compartments for the coordination of smooth muscle functions.

3.3.4 Ca^{2+} signals in the perinuclear and extraperinuclear nanocourses direct pulmonary arterial myocytes contraction

It was shown that adenylyl cyclase-coupled receptors such as β-adrenoceptors evoke Ca^{2+} release via RyRs from the SR by increasing the production of cADPR, which activates BKCa and triggers vasodilation (Boittin et al., 2003). However, in the same cell type, hypoxia, NAADP and Endothelin-1 have been shown to trigger Ca^{2+} release

via RyRs from the SR and induce vasoconstriction (Boittin et al., 2002, Kinnear et al., 2008). Therefore, it is intriguing that how the Ca^{2+} release via RyRs from the SR may regulate two distinct smooth muscle functions? The enigma might be resolved by the segregation of Ca^{2+} signals within the PASMCs as proposed previously (Evans et al., 2016).

My observations for maurocalcine described above show that induced Ca^{2+} release was restricted in subplasmalemmal nanocourses and nuclear invaginations, and led to PASMC relaxation. This is consistent with the view that Ca^{2+} release in the vicinity of plasma membrane activates BK_{Ca}, the resulting membrane hyperpolarization relaxes smooth muscle cells and subsequently causes vasodilation (Boittin et al., 2003). Therefore, the subplasmalemmal nanocourses can serve as segregated nanospaces for the generation of Ca^{2+} signals that deliver vasodilation.

In contrast, it has been proposed that vasoconstrictors might evoke Ca^{2+} signals in the bulk cytoplasm but not within PM-SR junctions, in order to promote PASMC constriction. Early studies illustrated that the activation of the RyRs causes a rapid increase in cytosolic Ca^{2+} concentration and support myocyte contraction. My data indicate a distinct path of Ca^{2+} flux that supports RyR-dependent smooth muscle contraction, because the Ca^{2+} wave induced by angiotensin II was initiated from the extraperinuclear nanocourses without causing a measurable rise in Ca^{2+} within subplasmalemmal nanocourses. Moreover, these signals were blocked by thapsigargin, tetracaine and 8-bromo cyclic ADP-ribose. In short and consistent with previous findings for angiotensin II (Fellner and Arendshorst, 2005), my data show that angiotensin II induces myocyte contraction, in part, by inducing a global Ca^{2+} wave by cADPR-dependent activation of RyRs in the vicinity of some extraperinuclear nanocourses, which triggers Ca^{2+} release in those extraperinuclear nanocourses that propagates across the cell. The induced Ca^{2+} wave propagates to, being amplified (via CICR by RyRs) and is carried on by the neighboring extraperinuclear nanocourses and RyR3 targeted perinuclear nanocourses, resulting in cell-wide Ca^{2+} release and smooth muscle contraction. Therefore, cytoplasmic nanocourses provide the mechanism for the segregation of intracellular Ca^{2+} signalling for the regulation of distinct smooth muscle functions.

In light of my findings it would appear that, as previously proposed (Evans et al., 2016), the signalling segregation by cytoplasmic nanocourses is underpinned by strategic positioning of RyR subtypes, because the RyR1, 2 and 3 display differential sensitivity to inactivation by Ca^{2+} (Li and Chen, 2001, Chen et al., 1997). Both RyR3 and RyR2 exhibit lower sensitivity to inactivation by Ca^{2+} compared to RyR1, their channel activity may still be observed at when the Ca^{2+} concentrations reach 10 mM or more (Chen et al., 1997; Li & Chen, 2001). Therefore, they are designed to carry propagating Ca^{2+} waves that are not prone to failure.

In marked contrast, RyR1 inactivation occurs within the micromolar range and full inactivation is achieved by 1 mM Ca^{2+}. This means, the RyR1 can cause the elevation of Ca^{2+} concentration in the subplasmalemmal nanocourses and reach the required Ca^{2+} concentration (around 10µM) for BK_{ca} channel activation (Zhuge et al., 2002) and the subsequent smooth muscle relaxation. However, when a global Ca^{2+} wave is triggered for smooth muscle contraction, which also leads to the opening of Ca^{2+} receptors on the plasma membrane, the RyR1s are perhaps inhibited by the high Ca^{2+} concentration and therefore favours cell contraction.

In this respect it is also interesting to note that Boittin et al showed that RyRs and IP_3Rs seem support Ca^{2+} release from segregated SR Ca^{2+} pools (Boittin et al., 2002). Although not studied here, it is therefore possible that some cytoplasmic nanocourses are IP_3R positive and RyR negative, or at least IP_3R dominant. In short, cytoplasmic nanocourses may provide for the segregation of different pathways to myocyte contraction, driven by, for example, RyR-dependent and IP_3R-dependent Ca^{2+} release.

3.3.5 Invaginations of the nucleoplasmic reticulum in arterial myocytes form trans nuclear networks of cytoplasmic nanospaces that give rise to spatially restricted Ca^{2+} signals

I have demonstrated that extensive invaginations of the nucleoplasmic reticulum exist

within nuclei of fully differentiated pulmonary arterial smooth muscle cells. It was shown that juxtaposed ONM membranes of these invaginations form a network of tubules that are continuous with the cytoplasm and project deep into the nucleus of arterial myocytes, conferring cytoplasmic nanotubes.

Fluorescent labelling for the sarcoplasmic reticulum and its luminal Ca^{2+} store demonstrated that invaginations of the nucleoplasmic reticulum not only demarcate cytoplasmic nanotubes but also provide a releasable Ca^{2+} store along the entire extent of their boundaries. This is consistent with the early finding that the NR can serve as a releasable Ca^{2+} pool (Papp et al., 2003). In support of the releasable NR Ca^{2+} store, a unique S/ER Ca^{2+} ATPase, SERCA1, was selectively targeted to nuclear invaginations, and thus provides for a Ca^{2+} store that is not only spatially but also functionally segregated from the perinuclear SR, fed by SERCA2a, and the superficial SR, fed by SERCA2b (Clark et al., 2010b). Moreover, of the three RyR subtypes expressed in arterial myocytes (Herrmann-Frank et al., 1991, Neylon et al., 1995), only RyR1 was identified within the boundary of the nucleus. RyR labelling lined tubular structures, spatially segregated from labelling for both RyR3 and RyR2. Clearly, NR resident SERCA1 and RyR1 deliver the capacity to support site-specific Ca^{2+} signalling within invaginations of the nucleoplasmic reticulum, because both pump and channel exhibit different kinetics, “affinities” for Ca^{2+} and mechanisms of regulation when compared to those subtypes targeted to the SR that feeds other aspects of the cell. For example, SERCA1 has a higher affinity for Ca^{2+} than perinuclear SERCA2a (Odermatt et al., 1998) and would therefore be the dominant path for Ca^{2+} uptake proximal to the ONM, while RyR1 may restrict signal propagation along the invaginations since it provides limited support for Ca^{2+}-induced Ca^{2+} release (Yang et al., 2001, Li and Chen, 2001, Chen et al., 1997).

Consistent with this view, I show that both the RyR1 agonist maurocalcine and the vasoconstrictor angiotensin II induced spatially restricted Ca^{2+} signals within nuclear invaginations, that did not propagate to the nucleus. The maurocalcine induced Ca^{2+} transients are clearly released via clusters of RyR1s, because they are blocked by tetracaine. Moreover, distances of separation for the hotspots of Ca^{2+} flux are around 300 nm along the length of the nuclear invaginations, reflecting the nanopatterning of the Ca^{2+} signals, although the effect of the Ca^{2+} signal is unclear.

I do not exclude the possibility that other Ca^{2+} releasing channels (i.e. IP_3R) may target to nuclear invaginations, although the contribution of IP_3Rs present in differentiated PASMCs observed here might be limited because the angiotensin II induced Ca^{2+} signals were blocked by the RyR inhibitor tetracaine.

3.3.6 Conclusion

Nanocourses of the SR form a cell-wide web for Ca^{2+} signaling in differentiated PASMCs, which is underpinned by strategic positioning of different subtypes of RyRs and perhaps SERCAs in those nanocourses as Figure 3.17 shows. These nanocourses provide mechanism by which intracellular Ca^{2+} signals are segregated for the regulation of smooth muscle functions, from relaxation by the subplasmalemmal nanocourses to contraction by the extraperinuclear and perinuclear nanocourses. The nuclear invaginations form a trans-nuclear network of cytoplasmic nanocourses for Ca^{2+} signaling, supported by RyR1 and the NR Ca^{2+} store fed by SERCA1. However, the function of the Ca^{2+} signalling in nuclear invaginations requires further investigation.

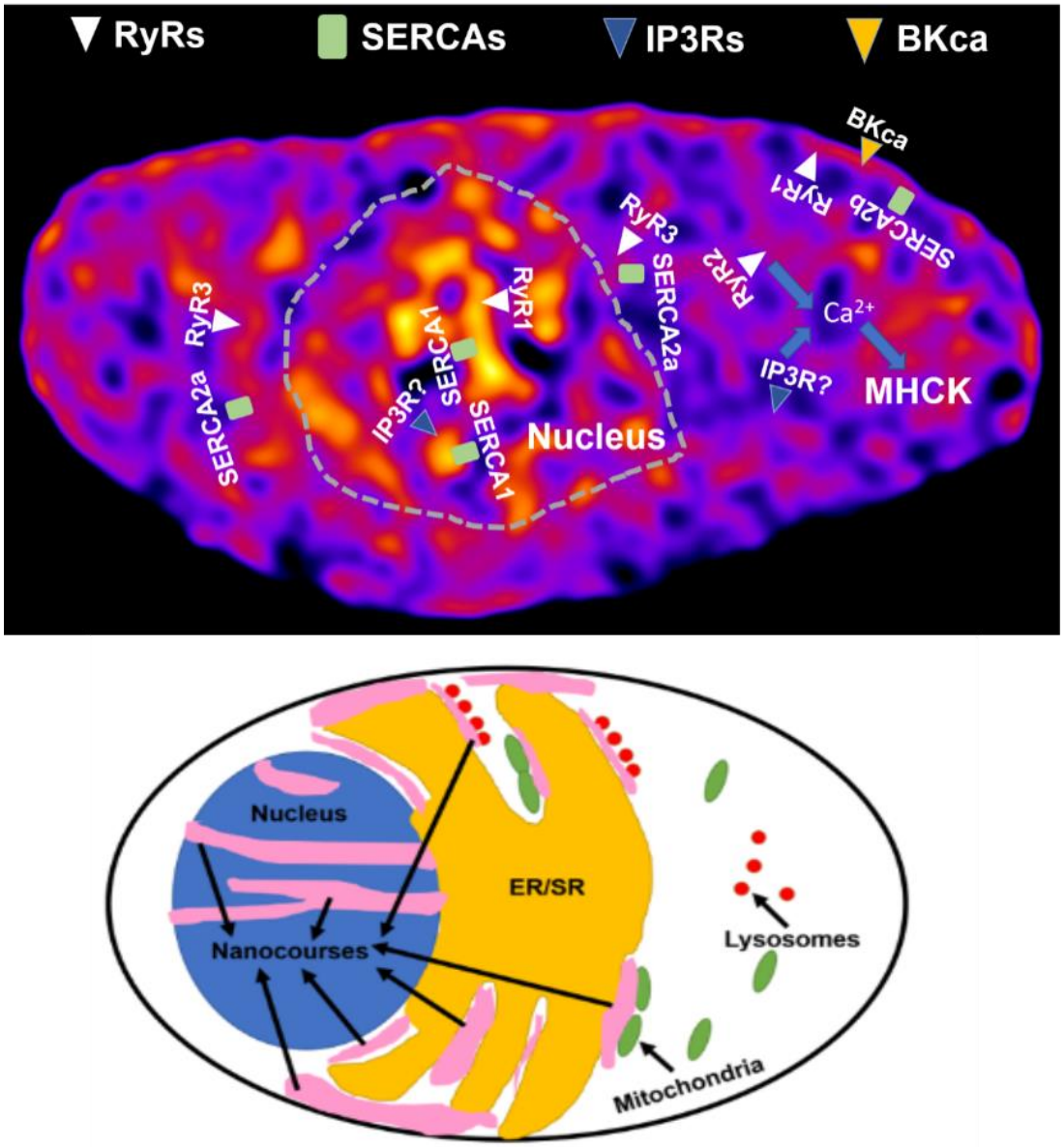

Figure 3.17 Schematic imaging showing the network of intracellular nanocourses

A PASMC was loaded with the Ca^{2+} indicator Fluo-4, pseudocolour was applied to show high fluorescence intensity in yellow and low fluorescence intensity in blue. Predicted position of RyR1, 2, 3; SERCA2a, 2b, 1; IP3R, and BKca channel are labelled. The nucleus is circled by grey dotted line. A diagram of the model is showed in the lower panel, nanocourses are indicated by pink.

Chapter 4: Nuclear invaginations harbour the machinery required to coordinate chromatin attachment

4.1 Introduction

4.1.1 Identification of nuclear invagination in a variety of cell types

The nuclear envelope (NE) is the structure that defines the boundary of the nucleus. It is composed of lipid bilayers, namely the outer nuclear membrane (ONM) and the inner nuclear membrane (INM). The luminal space that separates the ONM and INM by 30-50 nm has been termed perinuclear space (PNS) (Franke et al., 1981). It was proposed almost 30 years ago that the nucleus may harbour functionally segregated subdomains (Strouboulis and Wolffe, 1996), it was indicated that the transcriptional and translational activities involving DNA and RNA occur within defined territories, but these subdomains were not bound by membrane. Meanwhile, other scientists started to consider the possibility that the NE may contain intranuclear membrane extensions that form grooves, tubes or even channels that transverse the nucleus. As early as 1970s, researchers already identified nuclear invaginations in plant cells (Dickinson and Bell, 1972) and mammalian cells (Bourgeois et al., 1979). Benefiting from the improvement of confocal microscopy, people confirmed the existence of nuclear invaginations within the interphase nuclei of a series of established cultured cell lines including HeLa, Vero, NRK, 3T3, A431 and NOR10 (Fricker et al., 1997b). Therefore, it can be concluded that nuclear invaginations present in a wide range of cell types; they are a universal cellular structure. Nuclear invaginations have also been identified in primary cultures of human vascular smooth muscle cells (Avedanian et al., 2011). Intriguingly, these structures were not retained after nuclei were isolated from cells, which suggests that nuclear invaginations are dynamic structures that may be assembled and disassembled in short periods of time.

4.1.2 Nature of nuclear invaginations

As described above, nuclear invaginations are intranuclear extensions of the NE, forming either tubes that end in the centre of a nucleus, or channels that connect two sides of the nucleus. They can be classified into two groups based on their membrane components. Type 1 invaginations are defined only by the INM whereas type 2 invaginations are formed by both the ONM and INM as Figure 4.1 shows (Malhas et

al., 2011). The two types of invaginations can occur in the same cell, or even coexist in the form of type 1 branches at the intranuclear tip of a type 2 invagination. Together the NE and the nuclear invaginations form a complex network which has been termed as nucleoplasmic reticulum (NR). The number of nuclear invaginations found within a single cell varies from zero to more than ten (Fricker et al., 1997a, Broers et al., 2006), and it seems that the number of nuclear invaginations is not directly linked to cell-cycle stage (Fricker et al., 1997b). Consistent with other intracellular nanojunctions, the size of nuclear invaginations is on the nanoscale, with the upper limit of their diameter estimated, on the basis of immunostaining, ranges from 100-500 nm (Schoen et al., 2017). The electron micrographs showed in Figure 4.1 illustrated that the diameter of some invaginations may be within 100 nm.

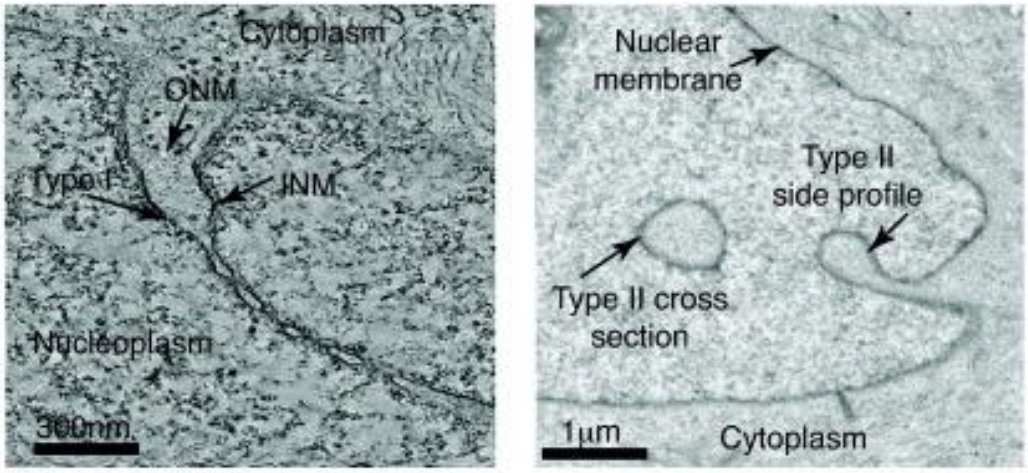

Figure 4.1 Type 1 and type 2 nuclear invaginations are revealed by electron microscopy.

Electron micrograph of mouse embryo fibroblast showing type 1 and type 2 nuclear invaginations. Adapted from “The nucleoplasmic reticulum: form and function”, by Malhas et al (Malhas et al., 2011).

4.1.3 Trans-nuclear envelope proteins

A particular group of trans-membrane proteins localises to the NE, and they are termed as Nuclear Envelope Transmembrane proteins (NETs). These proteins link the nucleoplasm to the cytoplasm, and they are responsible for the transduction of

signals across the NE. For example, the LINC (linkers of the nucleoskeleton and cytoskeleton) complex tethers the NE to the cytoskeleton, and has been proposed to transduce mechanical forces across the cell to the nucleus (Hieda, 2017, Kim et al., 2015, Banerjee et al., 2014). The LINC complex is composed of klarsicht-ANC-1-SYNE homology (KASH) domain proteins and sad1/UNC-84 homology (SUN) domain proteins. KASH domain proteins span the ONM, while the transmembrane domain of SUN forms trimers in between the inner and outer nuclear membranes. Moreover, either component of the LINC complex can associate with other inner nuclear proteins including emerin and the nuclear lamina (see review (Rothballer et al., 2013)).

The nuclear lamina is a protein meshwork that is roughly 15-20 nm thick (Gerace and Huber, 2012). It is a prominent feature of metazoan nuclear envelope (Burke and Stewart, 2013), lying directly underneath and forming close associations with the inner nuclear membrane. The meshwork is constructed with A-type lamins (lamin A, lamin C, lamin C2 and lamin AΔ10) and B-type lamins (lamin B1, lamin B2 and lamin B3). Considering that the nuclear lamina is extended across the entire inner surface of the inner nuclear membrane, it is reasonable to infer that the lamina could possibly delineate nuclear invaginations. Indeed, multiple studies identified nuclear invaginations by the immunostaining of lamin A or B (Bridger et al., 1993, Luo et al., 2009). Importantly, the nuclear lamina is proposed to contribute to chromatin organization and probably direct transcription and replication (Wilson and Foisner, 2010). Consistent with this view, a recent study has revealed that lamin A binds the lamin-associated-domains on chromatins and thus tethers the chromatin to the nuclear periphery, which results in the suppression of gene expression (Harr and Reddy, 2016).

Alternatively, chromatin anchoring may be achieved by LAP2-emerin-MAN1 (LEM)-domain containing proteins, which can facilitate transcriptional silencing (Brachner and Foisner, 2011). One well-studied example of LEMs is emerin, which is known to associate with the nuclear lamina and is able to bind the barrier-to-autointegration factor (BAF). BAF bridges chromatin to emerin, and by influencing histone post-translational modifications BAF may regulate gene expression (Segura-Totten and Wilson, 2004, Shimi et al., 2004).

4.1.4 Aim and hypothesis

The aim of this chapter is to characterize nuclear invaginations, and to investigate their function in pulmonary arterial myocytes. I hypothesize that the nuclear invaginations, as a distinct subset of cytoplasmic nanocourses, form a trans-nuclear network that provides sites for the regulation of chromatin attachment.

4.2 Results

4.2.1 Key elements of the nuclear envelope transmembrane protein complexes are selectively targeted to the NR

In Chapter 3 I provided the evidence in support of the view that: (1) Nuclear invaginations support highly localised Ca^{2+} release via the NR, into the cytoplasmic nanospaces they demarcate but not into the adjacent nucleoplasm; (2) The pharmacology of Ca^{2+} signals generated is consistent with the fact that they arise via RyR1 and in a manner supported by the refilling of NR Ca^{2+} stores via SERCA; (3) RyR1 and SERCA1 are selectively targeted to those sections of the NR that comprise nuclear invaginations. These findings raise the following question: do Ca^{2+} signals arising within nuclear invaginations regulate genome reorganization and gene expression?

Clearly, the transduction and interpretation of Ca^{2+} signals that enter the cytoplasmic nanotubes demarcated by nuclear invaginations cannot directly influence the machinery that orchestrates transcriptional processes within the nucleoplasm. Therefore, I considered the possibility that the release of NR Ca^{2+} via RyRs might regulate “outside-in” signalling via adjacent protein complexes, that may comprise effector proteins. The nuclear envelope transmembrane (NET) proteins are one such example. Key among these are the proteins that comprise the nuclear lamina, a protein meshwork that lines the entire inner surface of the inner nuclear membrane. This nuclear lamina serves as the bridge that connects the nucleoplasm to the cytoplasm through the LINC complex and its components, and has been widely used to identify and investigate the composition of nuclear invaginations in multiple studies (Avedanian et al., 2011, Legartova et al., 2014). My investigations of the role of NET proteins were founded on the characterization of nuclear invaginations with lamin A and lamin B.

4.2.1.1 Lamin A lines the entire inner nuclear surface of PASMCs, including the nuclear invaginations

It was confirmed by confocal imaging (Figure 4.2 Ai) of acutely isolated arterial myocytes labelled for lamin A (red, n=54) that this major component of the nuclear lamina lines the entire nucleoplasmic surface of the INM identified by Dapi (blue),

which is consistent with previous findings (Burke and Stewart, 2013). Importantly, labelling for lamin A not only resolved the entire boundary of the INM, but also clearly identified the larger nuclear invaginations (Figure 4.2Aii&Bii), which formed a network of tubular structures within the nucleoplasm boundary outlined by lamin A.

Based on morphology, three forms of nuclear invaginations could be identified by lamin A labelling. The left panel of Figure 4.2 Aii shows a section of the 3D reconstruction of the lamin A labelled nucleus, in the middle panel a region within this section is magnified to show an example of the trans-nuclear invaginations (indicated with T), which are nuclear invaginations that spanned the entire diameter of the nucleus. Next to the trans-nuclear invagination, there is also an example of the blind invaginations (indicated with B), which generally take the form of blind-ended tubes that exhibit various depths of extension into the surrounding nucleoplasm. The right panel of Figure 4.2 Aii displays the same trans-nuclear and blind invaginations at a different angle. It can be observed that these invaginations are not plain straight tubes, but instead structures that exhibit various curvatures along their lengths. A different section of the same 3D model of the nucleus was cropped out as shown in Figure 4.2 Bii (left panel). This section was magnified to reveal an example (Figure 4.2 Bii middle panel, indicated with S) of the superficial invaginations that form “short bridges” that appear to cross-connect two closely aligned sites on the NE (Figure 4.2 Bii right panel). Moreover, by showing the nuclear invaginations in high magnification, it is clear that the diameter of the same invagination varies along its length (Figure 4.8Aii&Bii), suggesting that the nuclear invaginations are non-uniform bodies, consistent with the observations with electron microscopy (Malhas et al., 2011). This raised the possibility that NET proteins might be differentially distributed along the length of nuclear invaginations, because NET proteins have been proposed to determine NE architecture and luminal diameters (Rothballer et al., 2013).

Unlike published data on the lamin A staining in mouse embryonic fibroblasts that showed rounded nuclei with relatively smooth surfaces (Legartova et al., 2014), the lamin A staining in acutely isolated PAMSCs uncovered irregularly shaped nuclei with “crumpled” surfaces. This is more obvious after the application of a digital skin to the 3D reconstruction showed in Figure 4.2 A&B (Figure 4.2 Ci), which reveals clear grooves and infoldings of the NE that were identified by lamin A labelling. One

example of such grooves/infoldings was cropped out from the 3D model and enlarged as the left panel of Figure 4.2Cii shows. The structure is displayed at different angles (Figure 4.2 Cii, middle and right panel) to show that it is in the shape of a cleft. These cleft-like structures have previously been identified by EM (Wittmann et al., 2009), and will be referred to from here on as clefts. Aside from clefts, by increasing the threshold above which lamin-A labelling was visualized by the image analysis software, I identified on the surface of nuclei, a large number of areas of variable sizes that could be separated by density from the surrounding lamin A positive lamina. These densities are shown in Figure 4.2 Di by displaying the 3D reconstruction of the same nucleus (as shown in Figure 4.2 A, B&C) with a digital skin under a higher detection threshold. These apparent linear structures ran for variable distances, and the rotated section of the 3D model shown in Figure 4.2 Dii revealed that these structures ran across the peripheral aspect of the nucleus. Based on the morphology of these linear structures as the high magnification images shown in Figure 4.2 Dii (middle and right panel), they were named as ridges. Notably, nuclear invaginations and the surface infoldings (clefts) have been reported previously (Wittmann et al., 2009, Fricker et al., 1997b), but these ridges do not appear to be identified before.

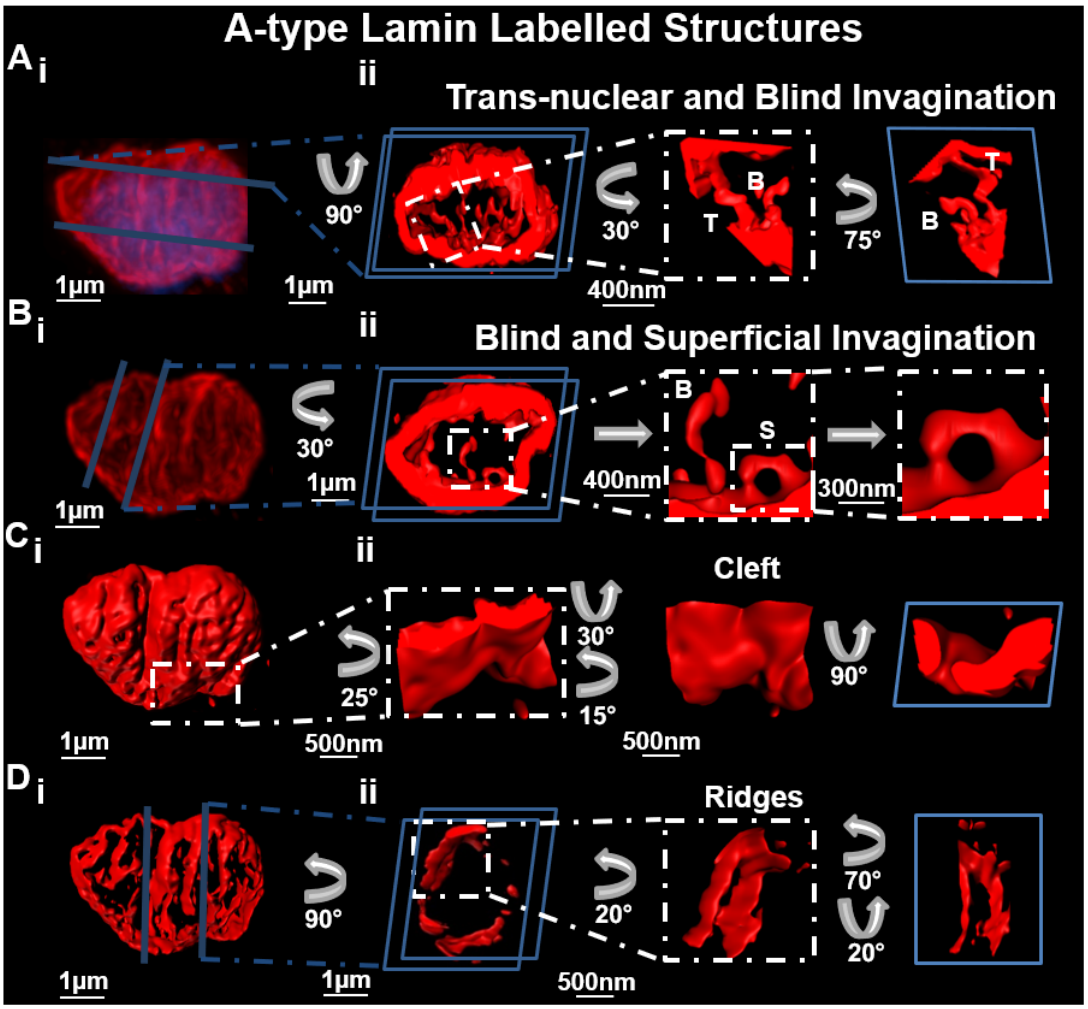

Figure 4.2 Lamin A labelling of the inner nuclear membrane reveals 3 types of nuclear invaginations and peripheral ridges and clefts.

(Ai) 3D reconstruction of deconvolved Z stacks of confocal images through the nucleus of a pulmonary arterial smooth muscle cell labelled for lamin A (red). (ii) Rotation and transverse section through the 3D image shown in (i) following application of a higher fluorescence threshold and blending (left panel), which identifies by sectioning and magnification blind (B) and transnuclear (T) invaginations (middle and right panels).

(B) as in (A) but identifying a blind invagination (B) and a superficial invagination (S).

(C) Digital skin is applied to the 3D reconstruction showed in (Ai), with low fluorescence threshold and blending. (ii) A peripheral cleft is identified by sectioning and rotation, and is shown in higher magnification.

(D) as in (C) but identifying peripheral ridges with high detection threshold.

To define and investigate the peripheral ridges, 3D reconstructions of lamin A labelled PASMCs were built in a manner that reveals the density of lamin A labelling. For example, as Figure 4.3 Ai shows, 3D reconstruction with low detection threshold allows the visualization of the entire inner nuclear surface defined by lamin A, which becomes evident after the application of a digital skin that sets the boundary (right panel). However, there were clearly densities of lamin A surrounded by the lamin A positive lamina as shown in the left panel, and they are the peripheral ridges. To reveal the ridges, the detection threshold was raised to remove the surrounding lamin A positive lamina but showing only the densities of lamin A as Figure 4.3 Aii shows (left panel). Following the application of the digital skin (Figure 4.3 Aii, right panel), the ridges can be clearly viewed and characterized.

Three types of ridges were identified in PASMCs based on their morphologies. The most obvious structures revealed by lamin A density are the deep Y/I shaped ridges, which are indicated by a blue box in Figure 4.3. The section of the 3D reconstruction outlined by the blue box was cut out and magnified as shown in Figure 4.3Bi with (left panel) or without (right panel) the digital skin. These linear structures generally extend for a couple of micrometers (n=54). Moreover, it can be seen from the example (Figure 4.3 Bi) that the deep Y/I shape ridge was the extension of a cleft (indicated with C). The same ridge was rotated 90 degrees clockwise and viewed from the side as Figure 4.3 Bii left panel shows. Judging by the shape and size of the extension, it can be concluded that the deep Y/I shape ridges are in fact sheets that extend into the nucleus. A section of the ridge was outlined by a white box (Figure 4.3 Bii, middle panel), which was magnified and rotated 90 degrees anticlockwise to allow the viewing from the front. A dark orange line indicates where the ridge is connected to a cleft, and a yellow line was positioned in the middle of the ridge. The 3D model was cut at where the dark orange and yellow lines indicate, and was rotated to reveal the cross-section (Figure 4.3 Bii, right panel). Judging by the shape of the cross-section indicated by the orange box, it can be postulated that the deep Y/I shape ridges are extensions of clefts, but not like the wide-open clefts, they are very narrow and deep infoldings of the NE. Within the regions indicated by the yellow box, the gaps of the infoldings were too narrow to be resolved by the limited resolution provided by confocal microscopy, which suggests that the sizes of gaps between their opposing membranes are less than 100 nm.

As Figure 4.3 Aii showed, there was a group of ridges that are in the shape of blind tubes (green box), and they were the tubular ridges. One section of the 3D reconstruction containing an example of the tubular ridges was cropped out and magnified as Figure 4.3 Ci shows. The lamin A density (right panel) can be clearly identified following the application of the digital skin, and it was obvious that, not like the deep Y/I shape ridges, the tubular ridges are stand-alone structures that are not extensions of clefts. The lengths of the tubular ridges range from several hundreds of nanometers to several micrometers. More importantly, by rotating the 3D model 90 degrees clockwise it can be observed that these tubular ridges are not sheet-like (Figure 4.3 Cii, left panel). Similarly, by cutting through the middle of this example ridge at where the yellow line indicates (Figure 4.3Cii, middle panel) and rotate the 3D model to show the cross-section, it was confirmed that the tubular ridges were not deep infoldings, but instead tubular structures spanning the nuclear surface.

In contrast, I have identified groups of lamin A densities that were not isolated linear structures, but resembled a tree branch (Figure 4.3 Aii, indicated by orange box), and they were termed as branched ridges. One example of the branched structures defined by lamin A densities (Figure 4.3 Di, right panel) was sectioned and magnified following the application of the digital skin (Figure 4.3 Di, left panel). Different from the tubular ridges, the branched ridges were smaller in size, and each branch was only several hundreds of nanometers in length. Rotating the section by 90 degrees, it can be seen that the branched ridges did not extend into the nucleoplasm like the deep Y/I shape ridges (Figure 4.3 Dii, left panel), which is confirmed by the shape of the cross-section (Figure 4.3 Dii, right panel).

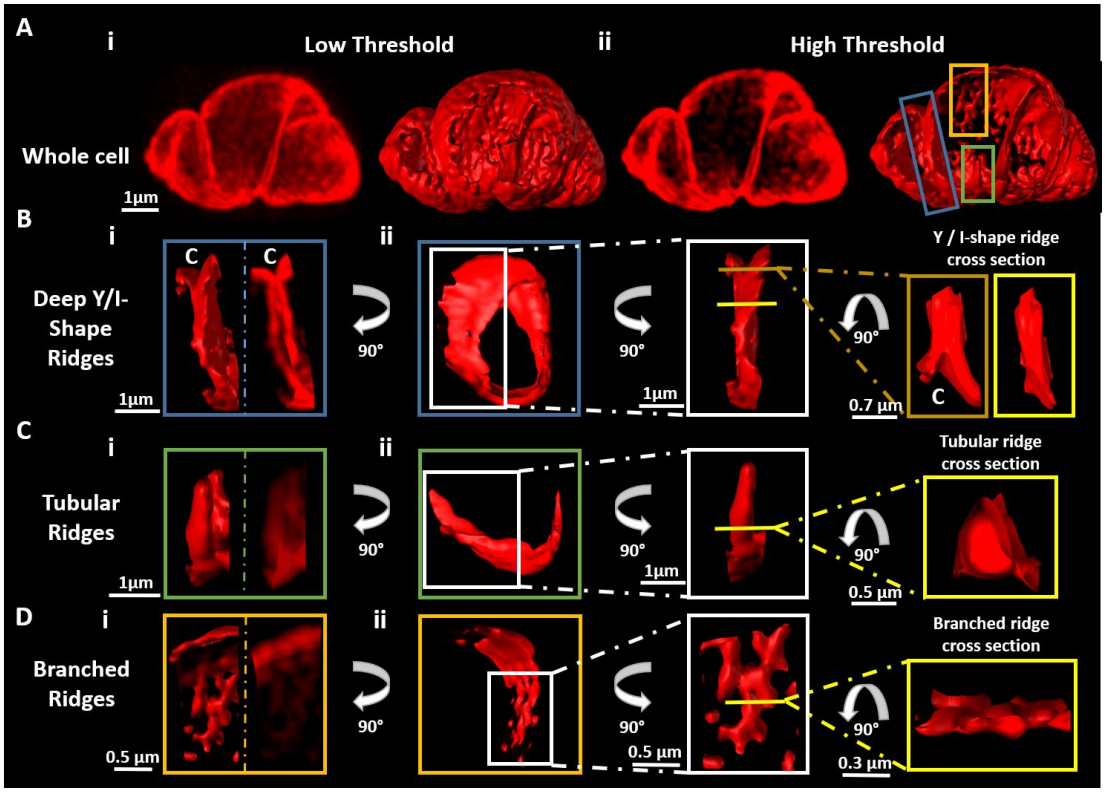

Figure 4.3 Labelling for lamin A identifies three types of peripheral ridges.

(A) PASMC nucleus labelled for A-type Lamin (red) in low detection threshold (i, left), a digital skin was applied to the 3D reconstruction to show detailed structures (i, right). (ii) As for (i), but at a higher detection threshold. Three ridges are pointed out with boxes in different colours.

(B) A deep Y/I shaped ridge is shown in higher magnification (i) with or without digital skin. (ii) The ridge coated with a digital skin is turned 90° clockwise (left panel), and is magnified with a 90° anticlockwise turn (middle panel). The cross section of (ii) is shown in the right panel by turning 90° downwards.

(C) As for (B), but showing a tubular ridge.

(D) As for (B), but showing a branched ridge.

The ridges and the clefts are peripheral structures that run along the perimeter of the NE; only the nuclear invaginations reach the interior of the nuclei. In this respect it is notable that ridges and clefts were identified in every cell studied, but only around 70% of the studied cells exhibited nuclear invaginations (Figure 4.4Ai, black). Blind invaginations were most common, and they were found in around 62% of cells

PASMCs (Figure 4.4Ai, blue); whereas 45% of cells harboured trans-nuclear invaginations (Figure 4.4Ai, red). By contrast, superficial invaginations were relatively rare, with only 28% of the studied cells harbouring clearly identifiable superficial invaginations (Figure 4.4Ai, orange); although this deficit might be due to the superficial invaginations being more prone to compression against the INM during the process of fixation.

The average number of each of these structures (Figure 4.4 Aii) suggested that there were significantly fewer nuclear invaginations than clefts or ridges. On average, 2.6±0.41 nuclear invaginations were identified per cell (Figure 4.4Aii, black) with 0.8±0.25 trans-nuclear invaginations (red), 1.4±0.21 blind invaginations (blue) and 0.4±0.09 superficial invaginations (orange) per cell (n = 54). However, by removing the 30% cells that did not exhibit nuclear invaginations (Figure 4.4 B), percentage of cells that harboured trans-nuclear (red), blind (blue) and superficial (orange) invagination increased to around 64%, 81% and 35% respectively (Figure 4.4 Bi, n=38). As the result, the average number of nuclear invagination per cell was raised to 3.8±0.36 (black), and the average number of trans-nuclear (red), blind (blue) and superficial (orange) invaginations per cell were 1.3±0.21, 2.0±0.12 and 0.5±0.06 respectively (Figure 4.4 Bii, n = 38). In great contrast, ridges and clefts were found in every cell studied (Figure 4.4 Aii), with 15±1.4 ridges (green) and 14±1.6 clefts (grey) per cell (n =54). The results show that there was evidently higher number of peripheral ridges and clefts compared to nuclear invaginations ($p<0.0001$). In terms of the three types of ridges (Figure 4.4 Aii), the tubular ridges (light grey) were most commonly found in PASMCs, 10±1.1 tubular ridges were identified per cell. On average, only 2.8±0.26 branched ridges (dark green) and 2.5±0.21 deep Y/I shaped ridges (pink) were found in the studied cells (n=54).

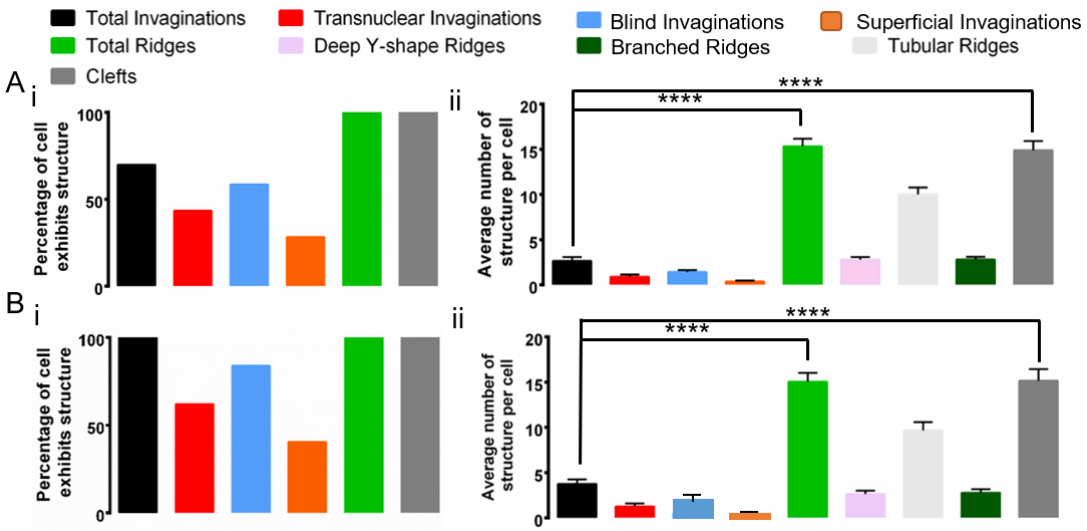

Figure 4.4 lamin A-positive nuclear invaginations are not evident in all cells

(A) Percentage of PASMCs that contain nuclear invaginations (black), trans-nuclear invaginations (red), blind invaginations (blue), superficial invaginations (orange), ridges (green) or clefts (grey) is shown in the left bar chart. Number of structures per cell is shown in the bar chart at right, with the total nuclear invagination in black, trans-nuclear invaginations in red, blind invaginations in blue, superficial invaginations in orange, ridges in green, deep Y/I shaped ridge in pink, tubular ridge in light grey, branched ridge in dark green and clefts in grey. n= 54, which includes all the cells studied. Data are presented as mean±SEM, *=p<0.05, **=p<0.01, *** =P<0.001, ****=p< 0.0001, n=52

(B) As for (A), but showing only the cells that exhibited nuclear invaginations, n=38.

Due to this apparent variation in number of lamin A labelled structures, I plotted the number of structures per cell that were identified by lamin A density (Figure 4.5A) with the trans-nuclear invaginations in red, blind invaginations in blue, superficial invaginations in orange, ridges in green, and clefts in grey. The total number of nuclear structures identified by lamin A density in any given cell varied from 57 to 14. Of these structures, the number of nuclear invaginations was not correlated to the number of peripheral structures as it was shown in Figure 4.5 A. This observation received strong support from the linear regression analysis which showed non-linear relationship between the two datasets with the R^2 of 0.01145 ($y=0.3499^{*}x+34.91$, Appendix 2 Table 4.1), suggesting that although both the nuclear invaginations and ridges/clefts were derived from the NE, their formation is most likely independently

regulated.

As shown in Figure 4.5 B, the total number of all three categories of nuclear invaginations (trans-nuclear invaginations in red, superficial invaginations in orange, and blind invaginations in blue) also varied from 17 to 0. Furthermore, the number of each form of nuclear invaginations in each cell appeared to vary randomly, and the linear regression analysis confirmed that the number each form of the nuclear invaginations was poorly correlated with the number of others (R^2 =0.2372 for trans-nuclear invaginations versus blind invaginations, R^2 =0.02343 for trans-nuclear invaginations versus superficial invaginations, Appendix 2 Table 4.1). This observation indicates that the formation of each type of invagination might be dynamically regulated.

Moreover, the numbers of ridges (green) and clefts (grey) per cell (Figure 4.5 C) varied, and it is apparent that the presence of a high number of ridges was not necessarily associated with the presence of more clefts and vice versa. This was confirmed by the linear regression analysis (R^2=0.1150, y=0.2033*x+14.12, Appendix 2 Table 4.1), which showed a poor fitness of linear relationship between the two datasets.

To conclude, nuclear invaginations appear to exhibit diversity with respect to form and number in PASMCs. Either comparing between the three forms of nuclear invaginations, or between the two peripheral structures, or compare the total invaginations with the total peripheral structures, the presence of one structure does not seem to be correlated with either the loss or presence of the others.

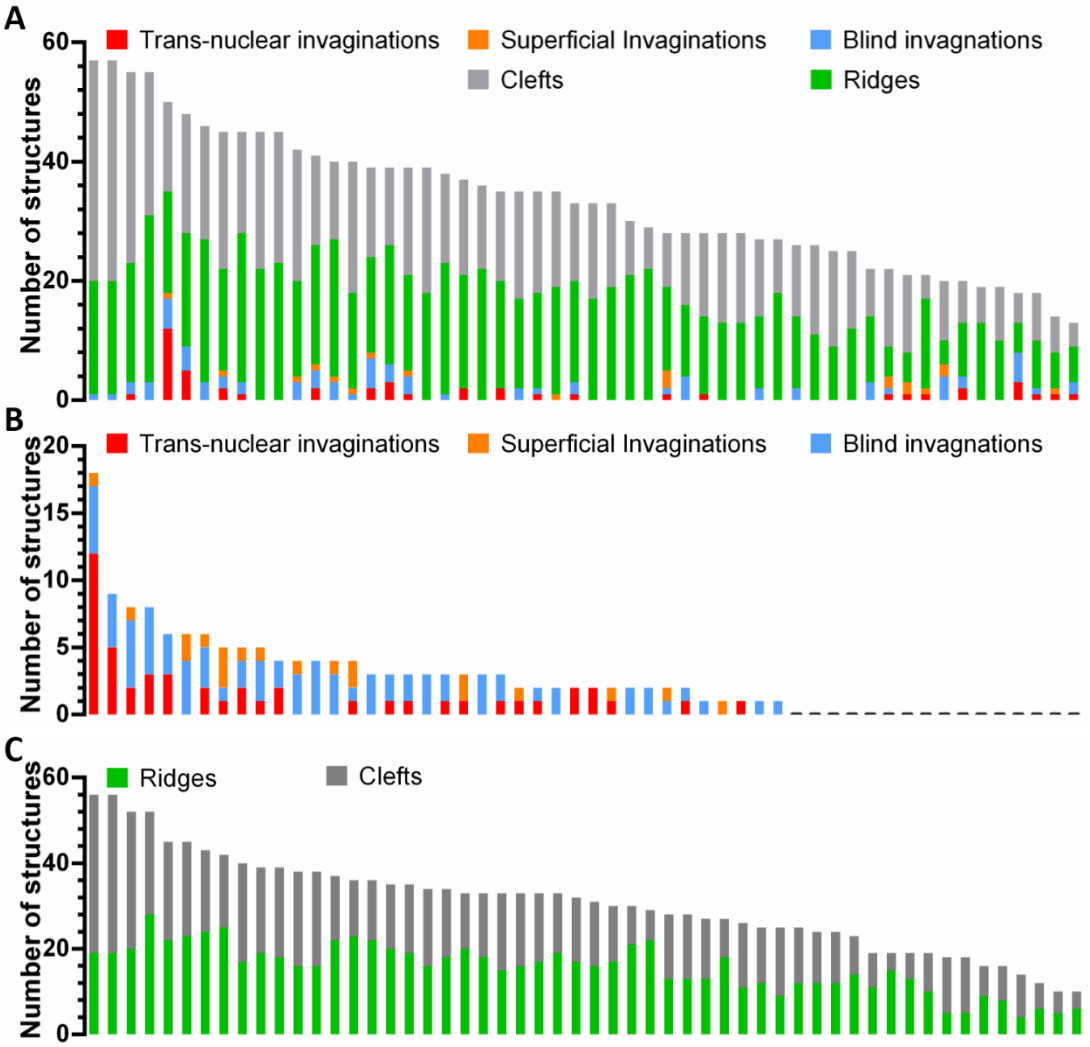

Figure 4.5 Variation in the number of nuclear invaginations between cells indicates a high level of plasticity

(A) The number of structures identified by lamin A in each cell is shown in the stacked bar chart, with the clefts in grey, ridges in green, trans-nuclear invaginations in red, blind invaginations in blue, superficial invaginations in orange. Each bar represents a cell, n=54

(B) The number of structures identified by lamin A in each cell is shown in the stacked bar chart, with the trans-nuclear invaginations in red, blind invaginations in blue, superficial invaginations in orange. Each bar represents a cell, and cells without nuclear invaginations were indicated by a black line, n=54

(C) The number of structures identified by lamin A in each cell is shown in the stacked bar chart, with the clefts in grey and ridges in green. Each bar represents a cell, n=54

4.2.1.2 Lamin B1 lines peripheral structures but not nuclear invaginations

The nuclear lamina is composed of not only A-type lamin but also B-type lamin, and labelling for both has been used to identify nuclear invaginations in other cell types (Luo et al., 2009, Avedanian et al., 2011). Therefore, PASMCs were also labelled for one member of the B-type lamin (lamin B1) to characterize the nuclear invaginations. As Figure 4.6 Ai shows, one PASMC was labelled for lamin B1 (purple), and the 3D reconstruction was displayed. Clearly and quite unlike the labelling for lamin A which lines the entire inner surface of the INM and its invaginations, lamin B1 labelling was punctate. This is more evident after raising the detection threshold and applying a digital skin to the 3D reconstruction (Figure 4.6 Aii). The density of lamin B labelling identified peripheral ridges (Figure 4.6 Aii, left and middle panel), by sectioning and rotating it was confirmed that the lamin B1 labelling also identified clefts (Figure 4.6 A ii, right panel). Indeed, as the statistical analysis showed (Figure 4.6 B), lamin B1 labels 14±1.1 ridges and 16±0.9 clefts per cell (magenta with grids, n=12, Appendix 2 Table 4.2), which is very similar to the numbers of lamin A (red) labelled ridges (compared by t-test, p=0.428) and clefts (compared by t-test, p=0.5829) per cell. In great contrast, across all 12 cells labelled by lamin B1, no nuclear invagination was identified. In short, lamin B1 appears to be restricted to the periphery of the INM and absent from the nuclear invaginations of acutely isolated PASMCs.

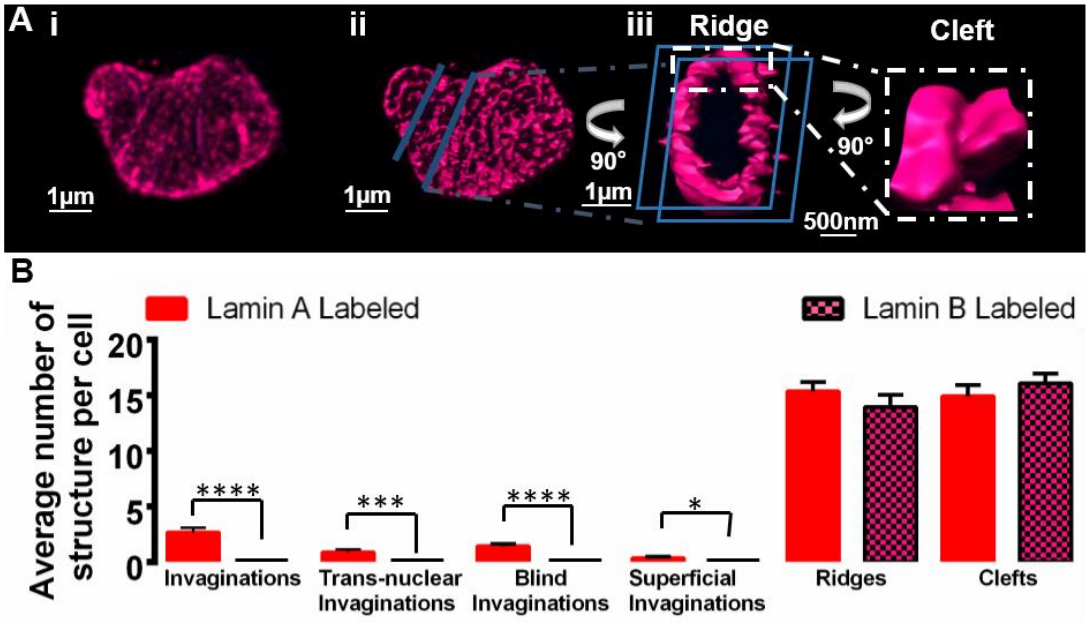

Figure 4.6 Lamin B1 labels peripheral structures but not nuclear invaginations

(Ai) The nucleus of a PASMC is labelled for lamin B1 (purple), (ii) 3D reconstruction of the nucleus is shown with the application of digital skin and blending. (iii) The 3D model was sectioned to show a ridge (iii. left panel), and then displayed at higher magnification with a 90° turn to show a cleft (iii, right panel).

(B) Average number of structures per cell identified by either lamin A (red) or lamin B1 (purple) are displayed in the bar chart. Structures include nuclear invaginations, trans-nuclear invaginations, blind invaginations, superficial invaginations, ridges, and clefts. Data are shown as mean±SEM, *=p<0.05, **=p<0.01, *** =P<0.001, ****=p< 0.0001, n=12 for lamin B staining, n=52 for lamin A staining.

4.2.1.3 The LINC complex is selectively targeted to nuclear invaginations

As mentioned previously, the nuclear lamina is the protein meshwork that serves as the bridge that connects the nucleoplasm to the cytoplasm through the LINC complex, with A-type lamin and B-type lamin acting as binding partners for different components of the LINC complex and/or inner nuclear membrane proteins. Due to the fact that lamin A, but not lamin B lined all three forms of nuclear invaginations, I decided to examine whether similar selectivity of targeting could be observed with respect to the

components of the LINC complex, with particular reference to nuclear invaginations.

Using lamin A labelling (red) to identify nuclear invaginations, it was shown in the 3D reconstruction of a lamin A-nesprin-1 double labelled PASMC (Figure 4.7Ai) that the labelling for nesprin-1 (magenta), a trans-outer nuclear membrane protein, was widely distributed across the entire surface of the NE, including the nuclear invaginations. It was notable that, however, unlike lamin A labelling which covers the entire inner nuclear surface albeit with variable density, nesprin-1 labelling was punctate throughout, and these puncta of nesprin-1 can be clearly viewed following the increase of detection threshold and the application of a digital skin to the 3D reconstruction (Figure 4.7 Ai). Focusing on nuclear invaginations, the middle section of the 3D reconstruction was cropped out (Figure 4.7 Aii, left panel), and the region containing a blind invagination (indicated with B) and a trans-nuclear invagination (indicated with T) was magnified (Figure 4.7 Aii, middle panel). The puncta of nesprin-1 spanned both the blind and trans-nuclear invaginations in a manner that wraps around the lamin A labelling. To investigate the possible localisation of the nesprin-1-lamin A protein complex, the colocalisation of the two was calculated using the Imaris software, and showed in yellow (Figure 4.7 Aii, right panel). The punctate nature of nesprin-1 labelling was most evident when examining regions of lamin-nesprin colocalisation, and particularly so along the length of the transnuclear and blind nuclear invaginations. The colocalisation in yellow revealed well-defined puncta along the length of all lamin A positive structures in every cell thus far studied (n=3).

The distribution of SUN2, the inner nuclear membrane protein that combines with nesprin-1 to form the LINC complex, was also studied. As shown in Figure 4.7 B, a PASMC was co-labelled by SUN 2 and lamin A. The 3D reconstruction of the nucleus is shown in the left panel, and the structures identified by lamin A density were revealed by increasing the threshold, which was followed by the application of the digital skin (right panel). SUN2 (green), like lamin A (red), covers almost the entire inner nuclear surface, exhibiting little or no evidence of the type of punctate labelling seen for nesprin-1 (n=7). By cropping out the middle section of the 3D model (Figure 4.7 Bii, left panel) and zooming into the superficial invagination identified (Figure 4.7 Bii, middle panel), it seems that SUN 2 lines the entire superficial invagination, which is confirmed by the colocalisation analysis of SUN2 and lamin A shown in yellow

(right panel). In fact, SUN2 lines some nuclear invaginations but are absent from others (Appendix 2 Table 4.3).

In support of this view, co-labelling for SUN2 and nesprin-1 was conducted to identify the possible localisation of the LINC complex. Figure 4.7 Ci (left panel) shows the 3D reconstruction of a co-labelled nucleus, in which nesprin-1 is displayed in magenta and SUN2 in green. Similarly, a digital skin was applied to the high threshold 3D reconstruction to illustrate structures (Figure 4.7 Ci, right panel). The rotated middle section of the 3D model and the magnified image clearly shows that a trans-nuclear invagination was selectively lined by nesprin-1 but not SUN 2 (Figure 4.7 Cii, left and middle panel). This is confirmed by the high magnification illustration with regions of colocalisation (yellow) between nesprin-1 and SUN2, the colocalisation was restricted to the periphery of the INM, evident at the entry point to nuclear invaginations but thereafter being entirely absent from the deeper, intranuclear sections of trans-nuclear invaginations. On average, 50±3.5% of nesprin-1 labelling colocalise with SUN2 labelling in PASMCs, and the Pearson's correlation coefficient is only 0.36±0.06 (n=3, Appendix 2 Table 4.4). This shows that the LINC complex formed by nesprin-1 and SUN2 are restricted to the periphery of the INM and to some nuclear invaginations, where nesprin-1 might serve to connect the cytoplasmic structures such as actin filaments to the peripheral NE and superficial invaginations, and perhaps the entry vestibule to trans-nuclear invaginations for mechano-sensing or nuclear positioning (Jorgens et al., 2017). By contrast punctate regions of nesprin-1 association with lamin-A are evident along the full length of blind and trans-nuclear invaginations, and may thus support the bridging between the nucleoplasm (chromatins) to the cytoplasm directly through the lamin associated domains (LADs) or indirectly by forming NET protein complexes with other INM proteins (i.e. emerin and BAF).

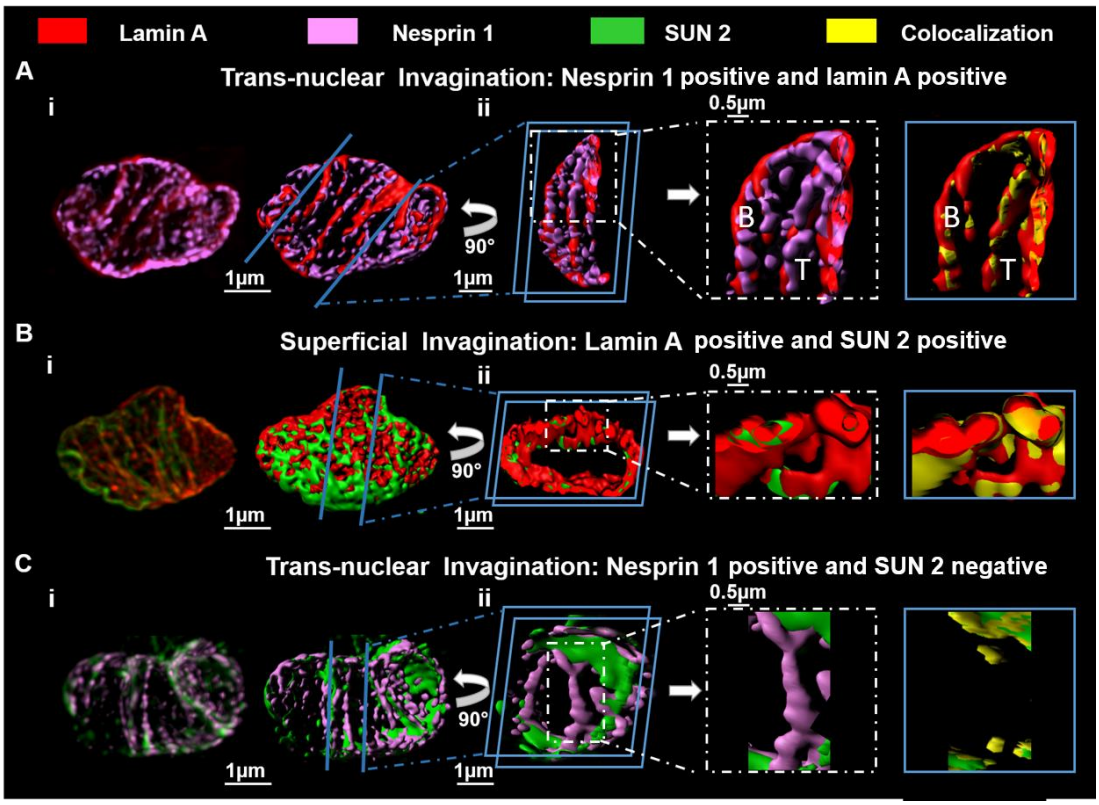

Figure 4.7 Components of the LINC complex are selectively targeted to nuclear invaginations

(A) Nucleus of a PASMC is labelled for lamin A (red) and Nesprin-1 (pink, i, left), and reconstructed into a 3D model of the nucleus (i, right panel), sectioned (ii, left panel) and displayed at higher magnification (ii, middle panel) shows nesprin-1 (magenta) and regions in which nesprin-1 colocalises (yellow) with lamin A (ii, right hand panel).

(B) As for A, but labelled for lamin A (red) and SUN 2 (green).

(C) As for A, but labelled for nesprin-1 (magenta) and SUN 2 (green).

In this respect, one must bear in mind that the selective positioning of the LINC complex was conferred by SUN2 rather than nesprin-1. This is significant because the antibody used for identifying nesprin-1 can recognize two isoforms of this NET, namely giant nesprin-1 and the small isoform nesprin-1α. Giant nesprin-1 is dominant on the ONM and here it is thought to interact with SUN domain proteins to form LINC complexes that cross the nuclear membranes (Sosa et al., 2012). By contrast, nesprin-1α sits on the INM, which is significant because nesprin-1α not only co-

associates lamin A (Mislow et al., 2002a) but has also been shown to associate with nuclear targeted RyR1 (Pare et al., 2005a, Pare et al., 2005b). Therefore, instead of forming the classical LINC complex within nuclear invaginations, it is feasible that nesprin-1 α may form distinct protein complexes with lamin A and RyR1 along the length of the nuclear invaginations, providing for chromatin attachment points that may be modulated in some way by Ca^{2+} flux across the ONM via RyR1.

4.2.1.4 Emerin is present at all lamin A positive nuclear invaginations, but also identifies lamin A negative invaginations.

In PASMCs it would appear that the LINC complex, comprising nesprin, SUN2 and lamin A, seems to be part of the machinery that bridges the gap between the cytoplasm and the nucleoplasm at the periphery of the INM, where it likely provides chromatin attachment points for repression of gene expression. By contrast, our data suggest that co-association of nesprin-1 with lamin A, but not SUN2, may support chromatin attachment within the trans-nuclear nuclear invaginations. I therefore investigated the possibility that nesprin-1 and lamin A might co-associate in trans-nuclear nuclear invaginations with emerin, a LEM domain-containing protein and an integral component of the INM (Demmerle et al., 2013, Zhang et al., 2005) which has previously been shown to interact with both nesprin-1α and lamin A (Mislow et al., 2002a). It is important to note in this respect that lamin A and emerin are known to support chromatin attachment through different mechanisms.

Figure 4.8 A, B& C show three acutely isolated PASMCs that were co-labelled for lamin A (red) and emerin (cyan). The 3D reconstructions of the three labelled nuclei are displayed in the left panels of Figure 4.8 Ai, Bi&Ci, whereas the right panels exhibit the high threshold 3D reconstruction coated with the digital skin. The middle sections of the three 3D models were cropped out and rotated to display the interior of the nuclei (Figure 4.8 Aii, Bii&Cii, left panel), and the regions containing examples of a ridge (Figure 4.8 Aii, middle panel), or trans-nuclear invaginations (Figure 4.8 Bii&Cii, middle panel) were magnified. The colocalisation between emerin and lamin A labelling was calculated and shown in yellow on top of the lamin A labelling (Figure 4.8 Aii, Bii&Cii, right panel). It can be observed in all three cells that the emerin labelling (cyan) extended across most of the INM identified by lamin A labelling (red), including the peripheral ridges and clefts (Figure 4.8 A, Figure 4.9). Most importantly

in the context of my investigations, labelling for emerin was present along the entire length of all 3 types of nuclear invaginations identified by lamin A (Figure 4.8 C, Figure 4.9 Ai). Moreover, as reported in section 4.2.1.1 for lamin A labelled invagination, the diameters of the nuclear invaginations identified by emerin labelling were variable both between such structures and along the length of a nuclear invagination, and this variability was also evident in co-labelled cells (Figure 4.8 Bii&Cii, left and middle panels). While not strictly punctate in nature at our working resolution, higher magnification images of emerin-positive nuclear invaginations (Figure 4.8 Cii, middle panel) show that the emerin appears to “wrap around” lamin A positive invaginations without completely covering the inner surface of lamin A labelling, i.e. while less obvious emerin labelling of nuclear invaginations exhibits non-uniformity too. This suggests that emerin and lamin A do not always co-associate along the length of a nuclear invaginations.

Consistent with this view, I also identified emerin-positive nuclear invaginations that could be sub-categorised into two groups, namely the lamin A positive (Figure 4.8 Cii) and lamin A negative (Figure 4.8 Bii) invaginations. This is evident when showing the lamin A-emerin colocalisation sites along the given nuclear invaginations. I have identified lamin A positive invaginations with the full length of the invagination covered by the colocalisation sites in yellow (Figure 4.8 Cii), and lamin A negative invaginations within which the colocalisation sites were absent from the main body of the trans-nuclear invagination (Figure 4.8 Bii).

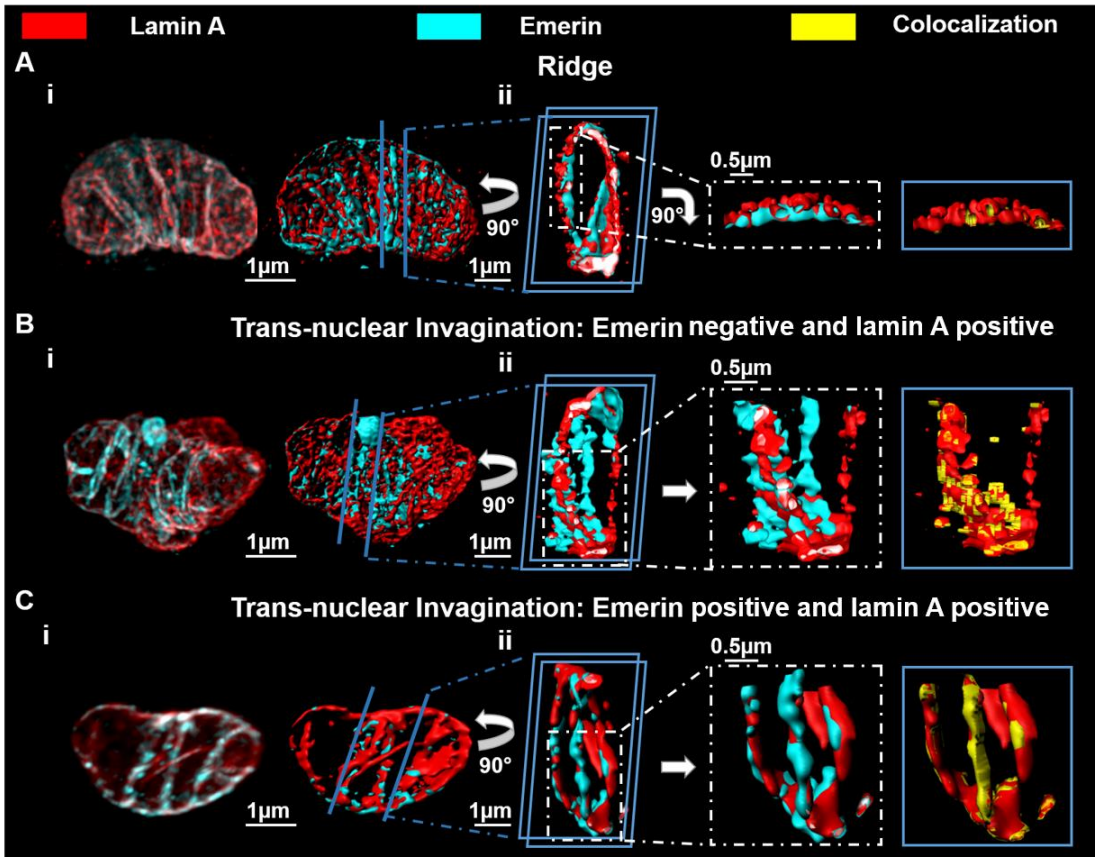

Figure 4.8 Labelling for emerin reveals that there are lamin A positive and negative invaginations.

(A) PASMC nucleus labelled for lamin A (red) and emerin (cyan, i, left panel), and 3D reconstruction of the nucleus (i, right panel), which was sectioned (ii, left panel) to show a peripheral ridge at higher magnification (ii, middle panel) with emerin (blue) and colocalisation (yellow) of emerin with lamin A (ii, right hand panel).

(B) As for A. but showing emerin labelling lamin A negative nuclear invaginations.

(C) As for A. but showing emerin labelling lamin A positive nuclear invaginations.

The fact that emerin identifies both lamin A positive and negative nuclear invaginations received the strongest possible confirmation through cross-comparison of the number of lamin A and emerin positive structures in co-labelled PASMCs.

Due to the fact that I was trying to label two INM proteins in a very narrow space

(nuclear invagination), competition for space may occur between antibodies (primary and/or secondary). To exclude the possibility of such effects, the antibodies were applied in different orders, either by applying one primary/secondary antibody after the other and vice versa, or by applying all primary antibodies mixed together at once. Irrespective of the approach used and across all co-labelled PASMCs (n=32), no emerin negative and lamin A positive nuclear invagination were identified, regardless of the order of antibody application. By contrast, I consistently identified two populations of emerin-positive nuclear invaginations, one being co-lablled for lamin A while the other was not.

Based on this finding, I plotted the number of structures per cell identified by emerin alone (Figure 4.9 Ai) or emerin-lamin A colocalisation (Figure 4.9 Aii) in the cells that exhibited nuclear invaginations. The number of total invaginations, trans-nuclear invaginations, superficial invaginations, blind invaginations, ridges and clefts are shown in black, red, orange, blue, green and grey respectively. Interestingly, in these cells lamin A colocalised with emerin at all the peripheral structures (Figure 4.9 Ai&ii), suggesting that the observed selectivity of labelling for emerin alone occurs at the nuclear invaginations but not the peripheral ridges (green) or clefts (grey). Moreover, the number of trans-nuclear invaginations (red), blind invaginations (red), superficial invaginations (blue) per cell were sorted based on the values and plotted in Figure 4.9 B, either identified by emerin alone (Figure 4.9 Bi) or emerin-lamin A colocalisation (Figure 4.9 Bii). Both the trans-nuclear and superficial invaginations could be identified as being positive for emerin alone or exhibiting emerin-lamin colocalisation (Figure 4.9 B), while it remains inconclusive for blind invaginations due to the limited sample size. In short, emerin positive lamin A negative nuclear invaginations were identified, while peripheral ridges and clefts were always positive for lamin A labelling.

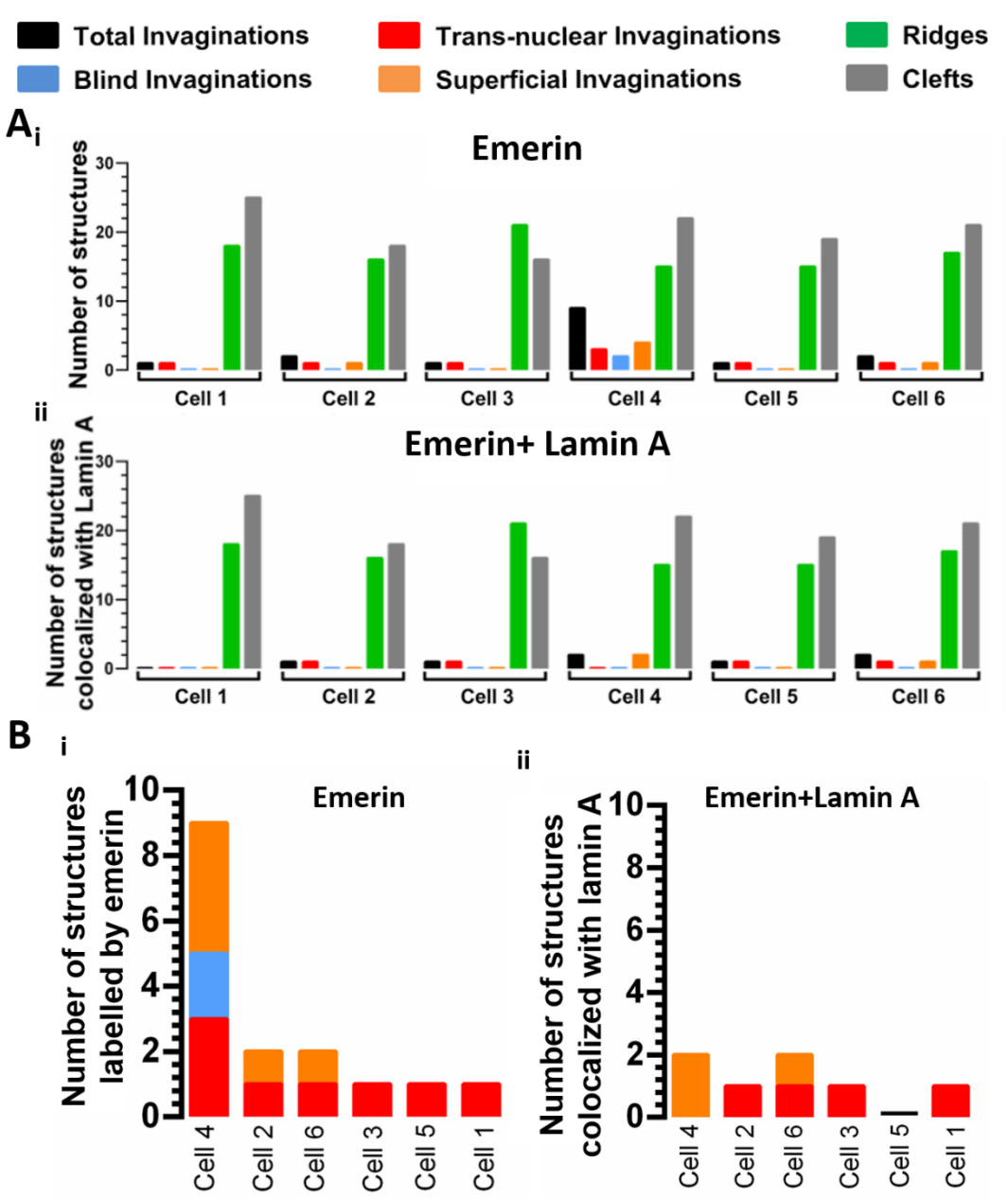

Figure 4.9 The number of emerin-positive nuclear invaginations varies between cells.

(Ai) Number of structures identified by emerin labelling per cell. (ii) Number of emerin identified structures colcalised with lamin A in each cell. Total nuclear invaginations (black), trans-nuclear invaginations (red), blind invaginations (blue), superficial invaginations (orange), ridges (green) or clefts (grey) are distinguished by colour, n=6.

(B) As for (A), but showing only the number of different forms of nuclear invaginations per cell, n=6.

Given the fact that emerin also identifies lamin A negative nuclear invaginations, emerin may serve as a better indicator for nuclear invaginations. To test whether emerin identifies more structures, the number of emerin labelled structures per cell (Figure 4.10 D) was plotted. In this instance the result was very similar to the number of lamin A identified structures. On average, 2.9±0.5 nuclear invaginations were identified in each cell with 0.9±0.2 trans-nuclear invaginations, 1.6±0.3 blind invaginations and 0.4±0.15 superficial invaginations per cell (n=22), these numbers are higher but not significantly different from those of the lamin A labelled nuclear invaginations (p=0.9619 for trans-nuclear invaginations, p=0.6842 for blind invaginations, and p=0.8267 for superficial invaginations). 77% of all cells labelled for emerin harboured nuclear invaginations whereas 70% of the lamin A labelled PASMCs displayed nuclear invaginations. Together these findings suggest that while emerin positive lamin A negative nuclear invaginations may well exist, there is a much lower probability of formation of this type of nuclear invagination.

Moreover, the inter-cell variability of structures observed with lamin A labelling was also confirmed for emerin labelling (Figure 4.10 A). The number of structures per cell labelled by emerin was plotted with the trans-nuclear invaginations in red, blind invaginations in blue, superficial invaginations in orange, ridges in green, and clefts in grey. Once again, the number of nuclear invaginations did not correlate with the number of peripheral structures, which was confirmed by the linear regression analysis (R^2=0.05368, y=-0.6420*x+33.41, Appendix 2 Table 4.5). This suggests that, consistent with the lamin A labelled structures, although both the nuclear invaginations and ridges/clefts were derived from the NE, they are formed independently. As Figure 4.10 B shows, the number of all three forms of emerin-positive nuclear invaginations (trans-nuclear invaginations in red, blind invaginations in blue, superficial invaginations in orange) was variable, ranging from 9 to 0 in the cells studied here. The number of each form of nuclear invagination that appeared in one cell seemed to be random, and the non-linear relationship between each forms of nuclear invaginations was confirmed by the linear regression analysis (Appendix 2 Table 4.5). Moreover, as Figure 4.10 C shows, the cells that displayed high numbers of ridges (green) did not necessarily harbor more clefts (grey), which supports the conclusion drawn based on lamin A identified structures that the formation of the peripheral ridges and clefts was regulated independently (R^2=0.001007,

y=0.04501*x+17.11, Appendix 2 Table 4.5).

I conclude that the numbers of all the structures identified by either lamin A or emerin densities in PASMCs showed a high degree of plasticity, and that the presence or absence of one structure did not correlate with the presence or absence of any others.

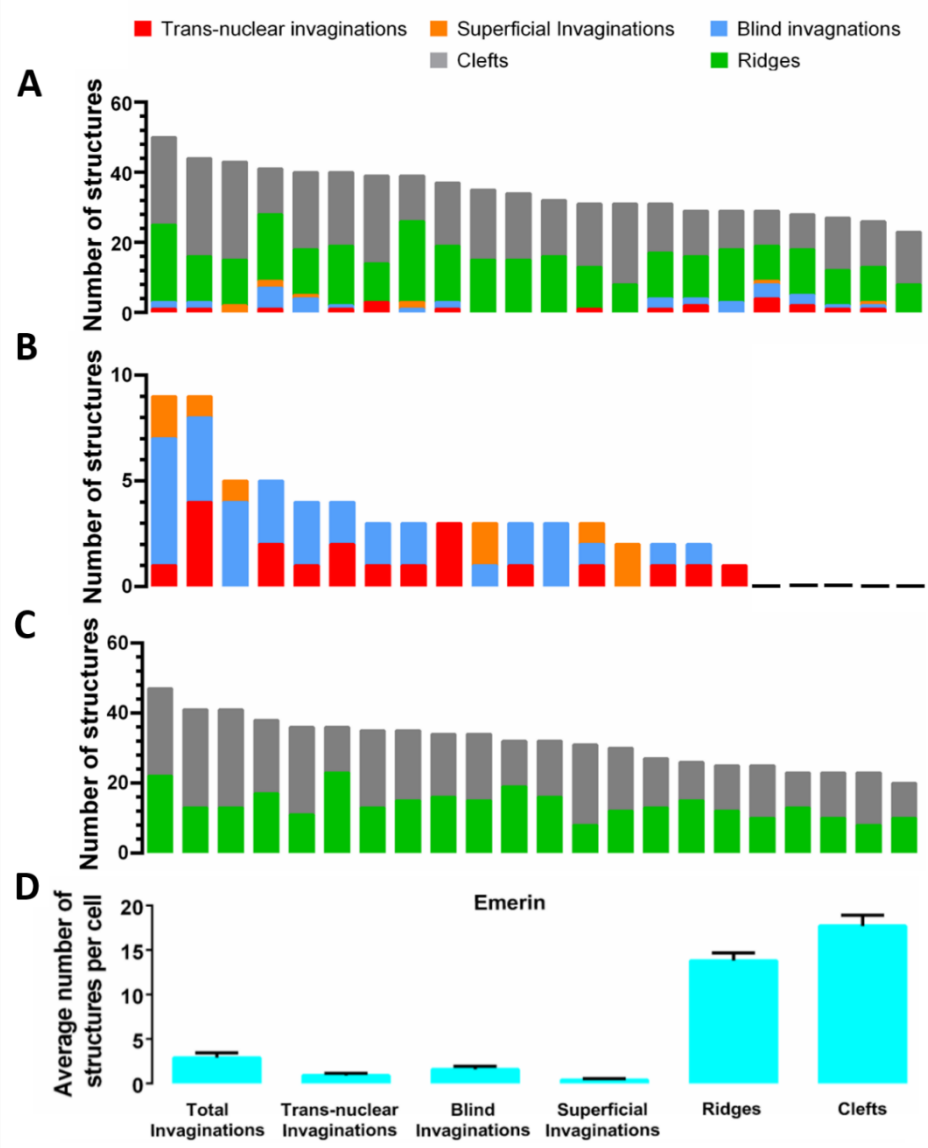

Figure 4.10 Emerin positive nuclear invaginations vary in number between cells, indicating a high degree of plasticity.

(A) The number of structures identified by emerin in each cell is shown in the stacked bar chart, with the clefts in grey, ridges in green, trans-nuclear invaginations in red, blind invaginations in blue, superficial invaginations in orange. Each bar represents a

cell, n=22.

(B) The number of structures identified by emerin in each cell is shown in the stacked bar chart, with the trans-nuclear invaginations in red, blind invaginations in blue, superficial invaginations in orange. Each bar represents a cell, cells without invaginations were indicated by a black line, n=22.

(C) The number of structures identified by emerin in each cell is shown in the stacked bar chart, with the clefts in grey and ridges in green, n=22.

(D) Average numbers of emerin-positive trans-nuclear invaginations, blind invaginations, superficial invaginations, ridges and clefts per cell are shown in the bar chart (mean±SEM), n=22.

4.2.2 The inner nuclear membrane of nuclear invaginations is lined by puncta of chromatin-anchoring protein complexes constructed by either lamin A or emerin

In section 4.2.1.3 it was illustrated that emerin identified two sub-sets of nuclear invaginations, one with and one without lamin A. More importantly, this selective targeting was observed only in nuclear invaginations while all the peripheral ridges and clefts were lamin A and emerin positive, suggesting that it is very likely that this selective targeting is associated with the function of nuclear invaginations. In fact, either lamin A or emerin may construct a NET protein complex capable of directing chromatin attachment. Lamin A can promote transcriptional suppression by binding to the lamina-associated domain (LAD) of heterochromatin (Burke and Stewart, 2013), in a manner facilitated by co-association with histones such as H3K9me2/3(Harr et al., 2015). By contrast, emerin has been shown to provide discrete chromatin attachment points along the surface of the INM through its co-association with BAF (barrier to auto-integration factor)(Berk et al., 2014, Cai et al., 2001, Lee et al., 2001), which binds DNA (Zheng et al., 2000) and may thus either repress or enhance gene expression (Takama et al., 2013, Cox et al., 2011). Given the above, I decided to investigate the possibility that different chromatin anchoring protein complexes might be formed by either emerin or lamin A.

4.2.2.1 Puncta of emerin-BAF complexes line nuclear invaginations, but were less commonly seen on peripheral ridges and clefts.

As emerin labelling can effectively identify all the structures I aimed to study, PAMSCs were co-labelled with emerin and BAF to investigate the distribution of the emerin-BAF complexes in relation to the nuclear structures identified above. Figure 4.11 A, B, C &D show 4 emerin and BAF co-labelled acutely isolated PASMCs, the colocalisation between the two labelling was calculated, and the 3D reconstructions of the four nuclei labelled by emerin (cyan) and the colocalisation (yellow) were shown in Figure 4.11 Ai, Bi, Ci&Di. To illustrate the structures identified by emerin density, the detection threshold was raised, followed by the application of the digital skin (Figure 4.11 Aii, Bii, Cii&Dii, left panels). The 3D models of nuclei defined by emerin labelling in Figure 4.11 Aii, Bii, Cii were sectioned and rotated to reveal the nuclear invaginations (middle panels). Interestingly, the colocalisation between emerin and BAF (yellow) forms puncta along the length of all three categories of nuclear invaginations. The right panel of Figure 4.11 Aii shows two trans-nuclear invaginations in higher magnification, puncta of colocalisation were observed on both invaginations, albeit quite separated. In contrast, the right panel of Figure 4.11 Bii shows two trans-nuclear invaginations that were fully covered by the puncta of colocalisation. These puncta were of variable sizes, and were separated by several hundreds of nanometers or less.

The right panel of Figure 4.11 Cii displays a section of the nucleus that harboured both superficial and blind invaginations. At a higher magnification, puncta of colocalisation can be clearly viewed on the superficial invaginations (indicated with S). More interestingly, it also shows a network of blind invaginations (indicated with B), with one major branch decorated by the puncta whereas the branch to the left of it was entirely free of such puncta. This suggests that these puncta targeted to the inner membrane of nuclear invaginations appear, in an invagination-dependent manner, to be either very abundant or relatively isolated, sometimes even absent. On average, they were separated from adjacent regions of BAF colocalisation by 495.5±62nm, with the diameters of these puncta range from ~150nm to 600 nm (Appendix 2 Table 4.6).

Figure 4.11 D focused on the peripheral ridges and clefts. One example cleft was sectioned and rotated as shown in Figure 4.11 Dii (middle and right panel), and no puncta of colocalisation were observed on this cleft. The 3D model of the same cell was sliced through the middle, and the top-half of the model was flipped (Figure 4.11 Diii). With the application of the digital skin, half of the NE was clearly visualized, which displayed various ridges (Figure 4.11 Div). This piece of NE is shown in a high magnification (Figure 4.11 Div, right panel), and it was evident that only some of the ridges, or certain branches of the branched ridges harboured the puncta of colocalisation.

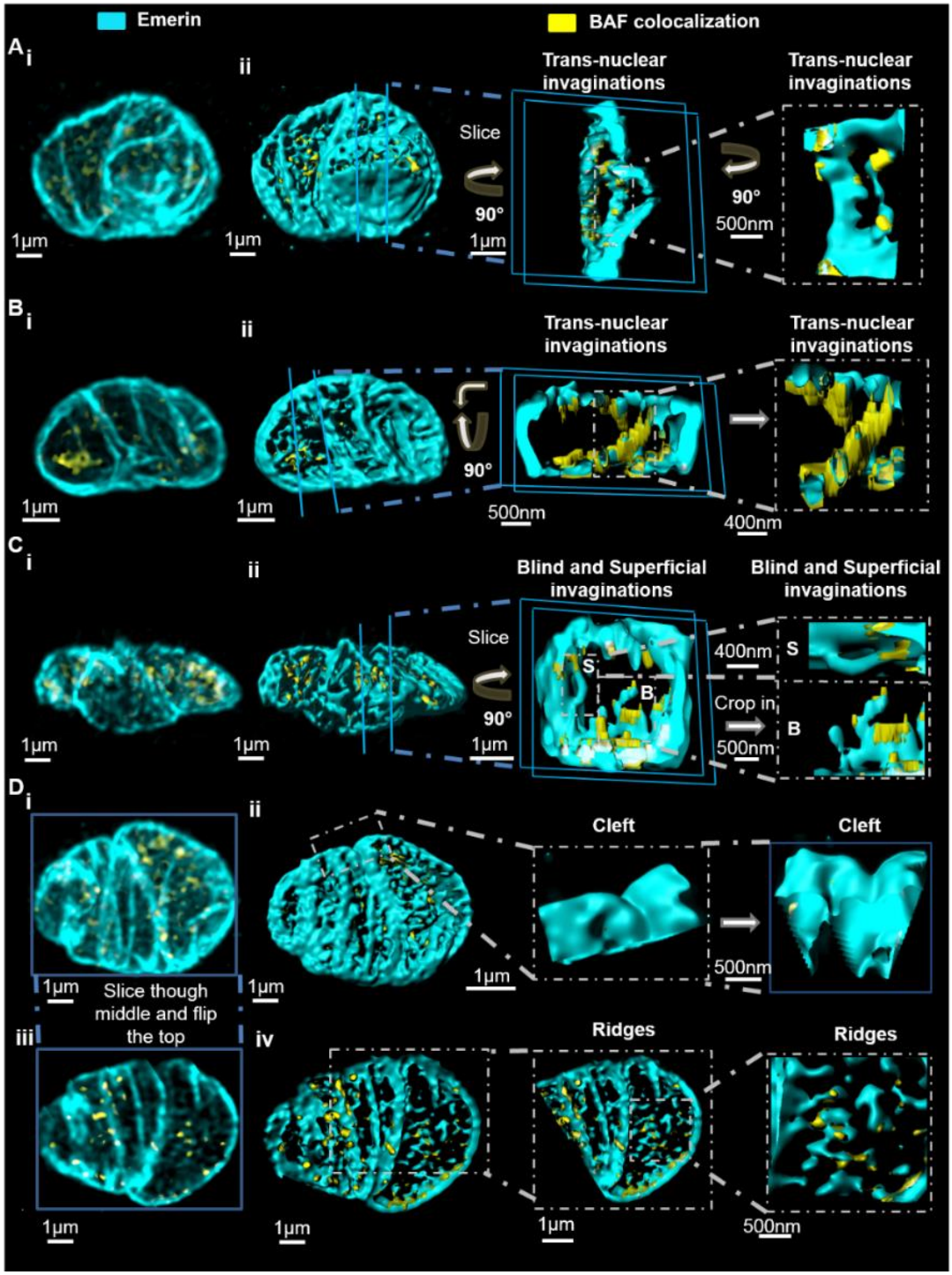

Figure 4.11 BAF and emerin preferentially co-localise on nuclear invaginations.

(Ai) 3D reconstruction of deconvolved Z stacks scanning through the nucleus of a pulmonary arterial smooth muscle cell labelled for emerin (cyan) and showing regions of colocalisation with BAF (yellow). (ii) From left to right, same 3D image as shown in (i) but following application of blending (Imaris image analysis software), and a transverse section through, rotated to identify a trans-nuclear invagination and a further section with magnification that shows punctate regions of BAF colocalisation on this structure.

(Bi-ii) As in (A) but showing a trans-nuclear invagination which exhibits BAF colocalisation across its entire surface.

(Ci-ii) As in (A), but showing BAF colocalisation on the surface of emerin labelled blind and superficial invaginations.

(Di-ii) As in (A), but showing BAF co-localization on the surface of an emerin labelled cleft. (iii-iv) Slice through the middle of the cell showed in (Di) and flip the top to reveal the top-half of the cell, showing BAF colocalisation on the surface of emerin labelled ridges.

The observation above seems to suggest that the emerin-BAF colocalisation preferentially targets nuclear invaginations compared to the peripheral structures. To test this, I plotted the number of structures per cell identified by emerin alone (Figure 4.12 Ai) or emerin-BAF colocalisation (Figure 4.12 Aii). The bar chart shows that a good number of ridges and clefts with no emerin-BAF colocalisation were identified in every cell studied (Figure 4.12 Bi&ii), whereas the majority of nuclear invaginations harboured the emerin-BAF colocalisation, and in some cells (i.e cell5, cell6) all the nuclear invaginations were positive for such colocalisation. This suggests that the emerin-BAF colocalisation is preferentially found on the INM of nuclear invaginations but not the peripheral structures. This view received support from the bar chart showing the percentage of structures exhibiting emerin-BAF colocalisation (Figure 4.12 C). 81% of all nuclear invaginations harboured sites of emerin-BAF colocalisation. Subdividing these, puncta of emerin-BAF colocalisation were identified along 67% superficial invaginations, 77% blind invaginations and 88% of trans-nuclear invaginations. In contrast, only 41% of the clefts and 63% of the ridges harboured sites of emerin-BAF colocalisation.

To conclude, the emerin-BAF colocalisation sites, which indicates where the chromatin anchoring NET protein complexes may form, were found on the inner membrane of nuclear invaginations in an invagination-dependent manner, they can be either very abundant or relatively isolated, sometimes even absent. However,

compared to the peripheral ridges and clefts, the chromatin anchoring NET protein complexes preferentially target the nuclear invaginations.

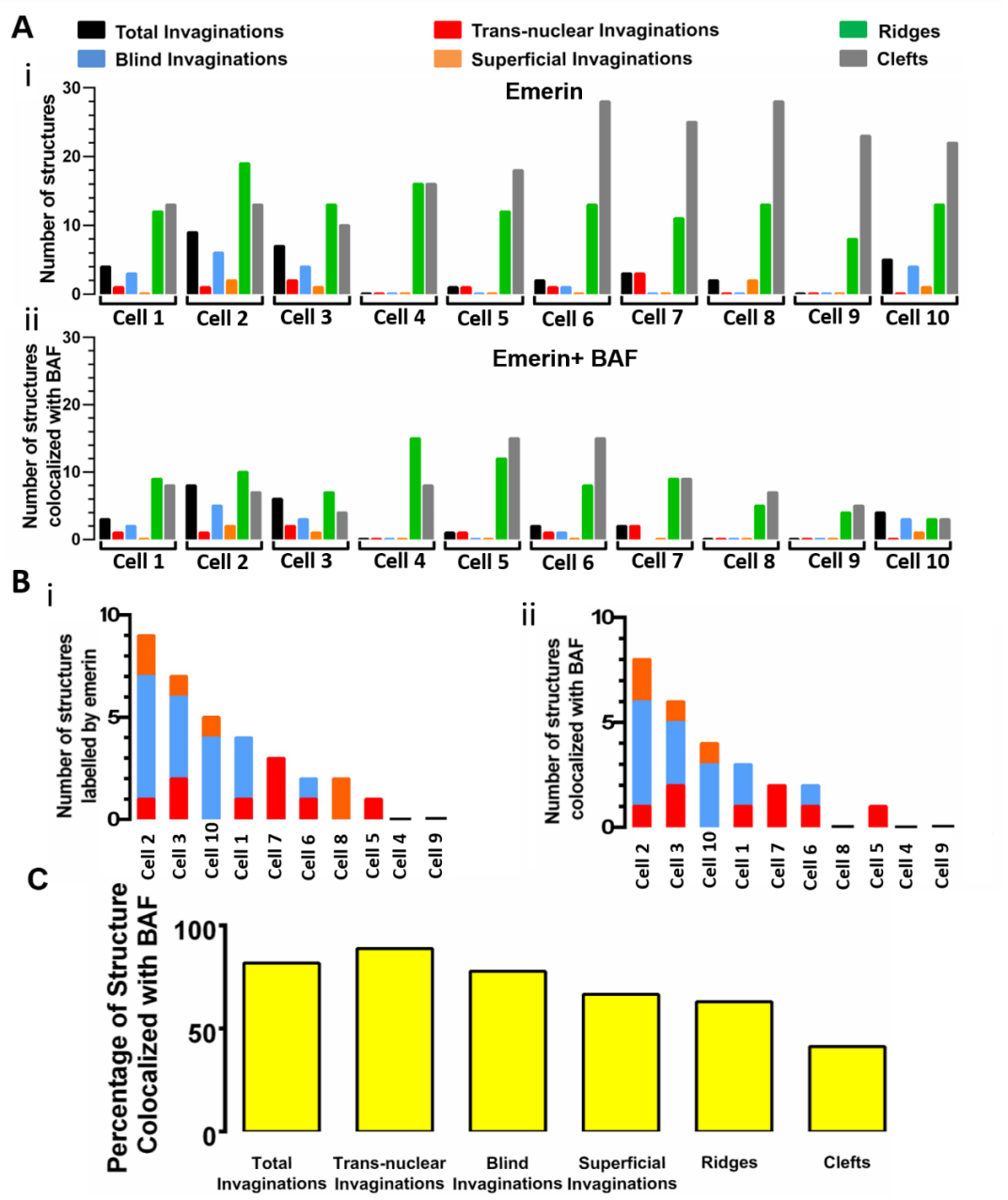

Figure 4.12 The number of BAF and emerin positive structures varies between cells.

(Ai) Number of emerin identified structures in each cell with the clefts in grey, ridges in green, trans-nuclear invaginations in red, blind invaginations in orange, superficial invaginations in blue. (ii) As for (i), but showing number of emerin identified structures per cell that exhibit colocalisation with BAF, n=10.

(B) As for (A), but showing only the counts for nuclear invaginations per cell, n=10

(C) Percentage of emerin identified structures colocalised with BAF, n=10.

4.2.2.2 Puncta of lamin A-H3K9me2 complexes line all types of lamin A positive nuclear membrane structures

I have identified two sub-sets of emerin-positive nuclear invaginations, one being lamin A-positive and one lamin A-negative. This led to the consideration that chromatin attachment might be regulated through distinct mechanisms via emerin or lamin A. Indeed, it is evident that lamin A may promote transcriptional suppression by binding to the LAD of heterochromatin (Burke and Stewart, 2013), in a manner facilitated by co-association with histones such as H3K9me2/3(Harr et al., 2015). Based on this possibility, I investigated the distribution of lamin A-H3K9me2 complexes on the lamin A identified structures.

Similar to section 4.2.2.1, PAMSCs were co-labelled by lamin A and H3K9me2 to investigate the distribution of the chromatin anchoring LADs in relation to the nuclear structures identified above. Figure 4.13 A, B, C &D show 4 lamin A and H3K9me2 co-labelled acutely isolated PASMCs. The colocalisation between the two labelling was calculated, and the 3D reconstructions of the four cells labelled by lamin A (red) and the colocalisation (white) are shown in Figure 4.13 Ai, Bi, Ci&Di. To demonstrate the structures defined by lamin A density, the detection threshold of the lamin A labelling was raised, which was followed by the application of the digital skin (Figure 4.13 Aii, Bii, Cii&Dii, left panels). The 3D models of nuclei in Figure 4.13 Aii, Bii, Cii were sectioned and rotated to reveal the nuclear invaginations (middle panels). Like the emerin-BAF colocalisation, the colocalisation between lamin A and H3K9me2 forms puncta along the length of all three categories of nuclear invaginations. The right panel of Figure 4.13 Aii shows a trans-nuclear invagination at high magnification, which was spanned by separated puncta of colocalisation. In contrast, the right panel of Figure 4.13 Bii shows a trans-nuclear invagination that was fully covered by such colocalisation.

The right panel of Figure 4.13 Cii shows a section of the nucleus that harboured a superficial invagination with a branch being a blind invagination. At a higher magnification, puncta of colocalisation can be clearly viewed on both the superficial invaginations (indicated with S) and the blind invaginations (indicated with B). Not like

the emerin-BAF colocalisation, the lamin A-H3K9me2 colocalisation did not seem to be absent from any nuclear invagination. The diameters of these puncta of lamin A-H3K9me2 colocalisation ranges from ~200 nm to ~600nm, and the separation between puncta was 335.50±46 nm on average (Appendix 2 Table 4.7).

Figure 4.13 D showed the puncta of colocalisation on the peripheral ridges and cleft. One example cleft was sectioned and rotated as shown in Figure 4.13 Dii (middle and right panel). In contrast to the emerin-BAF co-labelled cells, the cleft was fully covered by broad “plaques” of colocalisation. The 3D model of the same cell was sliced through the middle, and the top-half of the model was flipped (Figure 4.13 Diii). With the application of the digital skin, half of the nucleus was clearly visualized, which displayed various ridges, and each of the ridge carried abundant puncta of colocalisation (Figure 4.13 Div). One of the ridges is shown at a high magnification (Figure 4.13 Div, right panel), and it was evident that the entire length of the ridge was covered by the lamin A-H3K9me2 colocalisation.

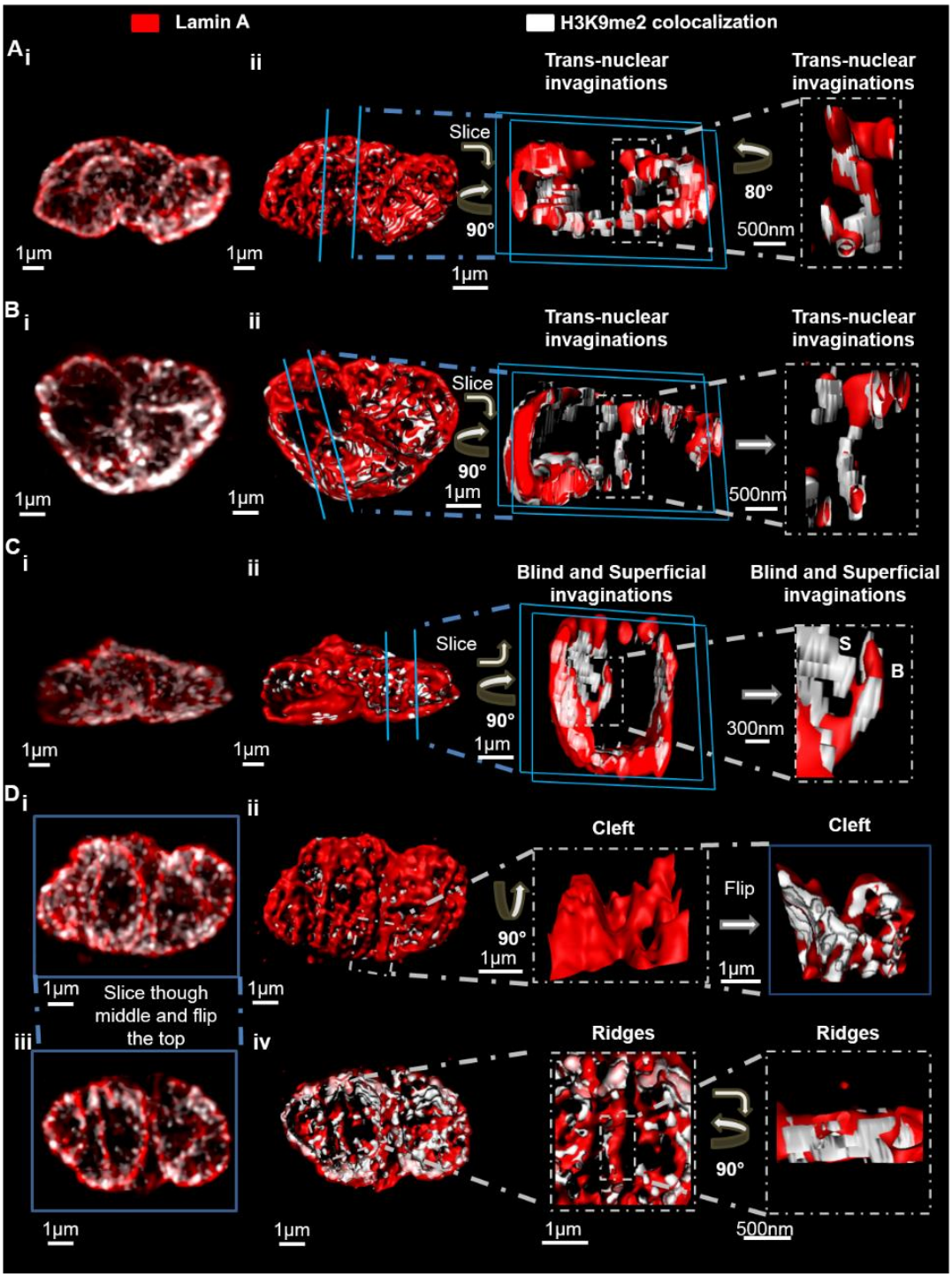

Figure 4.13 The histone mark H3K9me2 and lamin A co-localise at puncta on nuclear invaginations, but regions of colocalisation are most widespread at the periphery of the nucleus.

(Ai) 3D reconstruction of a deconvolved Z stacks through the nucleus of a pulmonary arterial smooth muscle cell labelled for lamin A (red), showing regions of colocalisation with H3K9me2 (white). (ii) From left to right, same 3D image as shown in (i) but following application of blending (Imaris image analysis software), and a transverse section through, rotated to identify a trans-nuclear invagination and a further section

with magnification that shows punctate regions of H3K9me2 colocalisation on this structure.

(Bi-ii) As in (A) but showing a trans-nuclear invagination, which exhibits H3K9me2 colocalisation across its entire surface.

(Ci-ii) As in (A), but showing H3K9me2 colocalisation on the surface of lamin A labelled blind and superficial invaginations.

(Di-ii) As in (A), but showing H3K9me2 colocalisation on the surface of a lamin A labelled cleft. (iii-iv) Slice through the middle of the cell showed in (Di) and flip the top to reveal the top-half of the cell, and shows H3K9me2 co-localisation on the surface of lamin A labelled ridges.

The evidence above seems to suggest that the lamin A-H3K9me2 colocalisation targets all the lamin A defined structures non-selectively. Indeed, I plotted the number of structures per cell identified by lamin A alone (Figure 4.14 Ai) or lamin A-H3K9me2 colocalisation (Figure 4.14 Aii). The result showed that all the peripheral ridges (green) and clefts (grey) in the studied cells displayed the colocalisation. Similarly, the number of nuclear invaginations identified by lamin A alone (Figure 4.14 Bi) or lamin A-H3K9me2 colocalisation (Figure 4.14 Bii) showed that all the trans-nuclear and superficial invaginations displayed the colocalisation sites. Among the 14 cells studied, only one cell (cell 7) exhibited one blind invagination that lacked the colocalisation.

Unlike the emerin-BAF colocalisation that prefers nuclear invaginations compared to peripheral ridges (yellow) and selects for certain nuclear invaginations, the lamin A-H3K9me2 colocalisation non-differentially flags almost all the structure thus far studied (white, Figure 4.14 C), which is significantly different from emerin-BAF colocalissation as the Chi-square tests showed ($p=0.0189$) In short, there appeared to be a large and variable number of BAF negative, emerin positive structures in all cells studied, indicative of great plasticity of association in comparison to the H3K9me2 negative, lamin A positive structures.

Part of the lamin A related immunocytochemistry mentioned in this Chapter (i.e. the lamin A-histone mark co-labelling and part of lamin A labelling) was done in

collaboration with Dr. Jorge Navarro-Dorado, who kindly provided technical supports, did part of the immunocytochemistry and confocal imaging.

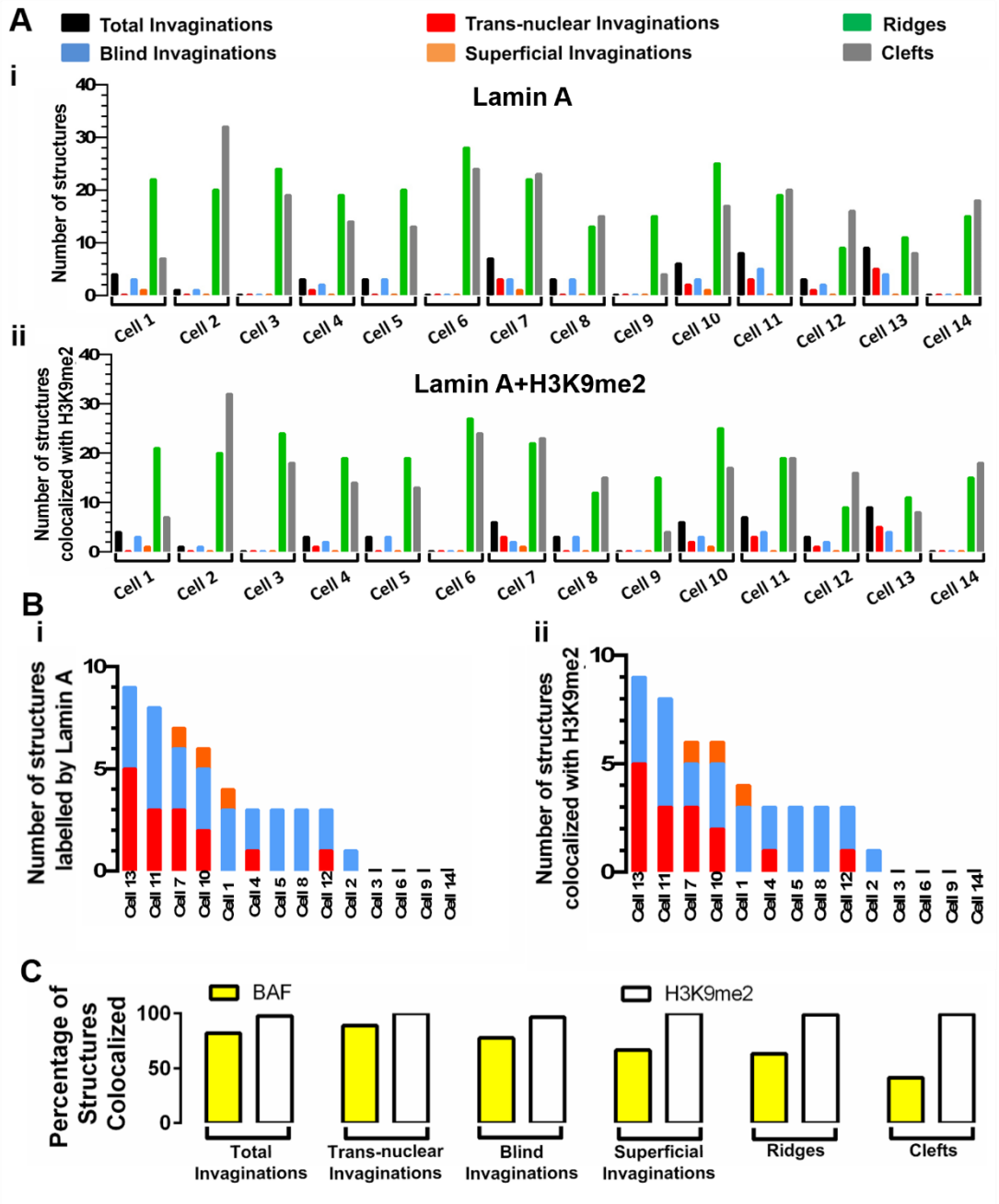

Figure 4.14 H3K9me2 and lamin A colocalisation is widespread

(Ai) Number of lamin A identified structures in each cell with the clefts in grey, ridges in green, trans-nuclear invaginations in red, blind invaginations in orange, superficial invaginations in blue. (ii) As for (i), but showing number of lamin A identified structures per cell that showed colocalisation with H3K9me2, n=14.

(B) As for (A), but showing the counts for nuclear invaginations only, n=14

(C) Percentage of lamin A identified structures colocalised with H3K9me2 (white) compared to that of emerin labelled structures colocalised with BAF, n=14.

4.3 Discussion

4.3.1 Summary of findings

Chapter 4 shows that nuclear invaginations of pulmonary arterial myocytes may provide sites for chromatin attachment and transcriptional regulation. Lamin A and emerin appear to line the inner nuclear surface of these cells, and each may colocalise with nesprin-1 positive puncta. Notably, lamin A was absent from some emerin positive nuclear invaginations. By contrast, lamin B1 is distributed only at the periphery of the INM, and is absent from all nuclear invaginations.

Intriguingly, a subpopulation of nuclear invaginations harboured punctate regions of colocalisation between lamin A and the suppressive heterochromatin mark H3K9me2. Moreover, emerin-positive invaginations harboured puncta of BAF colocalisation and thus may serve as an alternative pathway to the regulation of gene expression. In each case, the distances of separation between these chromatin anchoring puncta were in the range of 300-400 nm, which may be significant in terms of the cells capacity to independently regulate such associations. In short, nuclear invaginations may form a trans-nuclear network within which nano-patterning of chromatin anchoring protein complexes may support stochastic modulation of transcriptional suppressors.

4.3.2 Lamin A, but not lamin B1, lines the nuclear invaginations.

By their higher densities of labelling for lamin A, I defined a number of nuclear membrane structures. Most importantly, blind, superficial and trans-nuclear invaginations. Consistent with early studies (Broers et al., 2006, Fricker et al., 1997b), the number of nuclear invaginations identified within a single pulmonary arterial myocyte was variable and could range from 0 to 17. Therefore, these nuclear invaginations are truly dynamic structures. The trans-nuclear invaginations span the entire nucleoplasm, forming channels that connect the two sides of the nucleus. There are also blind invaginations that are in the shape of blind tubes that project variable distances into the middle of a nucleus. Superficial invaginations represent a distinct type, that form short bridges that span short distances of the nucleoplasm and connect to the same side of the nucleus from which they arise. Blind and trans-nuclear invaginations have been described previously (Fricker et al., 1997b, Legartova et al., 2014) but to my knowledge the superficial invaginations have not been presented as

a unique category.

I also identified, by density of lamin A labelling, large numbers of ridges and clefts at the periphery of the nucleus. These structures were very abundant but have not been extensively studied in the literature. However, previous studies may have considered nuclear infoldings (which form clefts) as a form of the nuclear invaginations (Wittmann et al., 2009). Moreover, it seems plausible that the deep Y shaped ridges may confer "nuclear infoldings" that demarcate small junctional spaces that cannot be resolved by confocal microscopy. The tubular and branched ridges described here have not been characterized previously, and these too may, by virtue of their high density of lamin A binding and the fact that they harbour lamin A-H3K9me2 association sites, represent sites of active regulation of chromatin attachment via lamin associated domains, but further investigation is required before any conclusion can be made.

That lamin B1 lines the entire periphery of the nuclei but strategically avoids all the nuclear invaginations, provides new insights into cell-specific organization of the nuclear lamina. This is evident from the fact that lamin B1 positive nuclear invaginations have been identified in other cell types, such as embryonic stem cells (Luo et al., 2009). In acutely isolated PASMCs, however, nuclear invaginations were lined by lamin A but not by lamin B1, whereas peripheral ridges and clefts were labelled for both. This piece of evidence strongly suggests that the nuclear invaginations are not simply an extension of the NE. Instead, they appear to be sophisticatedly designed structures that are selectively lined by chosen NET proteins, and they likely underpin region-specific functions.

4.3.3 NET proteins are selectively targeted to nuclear invaginations, providing nanopatterning for the regulation of chromatin attachment.

Lamin A is associated with multiple NET proteins, and may form NET protein complexes that link the nucleoplasm to the cytoplasm. Following this lead, I studied the distribution of a variety of NET proteins. Immunofluorescence labelling against nesprin-1 showed that this NET protein lines all the lamin A identified structures. It is important to note, however, that the antibodies used here do not discriminate between giant nesprin-1 and nesprin-1α. These proteins differ in terms of their size and nature

of association with the nuclear envelope. Nesprin-1α is a small isoform (131 kDa) of nesprin-1 that has been identified as an inner nuclear membrane protein, it has been shown to interact with lamin A/C (Mislow et al., 2002b). The expression of nesprin-1α had been reported in smooth muscle cells, and it was proposed that the nesprin-1α antiparallel dimers interact with both lamin A and emerin, serving as a scaffold at the inner nuclear membrane (Mislow et al., 2002a). Nesprin-1 giant, as the name suggests, is a ~1000kDa protein that localises to the ONM, and its expression has been confirmed in vascular smooth muscle cells (Duong et al., 2014). It forms the LINC complex with SUN domain proteins, which is responsible for mechanotransduction (Anno et al., 2012, Kim et al., 2015). For example, deletion of nesprin-1 altered nuclei positioning, shape, and the expression of biomechanical response genes upon mechanical stimulation (Banerjee et al., 2014).

As mentioned previously, SUN 2 was present in the superficial invaginations and the entry point of trans-nuclear invaginations identified. Due to the limited sample size, I would not assert that SUN2 only targets to the superficial invaginations and the entry point of trans-nuclear invaginations, but it is clear that for some reason the distribution of the LINC complex formed by nesprin-1 and SUN2 might be restricted to some nuclear invaginations or certain sites along the length of a nuclear invagination. They perhaps only appear at where the functional LINC complex (i.e. mechanotransduction) is required. However, nesprin-1α was shown to co-associate with emerin and lamin A as mentioned (Mislow et al., 2002), and it has also been shown to associate with RyR1 at the nuclear membrane (Pare et al., 2005a; Pare et al., 2005b). Given that my data show that nesprin-1 colocalises with lamin A on the nuclear invaginations, this raises the possibility that the RyR1-nesprin-1α-lamin A associations occur within nuclear invaginations.

All types of structure defined by relatively high densities of lamin A labelling were also identified by dense labelling of emerin, which appears to line the entire inner surface of the INM. Emerin may also form protein complexes with nesprin-1α (Mislow et al., 2002), which links to RyR1(Pare et al., 2005a; Pare et al., 2005b). Moreover, emerin can provide discrete chromatin attachment points along the surface of the INM through its co-association with BAF (Berk et al., 2014; Cai et al., 2001; Lee et al., 2001). It was evident, however, that there were two subpopulations of emerin-positive

invaginations, those that were positive and those that were negative for lamin A. In short, the molecular complexes that underpin chromatin attachment within different nuclear invaginations are heterogeneous in nature.

4.3.4 The inner nuclear membrane of nuclear invaginations is lined by puncta of chromatin-anchoring protein complexes.

Co-labelling for lamin A and H3K9me2, or emerin and BAF confirmed that chromatin anchoring NET protein complexes are formed along the length of nuclear invaginations. In fact, it was shown that sites of nuclear invaginations often displayed electron-dense heterochromatin in close proximity to the inner nuclear membrane (Jorgens et al., 2017). More than 90% of nuclear structures defined by dense labelling for lamin A exhibited well-defined regions of colocalisation with H3K9me2, including blind, superficial and trans-nuclear invaginations. Nuclear invaginations were either entirely covered or harboured small discrete puncta of colocalisation with H3K9me2 (~500 nm in diameter) that were generally separated by 300 nm. In short, while the numbers of lamin A positive nuclear invaginations per cell varied markedly, wherever they appeared they harboured at least one site of H3K9me2 co-localisation. Peripheral ridges and clefts also exhibited relatively large, broad “plaques” of co-labelling for H3K9me2 of the order of up to several micrometers across. These observations are significant because lamin A may facilitate transcriptional suppression by binding to the LADs of heterochromatin (Burke and Stewart, 2013), anchoring it to the IMN. LADs have been considered as repressive domains that are enriched in H3K9me2 (Towbin et al., 2012), and the formation of LADs appears to be dependent on H3K9me2/3 (Harr et al., 2015). H3K9me2 is generally considered to be a repressive histone mark. High-resolution profiling of histone methylation in the human genome has identified a modest correlation between H3K9me2 and gene silencing (Barski et al., 2007). However, it is very important to note that H3K9me2 signals were found on both silent and active genes (Barski et al., 2007). In human T cells, H3K9me2 enrichment partially overlapped with active histone signatures upstream of transcriptional starting sites (Smith et al., 2009). It predicted that co-occurrence of epigenetic marks with distinct functions might contribute to the rapid and dynamic regulation of changes in gene expression, and this may as well occur within nuclear invaginations. Consistently with this view the repressive modification H3K9me2 has been shown to spread to enhancers that exhibit transient co-

enrichment with activating modifications such as H3K27ac during epiblast priming in early mouse development (Zylicz et al., 2015). Co-associations with seemingly opposing epigenetic marks at enhancers has been proposed to confer responsiveness and plasticity of cells, allowing instant and dynamic transcriptional regulation in response to transient signals. In short, co-existence of lamin A and H3K9me2 is a hallmark of gene suppression, and suggests that the nuclear invaginations as well as the peripheral ridges and clefts identified here are sites of gene suppression. That this suppression by H3K9me2 may be considered to be instant and dynamic, through co-associations with activating histones, indicates that its target genes may well subject to modulation by intracellular signals such as transmembrane Ca^{2+} flux.

In contrast to the widespread distribution of H3k9me2, the majority of BAF labelling was clearly targeted to nuclear invaginations rather than the perimeter of the nucleus. Moreover, greater inter-cell variability was evident with respect to the number of emerin-positive nuclear invaginations per cell that co-labelled for BAF. This is indicative of greater plasticity of association than observed for lamin A and H3K9me2. Once more this observation may be of yet greater significance given the high level of plasticity exhibited by nuclear invaginations themselves and the gene-specific actions of BAF, which may either repress or activate gene expression (Takama et al., 2013, Cox et al., 2011).

Emerin has been shown to provide discrete chromatin attachment points along the surface of the INM through its co-association with BAF (Berk et al., 2014, Cai et al., 2001, Lee et al., 2001). One early study showed that BAF forms dodecamers that tightly binds double-stranded DNA in a sequence-independent manner (Zheng et al., 2000), but more recent studies argue that BAF binding has distinct effects on different genes. For example, depletion of BAF reduces Sox2, Oct4, Nanog expression in mouse embryonic stem cells(Cox et al., 2011), and BAF facilitates immediate-early gene expression in herpes simplex virus (Oh et al., 2015). All the evidence above seems to prove that BAF association promotes gene expression. However, in LHaCaT psoriasis cells, BAF depletion results in an increased expression of S100A9 and c-Jun(Takama et al., 2013). It has also been reported that BAF suppresses eef-1 expression in *C. elegans* (Margalit et al., 2007). When taken together the evidence

above indicates that while emerin-BAF association can modulate gene expression, it does not have the same effect on all genes. Moreover, the mode of its action is intriguing. BAF is more mobile when compared to its binding partner emerin, and it was proposed that BAF binds emerin frequently but transiently during interphase in a "touch-and-go" manner (Shimi et al., 2004). This theory is also supported by my data that the nuclear invaginations targeted by emerin-BAF complex exhibit a high degree of plasticity. Perhaps BAF should be considered as a "dynamic" regulator that is constantly associating and disassociating with its targets in response to upstream signals.

The sizes of the emerin-BAF and lamin A-H3k9me2 complexes range from 150-600 nm in diameter. Taking into consideration the spread of fluorescence albeit limited by deconvolution, these measurements are likely overestimated. However, it is the distances of separation between these puncta that are most revealing in the context of my study. In each case the puncta of co-localisation were separated by around 300-500 nm in all invaginations studied. This is intriguing because this is similar to the distances of separation I measured for the hotspots of Ca^{2+} release supported by RyRs within nuclear invaginations (see Chapter 3). This strongly suggests that the interactions between lamin A, emerin and their respective binding partners (Burke and Stewart, 2013), and the modulation of chromatin re-organisation and ultimately transcription, might be coordinated on the nanoscale, at least in part, by Ca^{2+} flux across the ONM.

4.3.5 Conclusion

Nuclear invaginations of differentiated PASMCs form a trans-nuclear network of nanodomains, to which chromatin anchoring NET protein complexes are selectively and strategically targeted. Here they form potential chromatin attachment sites for the regulation of gene expression. The nano-pattern of the chromatin attachment sites suggests that gene expression is perhaps regulated, in part, by Ca^{2+} signals generated on a nanoscale.

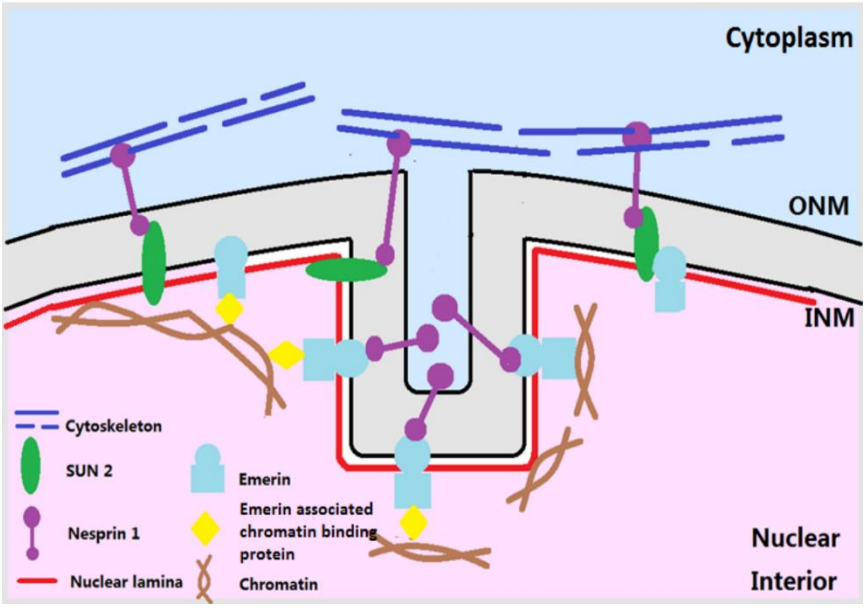

Figure 4.15 Schematic model showing the distribution of NET proteins.

Predicted distribution of NET proteins in on the inner nuclear membrane and nuclear invaginations are shown in the diagram.

Chapter 5: Nuclear invaginations are reduced and PASMCs are reconfigured during phenotypic switch

5.1 Introduction

5.1.1 Vascular smooth muscle cells display remarkable phenotypic plasticity

Vascular smooth muscle cells are the key components of the vasculature, their primary function is to regulate the blood vessel diameter by modulating vasoconstriction and dilation, which subsequently control blood flow distribution and blood pressure (Owens, 1995). One key feature that distinguishes the smooth muscle cells from the cardiac and skeletal smooth muscle cells is that they exhibit extensive plasticity as reviewed by Gomez & Owens (Gomez and Owens, 2012). They are not terminally differentiated in mature animals, instead, they are able to undergo reversible phenotypic switching in response to changes in the environment. The consensus is that smooth muscle cells can switch from the differentiated contractile phenotype to a synthetic, migratory and proliferative phenotype. In fact, the differentiated smooth muscle cells in adult blood vessels exhibit an extremely low proliferation rate (Hungerford and Little, 1999). They are nonmigratory and they synthesise very limited amounts of extracellular matrix components, because their primary function is contraction. However, in response to changes of the local environment, for example the occurrence of vascular injury, the differentiated smooth muscle cells switch to a synthetic, proliferative phenotype transiently during the healing process and switch back to the contractile phenotype once the tissues are repaired (Owens et al., 2004). Another example of the phenotypic switch is the proliferation of pulmonary arterial smooth muscle cells (PASMCs) in the pulmonary vasculature of patients with pulmonary arterial hypertension. The PASMCs of these patients exhibit the proliferative phenotype, which contributes to the thickening of the artery walls. The hypertrophy eventually leads to the elevation of pulmonary arterial pressure, which jeopardises the well-being of the patients (Wilson et al., 2015).

5.1.2 Smooth muscle cell phenotypic switch is underpinned by changes in gene expression

It is generally accepted that the phenotypic switch of the smooth muscle cell from the contractile state to the proliferative phenotype is underpinned by the down regulation

of differentiation/contractile markers and the upregulation of the proliferation markers (Owens et al., 2004, Gomez and Owens, 2012). A number of smooth muscle specific proteins and proteins that are selective for smooth muscle cells have been identified as smooth muscle markers or differentiation markers. For example, the α-actin has been shown to specifically express in vascular smooth muscle cells (Gabbiani et al., 1981); h1-calponin and SM 22α were used as a differentiation marker of smooth muscle cells in early research (Duband et al., 1993); smoothelin also identifies differentiated smooth muscles in human blood vessels (van der Loop et al., 1997). However, the most specific marker of the differentiated smooth muscle cells is perhaps the myosin heavy chain (MHC). It was shown by in situ hybridization that the expression of smooth muscle MHC was observed throughout the development and maturation of whole mouse embryos, and this protein was not expressed in any other cell types but smooth muscles (Miano et al., 1994). This observation is confirmed by other studies (Regan et al., 2000, Sartore et al., 1994), and MHC has been considered as one of the most reliable markers of smooth muscle cells (Rensen et al., 2007).

During the phenotypic switch from the contractile phenotype to the proliferative phenotype, the expression of the differentiated smooth muscle cell markers is gradually reduced, and the extent to which the expression is downregulated correlates to the degree of proliferation (Christen et al., 1999). Meanwhile, the expression of the proliferation markers, such as PDGF-A, CRBP-1 and Smemb is upregulated as reviewed by Rensen et al (Rensen et al., 2007). The changes in the protein expression eventually lead to the loss of the contractile apparatus, and proliferative smooth muscle cells gained the ability to migrate and increase synthesis.

5.1.3 Smooth muscle proliferation and Ca^{2+} signalling

Accompanied by changes in gene expression, the intracellular Ca^{2+} handling in proliferating smooth muscle cells is altered. It was reported that the smooth muscle proliferation is reliant on IP_3R dependent Ca^{2+} signalling (Wilkerson et al., 2006). Consistent with the view, it was shown that expression of RyR3 is reduced (Vallot et al., 2000), whereas the expression of all three IP3R isoforms are augmented in proliferating smooth muscle cells compared to differentiated smooth muscle cells (Berra-Romani et al., 2008). Therefore, it is possible that this altered Ca^{2+} handling

contributes to the changes in gene expression.

5.1.4 Aim

The nuclear invaginations/nucleoplasmic reticulum was observed in tumorous cells (Fischer et al., 2003), and it was stated that increased nucleoplasmic reticulum is common in tumour cells (Malhas et al., 2011). Moreover, it was shown that the nucleoplasmic Ca^{2+} is required for cell proliferation (Rodrigues et al., 2007). Based on these facts, it was proposed that the nuclear invaginations could provide further specificity to cell proliferation by allowing the focal delivery of Ca^{2+} to particular sites within the nucleus (Resende et al., 2013). Therefore, I decided to study nuclear invaginations and nuclear Ca^{2+} signalling in proliferating PASMCs.

Moreover, given that the phenotypic switch of the smooth muscle cells is underpinned by changes in gene expression, I also decided to study the regulation of chromatin attachment sites in proliferating PASMCs in comparison to differentiated PASMCs.

5.2 Result

5.2.1 Nuclear invaginations disassemble, and Ca^{2+} handling is altered during the phenotypic switch from contractile to proliferating myocytes

5.2.1.1 Day 7 cultured PASMCs switched from the contractile phenotype to a proliferative phenotype.

Consistent with previous publications on vascular smooth muscle cells (Zhang et al., 2016, Zhang et al., 2017), we observed phenotypic switch of the arterial smooth muscle cells (n=358) from the contractile phenotype to a proliferative phenotype induced by culture in the presence of serum containing growth factors. Smooth muscle cells were identified by myosin heavy chain (MHC) staining, which was proved to be an effective marker for smooth muscle cells up to and including the 7^{th} day of culture (Liu et al., 2013, Peng et al., 2017). The acutely isolated (i), day 1 cultured (ii), day 4 cultured (iii) and day 7 cultured (iv) PASMCs were identified in the bright field images by labelling the nuclei with Dapi (blue, Figure 5.1 A) and the myofilaments were identified with a sequence-specific antibody against MHC (green) as Figure 5.1B shows. One example cell of each group is magnified and shown with both the MHC (green) and Dapi (blue) staining in Figure 5.1 C. It was confirmed that 99% of the cells acutely isolated from the pulmonary arteries were smooth muscle cells (Figure 5.1 Bi), because they were MHC positive, and they were in an elongated, oval shape, which is typical for the contractile smooth muscle cells (Figure 5.1 Ci)(Rzucidlo et al., 2007). The good isolation efficiency guarantees that the cells that had been used for culture are almost pure population of smooth muscle cells.

In response to stimulation with growth factors, the morphology of PASMCs changed in culture (medium containing 10% of fetal bovine serum). The spindle-like PASMCs developed protrusions (indicated with arrow head) that were similar to filopodia and lamellipodia (Figure 5.1 Cii). However, 91% percent of the cells were still positive for MHC. After 4 days of culture with 10% serum, the cells developed spreading, epithelioid/rhomboid-like shapes (Figure 5.1 Cii), which is the typical morphology of the proliferative smooth muscle cells (Thakar et al., 2009). In contrast with acutely

isolated PASMCs, only 63% of the day 4 cultured PASMCs were labelled by MHC (Figure 5.1 Biii), suggesting a gradual loss of the contractile apparatus. The day 7 cultured cells were in similar morphology to the day 4 cultured cells (Figure 5.1 Civ), although at this stage 42% of the cells were MHC negative (Figure 5.1 Biv) perhaps due to the total loss of the contractile apparatus. Therefore, the proliferation has been initiated following 7 days of culture.

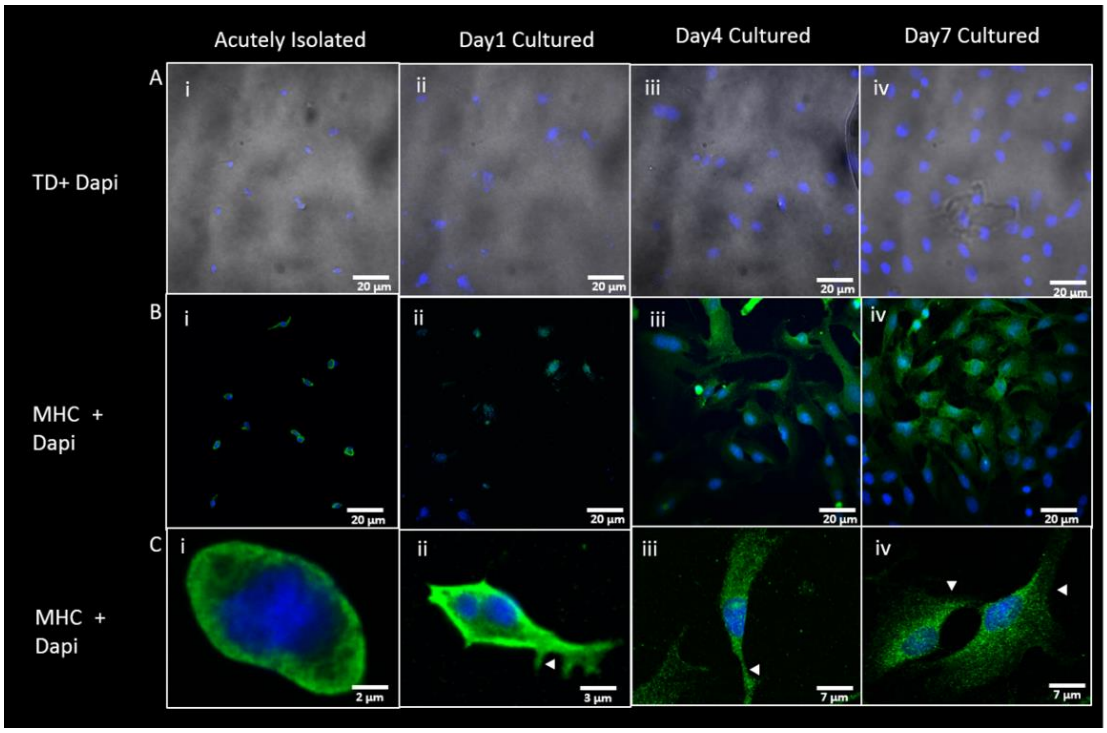

Figure 5.1 Smooth muscle cells were identified by MHC labelling

(A) Bright field images of (i) acutely isolated PASMCs, (ii) Day 1 cultured PASMCs, (iii) Day 4 cultured PASMCs and (iv) Day 7 cultured PASMCs are shown with the nuclei labelled by Dapi (blue).

(B) As for (A), but showing the immunostaining of myosin heavy chain (MHC) in green.

(C) Higher magnification images showing (i) a single acutely isolated PASMC, (ii) a single day 1 cultured PASMC, (iii) one day 4 cultured PASMC and (iv) two day 7 cultured PASMCs labelled for both MHC and Dapi. Protrusions are indicated with arrow heads.

5.2.1.2 Nuclear invaginations are lost in the majority of proliferating PASMCs

Day 7 cultured proliferating PASMCs were loaded with the Ca^{2+} indicator Fluo-4, the ER/OMN indicator ER-tracker, and Draq 5 which identifies the nucleoplasm. Z stacks through the nuclei of the labelled cells were taken at an interval of 0.2 μm. One example is shown in Figure 5.2. Z sections showing the bottom of the nucleus (i), the middle of the nucleus (ii, iii), and the top of the nucleus (iv) are displayed in Figure 5.2 A, B, C&D. Figure 5.2 Ai-iv show the confocal Z sections of the cell labelled by ER-tracker (orange) at the four positions (i-iv). In Figure 5.2 Bi-iv, Draq 5 labelling (blue) was merged on top of the images shown in Figure 5.2 A. With the Draq 5 identifying the nucleoplasm, it was observed that the ER-tracker identified the network of ER and ONM, the ONM was identified because it outlined the nucleoplasm in blue. Interestingly, the two sections through the middle of the nucleus reveal no nuclear invagination (Figure 5.2 A ii&iii). In fact, in all the day 7 cultured proliferating PASMCs studied so far (ER-tracker labelled), 80% of the cells showed no sign of nuclear invaginations, regardless of the depth of scanning into the nucleoplasm (n=25).

This representative cell was also loaded with the Ca^{2+} indicator Fluo-4, and the Z sections scanned at 3 positions (i-iii) as shown in Figure 5.2 A&B are displayed with the Fluo-4 intensity alone (green, Figure 5.2 Ci-iii) or Fluo-4 intensity together with the ER-tracker labelling (Figure 5.2 Di-iii). Based on the ER-tracker labelling, the cytoplasm and nucleoplasm can be distinguished, and it can be seen that the Fluo-4 intensity within the nucleoplasm appears to be lower than the cytoplasmic Fluo-4 intensity (which is confirmed by quantitative assessment in section 5.2.1.3&4). Judging by the intracellular distribution of free Ca^{2+} indicated by Fluo-4, no apparent tubular/linear structures were revealed by high Ca^{2+} concentrations as was commonly seen in acutely isolated cells; in other words, no nuclear invagination was identified in the nucleoplasm, and no nanocourse can be identified in the cytoplasm by the Ca^{2+} indicator.

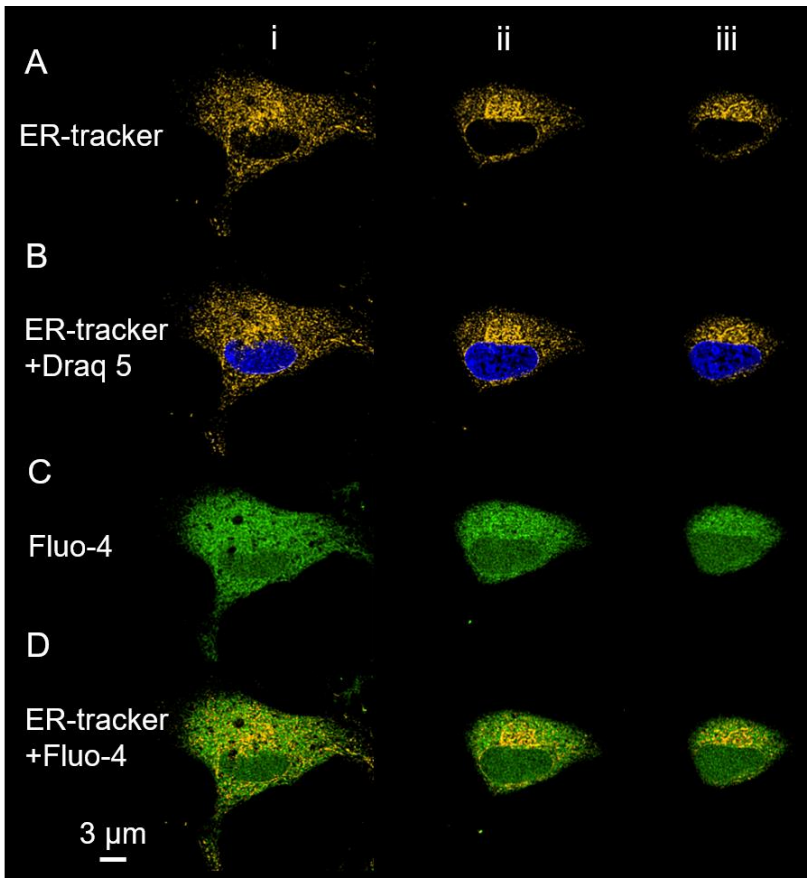

Figure 5.2 The nuclear invaginations are lost in proliferating PASMCs.

(A) A series of confocal z sections through a day 7 cultured PASMC with the ER/SR and nuclear membrane identified by ER-tracker (orange).

(B) As for (A), and also shows Draq 5 (blue) identified nucleoplasm.

(C) As for (A), but showing the Fluo-4 loading.

(D) As for (A), but showing merged images of the ER-tracker labelling and Fluo-4 loading.

5.2.1.3 Nuclear invaginations were infrequently observed in proliferating PASMCs, they did not retain higher levels of Ca^{2+} at rest comparing to the nucleoplasm.

Only 20% of the studied cells exhibited nuclear invaginations, and 1.8 ± 0.3741 nuclear invaginations were identified per cell (Appendix 3, Table 5.1). One example of such cells is shown in Figure 5.3. Confocal scans through the middle of the ER-tracker and Fluo-4 co-labelled proliferating PASMC are shown in Figure 5.3 Ai,ii&Bi. As Figure 5.3 Ai shows, apart from the ER and ONM, a very small, single dot in the middle of the nucleoplasm was revealed by the ER-tracker labelling (as indicated by the white arrow). It was easily neglected, even after magnification (Figure 5.3 Bi) it was still not very obvious. However, this dot at the same position appeared in every scan through the middle of the nucleus, suggesting that it might be the cross section of one nuclear invagination.

In terms of the distribution of intracellular Ca^{2+}, Fluo-4 loading (green) of the same confocal Z section indicates that the cytoplasm contained higher levels of free Ca^{2+} compared to the nucleoplasm (Figure 5.3 Aii). Interestingly, the analysis of the Fluo-4 fluorescence signal did not reveal this ER-tracker identified structure, although it appeared to represent a trans-nuclear invagination. To confirm this, a blue dotted line was drawn across the cytoplasm, nucleoplasm and this nuclear invagination-like structure as shown in Figure 5.3Aii, and the fluorescent intensities of both the ER-tracker and Fluo-4 along this line were plotted against distance as shown in Figure 5.3 Aiii. The regions of interest are indicated on the grey bar (C for cytoplasm, N for nucleus, I for nuclear invagination). The ER-tracker intensity (orange) along the line identifies from left to right the perinuclear cytoplasm (C) which contains perinuclear ER, the nucleoplasm (N) that was not labelled by the ER-tracker, and the cross-section of a nuclear invagination (I) that was evidently labelled by ER-tracker. The Fluo-4 intensity along the same line indicated that the perinuclear cytoplasm held higher levels of free Ca^{2+} than the nucleoplasm, whereas the Ca^{2+} level in the nucleoplasm was similar to that of the lumen of the nuclear invagination.

The confocal Z section shown in Figure 5.3 Ai and Aii were merged and magnified as Figure 5.3 Bi shows, and the dot that seems to be a nuclear invagination is indicated by a white arrow. To prove that it is indeed the cross section of a nuclear invagination, the cellular region containing the nuclear invagination was defined by two white dotted

lines, and the 3D reconstructed model of the cell was sectioned to show only this region. The sectioned 3D model was rotated 90 degrees upward to show the nuclear invagination from the side (Figure 5.3 Bii, iii&iv). Figure 5.3 Bii shows this sectioned 3D model built with the ER-tracker labelling, within which it is evident that one nuclear invagination traversing the nucleus was identified as the white arrow indicated; consistent with my prediction concerning the nature of the ER-tracker density observed in Figure 5.3 A. By contrast, the sectioned 3D model built with Fluo-4 loading shows that at no point along the entire length of the nuclear invaginations, did the Fluo-4 fluorescence intensity within the lumen of the nuclear invagination differ from that of the nucleoplasm.

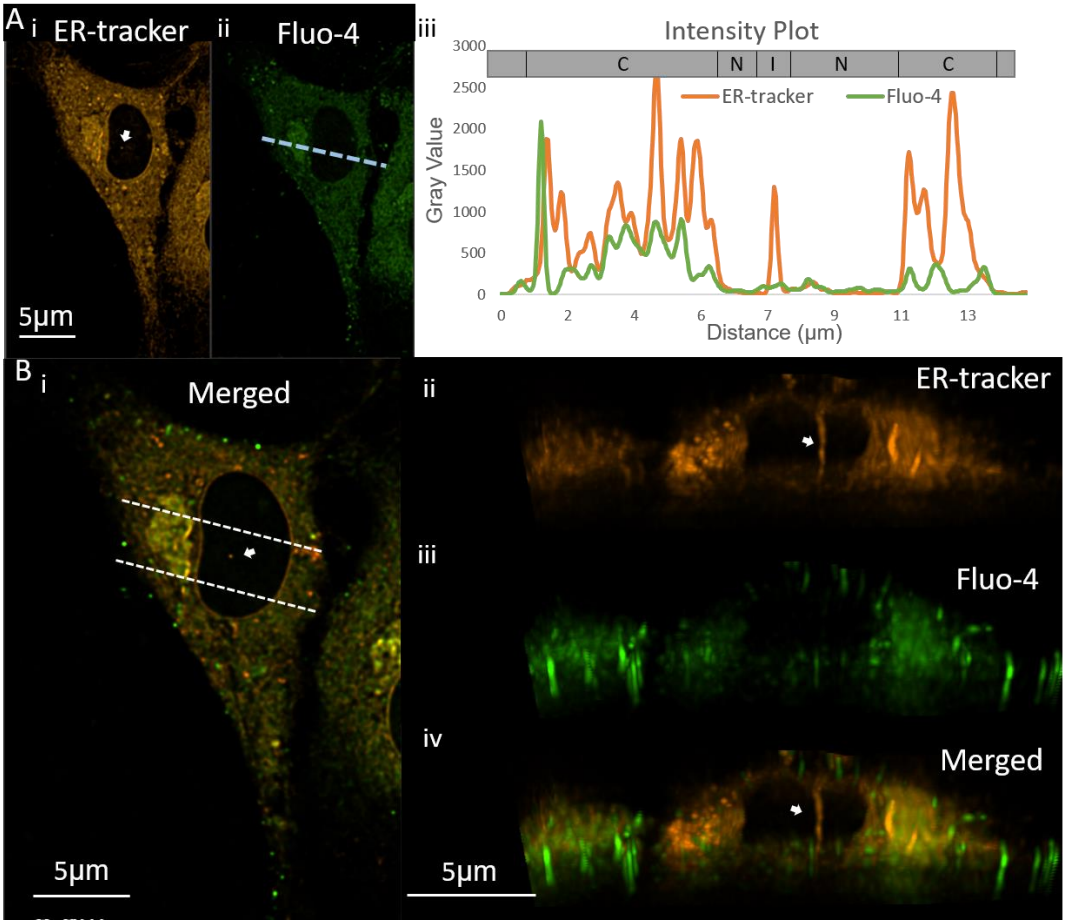

Figure 5.3 The lumen of nuclear invaginations in proliferating PASMCs does not retain high levels of free Ca^{2+} at rest.

(A) A confocal scan through the middle of a day 7 cultured PASMC labelled by ER-tracker (i, orange) or loaded with Fluo-4 (ii, green) is shown. A blue dotted line was drawn across the cell by passing the cytoplasm, nucleus and a nuclear invagination, the nuclear invagination is indicated by a white arrow. (iii) The fluorescence intensity along the line was plotted against distance, the ER-tracker intensity is shown in

orange and Fluo-4 intensity is shown in green. Regions of interest are indicated in the grey bar, C for cytoplasm, N for nucleus and I for invagination.
(Bi) The same confocal scan showed in (A) is displayed with the ER-tracker labelling in orange and Fluo-4 loading in green. The nuclear invagination is indicated by a white arrow. A region of the cell is defined by two dotted white lines. (ii) A 3D model of the cell was reconstructed based on confocal Z stacks, and the section of the cell indicated in (i) by the white dotted lines was cut out and turned 90 degrees upwards to show the view from the side of the section. The 3D model of the section with the ER-tracker labelling is shown. (iii) As for (ii), but showing the 3D model of the section with the Fluo-4 loading. (iv) As for (ii), but showing the 3D model of the section with both the ER-tracker labelling and the Fluo-4 loading.

5.2.1.4 RyR1 agonist cannot induce Ca^{2+} signals within either the nuclear invaginations or the cytoplasm of proliferating PASMCs

It was reported in Chapter 3 that the nuclear invaginations in acutely isolated PASMCs are able to generate spatially restricted Ca^{2+} signals within their lumen in response to the RyR1 agonist maurocalcine. Therefore, I decided to examine whether the nuclear invaginations in the proliferating PASMCs can generate such Ca^{2+} signals.

The nuclear invaginations in acutely isolated PASMCs can be identified by Fluo-4 intensity, because they can effectively restrict Ca^{2+} diffusion at rest. By contrast, the nuclear invaginations in proliferating PASMCs cannot be identified by Fluo-4 intensity, and the identification of those nuclear invaginations relied on the ER-tracker labelling. However, as the ER-tracker is toxic to live cells (see product safety sheet, ER-Tracker™ Blue-White DPX, ThermoFisher Scientific) and fast photobleaching of the ER-tracker signal was observed within 3 minutes. It was not recommended to apply ER-tracker in time course experiments that lasted longer than 3 minutes. Hence, the confocal time course experiments were conducted with proliferating PASMCs loaded with Fluo-4 alone. As RyR1 was shown to target the SR and nuclear invaginations of acutely isolated PASMCs (see Chapter 3), I hypothesized that RyR1 is also targeted to the nuclear invaginations of proliferating PASMCs, and I expected to visualize increases in Fluo-4 fluorescence intensity within nuclear invaginations of proliferating PASMCs after applying maurocalcine.

Live proliferating PASMCs were loaded with Fluo-4 (green) and viewed at a focal plane that provides a good view of the nucleoplasm. Extracellular application of maurocalcine was used as in Chapter 3 to stimulate the cells, and the cellular responses were recorded as time course videos. A series of frames showing several significant points of the entire process were selected from one example video and shown in Figure 5.4 A. Figure 5.4 Ai-v show the images of the cell at 5 different time points. Figure 5.4 Bi-v show the 3D surface plots of the nucleus at these 5 time points. Pseudocolour was applied to the 3D surface plots to indicate high Fluo-4 intensity in white and low Fluo-4 intensity in black. The index of changes in cytoplasmic (orange) or nuclear (blue) Ca^{2+} concentration versus time was derived from the Fluo-4 fluorescence ratio (Fx/FC0; C0 = Fluo-4 fluorescence intensity for the cytoplasm at time point 0; Fx = fluorescence intensity for the region of interest), and they were plotted against time as Figure 5.4 C shows, the selected 5 time points (i-v) were indicated by numbers and arrow heads. Images were taken at time point i show the Fluo-4 fluorescent intensity within the cell (Figure 5.4 Ai) and the nucleus (Figure 5.5 Bi) at rest. The Fluo-4 intensity indicates that the cytoplasmic Ca^{2+} concentration is higher than that of the nucleus. On average, the index of cytoplasmic basal Ca^{2+} was 1.0±0, which is significantly higher than the index of nuclear basal Ca^{2+}, which measured 0.72±0.04 (n=16, $p<0.0001$, Appendix 3, Table 5.2).

The RyR1 agonist maurocalcine (300nM) was added to the cell as indicated in Figure 5.4 C. Surprisingly, none of the studied proliferating PASMCs (n=18) responded to maurocalcine as Figure 5.4 Aii, Bii &C show. It was presented above that 19% of the studied proliferating PASMCs exhibited nuclear invaginations; hence, the chance that none of the 18 studied cells harbour any nuclear invagination is very low. Therefore, it is very likely that RyR1 expression is largely reduced in proliferating PASMCs, and they no longer target the S/ER, nuclear invaginations or any other part of the ONM. To examine whether the cells that did not respond to maurocalcine were able to generate any Ca^{2+} signal, 1µM of thapsigargin was added to some of these cells, which depletes SR Ca^{2+} stores supplied by SERCA (Lytton et al., 1991). Consistent with the presence of a viable, releasable S/ER Ca^{2+} store, marked Ca^{2+} release into the cytoplasm and the nucleoplasm was observed as Figure 5.4 Aiii, Biii &C show, and the responses in the cytoplasm and the nucleoplasm were synchronized. As

Figure 5.4 Aiii and Figure 5.4 C show, the Ca^{2+} transient in the nucleus is evidently larger than that of the cytoplasm. This received support from the fact that the average index of the peak change in nuclear Fluo-4 fluorescence is 3.9±0.4, which is significantly higher than the average index of the peak change of the cytoplasm (2.7±0.26, $p< 0.05$, n=16, Appendix 3, Table 5.2). When the response peaked, it can be observed from both Figure 5.4 Aiii&Biii that the Ca^{2+} spread homogeneously cross the entire nucleus, showing no sign of invagination-restricted Ca^{2+} signals. This indicates that there are no nuclear invaginations that can generate spatially restricted Ca^{2+} signals in any of the 16 cells studied. Moreover, comparison of the effects of maurocalcine and thapsigargin on Fluo-4 fluorescence in either the nucleoplasm ($p<0.0001$, Appendix 3, Table 5.2) or the cytoplasm ($p<0.0001$, Appendix 3, Table 5.2) demonstrates that cells were non-responsive to maurocalcine, while they harboured intracellular Ca^{2+} stores and receptors that are required to generate the intracellular Ca^{2+} signals.

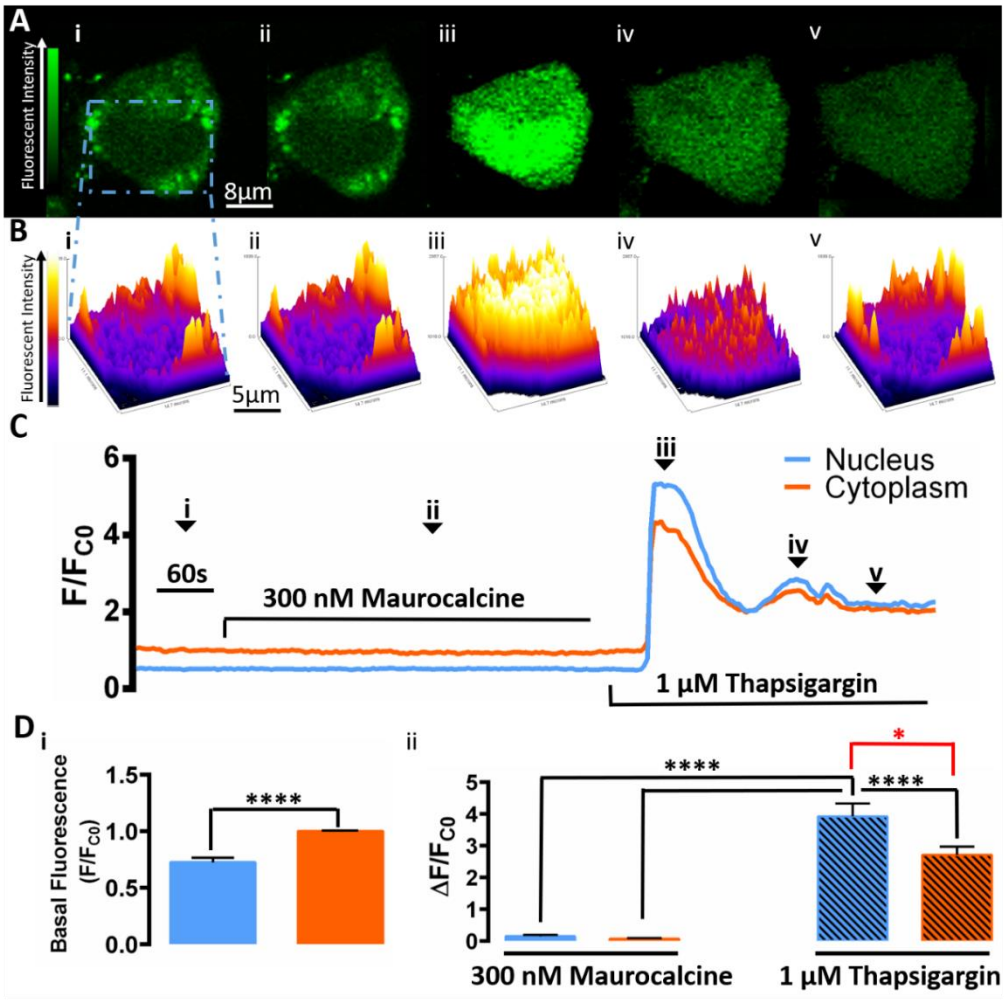

Figure 5.4. Maurocalcine fails to induce Ca^{2+} signal in proliferating PASMCs

(A) Confocal scans through the center of a proliferating pulmonary arterial smooth muscle cell loaded (25° C) with Fluo-4 are shown. Images show the same focal plane at (from left to right) different time points (i, ii, iii, iv and v) following extracellular application of 300 nM maurocalcine, and later on 1 µM thapsigargin.

(B) As in (A), but showing the 3D surface plots of the nucleus with a higher magnification, the Fluo-4 fluorescence intensity is indicated by pseudocolour representation.

(C) Fluo-4 fluorescence ratio (F_x/F_{C0}) versus time for each of the identified regions of the cytoplasm and nucleoplasm shown in (A) is plotted; F_{C0} = Fluo-4 fluorescence intensity for the perinuclear cytoplasm at time point 0, F_x = fluorescence intensity for region of interest).

(Di) Bar charts show the mean±SEM basal fluorescence within the cytoplasm (orange) and nucleoplasm (blue). (ii) Bar charts show the mean±SEM for the peak change in fluorescence ratio induced by 300 nM maurocalcine or 1 µM thapsigargin ; *=p<0.05, **=p<0.01, *** =P<0.001, ****=p< 0.0001, n=16.

It is evident from the results that the nuclear invaginations in proliferating PASMCs do not support spatially restricted Ca^{2+} signals in response to either maurocalcine or thapsigargin, although there is a slim chance that none of the studied cells harboured nuclear invaginations. The difficulty of the experiments lies in the fact that the nuclear invaginations in the proliferating PASMCs cannot be identified by Fluo-4 intensity, and there are no other means to identify the structure without introducing toxicity. However, one surprising finding is that among all the 53 Fluo-4 loaded proliferating PASMCs I studied, there was one peculiar cell that showed one nuclear invagination that seemed to retain Ca^{2+} at rest, and thus was identified by Fluo-4 intensity. Similarly, stimuli were added to the cell, and the response was recorded by a time course video. 5 frames showing the cell at 5 significant time points were selected, and the 3D surface plots of the nucleus in the 5 frames were produced with the application of pseudocolour (Figure 5.5 Ai-v). The index of changes in cytoplasmic (orange), nuclear (blue) Ca^{2+} concentration and Ca^{2+} concentration in the nuclear invagination (red) versus time were derived from the Fluo-4 fluorescence ratio (Fx/FC0; C0 = Fluo-4 fluorescence intensity for the cytoplasm at time point 0; Fx = fluorescence intensity for the region of interest), and they were plotted against time as Figure 5.5 B shows with the 5 selected time points indicated by numbers and arrow heads.

At rest one nuclear invagination traversing the nucleus was observed, which displayed slightly higher Fluo-4 fluorescence intensity compared to the rest of the nucleoplasm (Figure 5.5 Ai&B), but it was lower than the cytoplasmic Fluo-4 intensity (Figure 5.5 B). Following the addition of 300 nM maurocalcine, no change was observed in the nuclear invagination, nucleus or the cytoplasm (Figure 5.5 Aii&B). By depleting the SERCA supplied Ca^{2+}stores, dramatic Ca^{2+} transients were induced in both the nucleoplasm and the cytoplasm as Figure 5.5 Aiii &B show. Importantly, Figure 5.5 Aiii&iv show the 3D surface plots of the nucleus when the response peaked, and it seems that the nuclear invagination cannot be distinguished from the rest of the nucleoplasm. The observation received support from the plot of response shown in Figure 5.5C, which revealed that the nuclear invagination was not responsive to maurocalcine, despite the existence of releasable Ca^{2+} store.

These facts confirm that, unlike the nuclear invaginations in acutely isolated PASMCs, RyR1 is not targeted to the nuclear invaginations in the proliferating PASMCs. Upon

the depletion of thapsigargin-sensitive Ca^{2+} stores, Ca^{2+} was released directly into the nucleoplasm and cytoplasm but not the cytoplasmic nanodomains enclosed by nuclear invaginations. RyR1s are therefore absent from the ONM of nuclear invaginations, and these nuclear invaginations do not appear to support spatially restricted Ca^{2+} signalling.

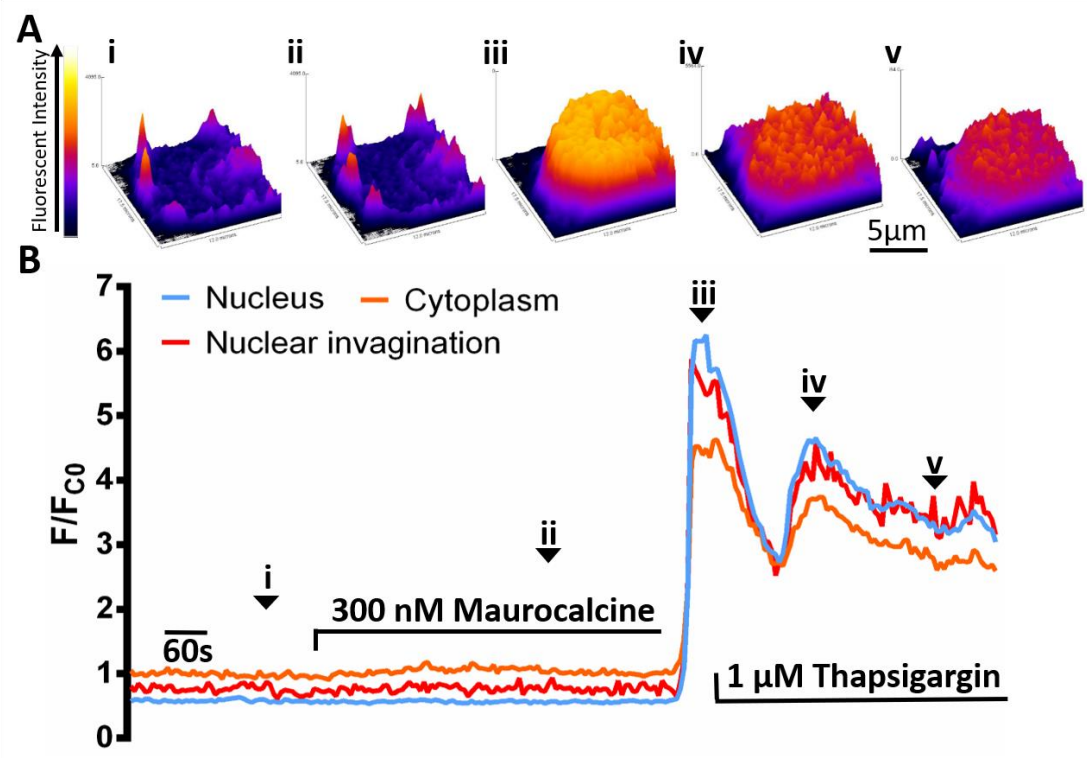

Figure 5.5 Nuclear invaginations in proliferating PASMCs are not able to generate spatially restricted Ca^{2+} signals within these nanotubes

(A) Confocal scans through the center of a day 7 cultured pulmonary arterial smooth muscle cell loaded (25° C) with Fluo-4 were selected. Images showing the 3D surface plots of the nucleus at (from left to right) different time points (i, ii, iii, iv and v) following extracellular application of 300 nM maurocalcine, and later on 1 µM thapsigargin. Pseudocolour representation was applied to show high fluorescent intensity in white and low fluorescent intensity in black.

(B) Fluo-4 fluorescence ratio (F_x/F_{C0}) versus time for each of the identified regions of the cytoplasm, nuclear invaginations, and nucleoplasm is plotted; F_{C0} = Fluo-4 fluorescence intensity for the perinuclear cytoplasm at time point 0, F_x = fluorescence intensity for region of interest).

The observations above showed that the RyR1 agonist failed to induce Ca^{2+} signal in proliferating PASMCs. Next, I investigated whether the physiological stimulation by angiotensin II could induce Ca^{2+} signals in these cells. 30μM angiotensin II was added to the proliferating PASMCs and the experiments were recorded by time course videos. One example experiment is shown in Figure 5.6. Figure 5.6 Ai-iv show 4 frames of the time course video at 4 different time points. Figure 5.6 Bi-iv show the 3D surface plots of the nucleus at these 4 time points, pseudocolour was applied to the 3D surface plots to indicate high Fluo-4 fluorescence intensity in white and low Fluo-4 fluorescence intensity in black. The index of changes in cytoplasmic or nuclear Ca^{2+} concentration versus time was derived from the Fluo-4 fluorescence ratio (Fx/F_{C0}; C0 = Fluo-4 fluorescence intensity for the cytoplasm at time point 0; Fx = fluorescence intensity for the region of interest), and they were plotted against time as Figure 5.6 C shows with the 4 time points (i-v) indicated by numbers and arrow heads.

The Fluo-4 intensity indicates that the cytoplasmic Ca^{2+} concentration is significantly higher than the nuclear Ca^{2+} concentration at rest as observed in other proliferating PASMCs (Figure 5.6 Ai&Di, n=4, $p<0.05$, Appendix 3, Table 5.3). Following the addition of the vasoconstrictor angiotensin II, synchronic Ca^{2+} transients were induced in both the cytoplasm (Figure 5.6 Aii &C) and nucleoplasm (Figure 5.6 Bii &C). The increase of Ca^{2+} was homogeneous across the nucleoplasm (Figure 5.6 Aii&Bii) in all the studied cells (n=8), suggesting that nuclear invaginations of proliferating PASMCs cannot generate spatially restricted Ca^{2+}signals above the peak response evoked within the nucleoplasm by angiotensin II.

The amplitude of the Ca^{2+} transient induced in the nucleoplasm is significantly larger than that in the cytoplasm (n=4, Figure 5.6 Dii, $p<0.0005$, Appendix 3, Table 5.3), quite unlike outcomes for acutely isolated cells. Interestingly, as the bar charts in Figure 5.6 Dii shows, angiotensin II induced Ca^{2+} signals were not blocked by preincubating the cells with the non-selective RyR inhibitor tetracaine (1 mM TTC, n=4, Appendix 3, Table 5.4). However, the angiotensin II induced Ca^{2+} signals were abolished following the depletion of S/ER stores by SERCA inhibition using thapsigargin (1μM, n=4, Appendix 3, Table 5.4), indicating that while these stores support the angiotensin II induced Ca^{2+} release they do so by alternative means. Consistent with this view, angiotensin II induced Ca^{2+} signals were abolished by

preincubating the cells with either 50 µM 2-APB (2-Aminoethoxydiphenyl borate, n=4, Appendix 3, Table 5.4) or 3 µM U73122 (n=4, Appendix 3, Table 5.4). 2-APB is a membrane permeable antagonist of Ins(1,4,5)P3 receptors and transient receptor potential cation channels (Maruyama et al., 1997, Togashi et al., 2008), whereas U73122 is a phospholipase C inhibitor that can effectively inhibit the production of Ins(1,4,5)P3 (Bleasdale et al., 1990). When these facts are taken together, it can be concluded that in proliferating PASMCs the vasoconstrictor angiotensin II induces Ca^{2+} release from SERCA supplied Ca^{2+} store (i.e.S/ER) into the nucleoplasm and the cytoplasm mainly via Ins(1,4,5)P3 receptors (IP_3Rs).

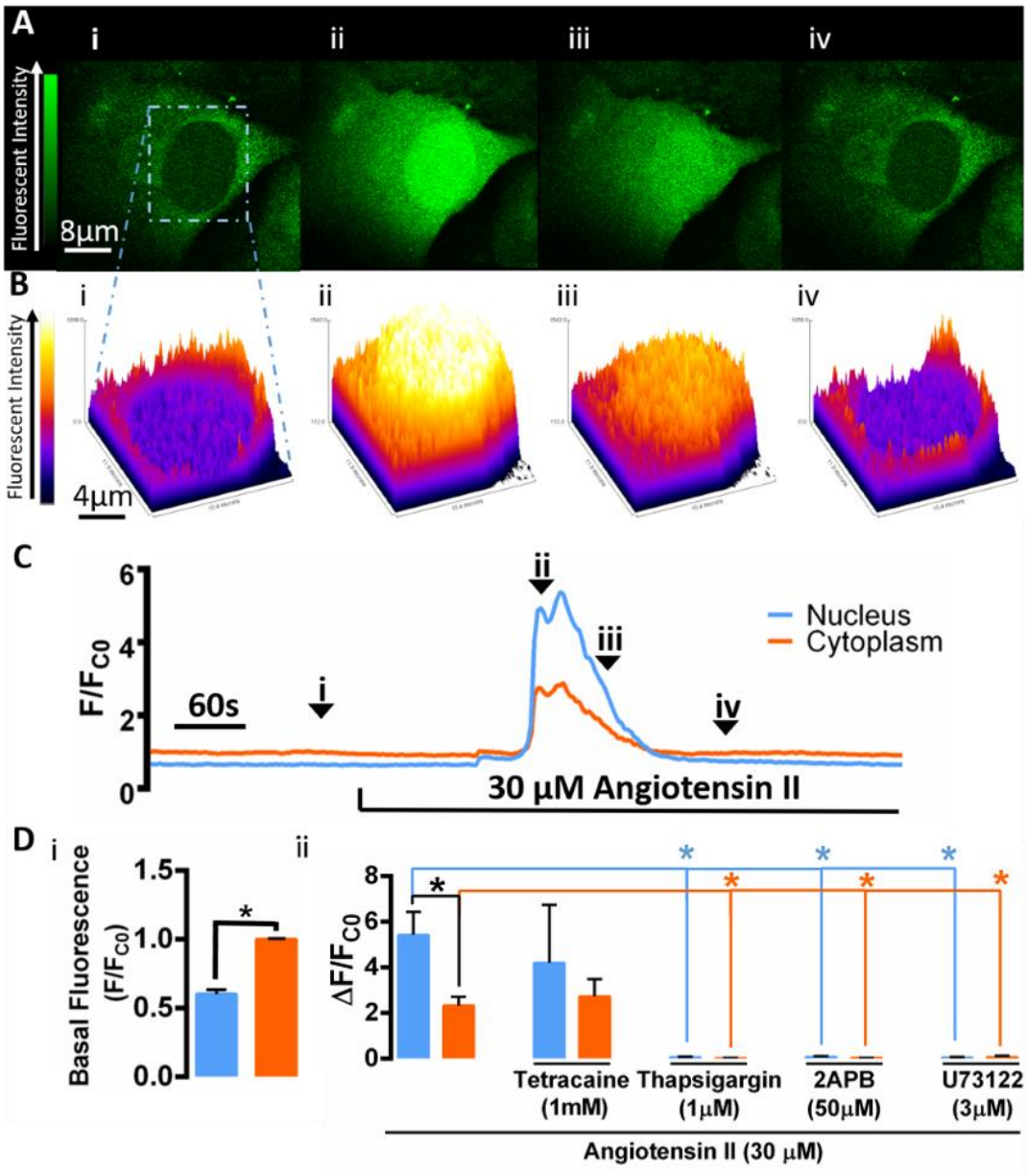

Figure 5.6 Angiotensin II induces Ca^{2+} signals in both the nucleoplasm and the cytoplasm of proliferating pulmonary arterial myocytes via IP3Rs but not RyRs

(A) Confocal scans through the middle of a proliferating pulmonary arterial smooth muscle cell loaded (25° C) with Fluo-4 are shown. Images show the same focal plane at (from left to right) different time points (i, ii, iii, and iv) following extracellular application of the vasoconstrictor angiotensin II (30 µM).

(B) As in (A), but showing the 3D surface plots of the nucleus at a higher magnification with the fluorescence intensity indicated by pseudocolour representation.

(C) Fluo-4 fluorescence ratio (F_x/F_{C0}) versus time for each of the identified regions of the cytoplasm and nucleoplasm shown in (A) is plotted; F_{C0} = Fluo-4 fluorescence intensity for the perinuclear cytoplasm at time point 0, F_x = fluorescence intensity for region of interest).

(D) Bar charts show the mean±SEM basal fluorescence within the cytoplasm (orange) and nucleoplasm (blue), and for the peak change in fluorescence ratio induced by angiotensin II (30 μM) in the absence and presence of 1 mM tetracaine (TTC, 4h pre-incubation), 1 μM thapsigargin (TG, 1h pre-incubation), 50 μM 2APB (30 minutes preincubation) or 3 μM U73122 (30 minutes preincubation) ; *=p<0.05, **=p<0.01, n=4.

5.2.2 Components of the chromatin anchoring NET protein complex are reconfigured in proliferating PASMCs

As previously mentioned, the nuclear invaginations were absent from the majority of proliferating PASMCs, while the remaining 19% of cells incorporated 1-2 nuclear invaginations per cell. Either way, when present they do not appear to support Ca^{2+} signalling in response to any stimulus applied here. This observation led to the next question: are the components of the chromatin anchoring NET protein complex that lines nuclear invaginations of acutely isolated PASMCs reconfigured in proliferating cells?

5.2.2.1 Reconfiguration of lamin A in proliferating PASMCs

Proliferating PASMCs were labelled for lamin A, and one example cell is shown in Figure 5.7. The 3D reconstruction of the lamin A (red) labelled nucleus is shown in Figure 5.7 A with Dapi (blue) indicating the nucleoplasm. The lamin A labelling alone is shown in Figure 5.7 B. Surprisingly, not only did lamin A labelling fail to identify nuclear invaginations in 100% of cells studied, but also revealed that the peripheral ridges or clefts seen in acutely isolated cells were absent from the nuclear membrane of proliferating PASMCs (n=20). However, it is very clear that the density of lamin A labelling is not uniform across the inner surface of the INM (Figure 5.7 C). Quite unlike the structure observed in acutely isolated PASMCs, lamin A labelling formed a dense mesh-like pattern across the entire surface of the INM. This indicates that sites for chromatin attachment and gene repression are massively reconfigured during proliferation. Furthermore, Figure 5.7 D shows the rotated section of the 3D reconstructed lamin A labelling, which reveals the nuclear interior of the exemplary

proliferating PASMC. it confirms that no nuclear invagination was identified by lamin A labelling, which is true across all the cells studied thus far (n=20, Figure 5.8A). In short, when present nuclear invaginations of proliferating cells are not lined by lamin A and do not support Ca^{2+} signalling. This further suggests that chromatin attachment points are lost from nuclear invaginations during proliferation.

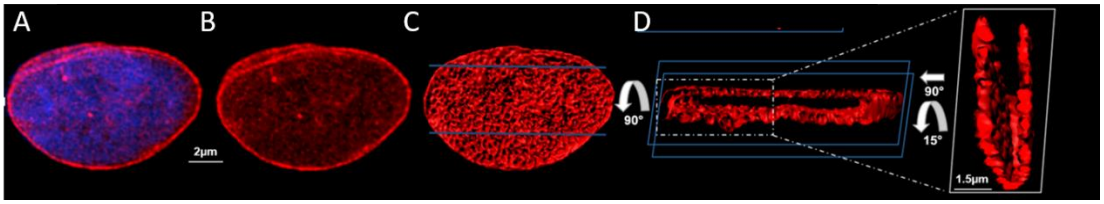

Figure 5.7 Lamin A forms a meshwork across the surface of the INM of proliferating PASMCs

The nucleus of a PASMC was labelled for lamin A (red) with (A) or without (B) Dapi (blue) identifying the nucleus. 3D reconstruction of the nucleus (C) was sectioned (D, left hand panel) and then displayed at higher magnification (D, right hand panel).

In acutely isolated PASMCs, peripheral ridges and clefts were revealed by raising the detection threshold of lamin A labelling. To study the peripheral structures on the nuclear surface of proliferating PASMCs, the 3D reconstructions were processed in the same way. As Figure 5.8 A shows, the 3D reconstruction of a lamin A (red) labelled nucleus is displayed with Dapi (blue) indicating the nucleoplasm. The lamin A labelling alone is shown in Figure 5.8 B, but the detection threshold was set to reveal only the density of lamin A by removing the surrounding lamina. It is clear following the application of the digital skin that the lamin A densities on the nuclear surface are segregated pieces (Figure 5.8 C&D), by sectioning, magnifying and rotating it can be confirmed that these densities of lamin A do not form linear structures like the peripheral ridges, or infoldings like clefts (Figure 5.8 D).

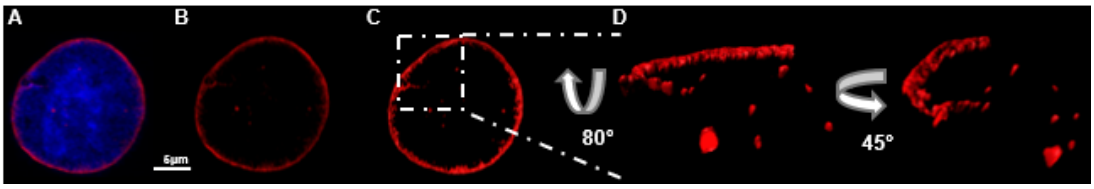

Figure 5.8 Lamin A does not identify peripheral ridges or clefts in proliferating PASMCs

The nucleus of a PASMC was labelled for lamin A (red) under high detection threshold with (A) or without (B) Dapi (blue) identifying the nucleus. 3D reconstruction of the nucleus (C) was sectioned (D, left hand panel) and then displayed at higher magnification (D, right hand panel). Dr. Jorge Navarro-Dorado conducted experiment in relation to this figure.

The nuclei of the acutely isolated (differentiated) and proliferating PASMCs also differed in respect of the surface area to volume ratio for lamin A labelling (Figure 5.9 A). For proliferating PASMCs this is reduced to 2.0±0.4 $\mu m^2/ \mu m^3$, which is significantly lower than the values for differentiated PASMCs (5.0±0.8, Figure 5.9 B, n=4, $p<0.005$, Appendix 3, Table 5.5). The significance of this finding lies in the fact that lamin A is the key component of the chromatin anchoring nuclear envelope transmembrane (NET) protein complexes. This indicates that the number of sites / relative area for chromatin attachment is reduced in the proliferating PASMCs.

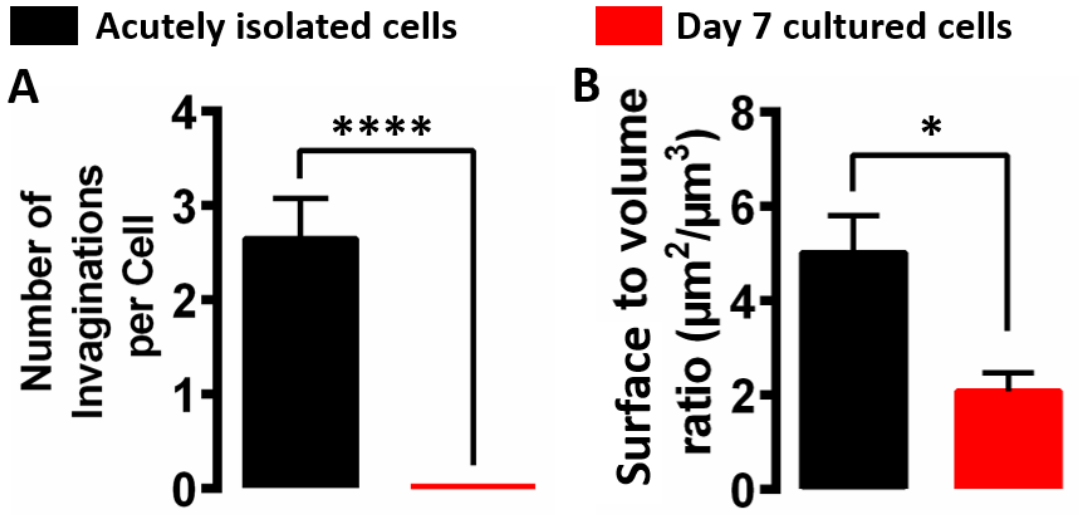

Figure 5.9 Lamin A does not identify nuclear invaginations and the surface to volume ratio of for lamin A is reduced in proliferating PASMCs

(A) Number of invaginations per cell in acutely isolated PASMCs (black) and day 7 cultured PASMCs (red) identified by lamin A are shown. Data are presented as mean±SEM; ****=p< 0.0001, n=4

(B) As for (A), but showing the surface to volume ratio (μM^2/ μM^3). *=p<0.05, n=4.

5.2.2.2 The chromatin anchoring protein complexes formed via lamin A are redistributed in proliferating PASMCs, lamin A and H3K9me2 association at the periphery of the nuclei are reduced in proliferating PASMCs

Next, I investigated the distribution of the lamin A-H3K9me2 association, considering that lamin A can promote transcriptional suppression by binding to the lamina-associated domain (LAD) of heterochromatin (Burke and Stewart, 2013), in a manner facilitated by co-association with histones such as H3K9me2/3(Harr et al., 2015). Proliferating PASMCs were co-labelled for lamin A (red) and H3K9me2 (green). Z stacks through the nuclei of the labelled cells were taken at 0.2 µm intervals. One example is shown in Figure 5.10. Z sections showing the top of the nucleus (i), the middle of the nucleus (ii, iii, iv), and the bottom of the nucleus (v) are displayed in Figure 5.10 with different labelling. Figure 5.10 shows the confocal Z sections of the cell labelled for lamin A at low detection threshold with (A) and without (B) Dapi (blue)

indicating the nucleoplasm. Figure 5.10 C shows the H3K9me2 labelling at low threshold. In Figure 5.10 D, the lamin A labelling is merged with the H3K9me2 labelling. The colocalisation between lamin A and H3K9me2 was calculated and displayed in yellow, and merged on top of the lamin A labelling as Figure 5.10 E shows.

It is important to note that the fixation method used in this approach (methanol fixation) causes dehydration of the samples and this appeared to result in shrinkage of cells and consequent reduction in the separation between the top and bottom of the NE. Subsequently, in many cells the separation of the upper and lower nuclear membranes was too small to be resolved by confocal microscopy. This is evident in Figure 5.10, which does not identify an empty space representative of the nuclear interior. However, this did not interfere with my further studies of the inner nuclear surface.

Similar to what was reported in Section 5.2.2.1, the series of confocal scans through the example nucleus show that lamin A (red) labelling covers the nucleoplasm identified by Dapi (blue, Figure 5.10 A). The images of lamin A labelling alone (Figure 5.17 B) confirmed that lamin A forms a network on the inner nuclear surface. H3K9me2 was enriched in the nucleoplasm as Figure 5.10 C shows, and by merging the H3K9me2 labelling with the lamin A labelling it was observed that half of the H3K9me2 labelling sits in the holes of the lamin A network (Figure 5.10 D), which indicates that possible lamin A-H3K9me2 association sites are limited. By superimposing the colocalisation of lamin A and H3K9me2 (yellow) onto the lamin A labelling as Figure 5.10 E shows, it can be concluded that only part of the lamin A labelling colocalised with H3K9me2.

The calculation of percentage of volume of lamin A colocalized with H3K9me2 showed that only 35±6% of the lamin A labelling (red dashed bar) colocalised with H3K9me2, whereas 40±5% of the H3K9me2 labelling (green dashed bar) colocalized with lamin A in the proliferating cells (n=4, Figure 5.11 A, Appendix 3, Table 5.9). In great contrast, in the differentiated PASMCs, 59±7% of the lamin A labelling (red bar) colocalised with H3K9me2, whereas 48±3% of the H3K9me2 labelling (green dashed bar) colocalized with lamin A (n=3, Figure 5.11 A, Appendix 3, Table 5.9). The volume

of lamin A colocalised with H3K9me2 drastically reduced in proliferating PASMCs ($p=0.053$). Moreover, the Pearson's correlation coefficient of the colocalisation in the proliferating cells is -0.1±0.03 (dashed grey bar), which is significantly lower than that of the differentiated PASMCs (grey bar, 0.1±0.03, $p<0.05$, $n=4$, Figure 5.11 B, Appendix 3, Table 5.9). Taking these facts together, it is very likely that the lamin A-H3K9me2 association is reduced in proliferating PASMCs. In fact, in differentiated PASMCs, the lamin A-H3K9me2 association lines almost all the nuclear invaginations and peripheral structures. Here the nuclear invaginations are not lined by the association, and it only targets to parts of the lamin A network. These facts show that the chromatin attachment machinery for gene suppression are redistributed and reduced in the proliferating PASMCs.

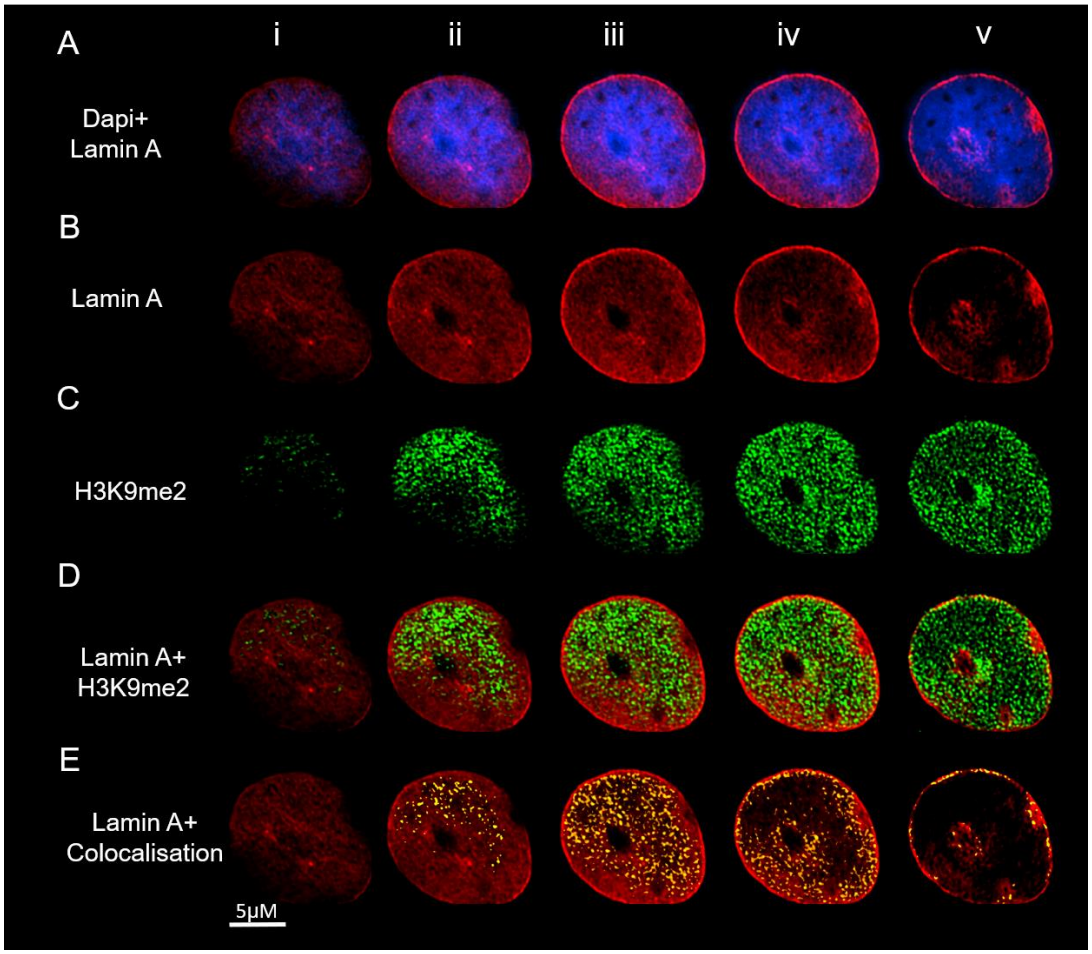

Figure 5.10 Lamin A and H3K9me2 colocalise at the nuclear periphery in proliferating PASMCs

(A) A series of confocal Z sections through a day 7 cultured PASMC labelled by lamin A (red), the nucleoplasm was identified by Dapi (blue).

(B) As for (A), but labelled for lamin A alone.

(C) As for (A), but labelled for H3K9me2 (green).

(D) As for (A), but showing the merged images.

(E) As for (A), but showing the colocalisation of lamin A and H3K9me2 in yellow, with lamin A labelling in red.

.

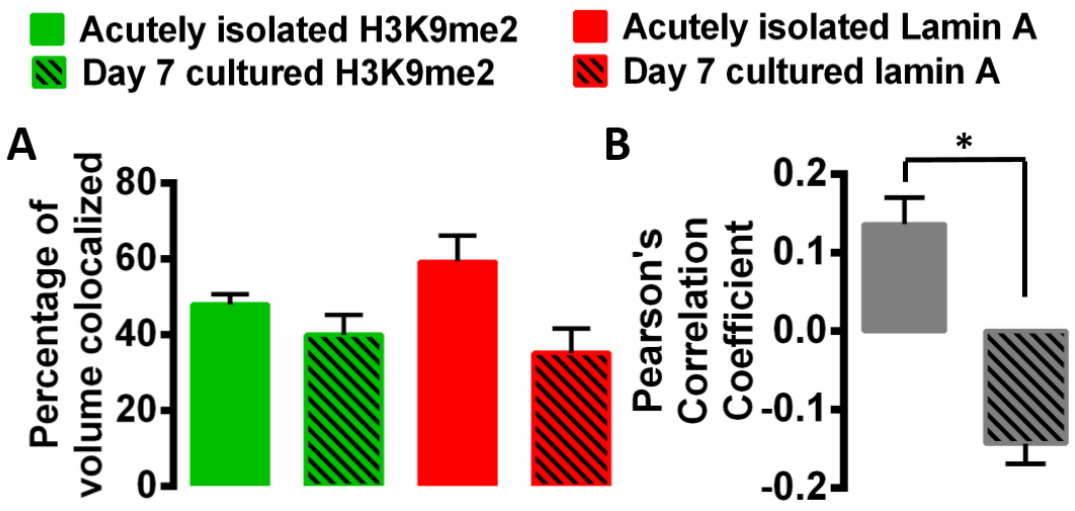

Figure 5.11 Lamin A and H3K9me2 colocalisation is reduced in proliferating PASMCs

(A) Percentage of volume of H3K9me2 (green) or lamin A (red) colocalised with the other channel (lamin A or H3K9me2 respectively) in acutely isolated cells or day 7 cultured cells (dashed) are shown in bar charts. Data are shown as mean±SEM, n=4.

(B) Colocalisation between lamin A and H3K9me2 labelling in acutely isolated cells or day 7 cultured cells were calculated, the Pearson's correlation coefficient was calculated and shown in the bar chart. Data are shown as mean±SEM, *=p<0.05, n=4.

5.2.2.3 Lamin A and emerin form two meshworks that are not fully aligned

Both lamin A and emerin can direct chromatin attachment but through distinct mechanisms. As discussed above, lamin A-H3K9me2 association indicates gene suppression. By contrast, emerin provides discrete chromatin attachment points along the surface of the INM through its co-association with BAF (barrier to auto-integration factor)(Berk et al., 2014, Cai et al., 2001, Lee et al., 2001), which binds DNA (Zheng et al., 2000) and may thus either repress or enhance gene expression (Takama et al., 2013, Cox et al., 2011). Furthermore, lamin A and emerin define two subsets of nuclear invaginations in differentiated PASMCs. Therefore, I decided to study the distribution of emerin in relation to lamin A in proliferating PASMCs and the possible sites of chromatin attachment formed via emerin.

Proliferating PASMCs were co-labelled for lamin A (red) and emerin (cyan). Z stacks through the nuclei of the labelled cells were taken at 0.2 µm intervals, and one example is shown in Figure 5.12. Z sections showing the top of the nucleus (i), the middle of the nucleus (ii, iii), and the bottom of the nucleus (iv) are displayed in Figure 5.12. Figure 5.12 Ai-iv show the confocal Z sections of the cell labelled for emerin at low detection threshold, and Figure 5.12 Bi-iv show the lamin A labelling at low threshold. In Figure 5.12 C, the emerin labelling is merged with the lamin A labelling. The colocalisation between emerin and lamin A was calculated and displayed in yellow as Figure 5.12 D shows.

Consistent with my findings for lamin A, no nuclear invagination was identified in the emerin labelled nuclei (n=10). Moreover, like the lamin A labelling in proliferating cells, the density of emerin labelling did not identify peripheral ridges or cleft on the nuclear surface. The series of scans through the co-labelled nucleus at low detection threshold show that emerin labelling forms a dense meshwork on the inner nuclear surface (Figure 5.12 Ai, ii, iii&iv). The scans at the same focal planes show that the lamin A labelling also forms a meshwork covering the inner nuclear surface (Figure 5.12 B i, ii, iii&iv). However, by merging the two it was observed that their meshworks do not fully overlap, the emerin meshwork seeming to cover large areas that were entirely lamin A free (Figure 5.12 Aii Vs Figure 5.12 Bii, Figure 5.12 Aiii Vs Figure 5.13 Biii). Moreover, lamin A appears to occupy the holes in the emerin meshwork (Figure 5.12 C).

To confirm this, the colocalisation between the lamin A and emerin labelling was calculated and showed in Figure 5.12 D (yellow). It was particularly obvious when comparing the colocalisation in Figure 5.12 Dii&iii with the emerin labelling in Figure 5.12 Aii&iii and the lamin A labelling in Figure 5.12 Bii&iii, only part of the lamin A or emerin labelling colocalised with the other, and they do form meshworks that are not fully overlapped.

Despite the fact that in differentiated PASMCs the percentage of volume of the emerin (57±5%, n=4, Appendix 3, Table 5.6) and lamin A (55±8%, n=3, Appendix 3, Table 5.7) labelling colocalised with the other are similar to the measurements of emerin

(48±2%, n=4) and lamin A (60±2%, n=3, Appendix 3, Table 5.7) in proliferating PASMCs (Figure 5.13 A, p=0.17 and p=0.62 respectively, Appendix 3, Table 5.7), the Pearson's correlation coefficient of colocalisation is significantly reduced in proliferating PASMCs (0.05±0.01, n=3, Figure 5.14 B, dashed grey bar, Appendix 3, Table 5.7) compared to differentiated PASMCs (0.3±0.01, n=4, $p<0.05$, Figure 5.13 B, grey bar, Appendix 3, Table 5.7). The fact that the Pearson's correlation coefficient of the colocalsation dropped to below 0.1 suggests that lamin A and emerin may form two meshworks that are mostly separated but retain some points of contact, at least at the resolution of the present experiments. The significance of this finding is that both lamin A and emerin can direct chromatin attachment but through distinct mechanisms. Therefore, it is plausible that lamin A and emerin form partially separated meshworks that modulate chromatin attachment through these two different mechanisms.

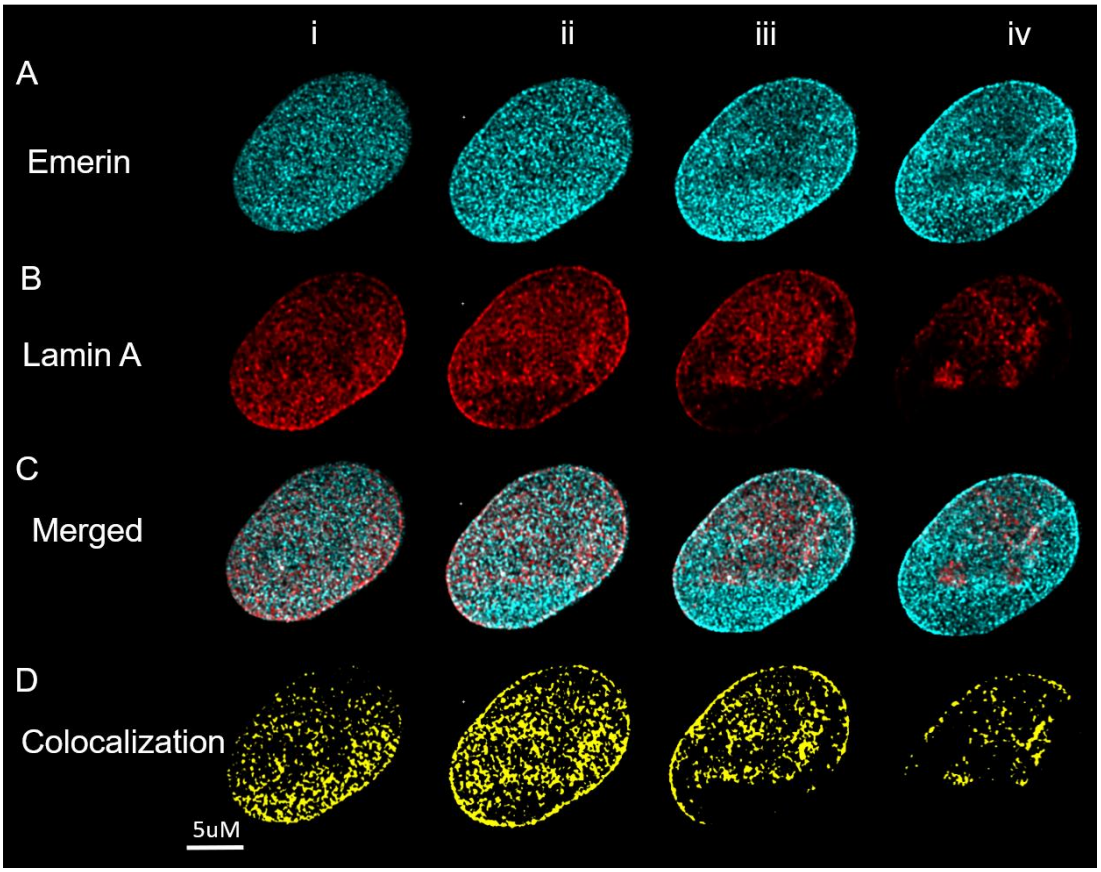

Figure 5.12 Lamin A forms a meshwork that only partially overlaps with the emerin meshwork in proliferating PASMCs

(A) A series of confocal z sections through a proliferating PASMC labelled for emerin

(cyan) with low detection threshold.

(B) As for (A), but labelled for lamin A (red)

(C) As for (A), but showing the merged images.

(D) As for (A), but showing the colocalisation of emerin and lamin A in yellow.

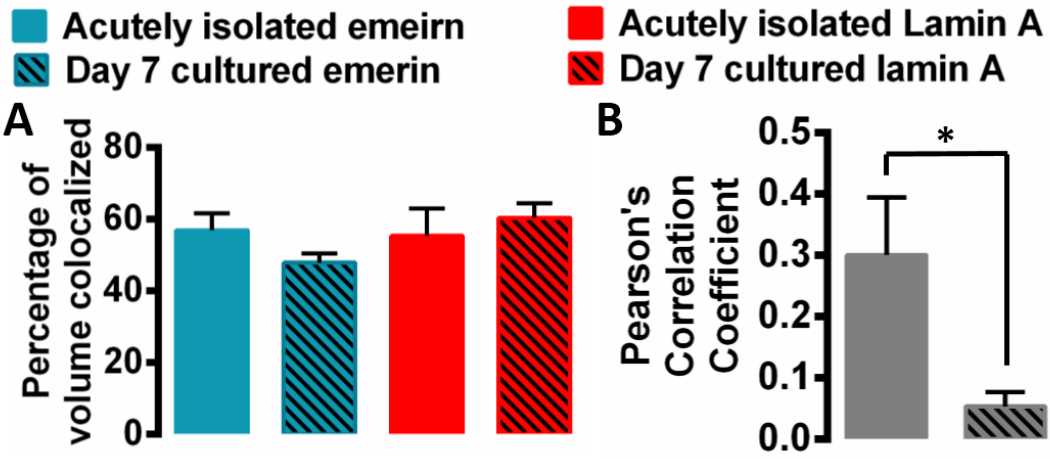

Figure 5.13 Lamin A and emerin colocalisation is reduced in proliferating PASMCs

(A) Percentage of volume of emerin (cyan) or lamin A (red) labelling colocalised with the other (lamin A or emerin respectively) in acutely isolated cells or day 7 cultured cells (dashed) are shown in bar charts. Data are shown as mean±SEM.

(B) Colocalisation between lamin A and emerin labelling in acutely isolated cells or day 7 cultured cells (dashed) were calculated, the Pearson's correlation coefficient was calculated and shown in the bar chart. Data are shown as mean±SEM, *=$p<0.05$, n=3.

5.2.2.4 Emerin and BAF associate at the periphery of proliferating PASMCs, providing a greater abundance of sites for chromatin attachment than observed in differentiated PASMCs

Proliferating PASMCs were co-labelled for emerin (cyan) and BAF (purple). Z stacks scanning through the nuclei of the labelled cells were taken at the step interval of 0.2 µm, and one example is shown in Figure 5.14. Z sections showing the top of the nucleus (i), the middle of the nucleus (ii, iii, iv), and the bottom of the nucleus (v) are displayed in Figure 5.14. Figure 5.14 i-v show the confocal Z sections of the cell labelled for emerin at low detection threshold with (A) and without (B) Dapi (blue) indicating the nucleoplasm, and Figure 5.14 Ci-v show the BAF labelling with a low threshold. In Figure 5.14 D, the emerin labelling is merged with the BAF labelling. The colocalisation between emerin and BAF was calculated and displayed in yellow, and merged on top of the emerin labelling as Figure 5.14 E shows.

As Figure 5.14 A shows, the emerin (cyan) labelling covers the entire perimeter of the nucleoplasm identified by Dapi (blue). The images of emerin labelling alone (Figure 5.14 B) confirmed that emerin forms a meshwork on the inner nuclear surface. On the other hand, BAF was identified in the nucleoplasm as Figure 5.14 C shows, and by merging the BAF labelling with the emerin labelling it can be seen that some of the BAF sits in the hole of the emerin meshwork, and it does not appear to always colocalise with emerin. Indeed, the colocalisation of emerin and BAF (yellow) was superimposed onto the emerin labelling as Figure 5.14 E shows, and it can be concluded that only part of the emerin colocalised with BAF.

This observation received support from the calculation of percentage of volume of emerin or BAF colocalized with each other. In proliferating PASMCs, 43±5% of the emerin labelling (cyan, dashed) and 59±9% of the BAF labelling (purple, dashed) colocalized with the other (Figure 5.15, n=4, Appendix 3, Table 5.8). This shows that around half of the emerin identified colocalised with BAF. However, in differentiated PASMCs, only 10±2% of the emerin labelling (cyan) and 25±4% of the BAF labelling (purple) colocalized with the other protein (Figure 5.15, n=10, Appendix 3, Table 5.8). The volumes of both emerin or BAF colocalised with each other were significantly increased in the proliferating PASMCs ($p<0.0005$). Moreover, the Pearson's correlation coefficient of the colocalisation increased significantly in the proliferating

PASMCs (0.005±0.01, Figure 5.15, grey bar, Appendix 3, Table 5.8) compared to the differentiated PASMCs (-0.080.05±0.02, n=10, Figure 5.16, dashed grey bar, p<0.001, Appendix 3, Table 5.8). Given the above, it can be postulated that perhaps the chromatin attachment governed by emerin-BAF association is more pronounced in the proliferating cells compared to the differentiated PASMCs.

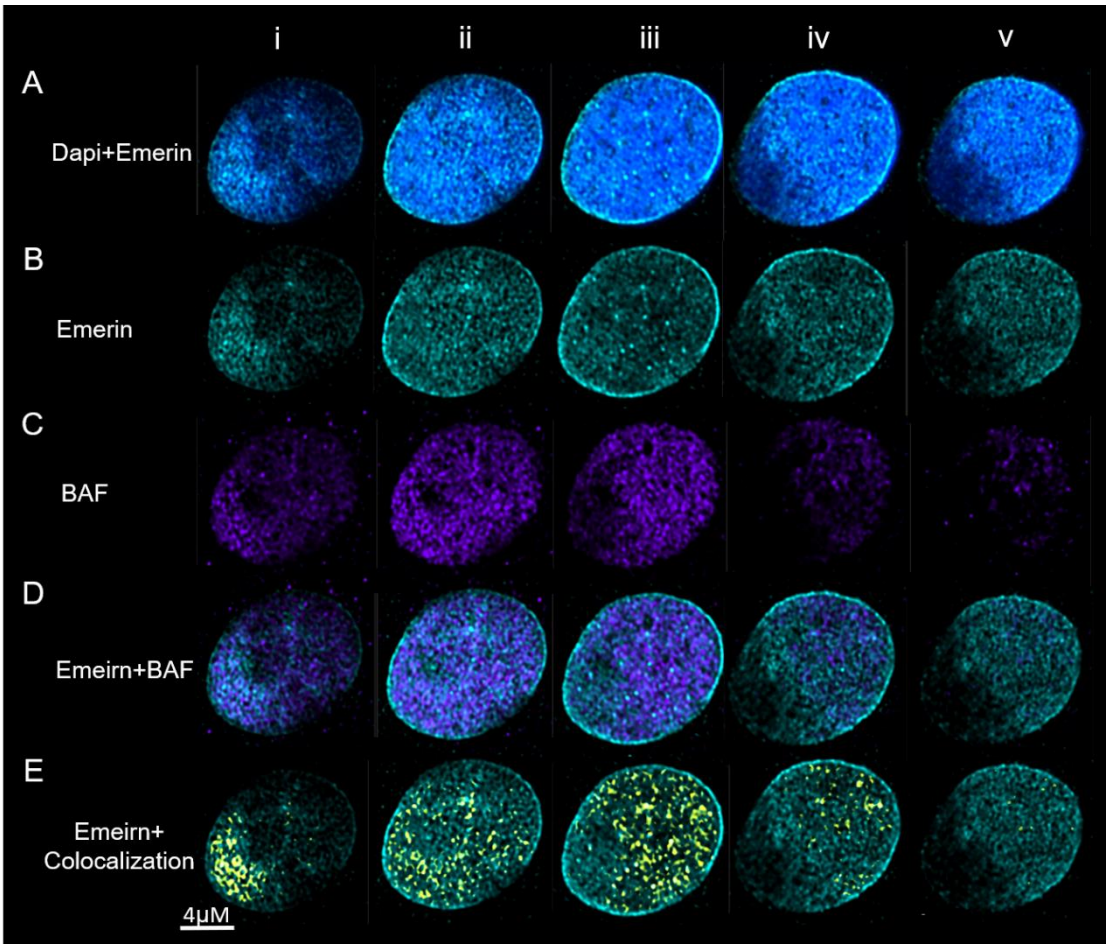

Figure 5.14 Emerin and BAF colocalise at the periphery of the nucleus in proliferating PASMCs

(A) A series of confocal z sections through a day 7 cultured PASMC labelled by emerin (cyan) with low detection threshold, the nucleoplasm was identified by Dapi (blue).

(B) As for (A), but labelled for emerin alone.

(C) As for (A), but labelled for BAF (purple).

(D) As for (A), but showing the merged images.

(E) As for (A), but showing the colocalization of emerin and BAF in yellow, with emerin labelling in cyan.

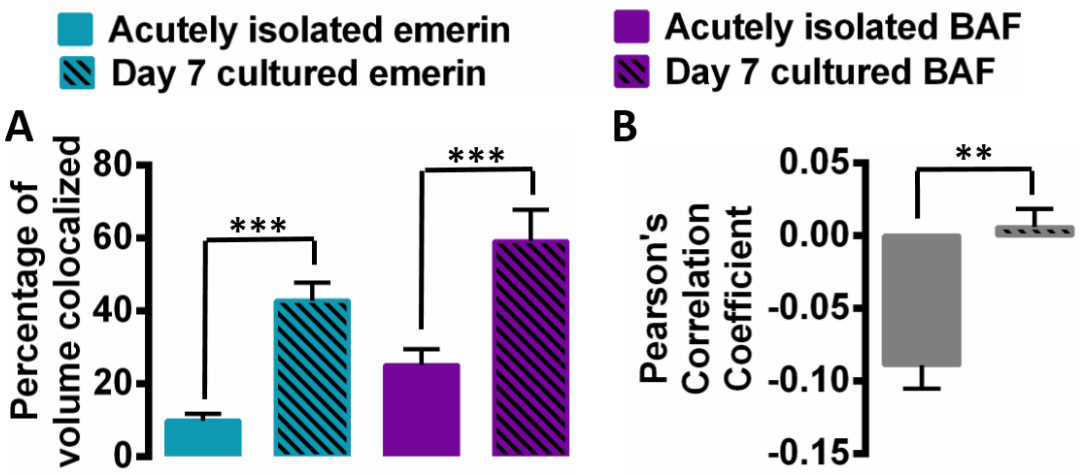

Figure 5.15 Emerin and BAF colocalisation is increased in proliferating PASMCs

(A) Percentage of volume of emerin (cyan) or BAF (purple) labelling colocalised with the other (BAF or emerin respectively) in acutely isolated cells or day 7 cultured cells (dashed) are shown in bar chart. Data are shown in mean±SEM, *** =P<0.001, n=10 for differenciated cells, n=4 for proliferating cells.

(B) Colocalisation between BAF and emerin labelling in acutely isolated cells or day 7 cultured cells (dashed) were calculated, the Pearson's correlation coefficient was calculated and shown in the bar chart. Data are shown in mean±SEM, **=p<0.01, n=10 for differenciated cells, n=4 for proliferating cells.

5.2.2.5 The distribution the LINC complex is reconfigured in proliferating PASMCs, components of the LINC exhibit a punctate distribution across the periphery of the nuclei.

Both emerin and lamin A are shown to bind to nesprin-1α or the LINC complex, allowing the signal transduction from the cytoplasm to the nucleoplasm. Following this lead, proliferating PASMCs were labelled for nesprin-1 (magenta) and SUN 2 (green), and Z stacks were taken through the nuclei of labelled cells at 0.2 µm intervals, (Figure 5.16). Z sections showing the top of the nucleus (i), the middle of the nucleus (ii, iii), and the bottom of the nucleus (iv) are displayed in Figure 5.16. Figure 5.16 Ai-iv shows the confocal Z sections of the cell labelled for nesprin-1 at low detection

threshold. Figure 5.16 Bi-iv show the SUN 2 labelling at the same focal planes. In Figure 5.16 C, nesprin-1 labelling is merged with the SUN 2 labelling. The colocalisation between nesprin-1 and SUN 2 was calculated and displayed in yellow as Figure 5.16 D shows.

The confocal scans through the nesprin-1 (magenta) labelled nucleus (Figure 5.16 Ai, ii, iii&iv) show that nesprin-1 labelled the entire inner nuclear surface in a very punctate manner. Similarly, the images showing SUN 2 labelling acquired at the same scanning planes (Figure 5.16 Bi, ii, iii&iv) show that SUN 2 was also present across the entire inner nuclear surface. In each case the labelling was very punctate. By merging the nesprin-1 and SUN 2 labelling it can be observed that, although labelling for both proteins was quite abundant, the two proteins seem to sit on two separated networks, and this was consistently observed across the four scans acquired at distinct focal planes (Figure 5.16 Ci, ii, iii&iv) and all other cells studied. This observation received support from the fact that very limited colocalisation (yellow) was observed Figure 5.16 D.

Moreover, the degree of colocalisation between nesprin-1 and SUN 2 is evidently reduced in proliferating PASMCs compared to the acutely isolated, fully differentiated PASMCs. As shown in the bar charts in Figure 5.17 A, the percentage of volume of nesprin-1 colocalised with SUN 2 is 50±3% in the differentiated PASMCs, which is similar to that of the proliferating PASMCs (53±11%, n=3, p=0.75, Appendix 3, Table 5.6). The percentage of volume of SUN 2 colocalised with nesprin-1 is 40±7% in the differentiated PASMCs, which is also similar to that of the proliferating PASMCs (32±10%, n=3, p=0.57, Appendix 3, Table 5.6). However, in the proliferating PASMCs, the Pearson's correlation coefficient of the colocalisation (0.12±0.01, Figure 5.17 B) is significantly lower than that of the differentiated PASMCs (0.37±0.06, n=3, $p<0.05$, Appendix 3, Table 5.6), suggesting that although there was overlap between nesprin-1 and SUN2 in the proliferating PASMCs, they are not so closely aligned as in acutely isolated cells. This fact further confirmed that the formation LINC complex is reduced in the proliferating PASMCs, and it can be concluded that although both nesprin-1 and SUN 2 are quite abundant on the NE of the proliferating PASMCs, they were poorly colocalised, suggesting that the LINC complex is reduced.

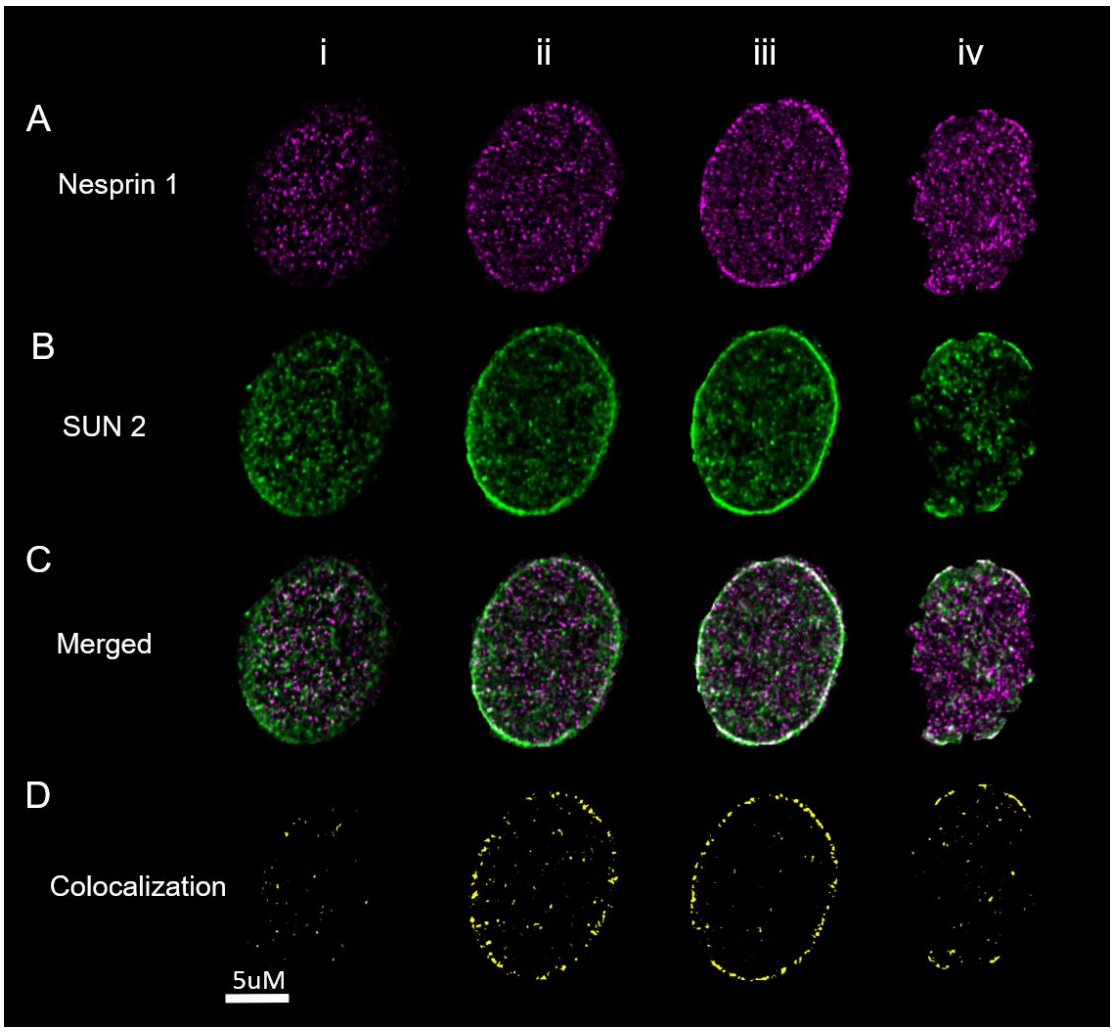

Figure 5.16 Nesprin-1 and SUN 2 are both abundant on the NE of proliferating PASMCs but their degree of colocalisation is reduced

(A) A series of confocal z sections through a proliferating PASMC labelled for nesprin -1 (magenta) with low detection threshold.

(B) As for (A), but labelled for SUN2 (green)

(C) As for (A), but showing the merged image.

(D) As for (A), but showing the colocalisation of nesprin -1 and SUN 2 in yellow.

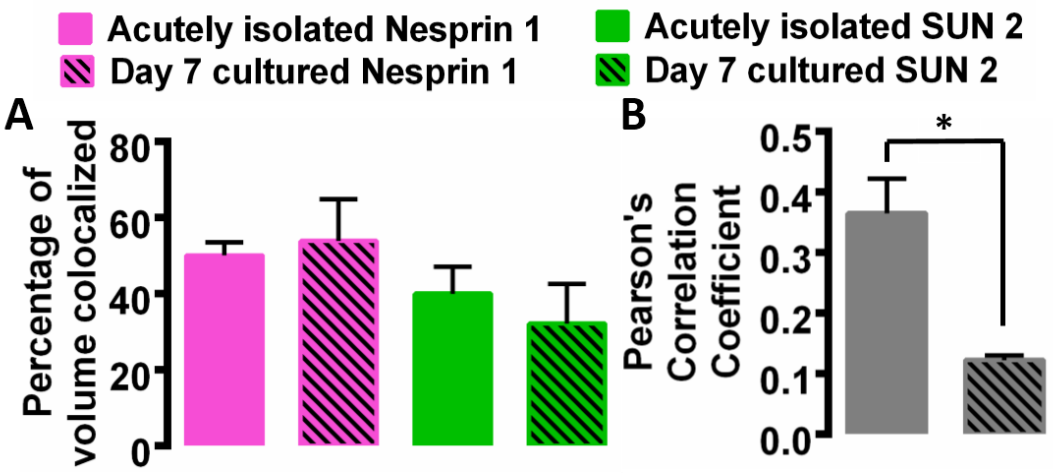

Figure 5.17 Colocalisation of nesprin-1 and SUN 2 is reduced in proliferating PASMCs

(A) Percentage of volume of nesprin-1 (magenta) or SUN 2 (green) labelling colocalised with the other (SUN2 or nesprin-1 respectively) in acutely isolated cells or day 7 cultured cells (dashed) were shown in the bar chart. Data are shown in mean±SEM.

(B) Colocalisation between nesprin-1 and SUN2 labelling in acutely isolated cells or day 7 cultured cells (dashed) were calculated, the Pearson's correlation coefficient was calculated and shown in the bar chart. Data are shown in mean±SEM, *=$p<0.05$, n=3.

5.3 Discussion

5.3.1 Summary of findings

Chapter 5 shows that the PASMCs undergo phenotypic switch in culture containing 10% serum. In proliferating PASMCs, synchronized Ca^{2+} transients are triggered in the nucleoplasm and cytoplasm in an IP_3R dependent but RyR independent manner. This is perhaps caused by the elimination of RyR1s and reduced expression of other RyRs. Coinciding with these changes in Ca^{2+} signalling, NET proteins are also reconfigured at the nuclear periphery. Both the lamin A-H3K9me2 association and emerin-BAF association are identified on the inner nuclear surface, albeit in a more limited fashion than observed in acutely isolated cells. The proportion of lamin A-H3K9me2 association is also reduced compared to what was observed in the differentiated PASMCs, whereas the proportion of emerin-BAF association is increased. Moreover, both nesprin-1 and SUN2 are identified on the inner nuclear surface, but they are poorly associated.

Among all the cells studied, only 19% of cells still harbour nuclear invaginations. The number of nuclear invaginations per cell is reduced, and the remaining nuclear invaginations lost the capacity to generate spatially restricted Ca^{2+} signals, while they no longer harbour any chromatin attachment sites constituted by NET proteins.

5.3.2 Intracellular Ca^{2+} handling in PASMCs is altered following phenotypic switching from a contractile to proliferative state

Consistent with the studies that stated that the proliferation of smooth muscle cells can be induced by serum in culture (Southgate and Newby, 1990, Zhong et al., 2014), I observed the initiation of proliferation in PASMCs following 7 days of culture in 10% of serum. The change of cell shape to the typical morphology of proliferating smooth muscle cells (Thakar et al., 2009), and the gradual loss of the smooth muscle specific marker MHC confirmed that the proliferation process was initiated.

Accompanied by the phenotypic switch, I observed changes in intracellular Ca^{2+} handling. Induced Ca^{2+} transients occurred synchronously within the cytoplasm and the nucleoplasm, indicating that there was no buffer barrier nor segregated Ca^{2+} signal

within nuclear invaginations. This was accompanied by a global alteration of SR targeted Ca^{2+} releasing channels. The RyR1 agonist that can effectively induce Ca^{2+} release in the differentiated PASMCs (see Chapter 3) failed to induce any Ca^{2+} signal in proliferating PASMCs, despite the fact that Ca^{2+} release can be triggered by depleting the thapsigargin-sensitive Ca^{2+} stores in these cells. This indicates that the expression of RyR1 is eliminated in proliferating PASMCs, and the Ca^{2+} release from the SR must rely on other receptors.

Consistent with this view, I show that angiotensin II induced dramatic Ca^{2+} release in the nucleoplasm and the cytoplasm of proliferating PASMCs. The Ca^{2+} originated from the SERCA fed stores (i.e. SR and the connected NR) because the Ca^{2+} release was blocked by thapsigargin (Lytton et al., 1991). This shows that activation of SR targeted Ca^{2+} release channels are responsible for the observed Ca^{2+} transients. Interestingly, however, my data show that blocking all subtypes of RyRs with tetracaine did not abolish the angiotensin II induced Ca^{2+} release. By contrast to findings for acutely isolated PASMCs, angiotensin II evoked release was abolished following blocking the IP_3Rs with 2APB (Maruyama et al., 1997) or suppressing IP_3 production by U73122 (Bleasdale et al., 1990). This strongly suggests that angiotensin II evoked Ca^{2+} signals arise preferentially via ER/SR targeted IP_3Rs but not RyRs.

This finding is consistent with earlier studies of others that showed that while RyR3, SERCA 2a and 2b, and IP_3R1 were present in freshly isolated rat aortic smooth muscle cells (ASMCs), following the induction of ASMC proliferation in culture for 5 days, the protein expression of RyR3 and SERCA2a were diminished, whereas the expression of SERCA 2b and IP_3Rs remained unchanged (Vallot et al., 2000). In arterial smooth muscle cells, the expression of all three IP3R isoforms and SERCA2b were augmented in cultured, proliferating ASMCs compared to the freshly dissociated arterial myocytes (Berra-Romani et al., 2008). In short, in proliferating smooth muscle cells, IP3Rs, not RyRs, are more likely to be the predominant Ca^{2+} release channel. This is consistent with the proposal that IP_3Rs and IP_3 induced Ca^{2+} waves are required for arterial smooth muscle proliferation, because proliferation was inhibited by a IP_3R antagonist (Wilkerson et al., 2006). Given the above, it can be postulated that the expression of RyRs is possibly reduced in the proliferating PASMCs, and that

IP_3Rs are the dominant Ca^{2+} release channel that is relied on during PASMC proliferation. Considering that synchronized Ca^{2+} transients were observed in both the nucleoplasm and cytoplasm, it can be inferred that the IP_3Rs are perhaps targeted to both the ER/SR and the INM of the nucleoplasmic reticulum of the proliferating PASMCs. They direct Ca^{2+} release from the ER/SR to the cytoplasm, and from the nucleoplasmic reticulum to the nucleoplasm.

5.3.3 The inner nuclear surface of the proliferating PASMCs is reconfigured compared to the differentiated PASMCs

Coinciding with the alteration in Ca^{2+} handling, the chromatin-anchoring NET protein complexes on the inner nuclear surface are reconfigured. Lamin A and emerin labelled the entire inner nuclear surface in differentiated PASMCs. However, their densities no longer depict ridges and clefts in proliferating PASMCs. Instead, they form meshworks that only partially overlap on the inner nuclear surface. As mentioned previously, both lamin A and emerin can direct chromatin attachment but through distinct mechanisms. Lamin A can promote transcriptional suppression by binding to the lamina-associated domain (LAD) of heterochromatin(Burke and Stewart, 2013), in a manner facilitated by co-association with histones such as H3K9me2/3(Harr et al., 2015). By contrast, emerin has been shown to provide discrete chromatin attachment points along the surface of the INM through its co-association with BAF (barrier to auto-integration factor)(Berk et al., 2014, Cai et al., 2001, Lee et al., 2001), which binds DNA (Zheng et al., 2000) and may thus either repress or enhance gene expression (Takama et al., 2013, Cox et al., 2011). Here, both the lamin A-H3K9me2 and emerin-BAF associations were observed on the inner nuclear surface. However, the lamin A-H3K9me2 association is largely reduced judging by the decreased Pearson's correlation coefficient. This indicates that in the proliferating PASMCs, the suppression of gene expression via lamin-associated domains is reduced. By contrast, and although their expression may be reduced, the degree of emerin-BAF association may be promoted in proliferating PASMCs judging by the increased Pearson's correlation coefficient, but the effect on global gene expression is unclear because BAF has distinct effects on different genes. Interestingly, one paper has shown that when the proliferation of vascular smooth muscle cells is promoted, the expression of lamin A and emerin is repressed. In addition, overexpressing emerin and lamin A in vascular smooth muscle can reverse stretch-induced proliferation (Qi et al., 2016). These findings support my conclusion that during PASMC phenotypic switching, the

chromatin anchoring NET protein complexes are reconfigured in a way that supports less gene suppression, favouring PASMC proliferation.

Moreover, the expression of nesprin-1 and SUN2, as well as their associations are also reduced in proliferating PASMCs. This shows that the formation of the LINC complex is reduced. The LINC complex associates with the cytoskeletons and is responsible for the transduction of mechano-forces (Anno et al., 2012, Kim et al., 2015, Chang et al., 2015). It is therefore possible that the reconfiguration of NET proteins in the proliferating PASMC affects multiple aspects of the cellular function, which requires further investigation.

5.3.4 Nuclear invaginations in proliferating PASMCs are reduced and remodelled.

Only 19% of the proliferating PASMCs display nuclear invaginations, and each of them only constitutes 1.8 nuclear invaginations on average. Notably, when observed the nuclear invaginations of proliferating PASMCs do not seem to demarcate nanocourses for Ca^{2+} signalling. Coinciding with the loss of the ability to generate spatially restricted Ca^{2+} signals, the nuclear invaginations in proliferating PAMSCs also lost their ability to modulate chromatin attachment. This is evident from the fact that none of the NET proteins (including lamin A, emerin, nesprin-1, SUN2 and BAF) labelled these nuclear invaginations. Therefore, the small number of nuclear invaginations remaining in this subpopulation (19%) of proliferating PASMCs no longer provide sites for chromatin attachment and thus gene suppression (Zheng et al., 2000, Harr and Reddy, 2016). This provides indirect support for my proposal that the generation of Ca^{2+} signals within the nuclear invaginations is related to the modulation of chromatin attachment, since the two functions of the nuclear invagination are either both observed in one phenotype (contractile) and are both absent from the other phenotype (proliferative).

One limitation of my study is that the cells can only be labelled for either the ER/SR/ONM (in live cells) or NET proteins (in fixed cells) because ER-tracker signal cannot be retained following immunocytochemistry. Due to this fact I cannot provide direct evidence to show that the ER-tracker labelled nuclear invaginations are not

lined by the NET proteins, although the fact that each label independently demonstrates the loss of invaginations strongly supports my conclusions. Nevertheless, it would be beneficial to receive further confirmation from co-labelling of the ONM and NET proteins, if it is possible in the future.

5.3.4 Conclusion

During the phenotypic switch of PASMCs, the intracellular Ca^{2+} handling is altered to an IP_3R-dependent, RyR-independent pathway (Figure 5.19). This is accompanied by the remodelling of the distribution of NET proteins on the inner nuclear surface. Here lamin A and emerin form partially overlapping meshworks, and the chromatin anchoring protein complexes formed via either lamin A or emerin are rearranged. In particular, the lamin A-H3K9me2 association is reduced, which perhaps favours PASMCs proliferation by reducing gene suppression. Moreover, the number of nuclear invaginations in proliferating PASMCs is also greatly reduced, while remaining nuclear invaginations lost the ability to generate spatially restricted Ca^{2+}signal and the infrastructure to support chromatin attachment.

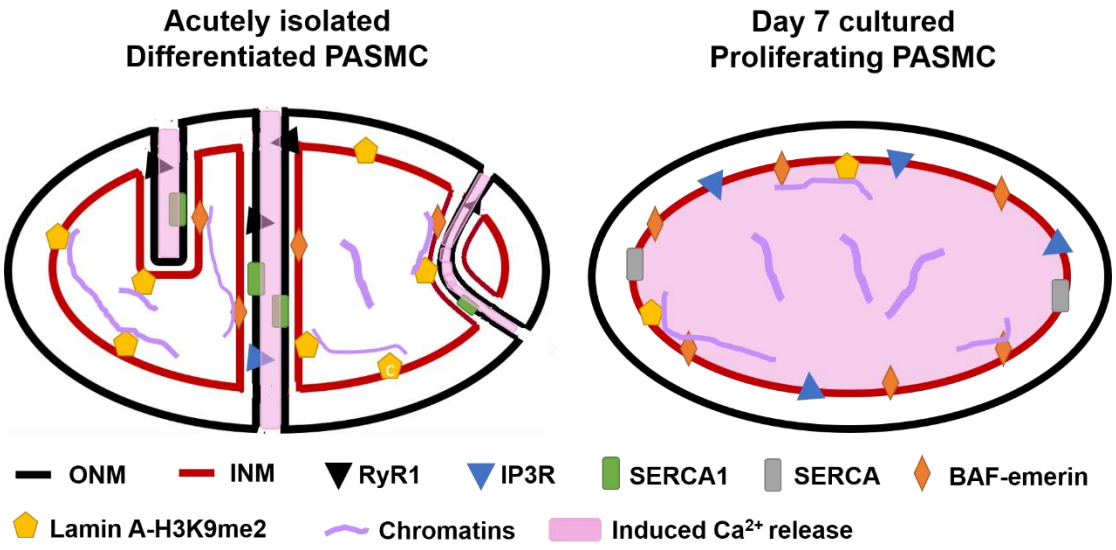

Figure 5.19 Schematic image showing the difference between differentiated and proliferating PASMCs.

Schematic images showing the nucleus of the differentiated PASMC (left) and the proliferating PASMC (right). The outer nuclear membrane (OMN), inner nuclear membrane (INM), RyR1, IP3R, SERCAs, BAF-emerin association, lamin A-H3K9me2 association, chromatins and intracellular free Ca^{2+} are labelled on the images.

Chapter 6: TPC2 mediates Ca^{2+} signalling in the lysosome-SR junction

6.1 Introduction

The two-pore segment channels (TPCs) (Ishibashi et al., 2000) were first identified as endolysosome targeted, NAADP-gated Ca^{2+} release channels (Calcraft et al., 2009, Schieder et al., 2010, Pitt et al., 2010). TPC1, 2 and 3, of which only TPCN1 and TPCN2 genes are present in humans, rats and mice (Calcraft et al., 2009, Zhu et al., 2010b), are homologous with and represent an evolutionary intermediate between Ca^{2+}-permeable TRPCs and voltage-gated Ca^{2+} channels (CaV), with an intermediate two-domain structure of subunits which likely assemble as homodimers (Zhu et al., 2010a).

Lysosome-SR nanojunctions have been identified in pulmonary arterial smooth muscle cells (Fameli et al., 2014). They were proposed to form a trigger zone for NAADP evoked Ca^{2+} bursts from the lysosomes (Kinnear et al., 2004). Lysosome targeted two-pore segmented channels have been proposed to support the generation of such Ca^{2+} bursts (Calcraft et al., 2009). However, significant controversy surrounds the capacity of TPC2 to support an NAADP-gated Ca^{2+} conductance, given that detailed investigations by others have demonstrated that stable expression of human TPC2 in several different mammalian cell types confers a phosphatidylinositol 3,5-bisphosphate [PI(3,5)P2-gated, Na^{+}-selective channel that is entirely insensitive to NAADP (Cang et al., 2013, Guo et al., 2017, Wang et al., 2012). Countering this, more recent studies suggest that PI(3,5)P2-mediated cation currents are observed in cells derived from Tpcn1 and Tpcn2 null mice while NAADP-gated Ca^{2+} currents are not. Moreover, NAADP-dependent Ca^{2+} currents are rescued in Tpcn1 and Tpcn2 null cells by overexpression of wild-type TPC2(Ruas et al., 2015). It is more intriguing that TPC2 has been shown to support a Na^{+} conductance that is gated by dissociation of mechanistic Target of Rapamycin (mTOR) from the cytoplasmic domain of TPC2 (Cang et al., 2013).

Given the above, I sought to determine whether or not TPC2 is a pre-requisite for the induction of lysosomal Ca^{2+} signals in pulmonary arterial myocytes and the role of

mTOR in these processes.

6.2 Results

6.2.1 Rapamycin induces Ca^{2+} signals via acidic stores in an mTOR- and TPC2-dependent manner in pulmonary arterial myocytes

The work of my colleague Dr. Oluseye Ogunbayo showed that extracellular application of the mTOR inhibitor rapamycin (30 μmol/L) induced Ca^{2+} transients in freshly isolated PASMCs (Ogunbayo et al., 2018). Figure 6.1 Ai-Di shows 4 different PASMCs loaded with the Ca^{2+} indicator Fura-2, the bright field images of cells are displayed on the left hand side, followed from left to right by a series of pseudocolour images representing the changes in Fura-2 fluorescence intensity in response to rapamycin; blue indicates low Ca^{2+}concentration whereas high Ca^{2+} concentrations are shown in red. The Fura-2 fluorescence ratio (F340 / F380) was calculated and plotted against time as the records in Figure 6.1 Aii-Dii show. Rapamycin induced pronounced Ca^{2+} transients in PASMCs, and the responses were mostly biphasic, characterized by a single rapid, global Ca^{2+} transient which was superimposed on an underlying, slower transient (black, Figure 6.1 Ai, Ci &Di). Occasionally the initial, fast Ca^{2+} transient was followed by multiple smaller transients, which were all superimposed on the slower underlying Ca^{2+} signal (black, Figure 6.1 Bi). Assessment of this response based on the peak of the first Ca^{2+} transient triggered by rapamycin demonstrated that the Fura-2 fluorescence ratio (F340 / F380) of the peak change is 1.2±0.14 (black, n=32, Figure 6.1 Ei, Appendix 4, Table 6.1). The Area Under Curve (AUC) was also calculated, and AUC of the response induced by rapamycin was 60±11.77 (black, n=56, Figure 6.1 Eii, Appendix 4, Table 6.1). To confirm that the response was truly induced by rapamycin, the effect of the drug vehicle was tested. Figure 6.1 Aii shows a record (green) which illustrates that the drug vehicle (DMSO) did not induce any response, the peak change and AUC of the DMSO responses were 0.03±0.007 (green, n=35, Figure 6.1 Ei, Appendix 4, Table 6.2) and 3.0±0.23 (green, n=35, Figure 6.2 Eii, Appendix 4, Table 6.2), respectively, which is significantly smaller than the peak change and AUC of the rapamycin response ($p<0.0001$).

Outcomes for pharmacological interventions against rapamycin-induced Ca^{2+} signals in pulmonary arterial myocytes are illustrated in Figure 6.1. The red record in Figure 6.1 Aii shows that rapamycin-evoked Ca^{2+} transients were blocked by prior depletion

of acidic Ca^{2+} stores with bafilomycin-A1 (1 μmol/L; n = 12, Figure 6.1 Bii). The peak change and AUC were 0.07±0.01 (red, n=12, Figure 6.1 Ei) and 13±3.5 (red, n=12, Figure 6.1 Eii), respectively, which were significantly reduced compared to that of the rapamycin responses obtained under control conditions ($p<0.001$). The Ca^{2+} transients induced by rapamycin were attenuated by depleting the SR Ca^{2+} stores with thapsigargin (1 μM ; n = 15, $P<0.0001$; Figure 6.1 Cii), the peak change and AUC were reduced to 0.24±0.05 (red, n=15, Figure 6.1 Ei) and 10.7±1.90 (red, n=15, Figure 6.1 Eii) respectively ($p<0.001$). Following block of RyRs with ryanodine at micromolar concentrations (100 μM), rapamycin-induced Ca^{2+} transients were also attenuated (n = 24, $P<0.001$; Figure 6.1 Cii) with the peak change and AUC reduced to 0.27±0.14 (red, n=8, Figure 6.1 Ei) and 23±10.15 (red, n=8, Figure 6.1 Eii) respectively ($p<0.001$). Moreover, the rapamycin induced response was abolished by pre-incubation with the L-type voltage-gated Ca^{2+} channel blocker nifedipine (10 μmol/L; n = 24; Figure 6.1 Di). The peak change and AUC were 0.12±0.01 (red, n=12, Figure 6.1 Ei) and 3.72±0.44 (red, n=12, Figure 6.1 Eii), and they both were significantly reduced compared to the rapamycin response.

The Ca^{2+} transients were blocked upon the depletion of bafilomycin-A1 sensitive Ca^{2+} store, suggesting that the Ca^{2+} is likely released from the lysosomal Ca^{2+} store (Ogunbayo et al., 2018). Moreover, the rapamycin-induced and NAADP-induced (not shown) Ca^{2+} transients were abolished by the VGCC blocker nifedipine, indicating that dihydropyridines block TPC2. Interestingly, the rapamycin induced Ca^{2+} transients were attenuated following the depletion of SR Ca^{2+} store and the blocking of RyRs. This is consistent with the view that the lysosome-SR junction forms a trigger zone for Ca^{2+}-induced Ca^{2+} release via RyRs targeted to the SR.

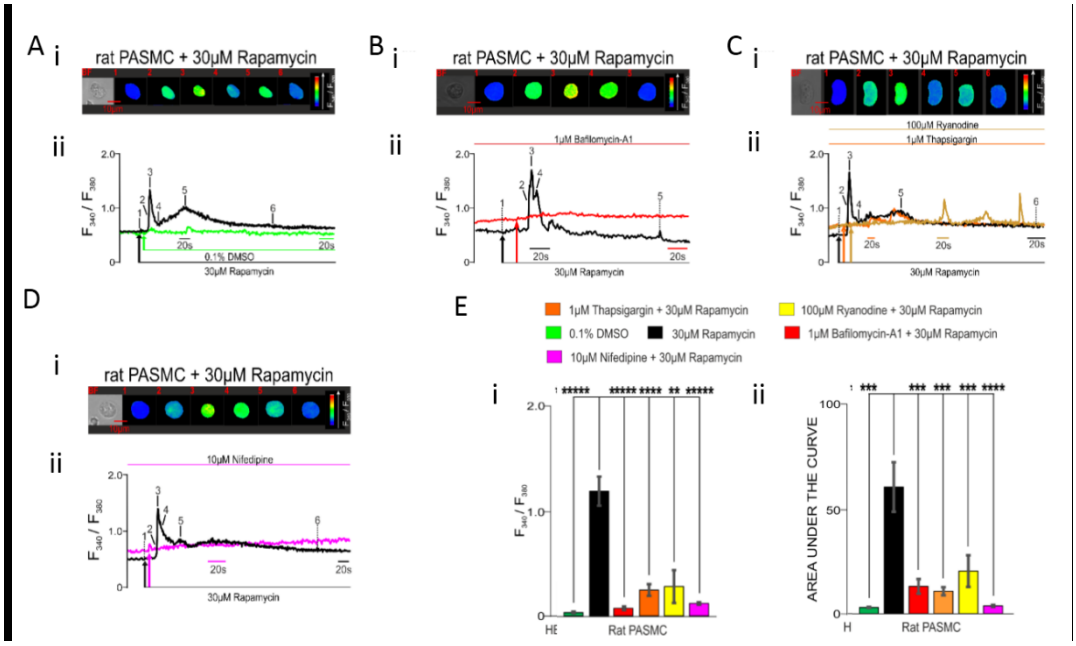

Figure 6.1 Rapamycin induces Ca^{2+} transients in pulmonary arterial myocytes, and the Ca^{2+} transients can be blocked by bafilomycin A1 and nifedipine

(Ai) The bright field image (BF) of an acutely isolated rat pulmonary arterial myocyte and a series of pseudocolour images of F340/F380 recorded in the same cell during extracellular application of 30μmol/L rapamycina are shown. (ii) Corresponding record (black) of F340/F380 ratio against time; the timepoints at which pseudocolour images were acquired are indicated by the numbered lines. The green record shows the effect of DMSO (vehicle control) in a different cell.
(B) As in (A) but with a red record showing the effect of rapamycin after pre-incubation (≥50 min) of a myocyte with 1 μmol/L bafilomycin A1.
(C) As in (A) but with an orange record showing the effect of rapamycin after pre-incubation (≥50 min) of a cell with 1 μmol/L thapsigargin.
(D) As in (A) but with a magenta record showing the effect of rapamycin after pre-incubation (≥50 min) of a myocyte with 10 μmol/L nifedipine, and a record in gold of the effect of rapamycin after pre-incubation (≥50 min) of a myocyte with 10 μmol/L ryanodine.
(Ei) Bar chart compares, under all conditions studied (see key), the mean ± SEM for the peak change in Rat PASMC with DMSO, n = 35; rapamycin, n = 32; rapamycin with bafilomycin-A1 preincubation, n = 12; rapamycin with thapsigargin preincubation, n = 15; rapamycin with ryanodine preincubation, n = 8; rapamycin with nifedipine preincubation n = 24. *P < 0.05, **P < 0.01, ***P < 0.001, ****P < 0.0001, *****P < 0.00001. (ii) as in (i) but for area under the curve.
Figure adapted from “mTORC1 controls lysosomal Ca(2+) release through the two-pore channel TPC2”, by Ogunbayo et al (Ogunbayo et al., 2018).

Moreover, Dr. Oluseye Ogunbayo also showed that rapamycin (30 μM) failed to induce measurable Ca^{2+} transients in pulmonary arterial myocytes derived from

Tpcn2 knockout mice as Figure 6.2 shows, the F340 / F380 ratio increasing marginally, from 0.40±0.03 to 0.45±0.03 (Figure 5A-B, n=18, P<0.00001 compared to wild type). This shows that rapamycin induces Ca^{2+} signals in an mTOR-and TPC2-dependent manner (Ogunbayo et al., 2018).

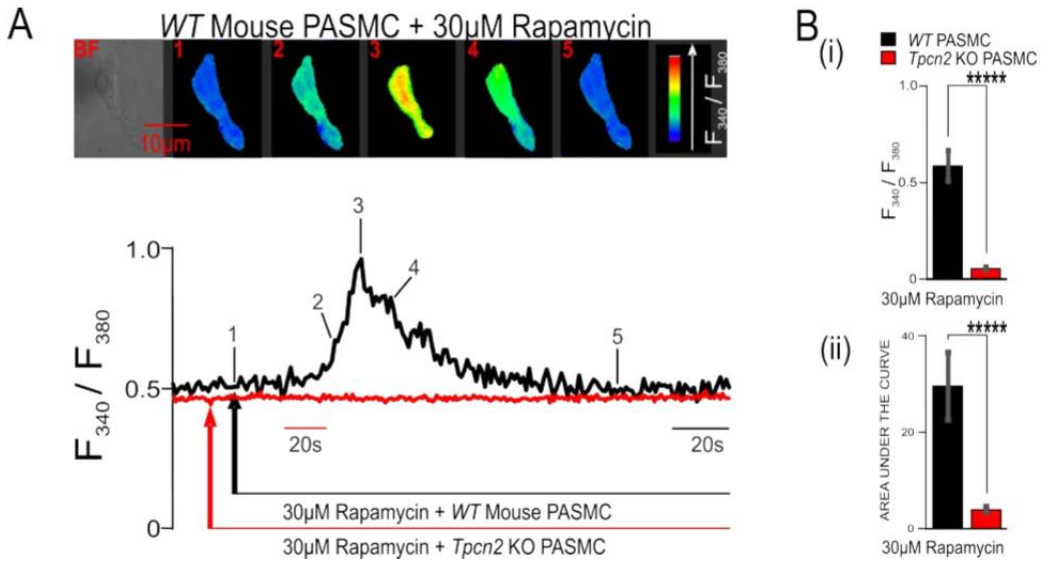

Figure 6.2 Rapamycin-induced Ca^{2+} transients in pulmonary arterial myocytes are blocked by deletion of TPC2
(A) Upper panel shows a bright field image (BF) of a wild type (WT) mouse PASMC, and a series of pseudocolour images of the Fura-2 fluorescence ratio (F340/F380) recorded in the same cell during extracellular application of 30 μmol/L rapamycin. Lower panel, corresponding record (black) of F340/F380 ratio against time; the time points at which pseudocolour images were acquired are indicated by the numbered lines. The red record shows the response to 30 μmol/L rapamycin of a myocyte isolated from a Tpcn2 knockout (Tpcn2KO) mouse.
(B) Bar charts show the mean ± SEM for (i) the peak change in F340/F380 during the 1st transient recorded and (ii) the area under the curve during the response of each cell to rapamycin: WT PASMC + 30μM rapamycin, n = 5; Tpcn2KO PASMC + 30μM rapamycin, n = 18. *****P < 0.00001.
Figure adapted from “mTORC1 controls lysosomal Ca(2+) release through the two-pore channel TPC2”, by Ogunbayo et al (Ogunbayo et al., 2018).

6.2.2 HEK293 cells that stably overexpress GCaMP5-TPC2 reveal that rapamycin evokes bafilomycin- and nifedipine-sensitive Ca^{2+} signals proximal to TPC2

To determine whether or not rapamycin-evoked Ca^{2+} signals were indeed elicited from lysosomes in a manner supported by TPC2, HEK293 cells that stably over-expressed GCaMP5-hTPC2 were used (generated and supplied by Dr. M.X. Zhu, University of Texas Medical School at Houston). In these cells the genetically encoded Ca^{2+} indicator GCaMP5 was fused to the cytoplasmic N-terminus of TPC2, allowing detection of Ca^{2+} signals arising proximal to TPC2. In order to confirm the localisation of GCaMP5-TPC2, HEK293 cells were co-labelled with Lysotracker Red (Figure 6.3). An exemplary HEK293 cell is shown in Figure 6.3A, with GCaMP5 fluorescence in green (left panel), the Lysotracker Red labelling in red (middle panel) and the two images merged to show co-localisation in yellow (right panel). Lysotracker Red labelled small vesicles, and some of the vesicles formed a big static cluster. Moreover, the merged image shows that GCaMP5-hTPC2 specifically labelled Lysotracker Red positive vesicles. To confirm this, the region of the cluster was magnified as Figure 6.3B shows. Indeed, by merging the GCaMP5 fluorescence (green, left panel) and the Lysotracker Red fluorescence (red, middle panel) it can be observed that the GCaMP5 tagged TPC2s were mostly colocalized with Lysotracker identified lysosomes (Pearson's correlation coefficient=0.56), suggesting that the TPC2s were specifically targeted to lysosomes. One example vesicle was selected and shown in Figure 6.3C. A digital skin was applied to the GCaMP5 and Lysotracker Red fluorescence, and a 3D model of the vesicle was rendered. The 3D model was sectioned through the middle, with half of it shown in Figure 6.3 C. It is obvious that the lysosome (red, middle panel) was lined by GCamP5 fluorescence (green, left panel) on the extracellular surface, consistent with the prediction that the TPC2s are specifically targeted to the lysosomes (Ogunbayo et al., 2018).

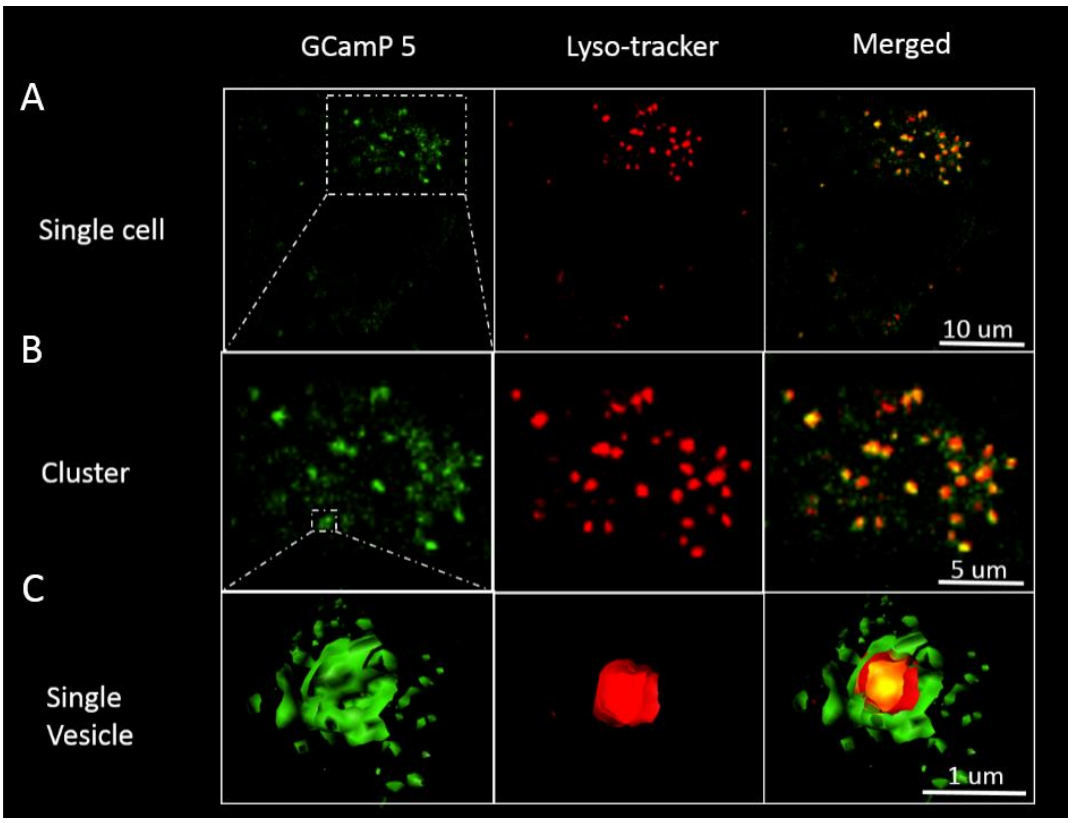

Figure 6.3 TPC2s were specifically targeted to lysosomes in HEK293 cells that stably over-express GCaMP5-TPC2.
(A) Deconvolved confocal images show a 3D reconstruction, from left to right, of a single HEK293 cell stably expressing GCaMP5-hTPC2 (green), the distribution of Lysotracker-red (red) labelling within the same cell and a merged image depicting regions of colocalisation (yellow).
(B) As for (A), but showing one identified cluster.
(C) As for (A), but showing half of an identified vesicle coated with digital skin.
Figure adapted from "mTORC1 controls lysosomal Ca(2+) release through the two-pore channel TPC2", by Ogunbayo et al (Ogunbayo et al., 2018).

Using confocal microscopy, I next investigated the effect of mTOR inhibition by rapamycin on GCaMP5-hTPC2 fluorescence intensity. Extracellular application of rapamycin induced pronounced increases in GCaMP5-hTPC2 fluorescence. Figure 6.4 A upper panels, show a series of pseudolour images that depict the time-dependent increase in GCaMP5 fluorescence after application of 30 μM rapamycin in

one examplary cell, the record of fluorescenc intensity versus time is shown in the lower panel. It is clear that extracellular application of rapamycin induced slowly developing increase in fluorescence that arose and decayed over the course of 60-120s (black record, Figure 6.4 A lower panel; n=11), and this was restricted to the vicinity of a static cluster of TPC2 positive lysosomes. The green record in Figure 6.4 A, lower panel shows the response to the vehicle control (DMSO; 1:1000), which confirms that vehicle alone failed to induce increases in GcAMP5 fluorescence at the concentration used. The peak change and AUC of the rapamycin response reached 276±61AU (black, n=11, Figure 6.4 Ci, Appendix 4, Table 6.3) and 299444±59487 (relative area, black, n=11, Figure 6.4 Cii, Appendix 4, Table 6.3) respectively, which is significantly higher than the peak change and AUC of the response to DMSO, which measured 57±15AU and 102395±13996 respectively (n=8, Appendix 4, Table 6.4, $p<0.001$).

Interestingly, following depletion of the thapsigargin-sensitive SR Ca^{2+} stores, rapamycin-induced increases in GCaMP5 fluorescence were similar to controls (black, Figure 6.4 B lower panel). The Peak change and AUC of the thapsigargin-insensitive signals were 229±15 AU (blue, n=5, Figure 6.4 Ci, Appendix 4, Table 6.5) and 333100±80628 (relative area, blue, n=5, Figure 6.2 Cii Appendix 4, Table 6.5) respectively, which are not statistically different from the measurements of the rapamycin response under control conditions. Importantly, outcomes for pharmacological interventions against rapamycin-induced increases in GCaMP5 fluorescence were consistent with what was shown in PASMCs. Rapamycin-induced increases in GCaMP5 fluorescence were blocked by prior depletion of acidic stores by bafilomycin (1 µmol/L, magenta, Figure 6.4 B lower panel), the peak change and AUC were reduced to 81±15 AU (magenta, n=10, Figure 6.4 Ci, Appendix 4, Table 6.6) and 167351±16636 (relative area, magenta, n=9, Figure 6.4 Cii, Appendix 4, Table 6.6) respectively ($p<0.001$). Furthermore, the response was also blocked by pre-incubation with nifedipine (10 µmol/L, red, Figure 6.4 B lower panel), the peak change and AUC were reduced to 71±8 AU (red, n=6, Figure 6.4 Ci Appendix 4, Table 6.7) and 97296±13875 (relative area, red, n=6, Figure 6.4 Cii Appendix 4, Table 6.7) respectively ($p<0.001$).

Therefore, I conclude that the inhibition of mTOR by rapamycin can trigger Ca^{2+} release lysosomal Ca^{2+} stores in a TPC2-dependent manner, due to the facts that

increases in GCaMP5-TPC2 fluorescence were abolished by either depleting lysosomal Ca^{2+} stores using bafilomycin or by blocking TPC2s with the VGCC blocker nifedipine (Ogunbayo et al., 2018). That increases in GCaMP5-TPC2 fluorescence in the vicinity of lysosomes was not affected by depleting the thapsigargin sensitive SR Ca^{2+} store suggest that the initial Ca^{2+} release was indeed from the lysosome targeted TPCs, which is subsequently amplified by CICR via RyRs at lysosome-SR nanojunctions in pulmonary arterial myocytes. Therefore, my data also indicate that the slow, relatively sustained increase in cytoplasmic concentration triggered by rapamycin observed in PASMCs is supported by Ca^{2+} release from lysosomal Ca^{2+} stores, while the fast Ca^{2+} transients superimposed upon this phase may result from cycles of SR Ca^{2+} release triggered by CICR; these are likely too fast to be resolved by confocal microscopy used for the GCaMP5 experiments.

The experiment is done in collaboration with Dr. Oluseye Ogunbayo, who maintained the cell line and helped with AUC analysis and figure making.

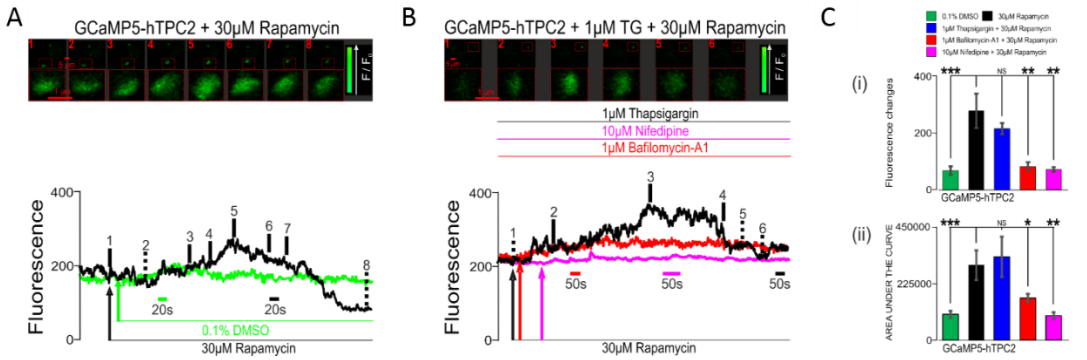

Figure 6.3 Rapamycin induces bafilomycin and nifedipine-sensitive Ca^{2+} signals proximal to lysosomes in HEK293 cells that stably over-express GCaMP5-TPC2.
(A) Upper panels show confocal images of an HEK293 cell overexpressing GCaMP5-hTPC2 (Green) during extracellular application of 30 μmol/L rapamycin. Lower panel, corresponding record (black) of fluorescence intensity (arbitrary unit, AU) against time; the time points at which confocal images were acquired are indicated by the numbered lines. The green record shows the effect of DMSO (vehicle control) in a different cell.
(B) As in B but showing the response of a thapsigargin (1μM) preincubated cell to 30 μmol/L rapamycin (black), and the effect of preincubation with bafilomycin A1 (1μM, red) and nifedipine (10μM, pink) on basal fluctuations in GCaMP5-hTPC2 fluorescence and the response of these cells to 30 μmol/L rapamycin.
(C) Bar charts show the mean ± SEM for (i) the peak change in GCaMP-5 fluorescence intensity (arbitrary unit, AU) and (ii) the area under the curve during the

response to rapamycin: GCaMP5-hTPC2 + DMSO, green, n = 8; GCaMP5-hTPC2 + rapamycin, black, n = 11; GCaMP5-hTPC2 + bafilomycin-A1 + rapamycin, red, n = 9; GCaMP5-hTPC2 + thapsigargin + rapamycin, blue, n =5; GCaMP5-hTPC2 + nifedipine + rapamycin, pink, n = 6). *P < 0.05, **P < 0.01, ***P < 0.001.
Figure adapted from “mTORC1 controls lysosomal Ca(2+) release through the two-pore channel TPC2”, by Ogunbayo et al (Ogunbayo et al., 2018).

6.3 Discussion

The role of TPC2 in lysosomal Ca^{2+} signalling was examined by using fully differentiated, acutely isolated pulmonary arterial myocytes to examine the (Fameli et al., 2014, Kinnear et al., 2004, Kinnear et al., 2008) in combination with HEK293 cell lines stably over-expressing human TPC2 and *Tpcn2* knockout mouse line, and the results showed that TPC2 is a pre-requisite for global Ca^{2+} transients in response to the mTOR inhibitor rapamycin (Ogunbayo et al., 2018).

We found that rapamycin, the mTOR inhibitor (Ballou and Lin, 2008), can effectively induce Ca^{2+} signals in rat PASMCs, and the Ca^{2+}signal was abolished following the preincubation with bafilomycin A1 (Ogunbayo et al., 2018). Bafilomycin A1 is a specific inhibitor of Vacuolar-type H^{+}-ATPase (Yoshimori et al., 1991), it was shown to increase lysosome PH and decrease lysosomal Ca^{2+} concentration by mobilising the lysosomal Ca^{2+} into the cytoplasm (Christensen et al., 2002). This suggests that the rapamycin induced Ca^{2+} release arose from the lysosomal Ca^{2+} store. Moreover, the rapamycin induced Ca^{2+} release was attenuated following the depletion of thapsigargin or ryanodine sensitive Ca^{2+} store. Thapsigargin blocks SERCAs that feed the ER/SR (Lytton et al., 1991), whereas the preincubation with ryanodine receptor at micro molar level inhibits the ryanodine receptors (Zhang and Zhu, 1997). Similar to NAADP induced Ca^{2+} signals, the rapamycin induced Ca^{2+} was attenuated following the depletion of the ER/SR Ca^{2+} store or blocking the ryanodine receptors, this indicates that the rapamycin induced Ca^{2+}release is possibly amplified by CICR via the ryanodine receptors on the ER/SR, assisted by the formation of the lysosome SR-nanojunction.

Furthermore, the NAADP induced Ca^{2+} release via TPC2 was inhibited by VGCC blockers (Genazzani et al., 1997), and here the rapamycin induced Ca^{2+} transient was also abolished by the VGCC blocker nifedipine. This finding led to the consideration that rapamycin my induced Ca^{2+}release via the TPC2s targeted to the lysosomes. To test this, Tpcn2 knockout mice were generated, and rapamycin failed to induce measurable Ca^{2+} transients in myocytes derived from Tpcn2 knockout mice. This shows that rapamycin induces Ca^{2+} in a TPC2-dependent manner.

This conclusion received further support from HEK293 cells that stably over-expressed GCaMP5-hTPC2. Our results showed that rapamycin can effectively induce Ca^{2+} release via the lysosome targeted TPC2s. This Ca^{2+} signal was not affected by depleting the thapsigargin sensitive Ca^{2+} stores, but is abolished following the depletion of the lysosomal Ca^{2+} store and the VGCC blocker nifedipine. Given above, it can be pustulated that the mTOR inhibitor rapamycin induces Ca^{2+} release from the lysosomal Ca^{2+} store mediated by the TPC2.

We conclude, albeit small when compared to their estimated Na^{+} permeability, it would appear that endogenous TPC2 may support Ca^{2+} signalling via lysosome-SR nanojunctions in pulmonary arterial myocytes and other cell types, and in a manner that may be triggered by inhibition of mTOR (Fameli et al., 2014, Kinnear et al., 2004, Kinnear et al., 2008, Ogunbayo et al., 2018), as has recently been suggested by computer simulations (Fameli et al., 2014) and electrophysiological investigations on the ion selectivity conferred by the filter sequence of the human TPC2 channel pore (Guo et al., 2017). This is not entirelyl inconsistent with the findings of others which suggest that mTOR is an endogenous inhibitor of PI(3,5)P2-gated Na^{+} currents carried by TPC2 (Cang et al., 2013). The significance of this observation may lie in the fact that mTOR-dependent autophagic flux has been implicated in the progression of pulmonary hypertension, for which current therapies are poor (Goncharov et al., 2014). TPC2 may therefore represent a novel therapeutic target for interventions against idiopathic pulmonary hypertension and pulmonary hypertension secondary to, for example, lysosomal dysfunction associated with Pompe and Gaucher disease (Noori et al., 2002, Jmoudiak and Futerman, 2005).

Chapter 7: General Discussion

7.1 Summary of Findings

Nanocourses of the SR are observed in the PASMCs, they form a cell-wide web for Ca^{2+} signalling underpinned by strategic positioning of RyRs. RyR1 is preferentially targeted to the subplasmalemmal nanocourses and nuclear invaginations, whereas the RyR 2& 3 may target to the extraperinuclear and perinuclear region as reported before. As the result, the Ca^{2+} signalling generated from different cytoplasmic nanocourses appear to support different smooth muscle functions. I show that the Ca^{2+} signals in the subplasmalemmal nanocourses triggered PASMC relaxation whereas the Ca^{2+} signals in the perinuclear and extraperinuclear nanocourses led to PASMC contraction.

Among the intracellular nanocourses, nuclear invaginations of the arterial myocytes are the most intriguing structure because they may demarcate site-and function-specific Ca^{2+} signalling in support of the transcriptional regulation. Invaginations of the outer nuclear membrane form a trans-nuclear network of cytoplasmic nanotubes in pulmonary arterial smooth muscle cells. Ca^{2+} pumps (SERCA1) and release channels (RyR1) are strategically positioned in the nuclear invaginations for the generation of Ca^{2+} signals arisen from the NR. Moreover, nuclear invaginations provide sites for transcriptional suppression, because lamin A and/or emerin line the entire surface of their inner nuclear membranes and co-localise with nesprin-1 positive puncta. Moreover, a subpopulation of these nuclear invaginations harboured punctate regions of colocalisation between lamin A and the suppressive heterochromatin mark H3K9me2, while emerin-positive invaginations harboured puncta of BAF co-localisation and thus an alternative pathway to the regulation of gene expression. Therefore, nuclear invaginations form cytoplasmic nanotubes within which nano-patterning of Ca^{2+} signals may support stochastic modulation of transcriptional regulators.

Chapter 5 shows that the proliferating PASMCs harboured less nuclear invaginations, and the remaining nuclear invaginations were reconfigured. In response to growth factor, the contractile phenotype PASMCs switched to a proliferating phenotype.

Following this change, the expression of RyRs, especially RyR1 seemed to be reduced and the Ca^{2+} release from the SR/NR relies majorly on IP3Rs. The nuclear invaginations in the proliferating PASMCs were reduced, and more importantly, they were remodelled compared to the nuclear invaginations identified in differentiated PASMCs. They were not lined by the NET proteins or protein complex, and therefore the chromatin attachment sites. Meanwhile, the remaining nuclear invaginations of the proliferating PASMCs lost the ability to generate spatially restricted Ca^{2+} signals due to the loss of RyR1s. Moreover, lamin A and emerin seemed to form two partially overlapped meshworks on the nuclear surface. Both the lamin A-H3K9me2 association and emerin-BAF association were identified on the meshworks albeit limited. The lamin A-H3K9me2 association was reduced compared to what is in the differentiated PASMCs whereas the emerin-BAF association is increased, and the changes perhaps favour less gene suppression that augments PASMC proliferation.

In this chapter, I will further discuss how the results in the thesis add to current understanding of intracellular Ca^{2+} signalling in PASMCs, and the means by which the spatially restricted Ca^{2+} signals demarcate smooth muscle functions.

7.2 Cytoplasmic nanocourses form a cell-wide web for the coordination of restricted intracellular Ca^{2+} signalling

The existence of multiple releasable SR pools in smooth muscle cell has been proposed and reported in multiple studies (Boittin et al., 2002, Clark et al., 2010a, Dipp et al., 2001, Yamazawa et al., 1992, Yang et al., 2005). These segregated SR Ca^{2+} pools are fed by different subtypes of SERCAs (Clark et al., 2010a), and the Ca^{2+} release from these segregated SR Ca^{2+} pools is mediated by different Ca^{2+} releasing channels. For example, IP3Rs and RyRs were reported to be spatially separated and non-gated in PASMCs (Boittin et al., 2002) and gallbladder smooth muscle (Morales et al., 2005). Moreover, RyR1, 2 and 3 are reported to target different SR compartments (Yang et al., 2005, Kinnear et al., 2008) and mediate Ca^{2+} signalling locally. However, it remains unclear that how the Ca^{2+} signals arisen from the segregated SR compartments are separated.

My data show that the cytoplasmic nanocourses of the SR span from the subplasmalemmal region to the nucleoplasm, forming a broad network for segregated

and spatially restricted Ca^{2+} signalling. Ca^{2+} signals arisen from and restricted within different nanocourses direct different smooth muscle functions. The Ca^{2+} signals in the subplasmalemmal nanocourses trigger pulmonary arterial myocytes relaxation whereas the Ca^{2+} signal in the perinuclear and extraperinuclear nanocourses induces pulmonary arterial myocytes contraction. The Ca^{2+} signals in the nuclear invaginations, on the other hand, is likely the key to the regulation of chromatin attachment sites. Given above, the cytoplasmic nanocourses allow the regulation of a variety of physiological processes, from the modulation of blood pressure to gene expression, by a single messenger - Ca^{2+}. It was further illustrated that the ability of generating differential Ca^{2+} signals in different nanocourses was conferred by the strategic targeting of RyRs subtypes.

7.2.1 Strategic targeting of the RyR subtypes in cytoplasmic nanocourses

In pulmonary arterial smooth muscle cells, RyR1, RyR2 and RyR3 were targeted to different compartments of SR (Clark et al., 2010; Gilbert, Ducret, Marthan, Savineau, & Quignard, 2014). In combination with the published data, I proposed that the RyR1 are localised to the subplasmalemmal nanocourses where SERCA2b serves as the dominant Ca^{2+} pump. RyR3s are primarily targeted to the perinuclear nanocourses where SERCA2a was found majorly. RyR2s are mainly clustered in the extraperinuclear nanocourses. In the nucleus, RyR1s are targeted to the NR for the generation of Ca^{2+} signals from this SERCA1 fed store. There is no doubt that the sophisticated arrangement of SERCAs and RyRs supports regulation of restricted Ca^{2+} signals in the cytoplasmic nanocourses and thus underpins a variety of physiological processes. The question is, what is the logic behind the arrangement of the Ca^{2+} releasing channels and pumps?

To address this issue, the characteristics of the three types of RyRs must be understood first. RyR 1 was identified primarily in skeletal muscles (Takeshima et al., 1989) whereas RyR2 was widely expressed in cardiac muscles (Otsu et al., 1990), RyR3 was found originally in the brain (Hakamata, Nakai, Takeshima, & Imoto, 1992). As the name indicated, the RyRs can be activated by ryanodine for Ca^{2+} release but only at the nanomolar range. When exposing to ryanodine at 100 micromolar or more, RyRs would be locked at a subconductance that inhibits Ca^{2+} release (Meissner,

1986). However, it should be noted that although all the RyR subtypes have similar threshold for activation by Ca^{2+} when cytoplasmic Ca^{2+} concentration is higher than 100 nM, each RyR subtypes display different half maximal activation by Ca^{2+} (EC50) and thresholds for inactivation by Ca^{2+} (Chen, Li, Ebisawa, & Zhang, 1997; Li & Chen, 2001). The Ca^{2+} release mediated by RyR3 is unlikely to be compromised considering its low sensitivity to inactivation by Ca^{2+}.Therefore, RyR3 can amplify Ca^{2+} signals by Ca^{2+} induced Ca^{2+} release, and contribute to the propagation of global Ca^{2+} waves. Moreover, RyR2 is primarily targeted to the extraperinuclear region and therefore the extraperinuclear nanocourses with no specific type of SERCA co-localised (Clark et al., 2010). Inferring from its low EC50 compared to RyR3 and relatively lower sensitivity to inactivation by Ca^{2+}, it was proposed that the RyR2 can be easily activated and is capable of carrying propagating Ca^{2+} waves in a manner that is not prone to failure (Evans, 2010, Evans et al., 2016). This role of RyR2 fits my observation that the vasoconstrictor triggered Ca^{2+} wave was initiated from extracellular nanocourses and propagated across the cells. In short, it is highly likely that RyR2 are majorly targeted to the extraperinuclear nanocourses that occupy the major volume of the “bulk cytoplasm”, the RyR2s in the extraperinuclear nanocourses that are close to the cell periphery are easily activated, which gives rise to Ca^{2+} signals that are amplified and propagated by neighbouring extraperinuclear nanocourses and perinuclear nanocourses, causing a global elevation of Ca^{2+} concentration which eventually leads to smooth muscle contraction.

RyR1, on the other hand, exhibits low IC50 of inhibition by Ca^{2+}, which means RyR1 is easily closed when exposing to high Ca^{2+} concentration. When the global Ca^{2+} wave is triggered by the vasoconstrictor, huge Ca^{2+} influx was induced from both the SR and the extracellular space, therefore it is very likely that the RyR1s in the subplasmalemmal nanocourses are rapidly inhibited. This explains why there is very limited subplasmalemmal Ca^{2+} increase in response to Angiotensin II. When RyR1 is activated alone, it may result in elevation of Ca^{2+}concentration within a range that is 1) sufficient to breach the threshold for the activation plasma membrane targeted BK_{ca} channels, and 2) not high enough to inhibit RyR1s in the subplasmalemmal nanocourses.

In the nuclear invaginations, the only resource of Ca^{2+} is the Ca^{2+} release from the

NR, therefore this signal is not readily inhibited, as I showed in Chapter 3. Due to the low IC50 of inhibition of RyR1, the Ca^{2+} transient generated within the nuclear invaginations are none propagative. Moreover, the huge Ca^{2+} waves originated form the perinuclear nanocourses are unlikely to diffuse to the nuclear invaginations due to their geometry. As the result, the nuclear invaginations can give rise to unique Ca^{2+} signals that are segregated from the perinuclear Ca^{2+} signals.

The aforementioned hypothesis depicts a simplified picture. In fact, each type of nanocourses harbour one major subtype of RyR, but clusters of all 3 types of RyRs might be found in one nanocourse. Moreover, the Ca^{2+} handling in those cytoplasmic nanocourses involves more types of Ca^{2+} channels and transporters, for example the BKca in the subplasmalemmal nanocourses as discussed above, and more commonly the SR targeted SERCAs and perhaps IP_3Rs.

7.2.2 Strategic targeting of the SERCA subtypes in cytoplasmic nanocourses

Similar to the RyR subtypes, SERCA2a and SERCA2b were strategically targeted to functionally segregated SR compartments to support distinct physiological processes (Clark et al., 2010). As I proposed in Chapter 3, SERCA2b may target to superficial SR, and underpins the functioning of subplasmalemmal nanocourses, which is consistent with the proposal that SERCA2b supports the function of PM-SR junction (Evans, Fameli, Ogunbayo, Duan, & Navarro-Dorado, 2016). In contrast, SERCA2a was proposed to target to central SR and support Ca^{2+} fluxes which underpins vasoconstriction (Clark et al., 2010), therefore it may target to the perinuclear nanocourses. SERCA1, is exclusively found in the nuclear region of the PASMCs and it targets to the nuclear invaginations and feeds the NR. Here one question was raised, what properties of the SERCAs underlie this sophisticated subcellular arrangement?

One early experiment reported that SERCA2b has a higher affinity for Ca^{2+} (K0.5 0.17±0.01μM) compared to SERCA2a (K0.5 0.31±0.02μM) (Verboomen et al., 1992). Moreover, SERCA2b displayed lower Vmax compared to SERCA2a (Verboomen et al., 1994). Based on those facts it was postulated that SERCA2b might be dominant at rest to maintain a low level of the cytoplasmic Ca^{2+} level near the contractile apparatus (Evans et al., 2016, Evans, 2010). When encounter a major influx of Ca^{2+}

that causes contraction, SERCA2b is easily saturated which 1) allows the increase of Ca^{2+} level near the contractile apparatus (Evans et al., 2016, Evans, 2010, Clark et al., 2010a), and 2) allow the increase of Ca^{2+} concentration in the subplasmalemmal nanocourses and consequently inhibit RyR1. SERCA2a on the other hand, is able to remove Ca^{2+} quickly due to the high Vmax, it may function to recycle Ca^{2+} into perinuclear SR to support regenerative Ca^{2+} waves, but it was proposed to be dominant only when huge amount of Ca^{2+} is restricted (Evans et al., 2016), i.e. in the nanocourses, and it is perhaps not heavily relied on under quiescent conditions considering the low affinity for Ca^{2+}.

SERCA1 was discovered in the fast type skeletal muscle, two isoforms of SERCA 1 were identified, namely the adult isoform SERCA1a and neonatal isoform SERCA1b (Maruyama and MacLennan, 1988). I showed the expression of SERCA1 in the nucleus of the PASMCs acutely isolated from rat. Our antibody does not differentiate between the two SERCA1 isoforms, but considering that the cells are isolated from adult rat, the nuclear SERCA1 we identified are most likely SERCA1a. No clear difference between SERCA1a and 1b in terms of their ability to transport Ca^{2+} and affinity for Ca^{2+} was identified (Maruyama and MacLennan, 1988), however, a functional difference between nuclear invagination targeted SERCA1a and perinuclear nanocourse targeted SERCA2a has been reported. SERCA2a and SERCA1 share similar affinity for Ca^{2+}, which is lower that than of SERCA2b (Periasamy and Kalyanasundaram, 2007), therefore SERCA1a facilitates fast accumulation of Ca^{2+} in the nuclear invaginations, which may give rise to fast Ca^{2+} signals when required. However, SERCA1a exhibits the highest pump velocity compared to the SERCA2s (Sumbilla et al., 1999, Periasamy and Kalyanasundaram, 2007), which suggests they can effectively remove Ca^{2+} from the nuclear invaginations when the Ca^{2+} concentration is too high. This would 1) prevent RyR1 inhibition by high Ca^{2+} concentration, and 2) quickly remove the Ca^{2+} and cease the Ca^{2+} signal. As the result, SERCA1a facilitates the generation of fast and transient Ca^{2+} signals, which may regulate downstream process dynamically. For example, as discussed in Chapter 4, the mode of BAF-emerin interaction is in a “touch-and-go” manner, and this fast and dynamic interaction must be directed by fast and instant upstream signals, just like the proposed mode of action of the Ca^{2+} signalling in the nuclear invaginations.

7.2.3 IP_3Rs may also target to the cytoplasmic nanocourses

Although not tested, I do not exclude the possibility that IP_3Rs are targeted to some of the cytoplasmic nanocourses. As the result, some of the spontaneous Ca^{2+} activity may as well be the Ca^{2+} puffs from IP_3Rs. Ca^{2+} puffs are localised Ca^{2+} transients that arise from the liberation of Ca^{2+} through the concerted opening of tightly clustered IP_3Rs from the ER/SR Ca^{2+} store (Smith and Parker, 2009, Dickinson et al., 2012). They are observed and characterized in smooth muscle cells (Boittin et al., 2000). Although it is shown that the angiotensin II induced Ca^{2+} signals in the cytoplasmic nanocourses are blocked by the RyR inhibitor tetracaine, one can not assert that IP_3 induced Ca^{2+} signals are not observed in nanocourses due to the fact that tetracaine was reported to inhibit IP_3 induced Ca^{2+} signals in one case (MacMillan et al., 2005). More importantly, it was documented that the IP3Rs clustered are separated by 500 nm or less, which fits with the nano-patterning of the hotspots observed in the nanocourses (Smith and Parker, 2009). Therefore, both the RyR clusters and IP_3R clusters might support Ca^{2+} signalling within the cytoplasmic nanocourses of PASMCs for the coordination of smooth muscle functions, and the role of IP_3Rs in the processes requires further investigation.

Moreover, it was reported that IP_3Rs and RyRs are spatially separated in smooth muscle cells (Boittin et al., 2002, Morales et al., 2005), however, the mechanism by which they are separated remains unclear. Here, I propose that the cytoplasmic nanocourses may provide the physical separation between RyRs, and IP_3Rs. As the result, the two receptors may give rise to spatially restricted Ca^{2+} signals that regulate different smooth muscle functions (Morales et al., 2005). To conclude, the Ca^{2+} signalling in the cytoplasmic nanocourses may involve multiple SR targeted Ca^{2+} channels and transporters and their strategic positioning, the current model is far more simplified, and it surely requires future studies.

7.3 Nuclear invaginations and their proposed function.

7.3.1 Proposed functions of nuclear invaginations in nuclear Ca^{2+} signalling in literature.

Nuclear invaginations have been identified in multiple cell types, and the consensus was that they are the extension of the NE that invaginate into the nuclear interior. The

NE was proposed to serve as a buffer barrier that prevents direct Ca^{2+} diffusion from the cytoplasm to the nucleoplasm in early research (al-Mohanna et al., 1994). Contradictory to this view, it was proposed that the formation of invaginations increases the surface area of the nuclear envelope, which consequently increased the number of nuclear pore complexes which would accelerate the entry of cytosolic Ca^{2+} into the nucleoplasm (Bootman et al., 2009). Other studies suggested the nucleoplasmic reticulum could be a potential releasable Ca^{2+} store, considering it is contiguous with ER, and it may play a fundamental role in nuclear Ca^{2+} signalling via ion channels targeted to the NE (Malhas et al., 2011, Echevarria et al., 2003). The nuclear invaginations may bring cytosolic messengers close to the nucleoli or other effectors located within the nucleus, and thus assists effective nuclear site-specific signalling.

In support of this view, it was reported that the IP3Rs are expressed on the nuclear envelope and deep invaginations that form nucleoplasmic reticulum (Avedanian et al., 2011). Whether IP3Rs are localised to the ONM or INM is still controversial. People had visualized the cytoplasmic domain of IP_3Rs on the NE of isolated nuclei of Sf9 cells with electron microscopy, this suggests that IP_3Rs are targeted to the ONM (Cardenas et al., 2010). However, it was described by other studies that IP_3 induces Ca^{2+} release toward the nucleus. IP_3 induced intranuclear Ca^{2+} elevations in isolated acinar pancreatic nuclei (Gerasimenko et al., 2003), and SKHep1 cells (Echevarria et al., 2003). Moreover, in GH3 pituitary cells, IP_3 induced nuclear response is not blocked by the addition of cytosolic heparin that selectively blocks cytoplasmic IP_3R because they cannot pass through the NPCs (Leite et al., 2003). In short, the aforementioned evidence supports the argument that IP_3Rs are targeted to the NE and thus to modulate nuclear Ca^{2+} signalling.

RyRs were also found on the NE and nuclear invaginations in human vascular smooth muscle cells (Avedanian et al., 2011). Nuclear Ca^{2+} release was achieved by applying the RyR agonist cADPR in the intranuclear region, and the Ca^{2+} signal was blocked by RyR inhibitors and inhibitory RyR antibodies (Santella and Kyozuka, 1997). In another study, uncaged Ca^{2+} was placed in the vicinity of the nucleoplasmic reticulum, which results in a significant nuclear Ca^{2+} burst that subsequently spread to the cytoplasm. The placement of caged Ca^{2+} in the nucleoplasm by photorelease also

generated a nuclear Ca^{2+} signal which was followed by an amplified Ca^{2+} signal that spread to the cytoplasm. Furthermore, the observed Ca^{2+} signals were abolished in the presence of dantrolene, a RyR inhibitor (Marius et al., 2006). These facts led to a consideration that RyRs might mediate Ca^{2+}signalling within the nucleus, which may spread to the cytoplasm.

7.3.2 Concurrent proposals of the role of nuclear Ca^{2+} signalling in the regulation of gene expression

Nuclear Ca^{2+} signals may affect gene transcription by manipulating the translocation of transcription factors into the nucleus from the cytosolic region. Alternatively, it also activates enzymes that are required for the translocation of transcription factors.

Nuclear factor of activated T cells (NFAT) are a group of proteins that activate gene transcription. They are majorly localised in the cytosol of quiescent cells. In response to increased cytosolic Ca^{2+} concentration. NFAT is dephosphorylated by calcineurin, a Ca^{2+}-calmodulin-sensitive-phosphatase. The modification enables NFAT translocation into the nucleus as well as the exposure of its conserved nuclear localization sequence. Increased Ca^{2+} concentration within the nucleus reinforces the association between NFAT and calcineurin while keeping calcineurin activated. The interplay is crucial to NFAT activation because calcineurin competes with kinases that re-phosphorylate NFAT which could subsequently export NFAT out of the nucleus (Rinne et al., 2009).

Similar regulatory patterns were also found in the activation of cyclic AMP response element-binding protein (CREB). Significant increases of cytosolic Ca^{2+} concentration near N-methyl-D-aspartate receptors or L-type Ca^{2+} channels initiate a signal cascade which ultimately leads to the phosphorylation of CREB on Ser133 by Ca^{2+}-calmodulin-dependent-kinase IV. Nuclear Ca^{2+} increase is also required for the activation of CREB co-activator to achieve gene transcription (Chawla et al., 1998).

Downstream regulatory element antagonist modulator (DREAM) is a transcriptional regulator that suppresses the expression of prodynorphin. Four Ca^{2+} binding EF

hands were found on DREAM, which enable it to be manipulated by nuclear Ca^{2+} signals directly. Under low nuclear Ca^{2+} concentration, DREAM competes with and results in the dissociation of transcription activators including CREB to supress gene transcription (Ledo et al., 2002).

7.3.3 My results suggest a new model of Ca^{2+} signalling in nuclear invaginations, which may regulate chromatin attachment and therefore gene expression

Against the views above, I show that the RyR1s are targeted to the ONM of nuclear invaginations in differentiated PASMCs. The nuclear invaginations form isolated cytoplasmic nanodomains that could effectively restrict Ca^{2+} signals generated via RyR1 from the local NR Ca^{2+} store. The released Ca^{2+} is buffered from the nucleoplasm, as my data showed no evidence of any propagation to the proximal nucleoplasm from these nanotubes in PASMCs, although this may not be true in other cell type.

The nuclear invaginations are selectively lined by the NET proteins and therefore the chromatin anchoring NET protein complexes. Not only emerin but also nesprin-1α co-localised with the nucleoplasmic surface of lamin A labelled nuclear invaginations. nesprin-1 α was shown to interact with RyR 1(Pare et al., 2005a, Pare et al., 2005b). As the result, charge redistribution across the NET protein complexes and thus the capacity for gene suppression by BAF or the lamin associated domains, could be triggered by the gating of RyR1 and further modulated by the subsequent regulation of RyR1 gating and/or desensitisation via the nano-scale Ca^{2+} signalling patterns arising along the length of a given nuclear invagination.

Invaginations of the NR form highly plastic and heterogeneous chromatin attachment sites that line the cytoplasmic nanotubes, they are demarcated by the strategic positioning of specific Ca^{2+} release channels (RyR1) and Ca^{2+} transporters (SERCA1), with different kinetics, “affinities” for Ca^{2+} and mechanisms of regulation when compared to those targeted to other cytoplasmic nanocourses as discussed in section 7.2. Here, for example, angiotensin II may evoke Ca^{2+} signals specific to a given invagination and in a manner segregated from, but informed by those signals that drive myocyte contraction. Although beyond the resolution of current technologies, within each nuclear invagination diverse Ca^{2+} signalling patterns may be delivered by

transients separated by ~300 nm, consistent with the dimensions and distances of separation between punctate complexes of BAF and emerin (~500nm), and lamin A and H3K9me2 (~300nm). Such signal segregation may help orchestrate interactions between lamin A, emerin and their respective binding partners (Burke & Stewart, 2013), informing chromatin re-organisation and ultimately transcription by modulating, for example, BAF and H3K9me2 attachment sites. Moreover, the sizes of the punctate complexes of BAF and emerin (150-600 nm), and lamin A and H3K9me2 (200-600nm) fit with the estimated size of the RyR1 clusters (several hundred nm). It appears plausible, therefore, that the activities of such nuclear envelope transmembrane complexes may be governed, as previously (Strelkov et al., 2004) predicted, by the redistribution of electrostatic charge across macromolecular complexes that span the ONM and INM of nuclear invaginations, and through chromatin-modifying enzymes (some of which are Ca^{2+}-dependent, i.e. HDAC) targeted to the nanospaces conferred by each invagination (Zuleger et al., 2011). In this way, nuclear invaginations could provide capacity for the coordination of transcription through parallel processing of nano-scale Ca^{2+} signals that govern alterations in transcriptional potential that contribute to, for example, vascular remodelling in health (Gomez et al., 2002) and disease (Bierer et al., 2011, Suzuki et al., 2002).

However, to confirm that the Ca^{2+} signalling can modulate gene expression by demarcating chromatin attachment, direct evidence must be provided. Due to the limitation of technology, we cannot monitor gene expression in live acutely isolated PASMCs upon Ca^{2+} signalling in the nuclear invaginations. To test the hypothesis, we might need to 1) induce Ca^{2+} signals in the nuclear invaginations alone but not the cytoplasm; 2) monitor the changes in chromatin attachment along the nuclear invaginations; 3) assess the changes in gene expression. This is one of the future experiment I aim to conduct.

7.3.4 Proliferating PASMCs provided a model of nuclear invagination that is not able to generate spatially restricted Ca^{2+} signals, and these nuclear invaginations are not lined by chromatin-anchoring proteins.

The proliferating PASMCs provided a great model for comparing with the nuclear invaginations in differentiated PASMCs. I show that the nuclear invaginations of the

differentiated PASMCs are lined by chromatin anchoring NET protein complexes, and I proposed that the nuclear invaginations give rise to specially restricted Ca^{2+} signals for the regulation of chromatin attachment and thus gene suppression. However, in proliferating PASMCs, the chromatin anchoring NET proteins are dissociated from the nuclear invaginations whereas the expression of RyR1 is heavily reduced or even eliminated. It is difficult to infer whether the rearrangement of NET proteins is induced by RyR1 reduction or the other way around, but the fact that the chromatin attachment sites and spatially restricted Ca^{2+} signals are either co-existing in one phenotype or both absent from the other phenotype further supports the argument that they are perhaps functionally correlated.

In support of this view, it was observed that the distribution of BAF-emerin association is correlated to the Ca^{2+} signalling pattern. In differentiated PASMCs, the Ca^{2+} signal is restricted in the nuclear invaginations, and the BAF-emerin association is majorly found on the nuclear invaginations compared to the nuclear periphery. In contrast, the induced Ca^{2+} signals were propagated across the entire nucleoplasm in proliferating PASMCs. Correspondingly, the BAF-emerin association is enriched at the nuclear periphery of the proliferating PASMCs. In either phenotype, the BAF-emerin association is always maintained in close contact with the Ca^{2+} signals, indicating the possibility that the chromatin attachment is modulated by the Ca^{2+} signals.

The major difference between the differentiated and proliferating PASMCs lies in the changes in gene expression, i.e. the expression of the contractile apparatus and proliferating markers (Gomez and Owens, 2012, Rensen et al., 2007). Perhaps the Ca^{2+} signals do modulate the suppression or induction of these markers in response to the environment, as the Ca^{2+} handling is altered during the smooth muscle phenotypic switch (Berra-Romani et al., 2008).

7.4 Conclusions

It was proposed before that the SR in smooth muscle cells form functionally segregated compartments underpinned by differential targeting of RyRs and SERCAs and that they give rise to Ca^{2+} signals for the regulation of smooth muscle functions (Figure 7.1 A). Adding pieces to the puzzle, I propose a new model (Figure 7.1B) that the segregated SR compartments give rise to Ca^{2+} signals that are segregated by and

restricted within the cytoplasmic nanocourses, because the RyR1, 2, 3 and SERCA2a, 2b,1 are strategically targeted to those nanocourses. These nanocourses and the spatially restricted Ca^{2+} signals demarcate a series of smooth muscle functions, from smooth muscle relaxation and contraction to gene expression.

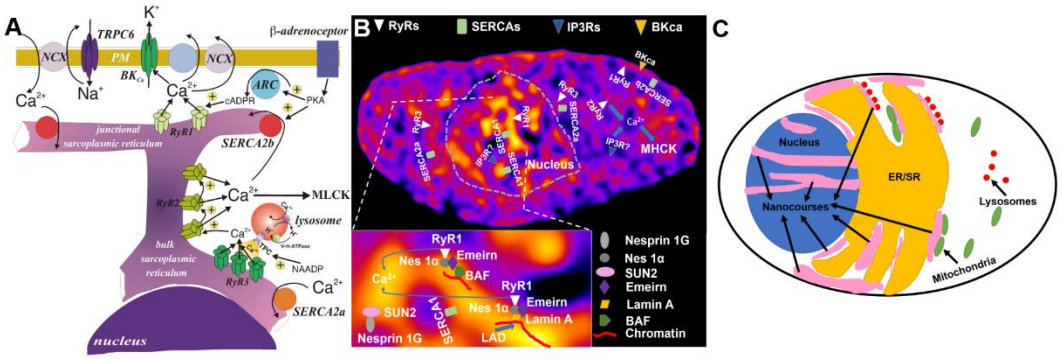

Figure 7.1 Developing view on spatially restricted Ca^{2+} signalling for the regulation of smooth muscle functions

(A) A schematic image showing the old view on functionally segregated SR compartments. Adapted from (Evans et al., 2016).

(B) The new model of spatially restricted Ca^{2+} signalling segregated by cytoplasmic nanocourses and how they demarcate smooth muscle functions.

(C) A schematic image showing the proposed new model of cytoplasmic nanocourses (pink) and Ca^{2+} signalling.

7.5 Limitations and future experiments

Acutely isolated PASMCs are physically stretched and treated with enzyme during the isolation process. During imaging, they are positioned under strong laser that may "fry" the cells. As the result, most of the cells are hampered, and it is difficult to find a cell that survives the isolation, remains resistant to the strong laser and stays intact and viable till the end of the confocal experiment. Within these cells, there is still a population that is moderately damaged that they are not able to maintain the nanocourses and respond to stimuli. Therefore, it is extremely difficult to record a cell that shows the nanocourses and is able to generate Ca^{2+} signals within. After months

of experimentation, I only managed to image 3 cells as such. To overcome this problem, live cell imaging with intact artery can be conducted. Cell isolation can be avoided by conducting whole artery issection and live tissue confocal imaging, which reduces damage to the cell. Moreover, it would be interesting to visualize the intracellular nanocourses in the intact arteries, as they would appear in nature. Different Ca^{2+} indicators should also be applied, which helps to confirm that the differential intensity of Fluo-4 in the nanocourses at rest is not caused by varied micro-environments but varied basal Ca^{2+} concentration. For example, Mag-fura 2 staining or Calcium crimson staining.

The amplitudes of Ca^{2+} fluxes and induced Ca^{2+} transients were only measured within selected nanocourses that displayed little movements, because the nanocourses are very dynamic, and tracing them manually would result in inaccurate and biased measurements. The quantitative analysis may benefit from the application of computer software that would trace the nanocourses automatically. As the result, relatively accurate measurement can be taken from all the nanocourses, which may reinforce my conclusion.

A third future experiment I aim to conduct is to monitor the BAF-emerin association and lamin-A association following the induction of Ca^{2+} signals in live cells, and assess the changes in gene expression in response to the Ca^{2+} signals in the nuclear invaginations. The experiment would provide direct evidence that shows 1) whether the chromatin attachment is modulated by Ca^{2+} signals, and 2) whether the Ca^{2+} signal in the nuclear invaginations regulates gene expression. The assessment of gene expression can be achieved by RT-qPCR, RNA sequencing or detecting the mRNA level by conducting RNA scope assays.

Appendix 1

Result Tables of Chapter 3

Table 3.1 Distance of separation between hotspots (nm) within the subplasmalemmal nanocourses, extraperinuclear nanocourses, perinuclear nanocourses and nuclear invaginations.

	Subplasmalemmal hotspots	Extraperinuclear hotspots	Perinuclear hotspots	Nuclear hotspots
	201	275	332	313
	236	253	435	295
	369	234	407	297
	469	321	379	330
	304	348	357	388
	395	374	359	308
	308	405	351	480
	315	434	618	297
	370	435	586	266
	431	530	579	437
	395	529	525	361
	508	499	259	408
	343	673	640	301
	304	518	625	310
	312	268	309	291
	359	417	467	325
	359	546		405
	481	348		358
	341	361		438
	374	333		390
	324	534		
	283	475		
	401	386		
	338	449		
	461			
Mean	359.2	414.4	451.8	349.9
S.E.M	14.75	22.42	31.63	13.49

Table 3.2 Amplitude of the Ca^{2+} sparks at hotspots (nm) within the subplasmalemmal nanocourses, extraperinuclear nanocourses, perinuclear nanocourses and nuclear invaginations in acutely isolated PASMCs. The index of amplitude was converted from ΔFX/F0 of the Fluo-4 intensity.

	Subplasmalemmal hotspots	Extraperinuclear hotspots	Perinuclear hotspots	Nuclear hotspots
	0.131569	0.166558	0.133988	0.150716
	0.157402	0.197348	0.123504	0.23179
	0.158674	0.166558	0.143178	0.269106
	0.251254	0.097348	0.141368	0.131568
	0.109225	0.200599	0.093909	0.160334
	0.161402	0.099046	0.165642	0.176198
	0.085476	0.107325	0.110269	0.21397
	0.132508	0.131816	0.110859	0.099456
	0.128482	0.104754	0.183797	0.209038
	0.138959	0.128821	0.107505	0.172258
	0.114364	0.076511	0.140358	0.131085
	0.078533	0.098623	0.149515	0.157969
	0.249131	0.173118	0.115201	0.160699
	0.365298	0.109897	0.069908	0.030743
	0.127836	0.038779	0.224009	0.016481
	0.068025	0.169781	0.152304	0.181409
	0.164866	0.12218	0.097652	0.139719
	0.057768	0.193237	0.227914	0.157666
	0.035673	0.175658	0.098241	0.091685
	0.17801	0.14238	0.37524	0.138779
	0.140343	0.360987	0.229389	0.141609
	0.220683	0.35189	0.255042	0.043598
	0.599305		0.163032	0.013197
	0.222436		0.148229	0.426819
	0.170442			0.102267
	0.455819			0.207409
	0.201754			0.096514
Mean	0.181675	0.155146	0.156669	0.150077
S.E.M	0.02362	0.016538	0.01362	0.016237

Table 3.3 Amplitude of the Ca^{2+} sparks at hotspots (nm) within the subplasmalemmal nanocourses, extraperinuclear nanocourses, perinuclear nanocourses and nuclear invaginations in PASMCs preincubated with 1μM of thapsigargin for 1 hour. The index of amplitude was converted from ΔFX/F0 of the Fluo-4 intensity.

	Subplasmalemmal hotspots	Extraperinuclear hotspots	Perinuclear hotspots	Nuclear hotspots
	0.039761	0.100028	0.069746	0.013985
	0.061225	0.131462	0.129566	0.077648
	0.118495	0.053462	0.069625	0.056738
	0.108271	0.043546	0.043639	0.052314
	0.035585	0.063761	0.058697	0.07284
	0.057203	0.051683	0.084801	0.068332
	0.036699	0.057695	0.070841	0.078988
	0.061971	0.091575	0.081227	0.092324
	0.036257	0.039423	0.049913	0.051151
	0.034469	0.054095	0.064628	0.078962
	0.113401	0.081476	0.030033	0.129241
	0.034382	0.095602	0.08156	0.0257
	0.028941	0.070349	0.025773	0.042879
	0.036877	0.042996	0.037416	0.095547
	0.028127	0.114912	0.080152	0.041915
	0.030123	0.08483	0.034316	0.049397
	0.036147	0.08391	0.068532	0.04105
	0.067766	0.123053	0.095612	0.152836
	0.012479	0.082725	0.152595	0.132921
	0.061093	0.131714	0.061505	0.093162
	0.12872		0.069185	
	0.167224		0.119188	
	0.082584			
	0.073251			
	0.154048			
Mean	0.065804	0.079915	0.071752	0.072397
S.E.M	0.008489	0.006609	0.006771	0.008089

Table 3.4 Frequencies of the Ca^{2+} sparks at hotspots (number per second) within the subplasmalemmal nanocourses, extraperinuclear nanocourses, perinuclear nanocourses and nuclear invaginations in PASMCs.

	Subplasmalemmal hotspots	Extraperinuclear hotspots	Perinuclear hotspots	Nuclear Hotspots
	0.15	0.16	0.17	0.12
	0.16	0.13	0.15	0.14
	0.15	0.16	0.15	0.13
	0.125	0.15	0.15	0.15
	0.15	0.15	0.125	0.15
Mean	0.147	0.15	0.149	0.138
S.E.M	0.005831	0.0054772	0.0071414	0.005831

Table 3.5 Frequencies of the Ca^{2+} sparks at hotspots (number per second) within the subplasmalemmal nanocourses, extraperinuclear nanocourses, perinuclear nanocourses and nuclear invaginations in PASMCs preincubated with 1μM of thapsigargin for 1 hour.

	Subplasmalemmal hotspots	Extraperinuclear hotspots	Perinuclear hotspots	Nuclear hotspots
	0.18	0.167	0.167	0.18
	0.16	0.2	0.183	0.15
	0.18	0.167	0.16	0.15
	0.125	0.15	0.15	0.15
	0.175	0.125	0.15	0.15
Mean	0.164	0.1618	0.162	0.156
S.E.M	0.0104163	0.0122613	0.0061563	0.006

Table 3.6 Amplitudes and frequencies of the Ca^{2+} sparks at nuclear hotspots in PASMCs preincubated with 1mM of tetracaine for 4 hour.

	Nuclear hotspot	
	Amplitudes	**Frequencies**
	0.066912	0.13
	0.192013	0.17
	0.120445	0.15
	0.074545	0.175
	0.139385	0.125
	0.149805	0.15
	0.086561	0.15
	0.059116	
	0.202875	
	0.12923	
	0.083446	
	0.030853	
	0.123916	
	0.058413	
	0.019413	
	0.073691	
	0.059368	
Mean	0.098235	0.15
S.E.M	0.012732	0.006986

Table 3.7 Peak changes of the Ca^{2+} transients after extracellular application of 300 nM maurocalcine, measured at the hotpots within the subplasmalemmal nanocourses, extraperinuclear nanocourses, perinuclear nanocourses and nuclear invaginations in PASMCs .

	Subplasmalemmal hotspots	**Extraperinuclear hotspots**	**Perinuclear hotspots**	**Nuclear hotspots**
	1.272071	0.503374	0.41125	1.291595
	1.073014	0.485226	0.288277	1.726202
	0.999028	0.422486	0.356511	0.70771
				2.114983
Mean	1.114704	0.470362	0.352013	1.460123
S.E.M	0.081531	0.024505	0.03557	0.301961

Table 3.8 Peak changes of the Ca^{2+} transients after extracellular application of 300 nM maurocalcine, measured within the subplasmalemmal nanocourses, extraperinuclear nanocourses, perinuclear nanocourses and nuclear invaginations in PASMCs .

	Subplasmalemmal nanocourses	Extraperinuclear nanocourses	Perinuclear nanocourses	Nuclear nanocourses
	1.009831	0.349799	0.247907	0.991589
	1.103231	0.434695	0.272455	1.429193
	1.000755	0.335009	0.154848	0.594752
				1.811832
Mean	1.037939	0.373168	0.22507	1.206842
S.E.M	0.032751	0.031058	0.035819	0.264014

Table 3.9 Cell area (μM^2) before and after extracellular application of 300 nM maurocalcine.

	Before maurocalcine addition	After maurocalcine addition
	21.645	23.454
	27.929	30.732
	32.609	34.587
Mean	27.39	29.59
S.E.M	3.176	3.264

Table 3.10 Peak changes of the Ca^{2+} transients after extracellular application of 30 μM angiotensin II, measured within the subplasmalemmal region, extraperinuclear region, perinuclear region and nuclear invaginations in PASMCs .

	Subplasmalemmal nanocourse	Extraperinuclear nanocourse	Perinuclear nanocourse	Nuclear Invagination
	0.125294	1.372749	1.112321	1.783748
	-0.04629	0.223504	0.216356	0.676727
	0.185156	1.27624	1.761254	2.293166
	0.629815	1.248178	1.522193	2.590571
	1.461936	2.009568	3.137771	
	0.962765	1.514761	1.65743	3.301197
	0.253627	0.511072	0.522853	0.988954
	-0.10283	0.162559	0.237438	0.567486
Mean	0.4337	1.04	1.271	1.743
S.E.M	0.1929	0.235	0.346	0.3945

Table 3.11 Cell area (μM^2) before and after extracellular application of 30 μM angiotensin II maurocalcine.

	Before angiotensin II addition	After angiotensin II addition
	129.987	122.44
	86.026	82.187
	125.44	105.28
	104.832	83.491
	118.018	109.737
	104.439	89.771
	110.361	93.163
	29.576	24.284
Mean	101.1	88.79
S.E.M	11.31	10.43

Table 3.12 Basal Ca^{2+} level in the nucleus or the nuclear invaginations of the PASMCs

	Nucleus	Nuclear Invagination
	1	1.63854
	1	2.351686
	1	2.455898
	1	2.157854
	1	2.199312
	1	2.452488
	1	1.926657
	1	3.886632
	1	1.453375
	1	1.485226
	1	2.861231
	1	2.090122
	1	2.391232
	1	4.178297
Mean	1	2.395
S.E.M	0	0.2139

Table 3.13 Peak changes of the Ca^{2+} transients after extracellular application of 300 nM maurocalcine, measured within the subplasmalemmal region, extraperinuclear region, perinuclear region and nuclear invaginations in PASMCs, or PASMCs preincubated with 1 µM thapsigargin for 1 hour, or 1nM tetracaine for 4 hours.

	Control		Thapsgargin preincubated		Tetracaine preincubated	
	Nucleus	Nuclear Invagination	Nucleus	Nuclear Invagination	Nucleus	Nuclear Invagination
	0.3337491	0.9915889	-0.21517	-0.26154	0.226776	0.464371
	1.007933	1.429193	0.018301	0.279764	0.303385	-0.00876
	-0.2727373	0.5947521	-0.02221	-0.1694	-0.22228	-0.23983
	0.1466857	1.811832	0.222742	0.517673	0.056163	-0.20428
	1.0500816					
	0.2636145					
Mean	0.4216	1.206842	0.0009158	0.09162	0.09101	0.002875
S.E.M	0.2105	0.264014	0.08979	0.1848	0.1165	0.162

Table 3.14 Peak changes of the Ca^{2+} transients after extracellular application of 30 μM angiotensin II, measured within the subplasmalemmal region, extraperinuclear region, perinuclear region and nuclear invaginations in PASMCs, or PASMCs preincubated with 1 μM thapsigargin for 1 hour, or 1nM tetracaine for 4 hours.

	Control		Thapsgargin preincubated	
	Nucleus	Nuclear Invagination	Nucleus	Nuclear Invagination
	1.125237	1.783748	0.19	0.25
	-0.0769	0.676727	0.19088	0.369722
	1.132993	2.293166	0.04	0.06
	0.197611	2.590571	0.37	0.25
	1.23964		0.078766	0.127927
	1.273363	3.301197		
	-0.03541	0.988954		
	-0.09747	0.567486		
Mean	0.5949	1.743	0.1739	0.2115
S.E.M	0.2288	0.3945	0.05744	0.05382

	Tetracaine preincubated		8-bromo cADPR preincubated	
	Nucleus	Nuclear Invagination	Nucleus	Nuclear Invagination
	0.120159	0.357267	0.302956	0.67123
	0.151981	0.203679	0.1125	0.11523
	0.208966	0.43937	0.426545	0.842806
	0.114616	0.106852		
Mean	0.1489	0.2768	0.2807	0.5431
S.E.M	0.02164	0.0748	0.09134	0.2196

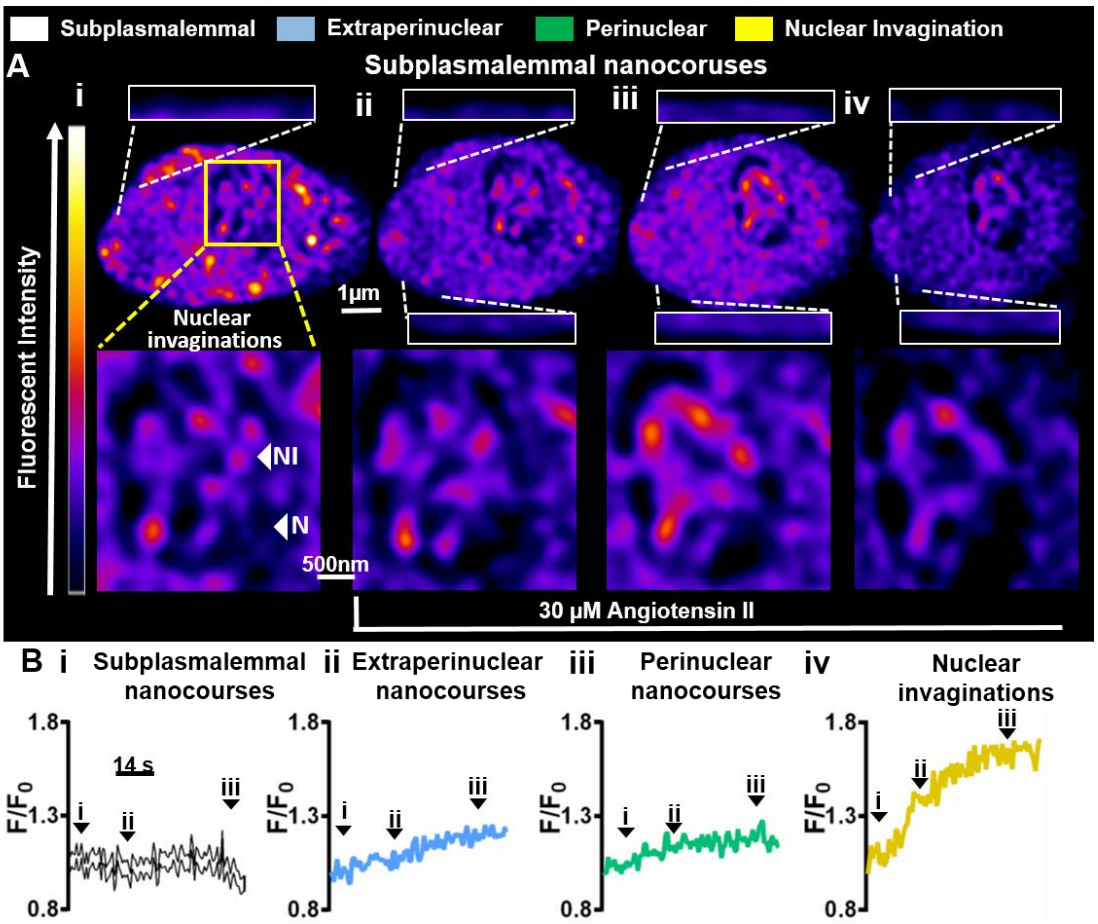

Figure 8.1 Vasoconstrictor triggers Ca^{2+} release in the extraperinuclear, perinuclear nanocourses and nuclear invaginations.

(A) A series of confocal scans through the middle of a pulmonary arterial smooth muscle cell loaded (25° C) with Fluo-4 is shown in the upper panels. Pseudocolour was applied to indicate high Fluo-4 intensity in white-yellow and low Fluo-4 intensity in blue-purple. The nucleus was drawn out by a yellow box. Subplasmalemmal nanocourses were magnified in the white boxes aligned at top and bottom. The response of the cell following the extracellular addition of 30 µM angiotensin II is shown by displaying the images of the cell at 4 time points (i-iv). The lower panels show the higher magnification images of the nucleus at the 4 time points (i-iv). Detection threshold was modified to show clearly the nuclear invaginations without signal saturation. The nucleus (N) and one nuclear invagination (NI) are indicated by white arrow heads.

(B) Fluo-4 fluorescence ratio (Fx/FC0) versus time for the regions of interests (subplasmalemmal region in white, extraperinuclear region in blue, perinuclear region in green, nucleus in black, nuclear invaginations in yellow) were plotted. F_0 = Fluo-4 fluorescence intensity for the region of interest at time 0; Fx = fluorescence intensity for the chosen region of interest at time point x.

Appendix 2

Results tables for Chapter 4

Table 4.1 Results of the linear regression analysis comparing lamin A density identified structures in pulmonary arterial smooth muscle cells, including the total invaginations with total peripheral structures, trans-nuclear invaginations with blind invaginations, trans-nuclear invaginations with superficial invaginations, ridges with clefts

	R Square	Equation
Total invaginations Vs Total peripheral structures	0.01145	Y = -0.3499*X + 34.91
Trans-nuclear invaginations Vs Blind invaginations	0.2373	Y = 0.4112*X + 1.060
Trans-nuclear invaginations Vs Superficial invaginations	0.02343	Y = 0.05637*X + 0.3203
Ridges Vs Clefts	0.11500	Y = 0.5658*X + 7.325

Table 4.2 Number of structures labelled by lamin B1 per acutely isolated pulmonary arterial smooth muscle cells

	Nuclear invaginations	Ridges	Clefts
	0	11	17
	0	10	10
	0	13	17
	0	22	15
	0	10	15
	0	14	13
	0	20	19
	0	12	18
	0	15	16
	0	10	16
	0	16	15
	0	14	22
Mean	0	13.92	16.08
S.E.M	0	1.125	0.8657

Table 4.3 Number of nuclear invaginations identified in each pulmonary arterial smooth muscle cell studied, and the number of nuclear invaginations labelled by SUN2 among those ones identified

Total Invaginations	Total Invaginations labelled by SUN2	Trans-nuclear invaginations	Trans-nuclear invaginations labelled by SUN2
0	0	0	0
2	2	0	0
0	0	0	0
0	0	0	0
1	1	0	0
0	0	0	0
1	0	1	0

Blind invaginations	Blind invaginations labelled by SUN2	Superficial invaginations	Superficial invaginations labelled by SUN2
0	0	0	0
0	0	2	2
0	0	0	0
0	0	0	0
0	0	1	1
0	0	0	0
0	0	0	0

Table 4.4 Volume of nesprin 1 labelling colocalized with SUN2 labelling in pulmonary arterial smooth muscle cells, and the Pearson's correlation coefficients between the two labelling

	Volume of Nesprin-1 labelling colocalised with SUN2 labelling	Pearson's correlation coefficiency
	56.98	0.4787
	47.31	0.2954
	45.94	0.321
Mean	50.08	0.365
S.E.M	3.474	0.05731

Table 4.5 Results of the linear regression analysis comparing emerin density identified structures in pulmonary arterial smooth muscle cells, including the total invaginations with total peripheral structures, trans-nuclear invaginations with blind invaginations, trans-nuclear invaginations with superficial invaginations, ridges with clefts

	R Square	Equation
Total invaginations Vs Total peripheral structures	0.05368	Y = -0.6420*X + 33.41
Trans-nuclear invaginations Vs Blind invaginations	0.105	Y = 0.5115*X + 1.126
Trans-nuclear invaginations Vs Superficial invaginations	0.005181	Y = -0.04962*X + 0.4542
Ridges Vs Clefts	0.001007	Y = 0.04501*X + 17.11

Table 4.6 Separations between the emerin-BAF colocalization puncta (nm) and the diameters of the puncta (nm) in pulmonary arterial smooth muscle cells

	Separation between the puncta (nm)	Diameters of the Puncta (nm)
	243	600
	212	210
	385	450
	1120	214
	251	250
	552	600
	994	150
	359	350
	502	462
	419	345
	240	254
	464	215
	450	580
	159	380
	907	
	644	
	367	
	660	
	486	
Mean	495.5	361.4
S.E.M	61.63	41.61

Table 4.7 Separations between the lamin A-H3K9me2 colocalization puncta (nm) and the diameters of the puncta (nm) in pulmonary arterial smooth muscle cells

	Separation between the puncta (nm)	Diameters of the Puncta (nm)
	340	230
	275	350
	183	576
	326	583
	152	470
	234	370
	363	487
	435	587
	918	467
	358	590
	248	
	270	
	326	
	390	
	215	
Mean	335.5	471
S.E.M	46.34	38.64

Appendix 3

Results tables for Chapter 5

Table 5.1 Number of nuclear invaginations per proliferating PASMC identified by ER-tracker.

	Number of nuclear invaginations per cell
	0
	0
	0
	0
	0
	0
	0
	0
	0
	0
	1
	1
	2
	3
	2
Mean	0.36
S.E.M	0.16207

Table 5.2. The index of basal Ca^{2+} concentration in the nucleoplasm and the cytoplasm of each cells studied, and peak changes in the nucleus and the cytoplasm in response to either 300 nM maorocalcine or 1μM thapsigargin

	Index of nuclear basal	Index of cytoplasmc basal	Index of nuclear peak change in response to maurocalicne	Index of cytoplasmic peak change in response to maurocalicne	Index of nuclear peak change in response to thapsigargin	Index of cytoplasmic peak change in response to thapsigargin
	0.509859	1	0.036358	0.020404	4.837826	3.404236
	0.523317	1	0.016949	0.000012	2.119578	1.780076
	0.842509	1	0.129325	0.106079	8.147806	5.117965
	0.526272	1	0.080489	0.046115	3.824164	2.37143
	0.588937	1	0.020045	0.038621	4.886705	3.473375
	0.581576	1	0.047261	0.176164	5.677141	3.633987
	0.629268	1	0.165791	0.001085	3.177792	2.075136
	0.697754	1	0.008314	-0.08179	2.384988	1.291088
	0.846434	1	0.59249	0.300968	2.480301	1.888536
	0.746802	1	0.328139	0.081002	2.856905	1.974071
	0.584531	1	0.276096	0.002665	3.2019	1.901735
	0.985156	1	0.0000034	0.025055	5.493281	3.329096
	0.768323	1	0.039722	0.043831	3.197432	1.880605
	0.973094	1	0.07316	0.046898	4.679192	2.973982
	0.928921	1	0.103943	0.324734	3.484982	2.22958
	0.854902	1	0.469832	-0.05784	2.278085	4.034003
Mean	0.7242	1	0.1492	0.06712	3.921	2.71
S.E.M	0.0415	0	0.04435	0.02826	0.4035	0.2591

Table 5.3 The index of basal Ca^{2+} concentration in the nucleoplasm and the cytoplasm of each cells studied, and peak changes in the nucleus and the cytoplasm in response to 30 μM Angiotensin II

	Nuclear Basal	Cytoplasmic Basal	Nuclear peak change Ang II	Cytoplasmic peak change Ang II
	0.5807299	1	6.94	2.755
	0.5230062	1	7.15	3.168
	0.6438746	1	2.89	1.452
	0.660381	1	4.72	1.92
Mean	0.6020	1	5.43	2.323
S.E.M	0.03143	0	1.01	0.39

Table 5.4 The index of peak changes in the nucleus and the cytoplasm in response to 30 μM Angiotensin II in the cells preincubated with 1 mM tetracaine (TTC), 1 μM thapsigargin (TG), 50 μM 2-APB or 3 μM U73122

	Nuclear Basal	Cytoplasmic Basal	Nuclear peak change Ang II	Cytoplasmic peak change Ang II
	1.07	1	6.94	2.755
	1.23	1	7.15	3.168
	0.64	1	2.89	1.452
	0.66	1	4.72	1.92
Mean	0.9	1	5.43	2.323
S.E.M	0.15	0	1.01	0.39

Nuclear peak change TTC preincubation	Cytoplasmic peak change TTC preincubation	Nuclear peak change TG preincubation	Cytoplasmic peak change TG preincubation
2.5271	1.32637	0.1471	0.02668
2.3296	1.54149	0.07362	0.0535
4.21057	2.46871	0	0
1.94765	1.02404	0.00624	0
5.62265	4.63797		
8.55002	5.40077		
4.198	2.733	0.05674	0.02005
1.038	0.7557	0.03442	0.0128

Nuclear peak change 2APB preincubation	Cytoplasmic peak change 2APB preincubation	Nuclear peak change U73122 preincubation	Cytoplasmic peak change U73122 preincubation
0.061	0.0234	0	0
0.0248	0.0433	0.06	0
0.1782	0.0446	0.01	0.02
0.0412	0.0092	0.11	0.25
0.0763	0.0301	0.04	0.07
0.0348	0.0085	0.03	0.06

Table 5.5 The number of nuclear invaginations per cell identified in the lamin A labelled proliferating PASMCs, and the surface to volume ratio ($\mu M^2/ \mu M^3$) in acutely isolated or proliferating PASMCs

	Number of nuclear invagination per proliferating PASMCs	Surface to volume ratio ($\mu M^2/ \mu M^3$) acutely isolated PASMCs	Surface to volume ratio ($\mu M^2/ \mu M^3$) proliferating PASMCs
	0	4.52906	1.43659
	0	7.13636	1.50355
	0	5.0152	2.34272
	0	3.41772	3.06154
Mean	0	5.025	2.086
S.E.M	0	0.7793	0.385

Table 5.6 The percentage of volume of nesprin-1 labelling colocalized with SUN 2 in acutely isolated cells or day 7 cultured cells, the percentage of volume of SUN 2 labelling colocalized with nesprin-1 in acutely isolated or day 7 cultured cells, The pearson's correlation coefficiency of the colocalization in acutely isolated cells or day 7 cultured cells Percentage of volume of SUN 2 labelling colocalized with nesprin-1 in acutely isolated cells

	Percentage of volume of nesprin-1 labelling colocalized with SUN 2 in acutely isolated cells	Percentage of volume of SUN 2 labelling colocalized with nesprin-1 in acutely isolated cells	Percentage of volume of nesprin-1 labelling colocalized with SUN 2 in day 7 cultured cells	Percentage of volume of SUN 2 labelling colocalized with nesprin-1 in day 7 cultured cells	Pearson's correlation coefficiency acutely isolated cells	Pearson's correlation coefficiency day 7 cultured cells
	56.98	53.24	75.56	52.34	0.4787	0.1252
	47.31	28.59	40.6	26.79	0.2954	0.1079
	45.94	38.19	45.49	17.42	0.321	0.1346
Mean	50.08	40.01	53.88	32.18	0.365	0.1226
S.E.M	3.474	7.174	10.93	10.44	0.05731	0.00782

Table 5.7 The percentage of volume of emerin labelling colocalized with lamin A in acutely isolated cells or day 7 cultured cells, the percentage of volume of lamin A labelling colocalized with emerin in acutely isolated or day 7 cultured cells, The pearson's correlation coefficiency of the colocalization in acutely isolated cells or day 7 cultured cells

	Percentage of volume of emeirn labelling colocalized with lamin A in acutely isolated cells	Percentage of volume of lamin A labelling colocalized with emerin in acutely isolated cells	Percentage of volume of emerin labelling colocalized with lamin A in day 7 cultured cells	Percentage of volume of lamin A labelling colocalized with emerin in day 7 cultured cells	Pearson's correlation coefficiency acutely isolated cells	Pearson's correlation coefficiency day 7 cultured cells
	44.74	33.85	45.26	64.4	0.0835	0.0767
	58.52	62.1	50.53	56.36	0.2893	0.03
	56.28	69.56	47	60	0.2876	0.058
	68.09	55.97			0.5423	
Mean	56.91	55.37	47.6	60.25	0.3007	0.0549
S.E.M	4.797	7.693	1.55	2.324	0.09392	0.01357

Table 5.8 The percentage of volume of emerin labelling colocalized with BAF in acutely isolated cells or day 7 cultured cells, the percentage of volume of BAF labelling colocalized with emerin in acutely isolated or day 7 cultured cells, The pearson's correlation coefficiency of the colocalization in acutely isolated cells or day 7 cultured cells

	Percentage of volume of emeirn labelling colocalized with BAF in acutely isolated cells	Percentage of volume of BAF labelling colocalized with emerin in acutely isolated cells	Percentage of volume of emerin labelling colocalized with BAF in day 7 cultured cells	Percentage of volume of BAF labelling colocalized with emerin in day 7 cultured cells	Pearson's correlation coefficiency acutely isolated cells	Pearson's correlation coefficiency day 7 cultured cells
	12.33	28.7	38.02	83.76	-0.1333	0.03
	14.76	20.16	48.14	58.58	-0.1204	-0.0288
	4.02	10.99	53.79	49.79	-0.0155	0.0048
	17	49.75	31.29	44.41	-0.1491	0.0177
	17.57	28			-0.0265	
	15.24	38			-0.0865	
	8.94	36.75			-0.0302	
	1.87	8.47			-0.0682	
	4.94	22.46			-0.1203	
	2.09	8.48			-0.1395	
Mean	9.876	25.18	42.81	59.14	-0.08895	0.005925
S.E.M	1.98	4.364	5.038	8.712	0.01609	0.01267

Table 5.9 The percentage of volume of lamin A labelling colocalized with H3K9me2 in acutely isolated cells or day 7 cultured cells, the percentage of volume of H3K9me2labelling colocalized with lamin A in acutely isolated or day 7 cultured cells, The pearson's correlation coefficiency of the colocalization in acutely isolated cells or day 7 cultured cells

	Percentage of volume of H3K9me2 labelling colocalized with lamin A in acutely isolated cells	Percentage of volume of lamin A labelling colocalized with H3K9me2 in acutely isolated cells	Percentage of volume of H3K9me2 labelling colocalized with lamin A in day 7 cultured cells	Percentage of volume of lamin A labelling colocalized with H3K9me2 in day 7 cultured cells	Pearson's correlation coefficiency acutely isolated cells	Pearson's correlation coefficiency day 7 cultured cells
	53.2	67.8	52.38	54.42	0.2279	-0.1841
	44.5	45.6	30.15	31.58	0.103	-0.1065
	46.5	64.5	32.68	26.82	0.0313	-0.1916
			44.99	28.2	0.2001	-0.0901
					0.2927	
					0.025	
					0.1216	
					0.0894	
Mean	48.07	59.3	40.05	35.26	0.1364	-0.1431
S.E.M	2.631	6.916	5.234	6.466	0.03377	0.02611

Appendix 4

Result tables for chapter 6

Table 6.1 Peak changes and area under curve of the Ca^{2+} response to 30μM rapamycin in PASMCs.

	30μM Rapamycin Peak Change	Area under curve	
	1.846288	193.8208	21.2602
	1.685022	284.1208	26.01439
	2.4005	202.4255	121.9845
	2.205113	59.01095	2.974608
	1.838464	132.3247	4.286159
	2.557419	71.28946	76.5145
	2.0758	362.4879	150.9634
	2.668044	442.4983	6.082609
	0.456	6.724051	3.516479
	0.824377	2.909037	89.59709
	0.546373	60.75317	31.80879
	0.736149	41.8527	8.948335
	0.364	36.45663	19.87766
	0.631941	22.10307	67.52199
	0.641724	21.06999	49.35669
	0.804339	7.452102	29.04057
	1.064549	31.18843	26.92941
	0.504113	32.57053	12.11392
	0.590381	8.018969	38.35737
	0.3525	32.51012	20.60985
	1.9797	108.5351	12.78839
	0.853891	86.97842	12.99878
	3.039872	5.565264	2.011897
	0.863074	1.659069	7.185016
	1.717431	1.923789	
	0.5122	39.19508	
	0.369165	4.630285	
	0.839385	54.91663	
	0.872021	128.5483	
	0.885329	20.88364	
	0.95219	13.92708	
	0.562	14.48983	
Mean	1.19498	60.27825675	
S.E.M	0.138969	11.76884924	

Table 6.2 Peak changes and area under curve of the Ca^{2+} response to 2μL DMSO in PASMCs

	2μL DMSO Peak Change		Area under curve	
	0.010667	0.004667	3.138071	2.764306
	0.007333	0.006381	2.563443	1.827629
	0.073333	0.029429	2.528163	3.238316
	0.037714	0.002857	3.952043	2.442861
	0.037048	0.008952	2.129717	2.196202
	0.020571	0.038667	2.680679	3.031384
	0.007143	0.072096	7.713808	3.704313
	0.002	0.030571	1.96709	1.848136
	0.035143	0.013121	5.781402	2.464735
	0.001905	0.12149	1.773827	2.334021
	0.031429	0.02284	2.698095	3.841661
	0.025238	0.016523	2.255026	1.656889
	0.035556	0.006318	6.436929	3.063363
	0.040794	0.003401	3.716242	1.947628
	0.016984	0.071619	3.667659	1.660012
	0.000476	0.063111	2.011877	2.545954
	0.00373	0.047841	3.485026	
	0.044286	0.002286	2.023573	
	0.046476	0.017079	2.773798	
	0.247143	0.458889		
Mean	0.033441422		2.967539143	
S.E.M	0.00700006		0.226303985	

Table 6.3 Peak changes and area under curve of the Ca^{2+} response to 30μM rapamycin in HEK293 cell stably expressing GCaMP5-hTPC2

	Peak change induced by 30uM Rapamycin	Area under curve
	233.1314	247736.7
	364.184	311506.3
	127.2018	361413.3
	130.4578	100375.3
	726.5482	100024.5
	107.8726	642808.9
	109.853	71837.02
	276.2546	182774.4
	233.7618	227307.8
	559.169	607097.3
	177.9142	441003.6
Mean	276.9408	299444.1
S.E.M	60.55672	59487.61

Table 6.4 Peak changes and area under curve of the Ca^{2+} response to 2µL DMSO in HEK293 cell stably expressing GCaMP5-hTPC2

	Peak change in response to 2uL DMSO	Area under curve
	70.71577	
	13.05383	87525.34
	78.5816	126326.5
	25.26674	68595.44
	3.999571	168175
	94.0896	115109.1
	116.6324	101637.5
	129.2326	36273.51
	72.83677	115521.3
Mean	67.15654	102395.5
S.E.M	14.8478	13996.06

Table 6.5 Peak changes and area under curve of the Ca^{2+} response to 30µM rapamycin in HEK293 cell stably expressing GCaMP5-hTPC2 preincubated with 1µM thapsigargin for 30 minutes.

	Peak change in response to Rapamycin+ Thapsigargin preincubation	Area under curve
	277.0086	619393
	184.2636	399569.7
	214.608	242931.7
	226.148	179133
	246.6546	224473.4
Mean	229.7366	333100.2
S.E.M	15.54092	80628.08

Table 6.6 Peak changes and area under curve of the Ca^{2+} response to 30μM rapamycin in HEK293 cell stably expressing GCaMP5-hTPC2 preincubated with 1μM Bafilomucin-A1 for 30 minutes.

	Peak change in response to Rapamycin+ Bafilomycin-A1 preincubation	Area under curve
	86.0082	
	55.19757	132863.4
	118.2486	88358.33
	69.61827	161821.8
	142.3346	210660.7
	79.03023	250072.1
	52.01317	173877.4
	26.9173	161768.6
	20.58983	206059
	163.0524	120681.5
Mean	81.30102	167351.4
S.E.M	14.95174	16636.82

Table 6.7 Peak changes and area under curve of the Ca^{2+} response to 30μM rapamycin in HEK293 cell stably expressing GCaMP5-hTPC2 preincubated with 10μM nifedipine for 30 minutes.

	Peak change in response to Rapamycin+ Nifedipine preincubation	Area under curve
		137480.9
	67.16047	107453.4
	77.2638	51273.71
	80.4877	57666.22
	65.5204	82033.56
	98.29657	146745.7
	39.52509	98421.2
Mean	71.37567	97296.38
S.E.M	7.976937	13875.34

References

ADACHI, T., WEISBROD, R. M., PIMENTEL, D. R., YING, J., SHAROV, V. S., SCHONEICH, C. & COHEN, R. A. 2004. S-Glutathiolation by peroxynitrite activates SERCA during arterial relaxation by nitric oxide. *Nat Med,* 10**,** 1200-7.

AL-MOHANNA, F. A., CADDY, K. W. & BOLSOVER, S. R. 1994. The nucleus is insulated from large cytosolic calcium ion changes. *Nature,* 367**,** 745-50.

ALBERTS, B. 2002. *Molecular biology of the cell,* New York, Garland Science.

ALTAFAJ, X., FRANCE, J., ALMASSY, J., JONA, I., ROSSI, D., SORRENTINO, V., MABROUK, K., DE WAARD, M. & RONJAT, M. 2007. Maurocalcine interacts with the cardiac ryanodine receptor without inducing channel modification. *Biochem J,* 406**,** 309-15.

ANNO, T., SAKAMOTO, N. & SATO, M. 2012. Role of nesprin-1 in nuclear deformation in endothelial cells under static and uniaxial stretching conditions. *Biochem Biophys Res Commun,* 424**,** 94-9.

ASTON, D., CAPEL, R. A., FORD, K. L., CHRISTIAN, H. C., MIRAMS, G. R., ROG-ZIELINSKA, E. A., KOHL, P., GALIONE, A., BURTON, R. A. & TERRAR, D. A. 2017. High resolution structural evidence suggests the Sarcoplasmic Reticulum forms microdomains with Acidic Stores (lysosomes) in the heart. *Sci Rep,* 7**,** 40620.

AVEDANIAN, L., JACQUES, D. & BKAILY, G. 2011. Presence of tubular and reticular structures in the nucleus of human vascular smooth muscle cells. *J Mol Cell Cardiol,* 50**,** 175-86.

BAKSH, S. & MICHALAK, M. 1991. Expression of calreticulin in Escherichia coli and identification of its Ca2+ binding domains. *J Biol Chem,* 266**,** 21458-65.

BALLOU, L. M. & LIN, R. Z. 2008. Rapamycin and mTOR kinase inhibitors. *J Chem Biol,* 1**,** 27-36.

BALSHAW, D. M., XU, L., YAMAGUCHI, N., PASEK, D. A. & MEISSNER, G. 2001. Calmodulin binding and inhibition of cardiac muscle calcium release channel (ryanodine receptor). *J Biol Chem,* 276**,** 20144-53.

BANERJEE, I., ZHANG, J., MOORE-MORRIS, T., PFEIFFER, E., BUCHHOLZ, K. S., LIU, A., OUYANG, K., STROUD, M. J., GERACE, L., EVANS, S. M., MCCULLOCH, A. & CHEN, J. 2014. Targeted ablation of nesprin 1 and nesprin 2 from murine myocardium results in cardiomyopathy, altered nuclear morphology and inhibition of the biomechanical gene response. *PLoS Genet,* 10**,** e1004114.

BARSKI, A., CUDDAPAH, S., CUI, K., ROH, T. Y., SCHONES, D. E., WANG, Z., WEI, G., CHEPELEV, I. & ZHAO, K. 2007. High-resolution profiling of histone methylations in the human genome. *Cell,* 129**,** 823-37.

BEARD, N. A., LAVER, D. R. & DULHUNTY, A. F. 2004. Calsequestrin and the calcium release channel of skeletal and cardiac muscle. *Prog Biophys Mol Biol,* 85**,** 33-69.

BENHAM, C. D. & BOLTON, T. B. 1986. Spontaneous transient outward currents in single visceral and vascular smooth muscle cells of the rabbit. *J Physiol,* 381**,** 385-406.

BERG, T. O., STROMHAUG, E., LOVDAL, T., SEGLEN, O. & BERG, T. 1994. Use of glycyl-L-phenylalanine 2-naphthylamide, a lysosome-disrupting cathepsin C

substrate, to distinguish between lysosomes and prelysosomal endocytic vacuoles. *Biochem J,* 300 (Pt 1)**,** 229-36.
BERK, J. M., SIMON, D. N., JENKINS-HOUK, C. R., WESTERBECK, J. W., GRONNING-WANG, L. M., CARLSON, C. R. & WILSON, K. L. 2014. The molecular basis of emerin-emerin and emerin-BAF interactions. *J Cell Sci,* 127**,** 3956-69.
BERNALES, S., MCDONALD, K. L. & WALTER, P. 2006. Autophagy counterbalances endoplasmic reticulum expansion during the unfolded protein response. *PLoS Biol,* 4**,** e423.
BERRA-ROMANI, R., MAZZOCCO-SPEZZIA, A., PULINA, M. V. & GOLOVINA, V. A. 2008. Ca2+ handling is altered when arterial myocytes progress from a contractile to a proliferative phenotype in culture. *Am J Physiol Cell Physiol,* 295**,** C779-90.
BERRIDGE, M. J., LIPP, P. & BOOTMAN, M. D. 2000. The versatility and universality of calcium signalling. *Nat Rev Mol Cell Biol,* 1**,** 11-21.
BIERER, R., NITTA, C. H., FRIEDMAN, J., CODIANNI, S., DE FRUTOS, S., DOMINGUEZ-BAUTISTA, J. A., HOWARD, T. A., RESTA, T. C. & BOSC, L. V. 2011. NFATc3 is required for chronic hypoxia-induced pulmonary hypertension in adult and neonatal mice. *Am J Physiol Lung Cell Mol Physiol,* 301**,** L872-80.
BLEASDALE, J. E., THAKUR, N. R., GREMBAN, R. S., BUNDY, G. L., FITZPATRICK, F. A., SMITH, R. J. & BUNTING, S. 1990. Selective inhibition of receptor-coupled phospholipase C-dependent processes in human platelets and polymorphonuclear neutrophils. *J Pharmacol Exp Ther,* 255**,** 756-68.
BLONDEL, O., TAKEDA, J., JANSSEN, H., SEINO, S. & BELL, G. I. 1993. Sequence and functional characterization of a third inositol trisphosphate receptor subtype, IP3R-3, expressed in pancreatic islets, kidney, gastrointestinal tract, and other tissues. *J Biol Chem,* 268**,** 11356-63.
BOITTIN, F. X., COUSSIN, F., MOREL, J. L., HALET, G., MACREZ, N. & MIRONNEAU, J. 2000. Ca(2+) signals mediated by Ins(1,4,5)P(3)-gated channels in rat ureteric myocytes. *Biochem J,* 349**,** 323-32.
BOITTIN, F. X., DIPP, M., KINNEAR, N. P., GALIONE, A. & EVANS, A. M. 2003. Vasodilation by the calcium-mobilizing messenger cyclic ADP-ribose. *J Biol Chem,* 278**,** 9602-8.
BOITTIN, F. X., GALIONE, A. & EVANS, A. M. 2002. Nicotinic acid adenine dinucleotide phosphate mediates Ca2+ signals and contraction in arterial smooth muscle via a two-pool mechanism. *Circ Res,* 91**,** 1168-75.
BOLZON, B. J. & CHEUNG, D. W. 1989. Isolation and characterization of single vascular smooth muscle cells from spontaneously hypertensive rats. *Hypertension,* 14**,** 137-44.
BOND, M., KITAZAWA, T., SOMLYO, A. P. & SOMLYO, A. V. 1984. Release and recycling of calcium by the sarcoplasmic reticulum in guinea-pig portal vein smooth muscle. *J Physiol,* 355**,** 677-95.
BOOTMAN, M. D., FEARNLEY, C., SMYRNIAS, I., MACDONALD, F. & RODERICK, H. L. 2009. An update on nuclear calcium signalling. *J Cell Sci,* 122**,** 2337-50.
BOURGEOIS, C. A., HEMON, D. & BOUTEILLE, M. 1979. Structural relationship between the nucleolus and the nuclear envelope. *J Ultrastruct Res,* 68**,** 328-40.

BRACHNER, A. & FOISNER, R. 2011. Evolvement of LEM proteins as chromatin tethers at the nuclear periphery. *Biochem Soc Trans,* 39**,** 1735-41.
BRAYDEN, J. E. 1990. Membrane hyperpolarization is a mechanism of endothelium-dependent cerebral vasodilation. *Am J Physiol,* 259**,** H668-73.
BRAYDEN, J. E. & NELSON, M. T. 1992. Regulation of arterial tone by activation of calcium-dependent potassium channels. *Science,* 256**,** 532-5.
BRIDGER, J. M., KILL, I. R., O'FARRELL, M. & HUTCHISON, C. J. 1993. Internal lamin structures within G1 nuclei of human dermal fibroblasts. *J Cell Sci,* 104 (Pt 2)**,** 297-306.
BROERS, J. L., RAMAEKERS, F. C., BONNE, G., YAOU, R. B. & HUTCHISON, C. J. 2006. Nuclear lamins: laminopathies and their role in premature ageing. *Physiol Rev,* 86**,** 967-1008.
BROZOVICH, F. V., NICHOLSON, C. J., DEGEN, C. V., GAO, Y. Z., AGGARWAL, M. & MORGAN, K. G. 2016. Mechanisms of Vascular Smooth Muscle Contraction and the Basis for Pharmacologic Treatment of Smooth Muscle Disorders. *Pharmacol Rev,* 68**,** 476-532.
BURATTI, R., PRESTIPINO, G., MENEGAZZI, P., TREVES, S. & ZORZATO, F. 1995. Calcium dependent activation of skeletal muscle Ca2+ release channel (ryanodine receptor) by calmodulin. *Biochem Biophys Res Commun,* 213**,** 1082-90.
BURKE, B. & STEWART, C. L. 2013. The nuclear lamins: flexibility in function. *Nat Rev Mol Cell Biol,* 14**,** 13-24.
CAI, M., HUANG, Y., GHIRLANDO, R., WILSON, K. L., CRAIGIE, R. & CLORE, G. M. 2001. Solution structure of the constant region of nuclear envelope protein LAP2 reveals two LEM-domain structures: one binds BAF and the other binds DNA. *EMBO J,* 20**,** 4399-407.
CALCRAFT, P. J., RUAS, M., PAN, Z., CHENG, X., ARREDOUANI, A., HAO, X., TANG, J., RIETDORF, K., TEBOUL, L., CHUANG, K. T., LIN, P., XIAO, R., WANG, C., ZHU, Y., LIN, Y., WYATT, C. N., PARRINGTON, J., MA, J., EVANS, A. M., GALIONE, A. & ZHU, M. X. 2009. NAADP mobilizes calcium from acidic organelles through two-pore channels. *Nature,* 459**,** 596-600.
CANG, C., ZHOU, Y., NAVARRO, B., SEO, Y. J., ARANDA, K., SHI, L., BATTAGLIA-HSU, S., NISSIM, I., CLAPHAM, D. E. & REN, D. 2013. mTOR regulates lysosomal ATP-sensitive two-pore Na(+) channels to adapt to metabolic state. *Cell,* 152**,** 778-790.
CARDENAS, C., ESCOBAR, M., GARCIA, A., OSORIO-REICH, M., HARTEL, S., FOSKETT, J. K. & FRANZINI-ARMSTRONG, C. 2010. Visualization of inositol 1,4,5-trisphosphate receptors on the nuclear envelope outer membrane by freeze-drying and rotary shadowing for electron microscopy. *J Struct Biol,* 171**,** 372-81.
CASE, R. M., EISNER, D., GURNEY, A., JONES, O., MUALLEM, S. & VERKHRATSKY, A. 2007. Evolution of calcium homeostasis: from birth of the first cell to an omnipresent signalling system. *Cell Calcium,* 42**,** 345-50.
CHANG, W., ANTOKU, S., OSTLUND, C., WORMAN, H. J. & GUNDERSEN, G. G. 2015. Linker of nucleoskeleton and cytoskeleton (LINC) complex-mediated actin-

dependent nuclear positioning orients centrosomes in migrating myoblasts. *Nucleus,* 6**,** 77-88.
CHAWLA, S., HARDINGHAM, G. E., QUINN, D. R. & BADING, H. 1998. CBP: a signal-regulated transcriptional coactivator controlled by nuclear calcium and CaM kinase IV. *Science,* 281**,** 1505-9.
CHEMALY, E. R., TRONCONE, L. & LEBECHE, D. 2017. SERCA control of cell death and survival. *Cell Calcium*.
CHEN-IZU, Y., MCCULLE, S. L., WARD, C. W., SOELLER, C., ALLEN, B. M., RABANG, C., CANNELL, M. B., BALKE, C. W. & IZU, L. T. 2006. Three-dimensional distribution of ryanodine receptor clusters in cardiac myocytes. *Biophys J,* 91**,** 1-13.
CHEN, L., ESTEVE, E., SABATIER, J. M., RONJAT, M., DE WAARD, M., ALLEN, P. D. & PESSAH, I. N. 2003. Maurocalcine and peptide A stabilize distinct subconductance states of ryanodine receptor type 1, revealing a proportional gating mechanism. *J Biol Chem,* 278**,** 16095-106.
CHEN, S. R., LI, X., EBISAWA, K. & ZHANG, L. 1997. Functional characterization of the recombinant type 3 Ca2+ release channel (ryanodine receptor) expressed in HEK293 cells. *J Biol Chem,* 272**,** 24234-46.
CHRISTEN, T., BOCHATON-PIALLAT, M. L., NEUVILLE, P., RENSEN, S., REDARD, M., VAN EYS, G. & GABBIANI, G. 1999. Cultured porcine coronary artery smooth muscle cells. A new model with advanced differentiation. *Circ Res,* 85**,** 99-107.
CHRISTENSEN, K. A., MYERS, J. T. & SWANSON, J. A. 2002. pH-dependent regulation of lysosomal calcium in macrophages. *J Cell Sci,* 115**,** 599-607.
CHURCHILL, G. C., OKADA, Y., THOMAS, J. M., GENAZZANI, A. A., PATEL, S. & GALIONE, A. 2002. NAADP mobilizes Ca(2+) from reserve granules, lysosome-related organelles, in sea urchin eggs. *Cell,* 111**,** 703-8.
CLARK, J. H., KINNEAR, N. P., KALUJNAIA, S., CRAMB, G., FLEISCHER, S., JEYAKUMAR, L. H., WUYTACK, F. & EVANS, A. M. 2010a. Identification of functionally segregated sarcoplasmic reticulum calcium stores in pulmonary arterial smooth muscle. *J Biol Chem,* 285**,** 13542-9.
CLARK, J. H., KINNEAR, N. P., KALUJNAIAB, S., CRAMB, G., FLEISCHER, S., JEYAKUMAR, L. H., WUYTACK, F. & EVANS, A. M. 2010b. Identification of Functionally Segregated Sarcoplasmic Reticulum Calcium Stores in Pulmonary Arterial Smooth Muscle. *J Biol Chem,* 285**,** 13542-13549.
COX, J. L., MALLANNA, S. K., ORMSBEE, B. D., DESLER, M., WIEBE, M. S. & RIZZINO, A. 2011. Banf1 is required to maintain the self-renewal of both mouse and human embryonic stem cells. *J Cell Sci,* 124**,** 2654-65.
CROWLEY, S. D., GURLEY, S. B., OLIVERIO, M. I., PAZMINO, A. K., GRIFFITHS, R., FLANNERY, P. J., SPURNEY, R. F., KIM, H. S., SMITHIES, O., LE, T. H. & COFFMAN, T. M. 2005. Distinct roles for the kidney and systemic tissues in blood pressure regulation by the renin-angiotensin system. *J Clin Invest,* 115**,** 1092-9.
CURTIS, T. M., TUMELTY, J., DAWICKI, J., SCHOLFIELD, C. N. & MCGEOWN, J. G. 2004. Identification and spatiotemporal characterization of spontaneous Ca2+ sparks and global Ca2+ oscillations in retinal arteriolar smooth muscle cells. *Invest Ophthalmol Vis Sci,* 45**,** 4409-14.

DAI, J., KUO, K. H., LEO, J. M., VAN BREEMEN, C. & LEE, C. H. 2005. Rearrangement of the close contact between the mitochondria and the sarcoplasmic reticulum in airway smooth muscle. *Cell Calcium,* 37**,** 333-40.

DEL CASTILLO, J. & KATZ, B. 1956. Biophysical aspects of neuro-muscular transmission. *Prog Biophys Biophys Chem,* 6**,** 121-70.

DEMMERLE, J., KOCH, A. J. & HOLASKA, J. M. 2013. Emerin and histone deacetylase 3 (HDAC3) cooperatively regulate expression and nuclear positions of MyoD, Myf5, and Pax7 genes during myogenesis. *Chromosome Res,* 21**,** 765-79.

DEVINE, C. E., SOMLYO, A. V. & SOMLYO, A. P. 1972. Sarcoplasmic reticulum and excitation-contraction coupling in mammalian smooth muscles. *J Cell Biol,* 52**,** 690-718.

DICKINSON, G. D., SWAMINATHAN, D. & PARKER, I. 2012. The probability of triggering calcium puffs is linearly related to the number of inositol trisphosphate receptors in a cluster. *Biophys J,* 102**,** 1826-36.

DICKINSON, H. G. & BELL, P. R. 1972. Structures resembling nuclear pores at the orifice of nuclear invaginations in developing microspores of Pinus banksiana. *Dev Biol,* 27**,** 425-9.

DIPP, M. & EVANS, A. M. 2001. Cyclic ADP-ribose is the primary trigger for hypoxic pulmonary vasoconstriction in the rat lung in situ. *Circ Res,* 89**,** 77-83.

DIPP, M., NYE, P. C. & EVANS, A. M. 2001. Hypoxic release of calcium from the sarcoplasmic reticulum of pulmonary artery smooth muscle. *Am J Physiol Lung Cell Mol Physiol,* 281**,** L318-25.

DOLGACHEVA, L. P., TUROVSKAYA, M. V., DYNNIK, V. V., ZINCHENKO, V. P., GONCHAROV, N. V., DAVLETOV, B. & TUROVSKY, E. A. 2016. Angiotensin II activates different calcium signaling pathways in adipocytes. *Arch Biochem Biophys,* 593**,** 38-49.

DU, G. G., ASHLEY, C. C. & LEA, T. J. 1994. Effects of thapsigargin and cyclopiazonic acid on the sarcoplasmic reticulum Ca2+ pump of skinned fibres from frog skeletal muscle. *Pflugers Arch,* 429**,** 169-75.

DUBAND, J. L., GIMONA, M., SCATENA, M., SARTORE, S. & SMALL, J. V. 1993. Calponin and SM 22 as differentiation markers of smooth muscle: spatiotemporal distribution during avian embryonic development. *Differentiation,* 55**,** 1-11.

DUCHEN, M. R. 2000. Mitochondria and calcium: from cell signalling to cell death. *J Physiol,* 529 Pt 1**,** 57-68.

DUONG, N. T., MORRIS, G. E., LAM LE, T., ZHANG, Q., SEWRY, C. A., SHANAHAN, C. M. & HOLT, I. 2014. Nesprins: tissue-specific expression of epsilon and other short isoforms. *PLoS One,* 9**,** e94380.

ECHEVARRIA, W., LEITE, M. F., GUERRA, M. T., ZIPFEL, W. R. & NATHANSON, M. H. 2003. Regulation of calcium signals in the nucleus by a nucleoplasmic reticulum. *Nat Cell Biol,* 5**,** 440-6.

EGGERMONT, J. A., WUYTACK, F., VERBIST, J. & CASTEELS, R. 1990. Expression of endoplasmic-reticulum Ca2(+)-pump isoforms and of phospholamban in pig smooth-muscle tissues. *Biochem J,* 271**,** 649-53.

EVANS, A. M. 2010. The role of intracellular ion channels in regulating cytoplasmic calciumin pulmonary arterial mmooth muscle: which store and where? *Adv Exp Med Biol,* 661**,** 57-76.
EVANS, A. M., FAMELI, N., OGUNBAYO, O. A., DUAN, J. & NAVARRO-DORADO, J. 2016. From contraction to gene expression: nanojunctions of the sarco/endoplasmic reticulum deliver site- and function-specific calcium signals. *Sci China Life Sci,* 59**,** 749-63.
EZAKI, J., HIMENO, M. & KATO, K. 1992. Purification and characterization of (Ca2+-Mg2+)-ATPase in rat liver lysosomal membranes. *J Biochem,* 112**,** 33-9.
FAMELI, N., OGUNBAYO, O. A., VAN BREEMEN, C. & EVANS, A. M. 2014. Cytoplasmic nanojunctions between lysosomes and sarcoplasmic reticulum are required for specific calcium signaling. *F1000Res,* 3**,** 93.
FAMELI, N., VAN BREEMEN, C. & KUO, K. H. 2007. A quantitative model for linking Na+/Ca2+ exchanger to SERCA during refilling of the sarcoplasmic reticulum to sustain [Ca2+] oscillations in vascular smooth muscle. *Cell Calcium,* 42**,** 565-75.
FELLNER, S. K. & ARENDSHORST, W. J. 2005. Angiotensin II Ca2+ signaling in rat afferent arterioles: stimulation of cyclic ADP ribose and IP3 pathways. *Am J Physiol Renal Physiol,* 288**,** F785-91.
FISCHER, A. H., TAYSAVANG, P. & JHIANG, S. M. 2003. Nuclear envelope irregularity is induced by RET/PTC during interphase. *Am J Pathol,* 163**,** 1091-100.
FLORES-SOTO, E., REYES-GARCIA, J., SOMMER, B. & MONTANO, L. M. 2013. Sarcoplasmic reticulum Ca(2+) refilling is determined by L-type Ca(2+) and store operated Ca(2+) channels in guinea pig airway smooth muscle. *Eur J Pharmacol,* 721**,** 21-8.
FRANKE, J., ABS, V., ZIZZADORO, C. & ABRAHAM, G. 2014. Comparative study of the effects of fetal bovine serum versus horse serum on growth and differentiation of primary equine bronchial fibroblasts. *BMC Vet Res,* 10**,** 119.
FRANKE, W. W., SCHEER, U., KROHNE, G. & JARASCH, E. D. 1981. The nuclear envelope and the architecture of the nuclear periphery. *J Cell Biol,* 91**,** 39s-50s.
FRANZINI-ARMSTRONG, C. 1970. STUDIES OF THE TRIAD : I. Structure of the Junction in Frog Twitch Fibers. *J Cell Biol,* 47**,** 488-99.
FRANZINI-ARMSTRONG, C., PROTASI, F. & RAMESH, V. 1999. Shape, size, and distribution of Ca(2+) release units and couplons in skeletal and cardiac muscles. *Biophys J,* 77**,** 1528-39.
FRANZINIARMSTRONG, C. 1964. Sarcolemmal Invaginations and the T-System in Fish Skeletal Muscle. *Nature,* 202**,** 355-7.
FRICKER, M., HOLLINSHEAD, M., WHITE, N. & VAUX, D. 1997a. The convoluted nucleus. *Trends Cell Biol,* 7**,** 181.
FRICKER, M., HOLLINSHEAD, M., WHITE, N. & VAUX, D. 1997b. Interphase nuclei of many mammalian cell types contain deep, dynamic, tubular membrane-bound invaginations of the nuclear envelope. *J Cell Biol,* 136**,** 531-44.
GABBIANI, G., SCHMID, E., WINTER, S., CHAPONNIER, C., DE CKHASTONAY, C., VANDEKERCKHOVE, J., WEBER, K. & FRANKE, W. W. 1981. Vascular smooth muscle cells differ from other smooth muscle cells: predominance of vimentin

filaments and a specific alpha-type actin. *Proc Natl Acad Sci U S A,* 78**,** 298-302.
GABELLA, G. 1971. Caveolae intracellulares and sarcoplasmic reticulum in smooth muscle. *J Cell Sci,* 8**,** 601-9.
GEISLER, M., FRANGNE, N., GOMES, E., MARTINOIA, E. & PALMGREN, M. G. 2000. The ACA4 gene of Arabidopsis encodes a vacuolar membrane calcium pump that improves salt tolerance in yeast. *Plant Physiol,* 124**,** 1814-27.
GENAZZANI, A. A., MEZNA, M., DICKEY, D. M., MICHELANGELI, F., WALSETH, T. F. & GALIONE, A. 1997. Pharmacological properties of the Ca2+-release mechanism sensitive to NAADP in the sea urchin egg. *Br J Pharmacol,* 121**,** 1489-95.
GERACE, L. & HUBER, M. D. 2012. Nuclear lamina at the crossroads of the cytoplasm and nucleus. *J Struct Biol,* 177**,** 24-31.
GERASIMENKO, J. V., MARUYAMA, Y., YANO, K., DOLMAN, N. J., TEPIKIN, A. V., PETERSEN, O. H. & GERASIMENKO, O. V. 2003. NAADP mobilizes Ca2+ from a thapsigargin-sensitive store in the nuclear envelope by activating ryanodine receptors. *J Cell Biol,* 163**,** 271-82.
GILBERT, G., DUCRET, T., MARTHAN, R., SAVINEAU, J. P. & QUIGNARD, J. F. 2014. Stretch-induced Ca2+ signalling in vascular smooth muscle cells depends on Ca2+ store segregation. *Cardiovasc Res,* 103**,** 313-23.
GOLOVINA, V. A. & BLAUSTEIN, M. P. 1997. Spatially and functionally distinct Ca2+ stores in sarcoplasmic and endoplasmic reticulum. *Science,* 275**,** 1643-8.
GOMEZ, D. & OWENS, G. K. 2012. Smooth muscle cell phenotypic switching in atherosclerosis. *Cardiovasc Res,* 95**,** 156-64.
GOMEZ, M. F., STEVENSON, A. S., BONEV, A. D., HILL-EUBANKS, D. C. & NELSON, M. T. 2002. Opposing actions of inositol 1,4,5-trisphosphate and ryanodine receptors on nuclear factor of activated T-cells regulation in smooth muscle. *J Biol Chem,* 277**,** 37756-64.
GONCHAROV, D. A., KUDRYASHOVA, T. V., ZIAI, H., IHIDA-STANSBURY, K., DELISSER, H., KRYMSKAYA, V. P., TUDER, R. M., KAWUT, S. M. & GONCHAROVA, E. A. 2014. Mammalian target of rapamycin complex 2 (mTORC2) coordinates pulmonary artery smooth muscle cell metabolism, proliferation, and survival in pulmonary arterial hypertension. *Circulation,* 129**,** 864-74.
GORDIENKO, D. V. & BOLTON, T. B. 2002. Crosstalk between ryanodine receptors and IP(3) receptors as a factor shaping spontaneous Ca(2+)-release events in rabbit portal vein myocytes. *J Physiol,* 542**,** 743-62.
GORDIENKO, D. V., BOLTON, T. B. & CANNELL, M. B. 1998. Variability in spontaneous subcellular calcium release in guinea-pig ileum smooth muscle cells. *J Physiol,* 507 (Pt 3)**,** 707-20.
GRAMOLINI, A. O., KISLINGER, T., ASAHI, M., LI, W., EMILI, A. & MACLENNAN, D. H. 2004. Sarcolipin retention in the endoplasmic reticulum depends on its C-terminal RSYQY sequence and its interaction with sarco(endo)plasmic Ca(2+)-ATPases. *Proc Natl Acad Sci U S A,* 101**,** 16807-12.
GRAYSON, T. H., HADDOCK, R. E., MURRAY, T. P., WOJCIKIEWICZ, R. J. & HILL, C. E. 2004. Inositol 1,4,5-trisphosphate receptor subtypes are differentially

distributed between smooth muscle and endothelial layers of rat arteries. *Cell Calcium,* 36**,** 447-58.
GRIFFITHS, E. J., OCAMPO, C. J., SAVAGE, J. S., RUTTER, G. A., HANSFORD, R. G., STERN, M. D. & SILVERMAN, H. S. 1998. Mitochondrial calcium transporting pathways during hypoxia and reoxygenation in single rat cardiomyocytes. *Cardiovasc Res,* 39**,** 423-33.
GUO, J., ZENG, W. & JIANG, Y. 2017. Tuning the ion selectivity of two-pore channels. *Proc Natl Acad Sci U S A,* 114**,** 1009-1014.
GUO, W. & CAMPBELL, K. P. 1995. Association of triadin with the ryanodine receptor and calsequestrin in the lumen of the sarcoplasmic reticulum. *J Biol Chem,* 270**,** 9027-30.
HAAK, L. L., SONG, L. S., MOLINSKI, T. F., PESSAH, I. N., CHENG, H. & RUSSELL, J. T. 2001. Sparks and puffs in oligodendrocyte progenitors: cross talk between ryanodine receptors and inositol trisphosphate receptors. *J Neurosci,* 21**,** 3860-70.
HAKAMATA, Y., NAKAI, J., TAKESHIMA, H. & IMOTO, K. 1992. Primary structure and distribution of a novel ryanodine receptor/calcium release channel from rabbit brain. *FEBS Lett,* 312**,** 229-35.
HALLER, T., VOLKL, H., DEETJEN, P. & DIETL, P. 1996. The lysosomal Ca2+ pool in MDCK cells can be released by ins(1,4,5)P3-dependent hormones or thapsigargin but does not activate store-operated Ca2+ entry. *Biochem J,* 319 (Pt 3)**,** 909-12.
HAMAD, M. I., KRAUSE, M. & WAHLE, P. 2015. Improving AM ester calcium dye loading efficiency. *J Neurosci Methods,* 240**,** 48-60.
HARR, J. C., LUPERCHIO, T. R., WONG, X., COHEN, E., WHEELAN, S. J. & REDDY, K. L. 2015. Directed targeting of chromatin to the nuclear lamina is mediated by chromatin state and A-type lamins. *J Cell Biol,* 208**,** 33-52.
HARR, J. C. & REDDY, K. L. 2016. Tagged Chromosomal Insertion Site System: A Method to Study Lamina-Associated Chromatin. *Methods Enzymol,* 569**,** 433-53.
HERRMANN-FRANK, A., DARLING, E. & MEISSNER, G. 1991. Functional characterization of the Ca(2+)-gated Ca2+ release channel of vascular smooth muscle sarcoplasmic reticulum. *Pflugers Arch,* 418**,** 353-9.
HIEDA, M. 2017. Implications for Diverse Functions of the LINC Complexes Based on the Structure. *Cells,* 6.
HIRSCH, N. P. 2007. Neuromuscular junction in health and disease. *Br J Anaesth,* 99**,** 132-8.
HIRSCHI, K. D., ZHEN, R. G., CUNNINGHAM, K. W., REA, P. A. & FINK, G. R. 1996. CAX1, an H+/Ca2+ antiporter from Arabidopsis. *Proc Natl Acad Sci U S A,* 93**,** 8782-6.
HOWAT, W. J. & WILSON, B. A. 2014. Tissue fixation and the effect of molecular fixatives on downstream staining procedures. *Methods,* 70**,** 12-9.
HUNGERFORD, J. E. & LITTLE, C. D. 1999. Developmental biology of the vascular smooth muscle cell: building a multilayered vessel wall. *J Vasc Res,* 36**,** 2-27.

ISHIBASHI, K., SUZUKI, M. & IMAI, M. 2000. Molecular cloning of a novel form (two-repeat) protein related to voltage-gated sodium and calcium channels. *Biochem Biophys Res Commun,* 270**,** 370-6.

JADOT, M., COLMANT, C., WATTIAUX-DE CONINCK, S. & WATTIAUX, R. 1984. Intralysosomal hydrolysis of glycyl-L-phenylalanine 2-naphthylamide. *Biochem J,* 219**,** 965-70.

JAGGAR, J. H., STEVENSON, A. S. & NELSON, M. T. 1998. Voltage dependence of Ca2+ sparks in intact cerebral arteries. *Am J Physiol,* 274**,** C1755-61.

JMOUDIAK, M. & FUTERMAN, A. H. 2005. Gaucher disease: pathological mechanisms and modern management. *Br J Haematol,* 129**,** 178-88.

JOHNSON, S., MICHALAK, M., OPAS, M. & EGGLETON, P. 2001. The ins and outs of calreticulin: from the ER lumen to the extracellular space. *Trends Cell Biol,* 11**,** 122-9.

JORGENS, D. M., INMAN, J. L., WOJCIK, M., ROBERTSON, C., PALSDOTTIR, H., TSAI, W. T., HUANG, H., BRUNI-CARDOSO, A., LOPEZ, C. S., BISSELL, M. J., XU, K. & AUER, M. 2017. Deep nuclear invaginations are linked to cytoskeletal filaments - integrated bioimaging of epithelial cells in 3D culture. *J Cell Sci,* 130**,** 177-189.

KANG, S., DAHL, R., HSIEH, W., SHIN, A., ZSEBO, K. M., BUETTNER, C., HAJJAR, R. J. & LEBECHE, D. 2016. Small Molecular Allosteric Activator of the Sarco/Endoplasmic Reticulum Ca2+-ATPase (SERCA) Attenuates Diabetes and Metabolic Disorders. *J Biol Chem,* 291**,** 5185-98.

KATO, K., OKAMURA, K., HATTA, M., MORITA, H., KAJIOKA, S., NAITO, S. & YAMAZAKI, J. 2013. Involvement of IP3-receptor activation in endothelin-1-induced Ca(2+) influx in rat pulmonary small artery. *Eur J Pharmacol,* 720**,** 255-63.

KHALIL, R. A., ENNA, S. J. & LECOUNT, L. 2017. *Vascular pharmacology : smooth muscle,* Cambridge, MA, United States, Elsevier/AP, Academic Press, an imprint of Elsevier.

KHO, C., LEE, A., JEONG, D., OH, J. G., CHAANINE, A. H., KIZANA, E., PARK, W. J. & HAJJAR, R. J. 2011. SUMO1-dependent modulation of SERCA2a in heart failure. *Nature,* 477**,** 601-5.

KIM, D. H., OHNISHI, S. T. & IKEMOTO, N. 1983. Kinetic studies of calcium release from sarcoplasmic reticulum in vitro. *J Biol Chem,* 258**,** 9662-8.

KIM, D. I., BIRENDRA, K. C. & ROUX, K. J. 2015. Making the LINC: SUN and KASH protein interactions. *Biol Chem,* 396**,** 295-310.

KINNEAR, N. P., BOITTIN, F. X., THOMAS, J. M., GALIONE, A. & EVANS, A. M. 2004. Lysosome-sarcoplasmic reticulum junctions. A trigger zone for calcium signaling by nicotinic acid adenine dinucleotide phosphate and endothelin-1. *J Biol Chem,* 279**,** 54319-26.

KINNEAR, N. P., WYATT, C. N., CLARK, J. H., CALCRAFT, P. J., FLEISCHER, S., JEYAKUMAR, L. H., NIXON, G. F. & EVANS, A. M. 2008. Lysosomes co-localize with ryanodine receptor subtype 3 to form a trigger zone for calcium signalling by NAADP in rat pulmonary arterial smooth muscle. *Cell Calcium,* 44**,** 190-201.

KNOT, H. J., STANDEN, N. B. & NELSON, M. T. 1998. Ryanodine receptors regulate arterial diameter and wall [Ca2+] in cerebral arteries of rat via Ca2+-dependent K+ channels. *J Physiol,* 508 (Pt 1)**,** 211-21.

KOBAYASHI, M., SHOJI, N. & OHIZUMI, Y. 1987. Gingerol, a novel cardiotonic agent, activates the Ca2+-pumping ATPase in skeletal and cardiac sarcoplasmic reticulum. *Biochim Biophys Acta,* 903**,** 96-102.

KOWARSKI, D., SHUMAN, H., SOMLYO, A. P. & SOMLYO, A. V. 1985. Calcium release by noradrenaline from central sarcoplasmic reticulum in rabbit main pulmonary artery smooth muscle. *J Physiol,* 366**,** 153-75.

KRAPIVINSKY, G., KRAPIVINSKY, L., STOTZ, S. C., MANASIAN, Y. & CLAPHAM, D. E. 2011. POST, partner of stromal interaction molecule 1 (STIM1), targets STIM1 to multiple transporters. *Proc Natl Acad Sci U S A,* 108**,** 19234-9.

LANGER, G. A. & PESKOFF, A. 1996. Calcium concentration and movement in the diadic cleft space of the cardiac ventricular cell. *Biophys J,* 70**,** 1169-82.

LANNER, J. T., GEORGIOU, D. K., JOSHI, A. D. & HAMILTON, S. L. 2010. Ryanodine receptors: structure, expression, molecular details, and function in calcium release. *Cold Spring Harb Perspect Biol,* 2**,** a003996.

LAVER, D. R. & VAN HELDEN, D. F. 2011. Three independent mechanisms contribute to tetracaine inhibition of cardiac calcium release channels. *J Mol Cell Cardiol,* 51**,** 357-69.

LEDO, F., KREMER, L., MELLSTROM, B. & NARANJO, J. R. 2002. Ca2+-dependent block of CREB-CBP transcription by repressor DREAM. *EMBO J,* 21**,** 4583-92.

LEE, C. H., POBURKO, D., KUO, K. H., SEOW, C. Y. & VAN BREEMEN, C. 2002. Ca(2+) oscillations, gradients, and homeostasis in vascular smooth muscle. *Am J Physiol Heart Circ Physiol,* 282**,** H1571-83.

LEE, K. K., HARAGUCHI, T., LEE, R. S., KOUJIN, T., HIRAOKA, Y. & WILSON, K. L. 2001. Distinct functional domains in emerin bind lamin A and DNA-bridging protein BAF. *J Cell Sci,* 114**,** 4567-73.

LEGARTOVA, S., STIXOVA, L., LAUR, O., KOZUBEK, S., SEHNALOVA, P. & BARTOVA, E. 2014. Nuclear structures surrounding internal lamin invaginations. *J Cell Biochem,* 115**,** 476-87.

LEITE, M. F., THROWER, E. C., ECHEVARRIA, W., KOULEN, P., HIRATA, K., BENNETT, A. M., EHRLICH, B. E. & NATHANSON, M. H. 2003. Nuclear and cytosolic calcium are regulated independently. *Proc Natl Acad Sci U S A,* 100**,** 2975-80.

LEMOS, V. S., POBURKO, D., LIAO, C. H., COLE, W. C. & VAN BREEMEN, C. 2007. Na+ entry via TRPC6 causes Ca2+ entry via NCX reversal in ATP stimulated smooth muscle cells. *Biochem Biophys Res Commun,* 352**,** 130-4.

LI, P. & CHEN, S. R. 2001. Molecular basis of Ca(2)+ activation of the mouse cardiac Ca(2)+ release channel (ryanodine receptor). *J Gen Physiol,* 118**,** 33-44.

LIOU, J., KIM, M. L., HEO, W. D., JONES, J. T., MYERS, J. W., FERRELL, J. E., JR. & MEYER, T. 2005. STIM is a Ca2+ sensor essential for Ca2+-store-depletion-triggered Ca2+ influx. *Curr Biol,* 15**,** 1235-41.

LIPSKAIA, L., KEUYLIAN, Z., BLIRANDO, K., MOUGENOT, N., JACQUET, A., ROUXEL, C., SGHAIRI, H., ELAIB, Z., BLAISE, R., ADNOT, S., HAJJAR, R. J., CHEMALY, E. R., LIMON, I. & BOBE, R. 2014. Expression of sarco (endo) plasmic reticulum calcium ATPase (SERCA) system in normal mouse cardiovascular tissues, heart failure and atherosclerosis. *Biochim Biophys Acta,* 1843**,** 2705-18.

LIU, Y., DENG, B., ZHAO, Y., XIE, S. & NIE, R. 2013. Differentiated markers in undifferentiated cells: expression of smooth muscle contractile proteins in multipotent bone marrow mesenchymal stem cells. *Dev Growth Differ,* 55**,** 591-605.

LLOYD-EVANS, E., MORGAN, A. J., HE, X., SMITH, D. A., ELLIOT-SMITH, E., SILLENCE, D. J., CHURCHILL, G. C., SCHUCHMAN, E. H., GALIONE, A. & PLATT, F. M. 2008. Niemann-Pick disease type C1 is a sphingosine storage disease that causes deregulation of lysosomal calcium. *Nat Med,* 14**,** 1247-55.

LUO, L., GASSMAN, K. L., PETELL, L. M., WILSON, C. L., BEWERSDORF, J. & SHOPLAND, L. S. 2009. The nuclear periphery of embryonic stem cells is a transcriptionally permissive and repressive compartment. *J Cell Sci,* 122**,** 3729-37.

LYTTON, J., WESTLIN, M., BURK, S. E., SHULL, G. E. & MACLENNAN, D. H. 1992. Functional comparisons between isoforms of the sarcoplasmic or endoplasmic reticulum family of calcium pumps. *J Biol Chem,* 267**,** 14483-9.

LYTTON, J., WESTLIN, M. & HANLEY, M. R. 1991. Thapsigargin inhibits the sarcoplasmic or endoplasmic reticulum Ca-ATPase family of calcium pumps. *J Biol Chem,* 266**,** 17067-71.

MACLENNAN, D. H., ABU-ABED, M. & KANG, C. 2002. Structure-function relationships in Ca(2+) cycling proteins. *J Mol Cell Cardiol,* 34**,** 897-918.

MACMILLAN, D., CHALMERS, S., MUIR, T. C. & MCCARRON, J. G. 2005. IP3-mediated Ca2+ increases do not involve the ryanodine receptor, but ryanodine receptor antagonists reduce IP3-mediated Ca2+ increases in guinea-pig colonic smooth muscle cells. *J Physiol,* 569**,** 533-44.

MACQUAIDE, N., TUAN, H. T., HOTTA, J., SEMPELS, W., LENAERTS, I., HOLEMANS, P., HOFKENS, J., JAFRI, M. S., WILLEMS, R. & SIPIDO, K. R. 2015. Ryanodine receptor cluster fragmentation and redistribution in persistent atrial fibrillation enhance calcium release. *Cardiovasc Res,* 108**,** 387-98.

MALHAS, A., GOULBOURNE, C. & VAUX, D. J. 2011. The nucleoplasmic reticulum: form and function. *Trends Cell Biol,* 21**,** 362-73.

MALLI, R., FRIEDEN, M., OSIBOW, K., ZORATTI, C., MAYER, M., DEMAUREX, N. & GRAIER, W. F. 2003. Sustained Ca2+ transfer across mitochondria is Essential for mitochondrial Ca2+ buffering, sore-operated Ca2+ entry, and Ca2+ store refilling. *J Biol Chem,* 278**,** 44769-79.

MARGALIT, A., NEUFELD, E., FEINSTEIN, N., WILSON, K. L., PODBILEWICZ, B. & GRUENBAUM, Y. 2007. Barrier to autointegration factor blocks premature cell fusion and maintains adult muscle integrity in C. elegans. *J Cell Biol,* 178**,** 661-73.

MARIUS, P., GUERRA, M. T., NATHANSON, M. H., EHRLICH, B. E. & LEITE, M. F. 2006. Calcium release from ryanodine receptors in the nucleoplasmic reticulum. *Cell Calcium,* 39**,** 65-73.

MARTINEZ-AZORIN, F. 2004. Cyclopiazonic acid reduces the coupling factor of the Ca2+-ATPase acting on Ca2+ binding. *FEBS Lett,* 576**,** 73-6.

MARUYAMA, K. & MACLENNAN, D. H. 1988. Mutation of aspartic acid-351, lysine-352, and lysine-515 alters the Ca2+ transport activity of the Ca2+-ATPase expressed in COS-1 cells. *Proc Natl Acad Sci U S A,* 85**,** 3314-8.

MARUYAMA, T., KANAJI, T., NAKADE, S., KANNO, T. & MIKOSHIBA, K. 1997. 2APB, 2-aminoethoxydiphenyl borate, a membrane-penetrable modulator of Ins(1,4,5)P3-induced Ca2+ release. *J Biochem,* 122**,** 498-505.

MARX, S. O., REIKEN, S., HISAMATSU, Y., GABURJAKOVA, M., GABURJAKOVA, J., YANG, Y. M., ROSEMBLIT, N. & MARKS, A. R. 2001. Phosphorylation-dependent regulation of ryanodine receptors: a novel role for leucine/isoleucine zippers. *J Cell Biol,* 153**,** 699-708.

MEISSNER, G. 1986. Ryanodine activation and inhibition of the Ca2+ release channel of sarcoplasmic reticulum. *J Biol Chem,* 261**,** 6300-6.

MEISSNER, G., DARLING, E. & EVELETH, J. 1986. Kinetics of rapid Ca2+ release by sarcoplasmic reticulum. Effects of Ca2+, Mg2+, and adenine nucleotides. *Biochemistry,* 25**,** 236-44.

MEKAHLI, D., BULTYNCK, G., PARYS, J. B., DE SMEDT, H. & MISSIAEN, L. 2011. Endoplasmic-reticulum calcium depletion and disease. *Cold Spring Harb Perspect Biol,* 3.

MIANO, J. M., CSERJESI, P., LIGON, K. L., PERIASAMY, M. & OLSON, E. N. 1994. Smooth muscle myosin heavy chain exclusively marks the smooth muscle lineage during mouse embryogenesis. *Circ Res,* 75**,** 803-12.

MICHALAK, M., CORBETT, E. F., MESAELI, N., NAKAMURA, K. & OPAS, M. 1999. Calreticulin: one protein, one gene, many functions. *Biochem J,* 344 Pt 2**,** 281-92.

MICHALAK, M., MILNER, R. E., BURNS, K. & OPAS, M. 1992. Calreticulin. *Biochem J,* 285 (Pt 3)**,** 681-92.

MICHELS, G., KHAN, I. F., ENDRES-BECKER, J., ROTTLAENDER, D., HERZIG, S., RUHPARWAR, A., WAHLERS, T. & HOPPE, U. C. 2009. Regulation of the human cardiac mitochondrial Ca2+ uptake by 2 different voltage-gated Ca2+ channels. *Circulation,* 119**,** 2435-43.

MISLOW, J. M., HOLASKA, J. M., KIM, M. S., LEE, K. K., SEGURA-TOTTEN, M., WILSON, K. L. & MCNALLY, E. M. 2002a. Nesprin-1alpha self-associates and binds directly to emerin and lamin A in vitro. *FEBS Lett,* 525**,** 135-40.

MISLOW, J. M., KIM, M. S., DAVIS, D. B. & MCNALLY, E. M. 2002b. Myne-1, a spectrin repeat transmembrane protein of the myocyte inner nuclear membrane, interacts with lamin A/C. *J Cell Sci,* 115**,** 61-70.

MIYAKAWA, T., MAEDA, A., YAMAZAWA, T., HIROSE, K., KUROSAKI, T. & IINO, M. 1999. Encoding of Ca2+ signals by differential expression of IP3 receptor subtypes. *EMBO J,* 18**,** 1303-8.

MOGAMI, H., TEPIKIN, A. V. & PETERSEN, O. H. 1998. Termination of cytosolic Ca2+ signals: Ca2+ reuptake into intracellular stores is regulated by the free Ca2+ concentration in the store lumen. *EMBO J,* 17**,** 435-42.

MORALES, S., CAMELLO, P. J., MAWE, G. M. & POZO, M. J. 2005. Characterization of intracellular Ca(2+) stores in gallbladder smooth muscle. *Am J Physiol Gastrointest Liver Physiol,* 288**,** G507-13.

MOREL, J. L., FRITZ, N., LAVIE, J. L. & MIRONNEAU, J. 2003. Crucial role of type 2 inositol 1,4,5-trisphosphate receptors for acetylcholine-induced Ca2+ oscillations in vascular myocytes. *Arterioscler Thromb Vasc Biol,* 23**,** 1567-75.

NAZER, M. A. & VAN BREEMEN, C. 1998. Functional linkage of Na(+)-Ca2+ exchange and sarcoplasmic reticulum Ca2+ release mediates Ca2+ cycling in vascular smooth muscle. *Cell Calcium,* 24**,** 275-83.

NELSON, B. R., MAKAREWICH, C. A., ANDERSON, D. M., WINDERS, B. R., TROUPES, C. D., WU, F., REESE, A. L., MCANALLY, J. R., CHEN, X., KAVALALI, E. T., CANNON, S. C., HOUSER, S. R., BASSEL-DUBY, R. & OLSON, E. N. 2016. A peptide encoded by a transcript annotated as long noncoding RNA enhances SERCA activity in muscle. *Science,* 351**,** 271-5.

NELSON, M. T., CHENG, H., RUBART, M., SANTANA, L. F., BONEV, A. D., KNOT, H. J. & LEDERER, W. J. 1995. Relaxation of arterial smooth muscle by calcium sparks. *Science,* 270**,** 633-7.

NEYLON, C. B., RICHARDS, S. M., LARSEN, M. A., AGROTIS, A. & BOBIK, A. 1995. Multiple types of ryanodine receptor/Ca2+ release channels are expressed in vascular smooth muscle. *Biochem Biophys Res Commun,* 215**,** 814-21.

NIXON, G. F., MIGNERY, G. A. & SOMLYO, A. V. 1994. Immunogold localization of inositol 1,4,5-trisphosphate receptors and characterization of ultrastructural features of the sarcoplasmic reticulum in phasic and tonic smooth muscle. *J Muscle Res Cell Motil,* 15**,** 682-700.

NOORI, S., ACHERMAN, R., SIASSI, B., LUNA, C., EBRAHIMI, M., PAVLOVA, Z. & RAMANATHAN, R. 2002. A rare presentation of Pompe disease with massive hypertrophic cardiomyopathy at birth. *J Perinat Med,* 30**,** 517-21.

ODERMATT, A., BECKER, S., KHANNA, V. K., KURZYDLOWSKI, K., LEISNER, E., PETTE, D. & MACLENNAN, D. H. 1998. Sarcolipin regulates the activity of SERCA1, the fast-twitch skeletal muscle sarcoplasmic reticulum Ca2+-ATPase. *J Biol Chem,* 273**,** 12360-9.

OGAWA, A., FIRTH, A. L., SMITH, K. A., MALIAKAL, M. V. & YUAN, J. X. 2012. PDGF enhances store-operated Ca2+ entry by upregulating STIM1/Orai1 via activation of Akt/mTOR in human pulmonary arterial smooth muscle cells. *Am J Physiol Cell Physiol,* 302**,** C405-11.

OGUNBAYO, O. A., DUAN, J., XIONG, J., WANG, Q., FENG, X., MA, J., ZHU, M. X. & EVANS, A. M. 2018. mTORC1 controls lysosomal Ca(2+) release through the two-pore channel TPC2. *Sci Signal,* 11.

OGUNBAYO, O. A., ZHU, Y., SHEN, B., AGBANI, E., LI, J., MA, J., ZHU, M. X. & EVANS, A. M. 2015. Organelle-specific subunit interactions of the vertebrate two-pore channel family. *J Biol Chem,* 290**,** 1086-95.

OH, H. S., TRAKTMAN, P. & KNIPE, D. M. 2015. Barrier-to-Autointegration Factor 1 (BAF/BANF1) Promotes Association of the SETD1A Histone Methyltransferase with Herpes Simplex Virus Immediate-Early Gene Promoters. *MBio,* 6**,** e00345-15.

OTSU, K., WILLARD, H. F., KHANNA, V. K., ZORZATO, F., GREEN, N. M. & MACLENNAN, D. H. 1990. Molecular cloning of cDNA encoding the Ca2+ release channel (ryanodine receptor) of rabbit cardiac muscle sarcoplasmic reticulum. *J Biol Chem,* 265**,** 13472-83.

OWENS, G. K. 1995. Regulation of differentiation of vascular smooth muscle cells. *Physiol Rev,* 75**,** 487-517.

OWENS, G. K., KUMAR, M. S. & WAMHOFF, B. R. 2004. Molecular regulation of vascular smooth muscle cell differentiation in development and disease. *Physiol Rev,* 84**,** 767-801.

PAPP, S., DZIAK, E., MICHALAK, M. & OPAS, M. 2003. Is all of the endoplasmic reticulum created equal? The effects of the heterogeneous distribution of endoplasmic reticulum Ca2+-handling proteins. *J Cell Biol,* 160**,** 475-9.

PARE, G. C., BAUMAN, A. L., MCHENRY, M., MICHEL, J. J., DODGE-KAFKA, K. L. & KAPILOFF, M. S. 2005a. The mAKAP complex participates in the induction of cardiac myocyte hypertrophy by adrenergic receptor signaling. *J Cell Sci,* 118**,** 5637-46.

PARE, G. C., EASLICK, J. L., MISLOW, J. M., MCNALLY, E. M. & KAPILOFF, M. S. 2005b. Nesprin-1alpha contributes to the targeting of mAKAP to the cardiac myocyte nuclear envelope. *Exp Cell Res,* 303**,** 388-99.

PARK, C. Y., HOOVER, P. J., MULLINS, F. M., BACHHAWAT, P., COVINGTON, E. D., RAUNSER, S., WALZ, T., GARCIA, K. C., DOLMETSCH, R. E. & LEWIS, R. S. 2009. STIM1 clusters and activates CRAC channels via direct binding of a cytosolic domain to Orai1. *Cell,* 136**,** 876-90.

PATEL, S., JOSEPH, S. K. & THOMAS, A. P. 1999. Molecular properties of inositol 1,4,5-trisphosphate receptors. *Cell Calcium,* 25**,** 247-64.

PENG, G., XU, J., LIU, R., FU, Z., LI, S., HONG, W., CHEN, J., LI, B. & RAN, P. 2017. Isolation, culture and identification of pulmonary arterial smooth muscle cells from rat distal pulmonary arteries. *Cytotechnology,* 69**,** 831-840.

PERIASAMY, M. & KALYANASUNDARAM, A. 2007. SERCA pump isoforms: their role in calcium transport and disease. *Muscle Nerve,* 35**,** 430-42.

PETERSEN, O. H., GERASIMENKO, O. V., GERASIMENKO, J. V., MOGAMI, H. & TEPIKIN, A. V. 1998. The calcium store in the nuclear envelope. *Cell Calcium,* 23**,** 87-90.

PITT, S. J., FUNNELL, T. M., SITSAPESAN, M., VENTURI, E., RIETDORF, K., RUAS, M., GANESAN, A., GOSAIN, R., CHURCHILL, G. C., ZHU, M. X., PARRINGTON, J., GALIONE, A. & SITSAPESAN, R. 2010. TPC2 is a novel NAADP-sensitive Ca2+ release channel, operating as a dual sensor of luminal pH and Ca2+. *J Biol Chem,* 285**,** 35039-46.

POBURKO, D., FAMELI, N., KUO, K. H. & VAN BREEMEN, C. 2008. Ca2+ signaling in smooth muscle: TRPC6, NCX and LNats in nanodomains. *Channels (Austin),* 2**,** 10-2.

POBURKO, D., KUO, K. H., DAI, J., LEE, C. H. & VAN BREEMEN, C. 2004. Organellar junctions promote targeted Ca2+ signaling in smooth muscle: why two membranes are better than one. *Trends Pharmacol Sci,* 25**,** 8-15.

POBURKO, D., LIAO, C. H., LEMOS, V. S., LIN, E., MARUYAMA, Y., COLE, W. C. & VAN BREEMEN, C. 2007. Transient receptor potential channel 6-mediated, localized cytosolic [Na+] transients drive Na+/Ca2+ exchanger-mediated Ca2+ entry in purinergically stimulated aorta smooth muscle cells. *Circ Res,* 101**,** 1030-8.

POZZAN, T., RIZZUTO, R., VOLPE, P. & MELDOLESI, J. 1994. Molecular and cellular physiology of intracellular calcium stores. *Physiol Rev,* 74**,** 595-636.

PROTASI, F. 2002. Structural interaction between RYRs and DHPRs in calcium release units of cardiac and skeletal muscle cells. *Front Biosci,* 7**,** d650-8.

QI, Y. X., YAO, Q. P., HUANG, K., SHI, Q., ZHANG, P., WANG, G. L., HAN, Y., BAO, H., WANG, L., LI, H. P., SHEN, B. R., WANG, Y., CHIEN, S. & JIANG, Z. L. 2016. Nuclear envelope proteins modulate proliferation of vascular smooth muscle cells during cyclic stretch application. *Proc Natl Acad Sci U S A,* 113**,** 5293-8.

RAPIZZI, E., PINTON, P., SZABADKAI, G., WIECKOWSKI, M. R., VANDECASTEELE, G., BAIRD, G., TUFT, R. A., FOGARTY, K. E. & RIZZUTO, R. 2002. Recombinant expression of the voltage-dependent anion channel enhances the transfer of Ca2+ microdomains to mitochondria. *J Cell Biol,* 159**,** 613-24.

REGAN, C. P., MANABE, I. & OWENS, G. K. 2000. Development of a smooth muscle-targeted cre recombinase mouse reveals novel insights regarding smooth muscle myosin heavy chain promoter regulation. *Circ Res,* 87**,** 363-9.

REMBOLD, C. M. & CHEN, X. L. 1998. The buffer barrier hypothesis, [Ca2+]i homogeneity, and sarcoplasmic reticulum function in swine carotid artery. *J Physiol,* 513 (Pt 2)**,** 477-92.

RENSEN, S. S., DOEVENDANS, P. A. & VAN EYS, G. J. 2007. Regulation and characteristics of vascular smooth muscle cell phenotypic diversity. *Neth Heart J,* 15**,** 100-8.

RESENDE, R. R., ANDRADE, L. M., OLIVEIRA, A. G., GUIMARAES, E. S., GUATIMOSIM, S. & LEITE, M. F. 2013. Nucleoplasmic calcium signaling and cell proliferation: calcium signaling in the nucleus. *Cell Commun Signal,* 11**,** 14.

RINNE, A., BANACH, K. & BLATTER, L. A. 2009. Regulation of nuclear factor of activated T cells (NFAT) in vascular endothelial cells. *J Mol Cell Cardiol,* 47**,** 400-10.

RIZZUTO, R., BRINI, M., MURGIA, M. & POZZAN, T. 1993. Microdomains with high Ca2+ close to IP3-sensitive channels that are sensed by neighboring mitochondria. *Science,* 262**,** 744-7.

RIZZUTO, R., PINTON, P., CARRINGTON, W., FAY, F. S., FOGARTY, K. E., LIFSHITZ, L. M., TUFT, R. A. & POZZAN, T. 1998. Close contacts with the endoplasmic reticulum as determinants of mitochondrial Ca2+ responses. *Science,* 280**,** 1763-6.

RODRIGUES, M. A., GOMES, D. A., LEITE, M. F., GRANT, W., ZHANG, L., LAM, W., CHENG, Y. C., BENNETT, A. M. & NATHANSON, M. H. 2007. Nucleoplasmic calcium is required for cell proliferation. *J Biol Chem,* 282**,** 17061-8.

ROTHBALLER, A., SCHWARTZ, T. U. & KUTAY, U. 2013. LINCing complex functions at the nuclear envelope: what the molecular architecture of the LINC complex can reveal about its function. *Nucleus,* 4**,** 29-36.

RUAS, M., DAVIS, L. C., CHEN, C. C., MORGAN, A. J., CHUANG, K. T., WALSETH, T. F., GRIMM, C., GARNHAM, C., POWELL, T., PLATT, N., PLATT, F. M., BIEL, M., WAHL-SCHOTT, C., PARRINGTON, J. & GALIONE, A. 2015. Expression of Ca(2)(+)-permeable two-pore channels rescues NAADP signalling in TPC-deficient cells. *EMBO J,* 34**,** 1743-58.

RUSSELL, J. T. 2011. Imaging calcium signals in vivo: a powerful tool in physiology and pharmacology. *Br J Pharmacol,* 163**,** 1605-25.

RZUCIDLO, E. M., MARTIN, K. A. & POWELL, R. J. 2007. Regulation of vascular smooth muscle cell differentiation. *J Vasc Surg,* 45 Suppl A**,** A25-32.

SANTELLA, L. & KYOZUKA, K. 1997. Association of calmodulin with nuclear structures in starfish oocytes and its role in the resumption of meiosis. *Eur J Biochem,* 246**,** 602-10.
SARTORE, S., SCATENA, M., CHIAVEGATO, A., FAGGIN, E., GIURIATO, L. & PAULETTO, P. 1994. Myosin isoform expression in smooth muscle cells during physiological and pathological vascular remodeling. *J Vasc Res,* 31**,** 61-81.
SCHIEDER, M., ROTZER, K., BRUGGEMANN, A., BIEL, M. & WAHL-SCHOTT, C. A. 2010. Characterization of two-pore channel 2 (TPCN2)-mediated Ca2+ currents in isolated lysosomes. *J Biol Chem,* 285**,** 21219-22.
SCHIKORSKI, T. & STEVENS, C. F. 1997. Quantitative ultrastructural analysis of hippocampal excitatory synapses. *J Neurosci,* 17**,** 5858-67.
SCHOEN, I., AIRES, L., RIES, J. & VOGEL, V. 2017. Nanoscale invaginations of the nuclear envelope: Shedding new light on wormholes with elusive function. *Nucleus***,** 1-9.
SCHWARZ, D. S. & BLOWER, M. D. 2016. The endoplasmic reticulum: structure, function and response to cellular signaling. *Cell Mol Life Sci,* 73**,** 79-94.
SEGURA-TOTTEN, M. & WILSON, K. L. 2004. BAF: roles in chromatin, nuclear structure and retrovirus integration. *Trends Cell Biol,* 14**,** 261-6.
SHARMA, P., PATCHELL, V. B., GAO, Y., EVANS, J. S. & LEVINE, B. A. 2001. Cytoplasmic interactions between phospholamban residues 1-20 and the calcium-activated ATPase of the sarcoplasmic reticulum. *Biochem J,* 355**,** 699-706.
SHIMI, T., KOUJIN, T., SEGURA-TOTTEN, M., WILSON, K. L., HARAGUCHI, T. & HIRAOKA, Y. 2004. Dynamic interaction between BAF and emerin revealed by FRAP, FLIP, and FRET analyses in living HeLa cells. *J Struct Biol,* 147**,** 31-41.
SHMIGOL, A. V., EISNER, D. A. & WRAY, S. 1999. The role of the sarcoplasmic reticulum as a Ca2+ sink in rat uterine smooth muscle cells. *J Physiol,* 520 Pt 1**,** 153-63.
SHUAI, J., ROSE, H. J. & PARKER, I. 2006. The number and spatial distribution of IP3 receptors underlying calcium puffs in Xenopus oocytes. *Biophys J,* 91**,** 4033-44.
SIECK, G. C., KANNAN, M. S. & PRAKASH, Y. S. 1997. Heterogeneity in dynamic regulation of intracellular calcium in airway smooth muscle cells. *Can J Physiol Pharmacol,* 75**,** 878-88.
SIKSOU, L., ROSTAING, P., LECHAIRE, J. P., BOUDIER, T., OHTSUKA, T., FEJTOVA, A., KAO, H. T., GREENGARD, P., GUNDELFINGER, E. D., TRILLER, A. & MARTY, S. 2007. Three-dimensional architecture of presynaptic terminal cytomatrix. *J Neurosci,* 27**,** 6868-77.
SIMMERMAN, H. K. & JONES, L. R. 1998. Phospholamban: protein structure, mechanism of action, and role in cardiac function. *Physiol Rev,* 78**,** 921-47.
SMITH, A. E., CHRONIS, C., CHRISTODOULAKIS, M., ORR, S. J., LEA, N. C., TWINE, N. A., BHINGE, A., MUFTI, G. J. & THOMAS, N. S. 2009. Epigenetics of human T cells during the G0-->G1 transition. *Genome Res,* 19**,** 1325-37.
SMITH, I. F. & PARKER, I. 2009. Imaging the quantal substructure of single IP3R channel activity during Ca2+ puffs in intact mammalian cells. *Proc Natl Acad Sci U S A,* 106**,** 6404-9.
SOARES, S., THOMPSON, M., WHITE, T., ISBELL, A., YAMASAKI, M., PRAKASH, Y., LUND, F. E., GALIONE, A. & CHINI, E. N. 2007. NAADP as a second messenger: neither

CD38 nor base-exchange reaction are necessary for in vivo generation of NAADP in myometrial cells. *Am J Physiol Cell Physiol,* 292**,** C227-39.
SOBOLOFF, J., ROTHBERG, B. S., MADESH, M. & GILL, D. L. 2012. STIM proteins: dynamic calcium signal transducers. *Nat Rev Mol Cell Biol,* 13**,** 549-65.
SOELLER, C., CROSSMAN, D., GILBERT, R. & CANNELL, M. B. 2007. Analysis of ryanodine receptor clusters in rat and human cardiac myocytes. *Proc Natl Acad Sci U S A,* 104**,** 14958-63.
SOMLYO, A. V. & SOMLYO, A. P. 1971. Strontium accumulation by sarcoplasmic reticulum and mitochondria in vascular smooth muscle. *Science,* 174**,** 955-8.
SONG, D. W., LEE, J. G., YOUN, H. S., EOM, S. H. & KIM, D. H. 2011. Ryanodine receptor assembly: a novel systems biology approach to 3D mapping. *Prog Biophys Mol Biol,* 105**,** 145-61.
SOSA, B. A., ROTHBALLER, A., KUTAY, U. & SCHWARTZ, T. U. 2012. LINC complexes form by binding of three KASH peptides to domain interfaces of trimeric SUN proteins. *Cell,* 149**,** 1035-47.
SOUTHGATE, K. & NEWBY, A. C. 1990. Serum-induced proliferation of rabbit aortic smooth muscle cells from the contractile state is inhibited by 8-Br-cAMP but not 8-Br-cGMP. *Atherosclerosis,* 82**,** 113-23.
SPINELLI, A. M. & TREBAK, M. 2016. Orai channel-mediated Ca2+ signals in vascular and airway smooth muscle. *Am J Physiol Cell Physiol,* 310**,** C402-13.
SRINIVAS, S. P., ONG, A., GOON, L. & BONANNO, J. A. 2002. Lysosomal Ca(2+) stores in bovine corneal endothelium. *Invest Ophthalmol Vis Sci,* 43**,** 2341-50.
STRELKOV, S. V., SCHUMACHER, J., BURKHARD, P., AEBI, U. & HERRMANN, H. 2004. Crystal structure of the human lamin A coil 2B dimer: implications for the head-to-tail association of nuclear lamins. *J Mol Biol,* 343**,** 1067-80.
STROUBOULIS, J. & WOLFFE, A. P. 1996. Functional compartmentalization of the nucleus. *J Cell Sci,* 109 (Pt 8)**,** 1991-2000.
SUMBILLA, C., CAVAGNA, M., ZHONG, L., MA, H., LEWIS, D., FARRANCE, I. & INESI, G. 1999. Comparison of SERCA1 and SERCA2a expressed in COS-1 cells and cardiac myocytes. *Am J Physiol,* 277**,** H2381-91.
SUZUKI, E., NISHIMATSU, H., SATONAKA, H., WALSH, K., GOTO, A., OMATA, M., FUJITA, T., NAGAI, R. & HIRATA, Y. 2002. Angiotensin II induces myocyte enhancer factor 2- and calcineurin/nuclear factor of activated T cell-dependent transcriptional activation in vascular myocytes. *Circ Res,* 90**,** 1004-11.
TAGAYA, M. & SIMMEN, T. Organelle Contact Sites.
TAKAMA, H., SUGIURA, K., OGAWA, Y., MURO, Y. & AKIYAMA, M. 2013. Possible roles of barrier-to-autointegration factor 1 in regulation of keratinocyte differentiation and proliferation. *J Dermatol Sci,* 71**,** 100-6.
TAKESHIMA, H., NISHIMURA, S., MATSUMOTO, T., ISHIDA, H., KANGAWA, K., MINAMINO, N., MATSUO, H., UEDA, M., HANAOKA, M., HIROSE, T. & ET AL. 1989. Primary structure and expression from complementary DNA of skeletal muscle ryanodine receptor. *Nature,* 339**,** 439-45.
TANG, C., TO, W. K., MENG, F., WANG, Y. & GU, Y. 2010. A role for receptor-operated Ca2+ entry in human pulmonary artery smooth muscle cells in response to hypoxia. *Physiol Res,* 59**,** 909-18.

TERASAKI, M., SHEMESH, T., KASTHURI, N., KLEMM, R. W., SCHALEK, R., HAYWORTH, K. J., HAND, A. R., YANKOVA, M., HUBER, G., LICHTMAN, J. W., RAPOPORT, T. A. & KOZLOV, M. M. 2013. Stacked endoplasmic reticulum sheets are connected by helicoidal membrane motifs. *Cell,* 154**,** 285-96.

THAKAR, R. G., CHENG, Q., PATEL, S., CHU, J., NASIR, M., LIEPMANN, D., KOMVOPOULOS, K. & LI, S. 2009. Cell-shape regulation of smooth muscle cell proliferation. *Biophys J,* 96**,** 3423-32.

TOGASHI, K., INADA, H. & TOMINAGA, M. 2008. Inhibition of the transient receptor potential cation channel TRPM2 by 2-aminoethoxydiphenyl borate (2-APB). *Br J Pharmacol,* 153**,** 1324-30.

TONG, W. C., SWEENEY, M., JONES, C. J., ZHANG, H., O'NEILL, S. C., PRIOR, I. & TAGGART, M. J. 2009. Three-dimensional electron microscopic reconstruction of intracellular organellar arrangements in vascular smooth muscle--further evidence of nanospaces and contacts. *J Cell Mol Med,* 13**,** 995-8.

TOWBIN, B. D., GONZALEZ-AGUILERA, C., SACK, R., GAIDATZIS, D., KALCK, V., MEISTER, P., ASKJAER, P. & GASSER, S. M. 2012. Step-wise methylation of histone H3K9 positions heterochromatin at the nuclear periphery. *Cell,* 150**,** 934-47.

TREBAK, M. 2012. STIM/Orai signalling complexes in vascular smooth muscle. *J Physiol,* 590**,** 4201-8.

TSIEN, R. W. & BARRETT, C. F. 2005. A brief history of calcium channel discovery. *Voltage-Gated Calcium Channels.* Springer.

VALLOT, O., COMBETTES, L., JOURDON, P., INAMO, J., MARTY, I., CLARET, M. & LOMPRE, A. M. 2000. Intracellular Ca(2+) handling in vascular smooth muscle cells is affected by proliferation. *Arterioscler Thromb Vasc Biol,* 20**,** 1225-35.

VAN BREEMEN, C. 1977. Calcium requirement for activation of intact aortic smooth muscle. *J Physiol,* 272**,** 317-29.

VAN BREEMEN, C., CHEN, Q. & LAHER, I. 1995. Superficial buffer barrier function of smooth muscle sarcoplasmic reticulum. *Trends Pharmacol Sci,* 16**,** 98-105.

VAN BREEMEN, C., FAMELI, N. & EVANS, A. M. 2013. Pan-junctional sarcoplasmic reticulum in vascular smooth muscle: nanospace Ca2+ transport for site- and function-specific Ca2+ signalling. *J Physiol,* 591**,** 2043-54.

VAN BREEMEN, C. & SAIDA, K. 1989. Cellular mechanisms regulating [Ca2+]i smooth muscle. *Annu Rev Physiol,* 51**,** 315-29.

VAN DER LOOP, F. T., GABBIANI, G., KOHNEN, G., RAMAEKERS, F. C. & VAN EYS, G. J. 1997. Differentiation of smooth muscle cells in human blood vessels as defined by smoothelin, a novel marker for the contractile phenotype. *Arterioscler Thromb Vasc Biol,* 17**,** 665-71.

VERBOOMEN, H., WUYTACK, F., DE SMEDT, H., HIMPENS, B. & CASTEELS, R. 1992. Functional difference between SERCA2a and SERCA2b Ca2+ pumps and their modulation by phospholamban. *Biochem J,* 286 (Pt 2)**,** 591-5.

VERBOOMEN, H., WUYTACK, F., VAN DEN BOSCH, L., MERTENS, L. & CASTEELS, R. 1994. The functional importance of the extreme C-terminal tail in the gene 2 organellar Ca(2+)-transport ATPase (SERCA2a/b). *Biochem J,* 303 (Pt 3)**,** 979-84.

VOLPE, P., MARTINI, A., FURLAN, S. & MELDOLESI, J. 1994. Calsequestrin is a component of smooth muscles: the skeletal- and cardiac-muscle isoforms are both present, although in highly variable amounts and ratios. *Biochem J,* 301 (Pt 2)**,** 465-9.

WANG, S., TRUMBLE, W. R., LIAO, H., WESSON, C. R., DUNKER, A. K. & KANG, C. H. 1998. Crystal structure of calsequestrin from rabbit skeletal muscle sarcoplasmic reticulum. *Nat Struct Biol,* 5**,** 476-83.

WANG, X., ZHANG, X., DONG, X. P., SAMIE, M., LI, X., CHENG, X., GOSCHKA, A., SHEN, D., ZHOU, Y., HARLOW, J., ZHU, M. X., CLAPHAM, D. E., REN, D. & XU, H. 2012. TPC proteins are phosphoinositide- activated sodium-selective ion channels in endosomes and lysosomes. *Cell,* 151**,** 372-83.

WILKERSON, M. K., HEPPNER, T. J., BONEV, A. D. & NELSON, M. T. 2006. Inositol trisphosphate receptor calcium release is required for cerebral artery smooth muscle cell proliferation. *Am J Physiol Heart Circ Physiol,* 290**,** H240-7.

WILSON, D. P., SUTHERLAND, C. & WALSH, M. P. 2002. Ca2+ activation of smooth muscle contraction: evidence for the involvement of calmodulin that is bound to the triton insoluble fraction even in the absence of Ca2+. *J Biol Chem,* 277**,** 2186-92.

WILSON, J. L., YU, J., TAYLOR, L. & POLGAR, P. 2015. Hyperplastic Growth of Pulmonary Artery Smooth Muscle Cells from Subjects with Pulmonary Arterial Hypertension Is Activated through JNK and p38 MAPK. *PLoS One,* 10**,** e0123662.

WILSON, K. L. & FOISNER, R. 2010. Lamin-binding Proteins. *Cold Spring Harb Perspect Biol,* 2**,** a000554.

WITTMANN, M., QUEISSER, G., EDER, A., WIEGERT, J. S., BENGTSON, C. P., HELLWIG, A., WITTUM, G. & BADING, H. 2009. Synaptic activity induces dramatic changes in the geometry of the cell nucleus: interplay between nuclear structure, histone H3 phosphorylation, and nuclear calcium signaling. *J Neurosci,* 29**,** 14687-700.

WOJCIKIEWICZ, R. J. 1995. Type I, II, and III inositol 1,4,5-trisphosphate receptors are unequally susceptible to down-regulation and are expressed in markedly different proportions in different cell types. *J Biol Chem,* 270**,** 11678-83.

WRAY, S. & BURDYGA, T. 2010. Sarcoplasmic reticulum function in smooth muscle. *Physiol Rev,* 90**,** 113-78.

WU, C., SUI, G. & FRY, C. H. 2002. The role of the L-type Ca(2+) channel in refilling functional intracellular Ca(2+) stores in guinea-pig detrusor smooth muscle. *J Physiol,* 538**,** 357-69.

WUYTACK, F., RAEYMAEKERS, L. & MISSIAEN, L. 2002. Molecular physiology of the SERCA and SPCA pumps. *Cell Calcium,* 32**,** 279-305.

XIAO, L., GURROLA, G. B., ZHANG, J., VALDIVIA, C. R., SANMARTIN, M., ZAMUDIO, F. Z., ZHANG, L., POSSANI, L. D. & VALDIVIA, H. H. 2016. Structure-function relationships of peptides forming the calcin family of ryanodine receptor ligands. *J Gen Physiol,* 147**,** 375-94.

XIONG, J. & ZHU, M. X. 2016. Regulation of lysosomal ion homeostasis by channels and transporters. *Sci China Life Sci,* 59**,** 777-91.

XU, L., JONES, R. & MEISSNER, G. 1993. Effects of local anesthetics on single channel behavior of skeletal muscle calcium release channel. *J Gen Physiol,* 101**,** 207-33.
XU, L. & MEISSNER, G. 2004. Mechanism of calmodulin inhibition of cardiac sarcoplasmic reticulum Ca2+ release channel (ryanodine receptor). *Biophys J,* 86**,** 797-804.
YAGODIN, S., PIVOVAROVA, N. B., ANDREWS, S. B. & SATTELLE, D. B. 1999. Functional characterization of thapsigargin and agonist-insensitive acidic Ca2+ stores in Drosophila melanogaster S2 cell lines. *Cell Calcium,* 25**,** 429-38.
YAMAZAWA, T., IINO, M. & ENDO, M. 1992. Compartments of the Ca store in single smooth muscle cells and agonist-induced Ca release. *Jpn J Pharmacol,* 58 Suppl 2**,** 411P.
YANG, D., PAN, Z., TAKESHIMA, H., WU, C., NAGARAJ, R. Y., MA, J. & CHENG, H. 2001. RyR3 amplifies RyR1-mediated Ca(2+)-induced Ca(2+) release in neonatal mammalian skeletal muscle. *J Biol Chem,* 276**,** 40210-4.
YANG, X. R., LIN, M. J., YIP, K. P., JEYAKUMAR, L. H., FLEISCHER, S., LEUNG, G. P. & SHAM, J. S. 2005. Multiple ryanodine receptor subtypes and heterogeneous ryanodine receptor-gated Ca2+ stores in pulmonary arterial smooth muscle cells. *Am J Physiol Lung Cell Mol Physiol,* 289**,** L338-48.
YOSHIKAWA, A., VAN BREEMEN, C. & ISENBERG, G. 1996. Buffering of plasmalemmal Ca2+ current by sarcoplasmic reticulum of guinea pig urinary bladder myocytes. *Am J Physiol,* 271**,** C833-41.
YOSHIMORI, T., YAMAMOTO, A., MORIYAMA, Y., FUTAI, M. & TASHIRO, Y. 1991. Bafilomycin A1, a specific inhibitor of vacuolar-type H(+)-ATPase, inhibits acidification and protein degradation in lysosomes of cultured cells. *J Biol Chem,* 266**,** 17707-12.
ZALK, R., CLARKE, O. B., DES GEORGES, A., GRASSUCCI, R. A., REIKEN, S., MANCIA, F., HENDRICKSON, W. A., FRANK, J. & MARKS, A. R. 2015. Structure of a mammalian ryanodine receptor. *Nature,* 517**,** 44-9.
ZHANG, F. & LI, P. L. 2007. Reconstitution and characterization of a nicotinic acid adenine dinucleotide phosphate (NAADP)-sensitive Ca2+ release channel from liver lysosomes of rats. *J Biol Chem,* 282**,** 25259-69.
ZHANG, Q., RAGNAUTH, C. D., SKEPPER, J. N., WORTH, N. F., WARREN, D. T., ROBERTS, R. G., WEISSBERG, P. L., ELLIS, J. A. & SHANAHAN, C. M. 2005. Nesprin-2 is a multi-isomeric protein that binds lamin and emerin at the nuclear envelope and forms a subcellular network in skeletal muscle. *J Cell Sci,* 118**,** 673-87.
ZHANG, X., CHEN, J. & WANG, S. 2017. Serum Amyloid A Induces a Vascular Smooth Muscle Cell Phenotype Switch through the p38 MAPK Signaling Pathway. *Biomed Res Int,* 2017**,** 4941379.
ZHANG, X. H. & ZHU, P. H. 1997. [Structure and pharmacology of ryanodine receptors]. *Sheng Li Ke Xue Jin Zhan,* 28**,** 224-8.
ZHANG, Y. N., XIE, B. D., SUN, L., CHEN, W., JIANG, S. L., LIU, W., BIAN, F., TIAN, H. & LI, R. K. 2016. Phenotypic switching of vascular smooth muscle cells in the 'normal region' of aorta from atherosclerosis patients is regulated by miR-145. *J Cell Mol Med,* 20**,** 1049-61.

ZHENG, R., GHIRLANDO, R., LEE, M. S., MIZUUCHI, K., KRAUSE, M. & CRAIGIE, R. 2000. Barrier-to-autointegration factor (BAF) bridges DNA in a discrete, higher-order nucleoprotein complex. *Proc Natl Acad Sci U S A,* 97**,** 8997-9002.

ZHONG, W., OGULJAHAN, B., XIAO, Y., NELSON, J., HERNANDEZ, L., GARCIA-BARRIO, M. & FRANCIS, S. C. 2014. Serum and glucocorticoid-regulated kinase 1 promotes vascular smooth muscle cell proliferation via regulation of beta-catenin dynamics. *Cell Signal,* 26**,** 2765-72.

ZHU, M. X., EVANS, A. M., MA, J., PARRINGTON, J. & GALIONE, A. 2010a. Two-pore channels for integrative Ca signaling. *Commun Integr Biol,* 3**,** 12-7.

ZHU, M. X., MA, J., PARRINGTON, J., CALCRAFT, P. J., GALIONE, A. & EVANS, A. M. 2010b. Calcium signaling via two-pore channels: local or global, that is the question. *Am J Physiol Cell Physiol,* 298**,** C430-41.

ZHUGE, R., FOGARTY, K. E., TUFT, R. A. & WALSH, J. V., JR. 2002. Spontaneous transient outward currents arise from microdomains where BK channels are exposed to a mean Ca(2+) concentration on the order of 10 microM during a Ca(2+) spark. *J Gen Physiol,* 120**,** 15-27.

ZULEGER, N., ROBSON, M. I. & SCHIRMER, E. C. 2011. The nuclear envelope as a chromatin organizer. *Nucleus,* 2**,** 339-49.

ZYLICZ, J. J., DIETMANN, S., GUNESDOGAN, U., HACKETT, J. A., COUGOT, D., LEE, C. & SURANI, M. A. 2015. Chromatin dynamics and the role of G9a in gene regulation and enhancer silencing during early mouse development. *Elife,* 4.

Publications

Research Publications

1. Ogunbayo OA, Duan J, Xiong J, Ma J, Zhu MX, Evans AM (2017). mTOR mediates lysosomal Ca^{2+} release by gating Two Pore Segment Channel 2. Science Signalling, Under review.
2. Duan J, Navarro-Dorado J, Clark JH, Kinnear NP, Meinke P, Schirmer EC, Evans AM. 2017. Nano-patterning of calcium signals within nuclear invaginations supports parallel processing and spatial segregation of chromatin types. Under revision for resubmission.
3. Duan JX, Rapti M, Tsigkou A, Lee MH. Expanding the Activity of Tissue Inhibitors of Metalloproteinase (TIMP)-1 against Surface-Anchored Metalloproteinases by the Replacement of Its C-Terminal Domain: Implications for Anti-Cancer Effects. PloS one. 2015;10(8):e0136384.

Review

1. Evans AM, Fameli N, Ogunbayo OA, Duan J, Navarro-Dorado J. From contraction to gene expression: Nanojunctions of the sarco/endoplasmic reticulum deliver site- and function-specific calcium signals. Sci China Life Sci. 2016;59:749-763

Abstracts

1. **POSTER PRESENTATION**
   Duan J, Navarro-Dorado J., Evans AM (2016). Strategic positioning of chromatin anchoring NET protein complexes in the nuclear invaginations of pulmonary arterial smooth muscle cells. Proc Physiol Soc 37, PCAA303 (2016)

   Physiology 2016, sponsored by the Physiological Society
   Convention Centre Dublin, Ireland
   29—31 July 2016

2. **POSTER PRESENTATION**
   Duan J, Navarro-Dorado J., Evans AM (2017) Strategic positioning of chromatin anchoring NET protein complexes in the nuclear invaginations of pulmonary arterial smooth muscle cells

The Pleiotropic Nuclear Envelope, sponsored by the Biochemical Society

John McIntyre Conference Centre, University of Edinburgh, UK

22—25 August 2017